The electron antineutrino angular correlation coefficient a in free neutron decay: Testing the Standard Model with the aSPECT-Spectrometer

Vorgelegt von:
Michael Borg
geb. in Mainz
Mainz, im Dezember 2010
D77

Tag der mündlichen Prüfung: 04.02.2011

Kurzzusammenfassung

Der β-Zerfall freier Neutronen ist ein Prozess, welcher im Standard Modell (SM) der Elementarteilchenphysik stark überbestimmt ist und durch eine Vielzahl von Observablen beschrieben wird. Einige dieser Observablen sind sensitiv auf Physik jenseits des SM. Hierzu zählen zum Beispiel die Korrelationskoeffizienten zwischen den beteiligten Teilchen. Das Spektrometer aSPECT wurde konzipiert, um das Energiespektrum der Zerfalls-Protonen präzise zu vermessen und hieraus den Elektron-Antineutrino-Winkel-Korrelationskoeffizienten a zu extrahieren.

Eine erste Testperiode (2005/ 2006) bestätigte die Funktionsweise des Messaufbaus. Der limitierende Einfluss von unkontrollierbarem Untergrund im Spektrometer machte aber eine verlässliche Angabe von a unmöglich (veröffentlicht in 2008 [1]). Ein zweiter Messzyklus (2007/ 2008) hatte zum Ziel, die relative Genauigkeit vorangegangener Experimente von $\frac{\delta a}{a} = 5\,\%$ [2], [3] zu unterschreiten. Der Schwerpunkt dieser Dissertationsarbeit liegt auf der von mir durchgeführten Analyse der hierzu aufgenommenen Daten. Einen zentralen Punkt bilden hierbei Untergrund-Studien. Der systematische Einfluss des Untergrundes konnte auf $\frac{\delta a^{(\text{syst.})}}{a} = 0.61\,\%$ reduziert werden. Die statistische Genauigkeit der analysierten Messungen beträgt $\frac{\delta a^{(\text{stat.})}}{a} \approx 1.4\,\%$. Darüber hinaus wurden erstmals aufgetretene Sättigungseffekte der Detektor-Elektronik untersucht. Diese stellten sich als nicht ausreichend korrigierbar heraus. Ein anwendbarer Lösungsvorschlag bzgl. des Sättigungseffektes wird im abschließenden Kapitel diskutiert.

Abstract

The β-decay of free neutrons is a strongly over-determined process in the Standard Model (SM) of Particle Physics and is described by a multitude of observables. Some of those observables are sensitive to physics beyond the SM. For example, the correlation coefficients of the involved particles belong to them. The spectrometer aSPECT was designed to measure precisely the shape of the proton energy spectrum and to extract from it the electron anti-neutrino angular correlation coefficient a .

A first test period (2005/ 2006) showed the "proof-of-principles". The limiting influence of uncontrollable background conditions in the spectrometer made it impossible to extract a reliable value for the coefficient a (published in 2008 [1]). A second measurement cycle (2007/ 2008) aimed to under-run the relative accuracy of previous experiments of $\frac{\delta a}{a} = 5\,\%$ [2], [3]. I performed the analysis of the data taken there which is the emphasis of this doctoral thesis. A central point are background studies. The systematic impact of background on a was reduced to $\frac{\delta a^{(\text{syst.})}}{a} = 0.61\,\%$. The statistical accuracy of the analyzed measurements is $\frac{\delta a^{(\text{stat.})}}{a} \approx 1.4\,\%$. Besides, saturation effects of the detector electronics were investigated which were initially observed. These turned out not to be correctable on a sufficient level. An applicable idea how to avoid the saturation effects will be discussed in the last chapter.

Contents

1 Introduction

1.1 Motivation

A general effort of physics is the exploration and characterization of the world that surrounds us on all length scales and to simplify its description to an elementary level. A unified theory describing all fundamental forces by the same mathematical formalism is one of the great aims of contemporary physics. A first step to approach this unification was the development of the Standard Model of Particle Physics (SM) starting in the 1960´s. It became the great success of particle physics in the 1970´s since it described all phenomena and observed particles known so far. And it predicted a multitude of particles which were later detected in experiments at high energy accelerators.

At present, the SM is the theory that describes precisely the known elementary particles and their interactions. It classifies them into two groups: quarks and leptons. Each group is divided in three generations containing two particles each. Each particle has its antiparticle which has the same mass. The antiparticle of a charged particle carries opposite charge. The SM unifies the strong, the weak and the electromagnetic interaction by a single Hamiltonian. But it does not include gravitation as field theory. Tab. 1.1 summarizes the particles[1] and their interactions in the SM. Gauge bosons are the carriers of

Type of particle	Generation			Effective interactions		
	1st	2nd	3rd	El.magn.	Strong	Weak
Leptons	e	μ	τ	yes	no	yes
	ν_e	ν_μ	ν_τ	no	no	yes
Quarks	u	c	t	yes	yes	yes
	d	s	b	yes	yes	yes

Table 1.1: The elementary particles and their interactions in the SM description. Gravity is not included.

the fundamental forces: the exchange of photons mediates the electromagnetic interaction and is experienced by all charged particles. The strong interaction is mediated by gluons and experienced only by quarks and gluons themselves. The formation of atomic

---

[1]A distinction of quarks by their color charge is not considered in this table.

nuclei is based on the strong force. The exchange of Z and $W^{\pm}$ bosons mediates the weak interaction. It affects both leptons and quarks which makes it more universal than the strong interaction. The flavor of particles is not conserved in weak interaction like in electromagnetic interaction. It manifests for example in the nuclear β-decay.

Despite its great success in the last decades, the SM cannot answer all questions that arise in modern particle physics. Beside the exclusion of gravity it cannot explain, for example, the baryon asymmetry in the universe, the number of quark generations, the observed symmetry breaking, the number of parameters in the theory as well as the existence of Dark Matter and Dark Energy.

Apart from experiments on the upper energetic scale (e.g., at high energy accelerators such as LHC at CERN / Geneva), another approach to physics beyond the SM is in the low energy limit. High precision measurements of small deviations from SM predictions could indicate new physics [4]. In this context, the neutron is a powerful and comparatively simple system. For example, one of the most important tests for physics beyond the SM is the ongoing search for a permanent electric dipole moment d_n (EDM) of the neutron: Although the neutron has no electrical charge, its constituents (the quarks) carry charge. An EDM might remain from their distribution. Up to now, all results of these studies are compatible with zero. They deliver an upper limit of $d_n < 2.9 \cdot 10^{-26}\,e\,\mathrm{cm}$ [6]. Still these investigations provided strong constraints on different theories going beyond the SM.

Free neutrons are unstable and decay with a mean life time of about 15 minutes into a proton p, an electron e^- and an electron antineutrino $\bar{\nu}_{\mathrm{e}}$:

$$n \rightarrow p + e^- + \bar{\nu}_{\mathrm{e}} + 782.3\,\mathrm{keV}. \tag{1.1}$$

The energy released is given by the mass difference of the neutron compared to proton and electron [7] (see sect. 2.3, tab. 2.1). In general, the decay of a nucleus with atomic numbers (A,Z) into a daughter nucleus (A,Z+1) by emission of an electron and an antineutrino is called beta-minus (β^-)-decay. The minus refers to the negative charge of the outgoing electron. In the SM, neutron decay is described by 3 parameters additional to the Fermi constant G_F which is known from μ-decay: $|V_{ud}|$, the matrix element that describes the transition of a down quark to an up quark, the ratio $\lambda = |g_A/g_V|$ of the axial-vector and vector coupling constants and a phase $e^{i\phi}$. The phase is real and $\phi = 180°$ in the SM. Free neutron decay is the basic form of β^--decay of nuclei. The wave functions of neutron and proton in the transition matrix element that characterizes neutron β-decay are identical. Therefore no nuclear structure effects occur and also no nuclear shell corrections are necessary, at least to first order. About a dozen different observables are accessible in free neutron decay which makes it a strongly over-determined process in the SM description. In chapter 2, I will focus on the detailed theory concerning β-decay as well as on the explanation of the various parameters.

The neutron life time τ_n is one of the measurable parameters in free neutron decay.

It is proportional to $|V_{ud}|$ and λ:

$$\tau_n^{-1} \propto (G_F)^2 \cdot (V_{ud})^2 \cdot (1 + 3\,|\lambda|^2) \tag{1.2}$$

There are ongoing disputes about the exact life time of the neutron in term of order seconds, as there are only two measurements with small error bars [8], [9]. But these two results differ by about 6 standard deviations. Only further measurements with high statistics and considerably reduced systematics may resolve this conflict.

In the description of the three body decay of the neutron one can define angular correlations between the momenta and spins of the participating particles. The differential decay probability $dW(\vec{p}_e, \vec{p}_{\bar{\nu}})$ can be expressed by [10]:

$$dW(\vec{p}_e, \vec{p}_{\bar{\nu}}) \propto 1 + b\frac{m_e}{E_e} + a\frac{\vec{p}_e \cdot \vec{p}_{\bar{\nu}}}{E_e E_{\bar{\nu}}} + \frac{\vec{P}_n}{P_n} \cdot \left(A\frac{\vec{p}_e}{E_e} + B\frac{\vec{p}_{\bar{\nu}}}{E_{\bar{\nu}}} + D\frac{\vec{p}_e \times \vec{p}_{\bar{\nu}}}{E_e E_{\bar{\nu}}} + R\frac{\vec{p}_e \times \vec{P}_e}{E_e} \right) + \ldots \tag{1.3}$$

where m_e is the mass of the electron. $\vec{p}_{\bar{\nu}}$, $\vec{p}_e$, $E_{\bar{\nu}}$ and E_e are the momenta and energies of antineutrino and electron, respectively. $\vec{P}_e$ and $\vec{P}_n$ are the polarizations of electron and neutron.

The coefficients $a, A, b, B, D, R \ldots$ can be determined experimentally as well as theoretically (a: Electron-antineutrino angular correlation, A: Beta asymmetry, b: Fierz interference term, B: Neutrino asymmetry, D and R: Triple correlation coefficients). Some of these coefficients explicitly contain parity (P) (e.g., A, B) and/ or time reversal (T) violation (e.g., D, R) [4], [5]. According to the SM, neutron beta decay can be described as a V-A type interaction (see chapter 2). Then, the Fierz interference term vanishes, $b = 0$ [1]. If time reversal invariance does hold (D=0, R=0 in the SM description), eq. 1.3 reduces to the terms expressed by the correlation coefficients a, A and B which all depend on a single parameter, λ:

$$a = \frac{1 - |\lambda|^2}{1 + 3\,|\lambda|^2} \tag{1.4}$$

$$A = -2\frac{|\lambda|^2 + Re\,\lambda}{1 + 3\,|\lambda|^2} \tag{1.5}$$

$$B = 2\frac{|\lambda|^2 - Re\,\lambda}{1 + 3\,|\lambda|^2} \tag{1.6}$$

The parameter λ takes into account the renormalization of the axial vector current by the structure of the nucleon. Its calculation from first principles cannot be done well enough, so λ has to be determined experimentally. Measurements of the correlation coefficients a, A and B give three independent ways of access to λ. Their systematic error budget is entirely different [1]. Taking the most recent value $\lambda = -1.2694(28)$ from the Particle Data Group (PDG) [7], the sensitivities are:

$$\frac{da}{d\lambda} = -0.298, \ \frac{dA}{d\lambda} = -0.374, \ \frac{dB}{d\lambda} = -0.076 \tag{1.7}$$

Highly precise measurements of these angular correlation coefficients, essentially of A and a, can provide direct tests of the validity of the SM. The search for scalar and tensor interactions is for example of particular interest here. These interactions would result in additional terms in eq. 1.4 to 1.6. They could be caused by the hypothetical existence of leptoquarks or charged Higgs bosons (for details see the review by Severijns *et al.* [4]).

Apart from being an intrinsic probe for physics beyond the SM, the correlation coefficients can be used to determine the upper left matrix element of the Cabibbo-Kobayashi-Maskawa[2] (CKM) matrix, V_{ud}. The determination of λ in combination with measurements of the neutron lifetime τ_n are required as introduced by eq. 1.2.

In the SM, the eigenstates of the quarks in weak interaction are not the same as their mass eigenstates. The weak eigenstates are linear combinations of the mass eigenstates from all three generations with the same charge. For the first two quark families, the linear combinations were formulated by Cabibbo in 1963 [39] as a rotation matrix with a rotation angle θ_C ("Cabibbo angle"):

$$\begin{pmatrix} |d'\rangle \\ |s'\rangle \end{pmatrix} = \begin{pmatrix} \cos\theta_C & \sin\theta_C \\ -\sin\theta_C & \cos\theta_C \end{pmatrix} \cdot \begin{pmatrix} |d\rangle \\ |s\rangle \end{pmatrix}, \tag{1.8}$$

The third quark generation was found later and eq. (1.8) was extended to a 3×3 matrix [40]. The CKM matrix (also called: quark mixing matrix) describes the mixing of quark mass eigenstates $|q\rangle$ of d-type quarks (eq. 1.9, right) to the eigenstates of the weak interaction $|q'\rangle$ (eq. 1.9, left) that couple to u-type quark eigenstates. Herewith, the CKM matrix describes the probability of a transition from one quark i to another quark j which is $\propto |Vij|^2$.

$$\begin{pmatrix} |d'\rangle \\ |s'\rangle \\ |b'\rangle \end{pmatrix} = \begin{pmatrix} V_{ud} & V_{us} & V_{ub} \\ V_{cd} & V_{cs} & V_{cb} \\ V_{td} & V_{ts} & V_{tb} \end{pmatrix} \cdot \begin{pmatrix} |d\rangle \\ |s\rangle \\ |b\rangle \end{pmatrix}. \tag{1.9}$$

The Standard Model assumes three quark generations and consequently requires unitarity of the CKM matrix. For example, one of the unitarity conditions for the first row is given by:

$$|V_{ud}|^2 + |V_{us}|^2 + |V_{ub}|^2 = 1 \tag{1.10}$$

V_{ud} can as well be determined from nuclear β-decay experiments. Its determination from neutron β-decay offers complementary informations to different systematics. Together with measurements of $|V_{us}|$ from, for example, K-decays ([11], [12]) and $|V_{ub}|$ from B-meson decays ([13]), unitarity can be tested. To date, there is an ongoing discussion whether or not unitarity is violated [1] (for more details see [14] and [15]).

---

[2]Kobayashi and Maskawa were awarded with the Nobel Price for Phyics in 2008 for their studies on symmetry breaking in the Kaon decay which initially lead to the postulation of further quark generations.

The coefficient A has the highest sensitivity towards λ (see eq. 1.4). A describes the angular correlation between the electron momentum and the spin of the neutron (measured with a polarized cold neutron beam) which violates parity (equivalent to the Wu-experiment [16]). In the last decades it was measured in several experiments with increased accuracy by reducing both the statistical and, in particular, the systematic errors. One of the systematic limitations of recent measurements of A is the polarization of the neutrons. The PDG uses at the moment data from three collaborations for the determination of λ extracted from measurements of A : Heidelberg University ([17], [18]), LNPI/PNPI Gatchina ([19]) and the Technical University of Munich ([20]), [5]. The most precise value was measured by the Perkeo II collaboration. The average of all Perkeo II measurements gives a preliminary value of $A = 0.11933(34)$ [5]. But it is not in good agreement with other previous experiments. Therefore the PDG decided to increase the error bars of the world average value to $A = 0.1173(13)$ [7]. Further measurements of A with a new spectrometer Perkeo III are in progress and one aims to verify the A-value of Perkeo II [21].

The inconsistent values of A motivate the determination of λ via other correlation coefficients such as a. a is only slightly less sensitive to λ, but offers a good possibility to extract λ with totally different systematics than A. a describes the angular correlation between the momenta of the electron and the antineutrino, $\vec{p}_e$ and $\vec{p}_{\bar{\nu}}$, respectively. The term in eq. 1.3 described by a comprises the scalar product $\vec{p}_e \cdot \vec{p}_{\bar{\nu}}$. Therefore, a conserves both time reversal invariance and parity. a is measured with unpolarized neutrons.

The accuracy of the most accurate measurements performed by C. Stratowa et $al.$ [2] and J. Byrne et $al.$ [3] was about 5% and results in an average of $a = -0.103(4)$ [7]. The measurement of Stratowa et $al.$ was limited by the knowledge of the detector response function. The experiment of Byrne et $al.$ used also the retardation spectrometer technique and lead to the design of the aSPECT spectrometer. Details concerning this technique will be discussed in chapter 3. The measurement of Byrne et $al.$ was basically limited by non-adiabatic transitions. The extraction of λ from the present value of a gives an error which is about a factor of 5 higher than its extraction from the coefficient A [5].

aSPECT is a newly developed retardation spectrometer based on the MAC-E filter technique. Its concept and technical realization is discussed in detail in chapter 3 and in the paper of F. Glück et $al.$ [22]. aSPECT aims to measure a with a relative accuracy of 0.3%. Since the antineutrino can hardly be detected, we extract the coefficient from a precise measurement of the proton recoil spectrum in free neutron decay. The proton spectrum can be written as

$$dw_p(T) \propto g_1(T) + ag_2(T) \tag{1.11}$$

$g_1(T)$ and $g_2(T)$ are known functions of the kinetic energy T of the proton as given by [23]. In [24], g_1 and g_2 are calculated including radiative corrections on T. Fig. 1.1a illustrates the dependence of these functions. In fig. 1.1b, the effect of a non-vanishing value of a on the proton recoil spectrum is shown. Positive values of a deform the spectrum towards

higher kinetic energies, negative values to lower energies. Most of the released energy is carried away by the electron and the antineutrino due to momentum conservation (see sect. 2.3). The proton gains a maximal kinetic energy of 751.4 eV.
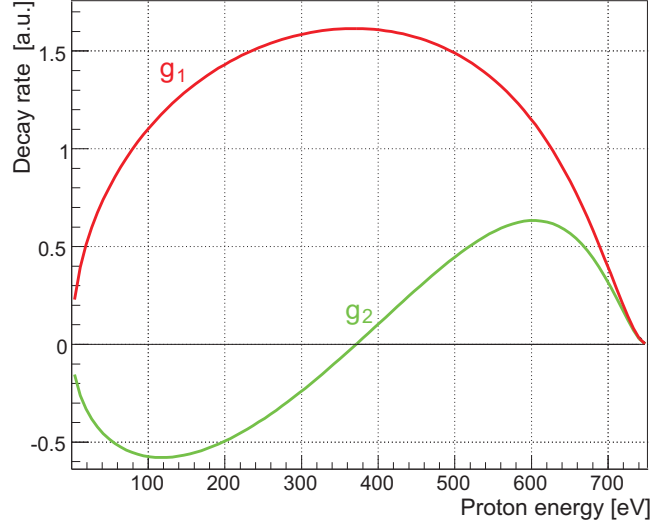
(a) Functions g_1 and g_2. The decay rate is $\propto g_1 + ag_2$.
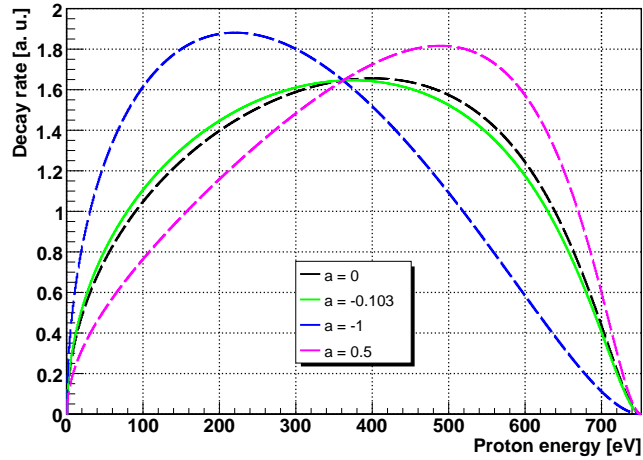
(b) Spectra for different a values.

Figure 1.1: (a) Dependence of the functions $g_1(T)$ and $g_2(T)$. (b) Proton spectra for hypothetical values of a to demonstrate its impact on the spectrum. $a = -0.103(4)$ is the present value given by the PDG [7] (green line).

The consideration of two extreme kinematic cases, depicted in fig. 1.2, helps to understand the impact of a on the proton recoil spectrum: If electron and antineutrino are emitted with parallel momenta, the proton carries a maximal recoil momentum due to momentum conservation. If electron and antineutrino are emitted with perpendicular mo-

menta, the proton will carry a rather low momentum. In this case, its energy spectrum will be shifted towards lower energies, as shown in fig. 1.1, (b).
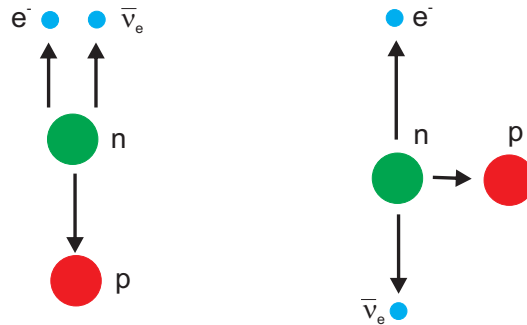
Figure 1.2: Scheme to illustrate the impact of the emission angle between electron and antineutrino on the proton spectrum: In the case depicted on the left side, the proton recoil energy is maximal. In the case depicted on the right it is minimal.

1.2 Prologue

The construction of the new spectrometer aSPECT was proposed in 2000 [26]. The design was finished end of 2003 and published in 2005 [22]. In March 2005, the spectrometer was finally delivered to the Johannes Gutenberg-Universität Mainz. We performed first tests of functionality at the TRIGA reactor of the Institut für Kernchemie until end of June 2005. From July 2005 to end of May 2006, we had a first measurement cycle ("beam time") at the Forschungsneutronenquelle Heinz Maier-Leibnitz ("FRM II") in Garching. Our focus was a first proof of principles of the spectrometer itself and its setup (e.g., detector setup, beam line and data acquisition (DAQ) system). One of my most appropriate tasks was the simulation and construction of a neutron collimation system.

At that time, the aSPECT collaboration split up in two main participating groups: Our partners of the Technische Universität München (TUM), Physik Department E18 under leadership of Prof. Dr. O. Zimmer and our group of the Institut für Physik of the Johannes Gutenberg-Universität Mainz, WA QUANTUM/ AG Heil under leadership of Prof. Dr. W. Heil. Our collaborators of the TUM were primary responsible for the entire detector setup and the DAQ-system. Our group was responsible for the magnetic and electric field performances, the vacuum system and the neutron collimation. In the FRM II beam time, we performed dozens of systematic tests. Further, the setup could be upgraded by various improvements in both hardware and software. The FRM II beam time resulted in two diploma theses of F. Ayala [27] and M. Simson [28] as well as in two PhD theses of G. Petzoldt [29] and of R. Muñoz [25]. The latter one is ongoing but probably will be finished beginning of 2011.

aSPECT was reinstalled in June 2006 in Mainz and its performance was improved. The Institut für Kernchemie offered us the opportunity to use its infrastructure at the TRIGA reactor. The spectrometer was prepared for the next measurement runs that started end of 2007 until June 2008 at the Institut Laue-Langevin (ILL) in Grenoble/ France. Four PhD students[3] with different individual tasks were responsible for the realization of the beam time:

(1) G. Konrad [30]: Calculations on the electric and magnetic field system. Calculations and construction of an antimagnetic screen for aSPECT. Calculation of particle trajectories, trapping effects and other systematic corrections.

(2) F. Ayala [31]: Magnetic field performance and systematic studies on reproducibility and stability of the field parameters. Development of a NMR-system for on-line monitoring of the magnetic field of aSPECT. Preparation and realization of new parts of the inserted electrode system (see sect. 3.2.3.

(3) M. Simson [32]: Detection system including the assortment of a new detector type and its integration into the existing system. Characterization and computation of detector properties. Hard- and software realization of the DAQ system as well as on-line raw data decoding. Data analysis of the ILL data on detector properties and its performances.

(4) My tasks were on the one hand the technical improvement of the setup: HV-stability tests, implementation of necessary modifications (e.g., electric field simulation and construction of a new upper ExB-drift electrode). Vacuum tests, detector tests with the detector used at FRM II (see section 3.5.2). I performed tests of all modified parts of the aSPECT setup. On the other hand, I planned a new beam line setup. It was adapted to the circumstances at ILL. The planning (e.g., transport from Mainz to Grenoble and build-up at ILL) and coordinative scheduling (e.g., mounting and adjusting of the setup) of the ILL beam time in correspondence with the beam line responsible were additional tasks. Besides, I designed in 2006 a helium ion source prototype which was tested in 2007 on aSPECT at TRIGA/ Mainz (see Appendix 12).

After the ILL beam time, I took responsibility for data analysis. In co-operation with M. Simson, I developed a reliable pulse shape analysis method. Different types of studies necessary for an extraction of the coefficient a were performed: Analysis of the stabilities of various parameters of the experimental setup (e.g., DAQ, HV, neutron flux), time-of-flight analysis, exploration of an applicable background analysis and derivation of corrections. Detection and analysis of detector effects (e.g., trigger efficiency and saturation effects) and effects of the DAQ system. Analysis of the neutron beam profiles measured at ILL.

The thesis at hand is structured in six main parts: In chapter 2 I will give a more detailed view on the theoretical background. Chapter 3 focusses on the technical setup of the experiment and recent modifications. It ends with an overview on the expected systematic effects. Chapter 4 contains both data analysis and results. Chapter 5 summarizes my thesis. An appendix comprises manuals, additional technical informations and studies.

---

[3]I will not discuss here the various and needful work of others collaborators (e.g., the beam line responsible T. Soldner).

2 Theory

This chapter contains a brief overview on the theory of weak interaction, in particular on neutron β^--decay. It is a well-known field which has been reviewed in many books and articles. The overview is generally based on reviews by N. Severijns *et al.* [4] and H. Abele [5] as well as on former publications by our *a*SPECT collaboration ([22], [26] and [1]).

2.1 Theory of β-decay

2.1.1 Selection rules

Neutron β^--decay as shown in eq. (1.1), as well as any other nuclear β-decay is a phenomenon of weak interaction. In general, β-transitions are divided into *allowed* and *forbidden* transitions. The classification depends on the transfer of orbital angular momentum to lepton pairs: Allowed transitions correspond to processes in which no orbital angular momentum is transfered. In contrast, transitions with $l \neq 0$ are called forbidden and are strongly suppressed. The selection rules of allowed transitions are

$$\Delta J = J_i - J_f = 0, \pm 1,$$
$$\pi_i \pi_f = +1,$$

where $J_{i,(f)}$ and $\pi_{i,(f)}$ designate the spin and parity of the initial (final) state [4]. The spins of electron and antineutrino are 1/2 each. Thus, they can couple to a total spin $\vec{S}$ of 0 or 1. If the spins couple to the singlet state $S = 0$, the transition is called Fermi decay. The transition to the triplet state $S = 1$ is called Gamow-Teller decay. Or, if we regard the spin $\vec{J}$ of the daughter nucleus (or proton in our case):

$$\Delta J \quad = \quad 0 : \text{ Fermi selection rules}$$

$$\Delta J \quad = \quad 0 \text{ (but not } 0 \to 0), \pm 1 : \text{ Gamow} - \text{Teller selection rules}$$

In the case of Gamow-Teller decays, transitions between states of zero angular momentum $(0\to0)$ are excluded: It is not possible to generate a triplet state for $J_i = J_f = 0$ [4]. In

Fermi decays the spin of the nucleus does not change. In Gamow-Teller decays the spin can change if the spins of e^- and $\bar{\nu}_e$ couple to $S_z = \pm 1$. The observation of decays which fulfill only one of the selection rules allow for exclusive studies on the different transition modes (e.g., pure Fermi decays such as $^{14}O \rightarrow {}^{14}N$ and pure Gamow-Teller decays such as $^6He \rightarrow {}^6Li$). In the case of the free neutron both decay modes are realized.

2.1.2 Classical theory

The first theory concerning β-decay was proposed by Enrico Fermi in 1934 [34]. It was a phenomenological description deduced from the analogy to the theory of the electromagnetic interaction as illustrated in fig. 2.1: (a) shows an electron-photon vertex, (b) the analogous graph for a neutron decay in Fermi's theory. The coupling of the photon to the

Figure 2.1: Feynman graphs: (a) An electron-photon vertex. (b) Neutron decay in Fermi's presentation. The time arrow is pointing to the right.

electron is given by the Hamiltonian density[1]

$$\mathcal{H} = ej_\mu^{\text{em}} \cdot A^\mu, \qquad (2.1)$$

with the electron charge e, the 4-vector potential of the electromagnetic field A^μ and the electromagnetic current density $j_\mu^{\text{em}} = \bar{\Psi}_e \gamma_\mu \Psi_e$. Ψ_e is the electron spinor field function and $\bar{\Psi}_e$ the corresponding adjoint function. $\gamma^\mu = (\gamma^0, \gamma^1, \gamma^2, \gamma^3)$ are the γ-matrices[2].

Fermi´s theory assumes a point like interaction between the participating particles. Fermi replaced the 4-vector potential by a leptonic current, the electromagnetic by a

---

[1]The sum convention by Bjorken-Drell [35] is used here.

[2]$\gamma^0 = \begin{pmatrix} \mathbf{I} & 0 \\ 0 & -\mathbf{I} \end{pmatrix}, \vec{\gamma} = \begin{pmatrix} 0 & \vec{\sigma} \\ -\vec{\sigma} & 0 \end{pmatrix}, \gamma^5 = i\gamma^0\gamma^1\gamma^2\gamma^3 = \begin{pmatrix} 0 & \mathbf{I} \\ \mathbf{I} & 0 \end{pmatrix}, \vec{\sigma}$ are the Pauli matrices.

hadronic current and the electric charge e by the Fermi coupling constant G_{F}:

$$A^{\mu}(x) \quad \rightarrow \quad J^{\mu,\ \mathrm{lep}}(x) = \bar{\Psi}_{\mathrm{e}}(x)\gamma^{\mu}\Psi_{\bar{\nu}}(x) \tag{2.2}$$

$$j^{\mathrm{em}}_{\mu}(x) \quad \rightarrow \quad J^{\mathrm{had}}_{\mu}(x) = \bar{\Psi}_{\mathrm{p}}(x)\gamma_{\mu}\Psi_{\mathrm{n}}(x) \tag{2.3}$$

$$e \quad \rightarrow \quad \left(\frac{G_{\mathrm{F}}}{\sqrt{2}}\right) \tag{2.4}$$

The Fermi coupling constant can be determined with high accuracy from μ-decay: $G_{\mathrm{F}}/(\hbar c)^3 = 1.16637(1)$ GeV^{-2} [7]. In analogy to eq. (2.1) the Hamiltonian density for the β-decay can now be written as

$$\mathcal{H}_{Fermi}(x) = \frac{G_{\mathrm{F}}}{\sqrt{2}}(J^{\dagger}_{\mu}(x) \cdot J^{\mu}(x) + \mathrm{h.c.}) \tag{2.5}$$

where the current J_{μ} is the sum of the hadronic and the leptonic currents:

$$J_{\mu} = J^{\mathrm{had}}_{\mu} + J^{\mathrm{lep}}_{\mu}. \tag{2.6}$$

Please note, that in following convenient formulations the convention on the metric is changed to the one used by Severijns *et al.* [4] which is adopted from Jackson *et al.* [10]. This metric is used by most publications concerning experiments on weak interaction. It introduces a different representation of the γ-matrices compared to the convention used by Bjorken-Drell [35]. In particular, the signs of γ_5 are opposite in the two representations [4]:

$$\gamma^5 = \begin{pmatrix} 0 & -\mathbf{I} \\ -\mathbf{I} & 0 \end{pmatrix} \tag{2.7}$$

Fermi considered only vector-vector coupling since $\bar{\Psi}\gamma_{\mu}\Psi$ behaves like a polar vector under Lorentz transformations. Gamov and Teller extended Fermi´s formulation in 1936 [36] to describe transitions which required the introduction of other possible Lorentz invariants. They formulated a general Hamiltonian by including all possible interaction terms which are invariant under Lorentz-, parity- and time-reversal transformation [4]:

$$\mathcal{H}_{\beta} = \left(\bar{\Psi}_{\mathrm{p}}\Psi_{\mathrm{n}}\right) \cdot \left(\bar{\Psi}_{\mathrm{e}}[C_S + C'_S\gamma_5]\Psi_{\nu}\right) + \left(\bar{\Psi}_{\mathrm{p}}\gamma_{\mu}\Psi_{\mathrm{n}}\right) \cdot \left(\bar{\Psi}_{\mathrm{e}}\gamma_{\mu}[C_V + C'_V\gamma_5]\Psi_{\nu}\right)$$
$$+ \frac{1}{2}\left(\bar{\Psi}_{\mathrm{p}}\sigma_{\lambda\mu}\Psi_{\mathrm{n}}\right) \cdot \left(\bar{\Psi}_{\mathrm{e}}\sigma_{\lambda\mu}[C_T + C'_T\gamma_5]\Psi_{\nu}\right) - \left(\bar{\Psi}_{\mathrm{p}}\gamma_{\mu}\gamma_5\Psi_{\mathrm{n}}\right) \cdot \left(\bar{\Psi}_{\mathrm{e}}\gamma_{\mu}\gamma_5[C_A + C'_A\gamma_5]\Psi_{\nu}\right)$$
$$+ \left(\bar{\Psi}_{\mathrm{p}}\gamma_5\Psi_{\mathrm{n}}\right) \cdot \left(\bar{\Psi}_{\mathrm{e}}\gamma_5[C_P + C'_P\gamma_5]\Psi_{\nu}\right) + \mathrm{h.c.} \tag{2.8}$$

with the tensor operator $\sigma_{\lambda\mu}$ given by

$$\sigma_{\lambda\mu} = -\frac{i}{2}(\gamma_{\lambda}\gamma_{\mu} - \gamma_{\mu}\gamma_{\lambda}). \tag{2.9}$$

The interactions are described by five operators: The scalar $\Gamma_S = 1$, the vector $\Gamma_V = \gamma_\mu$, the tensor $\Gamma_T = \frac{\sigma_{\lambda\mu}}{\sqrt{2}}$, the axial vector $\Gamma_A = -i\gamma_\mu\gamma_5$ and the pseudoscalar $\Gamma_P = \gamma_5$. The coefficients C_i and C_i' ($i \in [S, V, T, A, P]$) determine the relative amplitude of each interaction [4]. These amplitudes can be complex corresponding to a total of 20 real parameters. In principle, any two of the given five operators can be used to define current densities. These current densities could be combined to a current-current-type interaction. But since the Hamiltonian has to be either of scalar or pseudoscalar form, only couplings of the types S-S, V-V, T-T, A-A, P-S and V-A are possible.

The Hamiltonian density eq. 2.8 can be simplified as shown in [37]:

$$\mathcal{H} = \frac{G_W}{\sqrt{2}} \sum_i \left[L_i \left(\bar{\Psi}_p \Gamma_i \Psi_n \right) \cdot \left(\bar{\Psi}_e \Gamma_i (1 + \gamma_5) \Psi_\nu \right) + R_i \left(\bar{\Psi}_p \Gamma_i \Psi_n \right) \cdot \left(\bar{\Psi}_e \Gamma_i (1 - \gamma_5) \Psi_\nu \right) \right] + \text{h.c.}$$

(2.10)

by using the following parametrization of the weak coupling constants C_i and C_i' [37]:

$$C_i = \frac{G_W}{\sqrt{2}}(L_i + R_i), \quad C_i' = \frac{G_W}{\sqrt{2}}(L_i - R_i).$$

(2.11)

$G_W = G_F \cdot V_{ud}$ is a general weak coupling constant also introduced in [37].

Eq. (2.10) is constructed in a way that the first part of the sum corresponds to left-handed currents and the second part to right-handed currents. $(1 + \gamma_5)\Psi_\nu/2$ and $(1 - \gamma_5)\Psi_\nu/2$ are the left- and right-handed projections of the antineutrino wave functions, respectively. The coupling constants L_i and R_i in eq. 2.11 have to be determined experimentally. The Hamiltonian violates parity if $L_i \neq R_i$, time reversal invariance is violated if the coupling constants have an imaginary part.

Gamow-Teller transitions change the spin ($\Delta J = 1$) and are mediated by axial-vector and tensor couplings, whereas scalar and vector couplings contribute to Fermi transitions ($\Delta J = 0$).

2.1.3 V-A theory

Lee and Yang [38] postulated in 1956 that parity might not be conserved in β-decay and Wu *et al.* [16] proved this theory experimentally in the decay of ^{60}Co shortly after. In this experiment, radioactive cobalt-60 atoms at a low temperature were aligned with their spins parallel to a strong magnetic field. The preferred direction of electron emission was observed. Wu *et al.* showed that the electrons are preferentially emitted in a direction opposite to the direction of the nuclear spin.

So far parity was found to be maximally violated in weak interaction by all experiments. This means, only left-handed components of vector and axial-vector couplings

contribute to β-decay. In terms of the coupling constants this leads to $C_V/C_V' = 1$, $C_A/C_A' = 1$, $C_S = C_S' = C_T = C_T' = C_P = C_P' = 0$, and $\text{Im}(C_i) = 0$ for all i [4]. In the parametrization in eq. 2.11 only L_A and L_V remain and eq. 2.10 is simplified to

$$
\begin{aligned}
\mathcal{H} &= \frac{G_\text{W}}{\sqrt{2}} \sum_{\text{V,A}} L_i \left(\bar{\Psi}_\text{p} \Gamma_i \Psi_\text{n} \right) \cdot \left(\bar{\Psi}_\text{e} \Gamma_i (1 + \gamma_5) \Psi_\nu \right) + \text{h.c.} \\
&= g_\text{V} (\bar{\Psi}_\text{p} \gamma_\mu (1 - \lambda \gamma_5) \Psi_\text{n}) \cdot (\bar{\Psi}_\text{e} \gamma_\mu (1 + \gamma_5) \Psi_\nu) + \text{h.c.}
\end{aligned}
\tag{2.12}
$$

$$
\text{with} \quad g_\text{V} = \frac{G_\text{W}}{\sqrt{2}} L_\text{V} \quad \text{and} \quad g_\text{A} = \frac{G_\text{W}}{\sqrt{2}} L_\text{A}
\tag{2.13}
$$

being the vector and axial-vector coupling constants and λ being their ratio:

$$
\lambda = \frac{g_\text{A}}{g_\text{V}} = \frac{|g_\text{A}|}{|g_\text{V}|} \cdot e^{i\phi}.
\tag{2.14}
$$

with $\phi{=}180°$ in the SM.

2.1.4 Neutron decay in the Standard Model formalism

Although the Hamiltonian in eq. 2.12 describes the parity violation in β-decay, it still assumes a point-like interaction. The SM follows the V-A theory but without the assumption of a point-like interaction. β-decay is described by the transition of an up-quark into a down-quark by exchange of a W^--boson (see fig. 2.2). Generally, the weak interaction is mediated by the exchange of 3 gauge bosons $W^\pm$ and Z^0, underlying the symmetries of the $SU_L(2) \times U(1)$ gauge group.
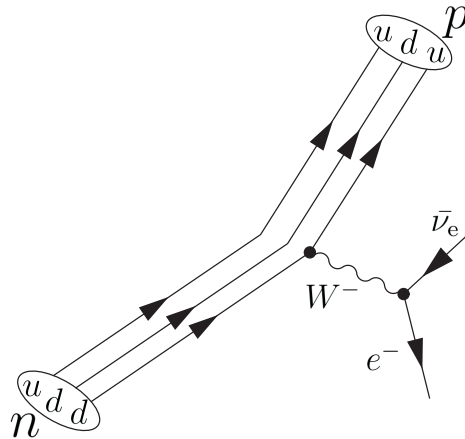

Figure 2.2: Feynman graph of neutron β^--decay in the SM: A neutron (udd) decays into proton (uud), electron and antineutrino by the exchange of a W^--boson.

The exchange bosons are very massive and thus can only exist for very short times, determined by Heisenberg's uncertainty principle $\tau < \hbar/M_{\mathrm{W,Z}}$. With $M_{\mathrm{W}} = 80.398(25)\mathrm{GeV/c^2}$ and $M_{\mathrm{Z}} = 91.1876(21)\mathrm{GeV/c^2}$ [7] and assuming the speed of light c as maximum speed, the interaction has a range of $\sim 2.5 \cdot 10^{-18}\,\mathrm{m}$. Thus, the point-like V-A model for β-decay is included as low energy limit in the SM. The charged bosons couple only to left-handed fermions and right-handed antifermions, what includes parity violation in the SM description of the weak interaction.

The SM groups the six known quarks into three families, depending on their charges and masses (see also tab. 1.1):

$$\begin{pmatrix} u \\ d \end{pmatrix}, \quad \begin{pmatrix} c \\ s \end{pmatrix}, \quad \begin{pmatrix} t \\ b \end{pmatrix}. \tag{2.15}$$

The quarks have a charge of $+2/3$ in the upper row and $-1/3$ in the lower row.

The assumption of universality of the weak interaction includes, for example, that the weak charge g is the same for all charged particles (leptons and quarks). However, it was found in experiments that the coupling constant is larger when determined from purely leptonic decays (e.g., μ-decay) than from semileptonic decays. This discrepancy is explained in the SM by the fact that the eigenstates of the quarks in weak interaction are not the same as their mass eigenstates, described by the CKM-matrix. An introduction was already given in section 1.1 by eq. 1.9 and eq. 1.10.

The squares of the single matrix elements $|V_{\mathrm{qq'}}|^2$ of the CKM-matrix give the probability of the transition of a quark $|q\rangle$ to $|q'\rangle$. A test of the unitarity condition (see also eq. 1.10)

$$|V_{\mathrm{ud}}|^2 + |V_{\mathrm{us}}|^2 + |V_{\mathrm{ub}}|^2 = 1. \tag{2.16}$$

motivated measurements to extract this matrix elements. Since $|V_{ud}|^2$ contributes most to the sum of eq. 2.16, a high precision determination of this value is desirable. As pointed out in chapter 1, this determination can be done either by nuclear β-decays[3] or neutron β-decay experiments in combination with measurements of the neutron lifetime τ_n (see eq. 1.2). Both should give complementary results. Combining all measurements of $|V_{ud}|$, $|V_{us}|$ and $|V_{ub}|$ taken into account by the PDG (including recent corrections), the unitarity condition eq. 2.16 is fulfilled: $|V_{ud}| = 0.9999 \pm 0.0011$ [7]. By taking only results from neutron decay experiments and including the mentioned discrepancy of the latest neutron lifetime values ([8], [9]), the question of unitarity can not be answered yet.

The CKM matrix elements can be determined most precisely by a global fit that uses all available measurements and imposes the SM constraints. The fit must also use theoretic predictions for hadronic matrix elements, which sometimes have significant uncertainties. The fit results for the magnitudes of all nine CKM elements are [7]:

---

[3]The knowledge on nuclear wave functions limits the values.

$$(|V_{ij}|) = \begin{pmatrix} 0.97419 \pm 0.00022 & 0.2257 \pm 0.0010 & 0.00359 \pm 0.00016 \\ 0.2256 \pm 0.0010 & 0.97334 \pm 0.00023 & 0.0415^{+0.0010}_{-0.0011} \\ 0.00874^{+0.00026}_{-0.00037} & 0.0407 \pm 0.0010 & 0.999133^{+0.000044}_{-0.000043} \end{pmatrix}. \quad (2.17)$$

2.2 Measurable parameters in neutron decay

To calculate the total decay probability, Fermi's golden rule can be used:

$$W = 2\pi \left| \mathcal{M}_{\text{fi}} \right|^2 \cdot \rho'_{\text{e}}(E_{\text{e}}), \quad (2.18)$$

where $\rho'_{\text{e}}(E_{\text{e}})$ denotes the phase space density of the final states and $\mathcal{M}_{\text{fi}}$ is the transition matrix element. Natural units are used such that $c=\hbar=1$ in eq. 2.18 and the following equations.

With the Hamiltonian given in the 2nd row of eq. (2.12), the decay probability can be expressed as a function of the coupling constants. For β-decay this was done by Jackson *et al.* in 1957 [10]. The distribution of electron and antineutrino energies (E_{e} and E_{ν}, respectively) and momenta ($\vec{p}_{\text{e}}$, $\vec{p}_{\nu}$) was calculated to be

$$\frac{dW}{dE_{\text{e}} d\Omega_{\text{e}} d\Omega_{\nu}} = \frac{G_{\text{W}}^2}{(2\pi)^4 \hbar} \rho'_{\text{e}}(E_{\text{e}}) \xi \cdot \left\{ 1 + a \frac{\vec{p}_{\text{e}} \vec{p}_{\nu}}{E_{\text{e}} E_{\nu}} + \frac{\vec{P}_{\text{n}}}{P_{\text{n}}} \cdot \left(A \frac{\vec{p}_{\text{e}}}{E_{\text{e}}} + B \frac{\vec{p}_{\bar{\nu}}}{E_{\bar{\nu}}} \right) + \dots \right\}. \quad (2.19)$$

by using the dependence of the correlation coefficients on λ (eq. 1.4 to 1.6). Jackson *et al.* derived more correlation coefficients (see eq. 1.3) which are not important for the following discussion and thus are not shown. ξ is the sum of the squares of the coupling constants as presented in general form in [37]:

$$\xi = \left(|L_{\text{S}}|^2 + |L_{\text{V}}|^2 + |R_{\text{S}}|^2 + |R_{\text{V}}|^2 \right) + 3 \left(|L_{\text{A}}|^2 + |L_{\text{T}}|^2 + |R_{\text{A}}|^2 + |R_{\text{T}}|^2 \right). \quad (2.20)$$

The pre-factor 3 of the second part of the formula indicates the triplet state of the Gamow-Teller decay, in contrast to the singlet state of the Fermi decay.

Within the standard model the equation simplifies to

$$\xi = |L_{\text{V}}|^2 + 3|L_{\text{A}}|^2, \quad (2.21)$$

or with the commonly known coupling constants of the weak interaction (eq. 2.13):

$$\xi = \frac{|g_{\text{V}}|^2 + 3|g_{\text{A}}|^2}{G_{\text{W}}^2 / 2}. \quad (2.22)$$

Each correlation coefficient in eq. 2.19 can be expressed as a function of the coupling constants L_i, R_i. In the SM description, the coefficients depend only on the parameter λ. Therefore a measurement of one of the coefficients allows to infer λ. Measuring several parameters provides cross-checks of these results. Additionally, deviations from the SM description would indicate physics beyond the SM and herewith tests of theoretic extensions to the SM.

2.2.1 The electron antineutrino correlation coefficient a

aSPECT aims to measure the electron antineutrino angular correlation a, thus only this parameter will be discussed here. For information on the other parameters the reader is referred to [4], [5] and [37].

In the general form, a can be written as

$$a = \frac{1}{\xi} \left(|L_\mathrm{V}|^2 - |L_\mathrm{S}|^2 + |L_\mathrm{T}|^2 - |L_\mathrm{A}|^2 + |R_\mathrm{V}|^2 - |R_\mathrm{S}|^2 + |R_\mathrm{T}|^2 - |R_\mathrm{A}|^2 \right) \qquad (2.23)$$

In terms of the SM ($L_S{=}L_T{=}0$, $R_i{=}0$) using eq. 2.13 / 2.14 and 2.21, eq. 2.23 is reduced to

$$a_{SM} = \frac{1 - |\lambda|^2}{1 + 3|\lambda|^2}. \qquad (2.24)$$

A pure Fermi decay implies $a = 1$ whereas it should be $a = -\frac{1}{3}$ for a pure Gamow-Teller decay. A measurement of a can be used to search for contributions of scalar and tensor type interactions: The coupling constants (e.g., L_S and L_T) included in eq. 2.23 can be used to extent the SM description of a as given by [4][4]

$$a = a_{SM} - \frac{2}{(1 + 3\lambda^2)^2} \times$$
$$\left[(1 + \lambda^2) \cdot \left(\frac{|L_S|^2 + |R_S|^2}{|L_V|^2 + |R_V|^2 + 2\,|L_V|\,|R_V|} \right) + \lambda^2 \cdot (1 - 3\lambda^2) \cdot \left(\frac{|L_T|^2 + |R_T|^2}{|L_A|^2 + |R_A|^2 + 2\,|L_A|\,|R_A|} \right) \right]$$
$$+ \frac{Z\alpha m_e}{p_e} \cdot \frac{2}{1 + 3\lambda^2} \cdot \left[\mp \mathrm{Im}\left(\frac{L_S}{L_V + R_V} \right) \pm \mathrm{Im}\left(\frac{L_T}{L_A + R_A} \right) \right] \quad (2.25)$$

Eq. 2.25 contains model- and nucleus-independent Coulomb corrections of order αZ. α is the fine-structure constant and Z is the atomic number of the daughter nucleus ($Z{=}1$ in the decay of the free neutron). m_e is the electron mass and p_e its momentum.

a can not be measured directly due to the difficulty of detecting neutrinos. It has to be inferred from other properties which are accessible in experiments. So far, only two ways have been realised: The aCORN experiment plans to determine a by measuring the distribution of decay events as a function of the angle between the proton and the electron [41]. The second option is to measure the shape of the proton spectrum as it is done by aSPECT (see section 1). This method was also used by prior experiments [2], [3] and [42]. The world average value resulting from this three experiments is $a = -0.103(4)$ [7].

---

[4]Equation (C8) on page 1033 of this publication was re-written here in terms of $\lambda^2{=}\frac{1}{3}\rho^2$. Additionally, the parametrization of C_i and $C_i^{'}$ by L_i and R_i in eq. 2.11 was used.

2.2.2 The neutron lifetime τ_n

As already addressed in chapter 1, a measurement of the coefficient a can be used in combination with the neutron lifetime τ_n to determine $|V_{ud}|$. τ_n can be obtained by integration of the differential decay probability eq. 2.19 and inversion (using $\hbar=c=1$) [5]:

$$\tau_n = \frac{2\pi^3}{m_e^5 G_W^2 \xi f(1+RC)}.$$ (2.26)

f is the phase space factor, which includes the Fermi function contribution [46]:

$$f = m_e^{-5} \int_{m_e}^{E_{0,e}} \rho'_e \mathrm{d}E_e = 1.6887 \pm 0.00015.$$

$(1+RC)=1.03886 \pm 0.00039$ is an overall electroweak radiative correction factor [5].

In the V-A theory, eq. 2.26 simplifies to:

$$\tau_n = \frac{2\pi^3}{m_e^5 f} \frac{1}{|g_V|^2 + 3|g_A|^2}.$$ (2.27)

The neutron lifetime is the only observable which contains direct information about the coupling constants g_A, g_V. The correlation coefficients contain only information about their relative strengths λ. The current world average is $\tau_n = 885.7(8)\,\mathrm{s}$, but from the latest measurement of Serebrov *et al.* [9] a value of $\tau_n = 878.5(7)\,\mathrm{s}$ was extracted which is 6σ away from the average. Several new experiments to determine τ_n are planned or built at the moment to resolve this discrepancy. These experiments can be divided into beam experiments and storage experiments (latter use ultra cold neutrons) [4], [5].

2.3 Kinematics

The decay of the free neutron is a three-body decay. Since the energies involved are large compared to the rest masses of both the electron and the antineutrino, the process has to be treated relativistically for these two particles. In the following, all particles will be treated relativistically using the four-momenta $p_i = (E_i, \mathbf{p}_i)$.

A general three-body decay is depicted in fig. 2.3.

We want to derive a kinematic model to calculate the endpoint energies of the spectra of the decay particles 1, 2 and 3 [48]. Therefore, we assume that particle 1 is emitted isotropically with a total energy E_1 and a momentum $\vec{p}_1$. We regard now a center-of-mass system (cms) defined by particle 2 and 3, where E_{cms} and $\vec{p}_{cms}$ denote its energy and momentum. M is the mass of the decaying particle (e.g., the neutron). m_i, E_i and $\vec{p}_i$ are the masses, energies and momenta of the decay products (see fig. 2.3), respectively. The convention $c = 1$ is used here for convenience.
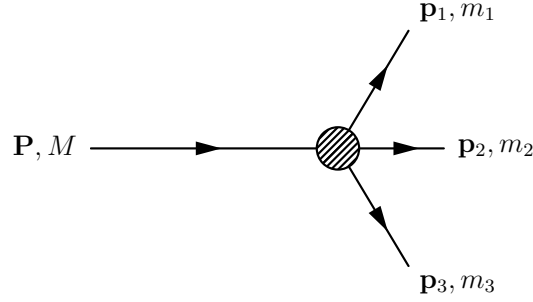
Figure 2.3: A particle with momentum **P** and mass M decaying into three daughter particles with momenta $\mathbf{p_i}$ and masses m_i (i = 1,2,3).

The following energy- and momentum conservation rules have to be fulfilled:

$$\vec{p}_1 = -\vec{p}_{cms} \tag{2.28}$$

$$M = E_1 + E_{cms} \tag{2.29}$$

with the relativistic energy-momentum relations

$$E_1 = \sqrt{m_1{}^2 + \mathbf{p}_1^2} \iff p_1^2 = E_1^2 - m_1^2 \tag{2.30}$$

and

$$E_{cms} = \sqrt{m_{cms}{}^2 + \mathbf{p}_{cms}^2}. \tag{2.31}$$

A rest mass m_{cms} can be assigned to the *cms*-system by using eqs. 2.28 to 2.30 in eq. 2.31:

$$m_{cms} = \sqrt{M^2 - 2E_1 M + m_1^2} \tag{2.32}$$

This is equivalent to the mass (and accordingly to the energy) that is distributed to particle 2 and 3 in the *cms*-system. Obviously, m_{cms} has to be minimum the sum of the masses of these two particles:

$$m_{cms, min} = m_2 + m_3. \tag{2.33}$$

In that case, the energy transfer to particle 1 reaches its maximum. Its endpoint energy $E_{\mathrm{max},1}$ in the laboratory system can be calculated by using eq. 2.33 with eq. 2.32:

$$E_{\mathrm{max},1} = \frac{M^2 + m_1^2 - (m_2 + m_3)^2}{2M} \tag{2.34}$$

This formula can be used to calculate the endpoint energies $E_{\mathrm{max},i}$ (with i$\in$(p, e, $\bar{\nu}_e$)) of all daughter particles in neutron decay as shown in [48]. The masses used are listed by the

PDG [7]. Here, the antineutrino will be treated as massless. Measurements of the neutrino mass [47] give so far an upper limit of $m_{\bar{\nu}} < 2.2\,\mathrm{eV}/\mathrm{c}^2$, which is negligibly small compared to the other masses involved. The calculated endpoint energies $E_{\mathrm{max,i}}$ are shown in tab. 2.1 along with the masses and the maximum kinetic energies $T_{\mathrm{max,i}}$ of the particles.

Particle	Index i	m_{i}	$E_{\mathrm{max,i}}$	$T_{\mathrm{max,i}} = E_{\mathrm{max,i}} - m_{\mathrm{i}}$
		[MeV]	[MeV]	[MeV]
Neutron	n	939.565346(23)		
Proton	p	938.272013(23)	938.272764(23)	0.000751(33)
Electron	e	0.510998910(13)	1.292581(53)	0.781582(53)
Antineutrino	$\bar{\nu}$	< 0.0000022	0.782008(54)	0.782008(54)

Table 2.1: Rest masses m_{i}, endpoint energies $E_{\mathrm{max,i}}$ and maximal kinetic energies $T_{\mathrm{max,i}}$ of the particles participating in neutron β-decay ($m_n - m_p - m_e - m_{\bar{\nu}} = 0.78233(11)\,\mathrm{MeV}$).

2.3.1 Lepton spectra

The energy distribution of the daughter particles depends on the available phase space of the reaction. We neglect for a moment the kinetic energy of the proton and purely consider the phase space of electron and antineutrino. With this assumption, we can calculate the β-spectrum of the electron from the number of states in a given phase space volume $\mathrm{d}^3 p_e \mathrm{d}^3 p_{\bar{\nu}}$ using the energy relation (with $c = 1$) $E_e + E_{\bar{\nu}} = m_n - m_p =: E_{max}$ [33]:

$$\mathrm{d}\rho_e = \frac{(4\pi)^2}{(2\pi\hbar)^6} E_e \sqrt{E_e^{\,2} - m_e^{\,2}} \cdot (E_{max} - E_e)^2 \mathrm{d}E_e. \tag{2.35}$$

E_e is the total energy of the electron given by $E_e = T_e + m_e$. Instead of using E_{max}, we will consider the kinetic energy of the proton and use the exact value $E_{\mathrm{max,e}}$ in the following calculations.

The Coulomb interaction between proton and electron leads to a shift of the electron spectrum to slightly lower energies. To take this effect into account, the Fermi-function $F(Z, E)$ is introduced with Z being the atomic number of the daughter nucleus. Therefore, the electron spectrum eq. 2.35 is modified to

$$\begin{aligned} \rho_e'(E_e) &:= F(Z, E_e)\rho_e(E_e) \\ &= \frac{(4\pi)^2}{(2\pi\hbar)^6} F(Z, E_e) E_e \sqrt{E_e^{\,2} - m_e^{\,2}} \cdot (E_{\mathrm{max,e}} - E_e)^2. \end{aligned} \tag{2.36}$$

For non-relativistic electrons in the field of a point-like nucleus the function $F(Z, E)$ is given by [33]:

$$F(Z, E) = \frac{2\pi\eta}{1 - e^{2\pi\eta}} \quad \text{with} \quad \eta = \pm\frac{Z\alpha}{v_e} \quad \text{for} \quad \beta^{\mp}. \qquad (2.37)$$

Here, v_e is the velocity of the electron in units of c and α is the fine-structure constant. In the decay of the free neutron ($Z = 1$), $\eta \ll 1$ even for small electron energies and thus one can set $F \approx 1$.

Analogous to the electron spectrum eq. 2.35, the antineutrino spectrum can be calculated to be

$$\mathrm{d}\rho_{\bar{\nu}} = \frac{(4\pi)^2}{(2\pi\hbar)^6} \sqrt{(E_{\max,\bar{\nu}} + m_e - E_{\bar{\nu}})^2 - m_e{}^2} (E_{\max,\bar{\nu}} + m_e - E_{\bar{\nu}}) E_{\bar{\nu}}{}^2 \mathrm{d}E_{\nu} \qquad (2.38)$$

The spectra for both electrons and neutrinos are depicted in fig. 2.4.

(a) Electron spectrum.

(b) Antineutrino spectrum.
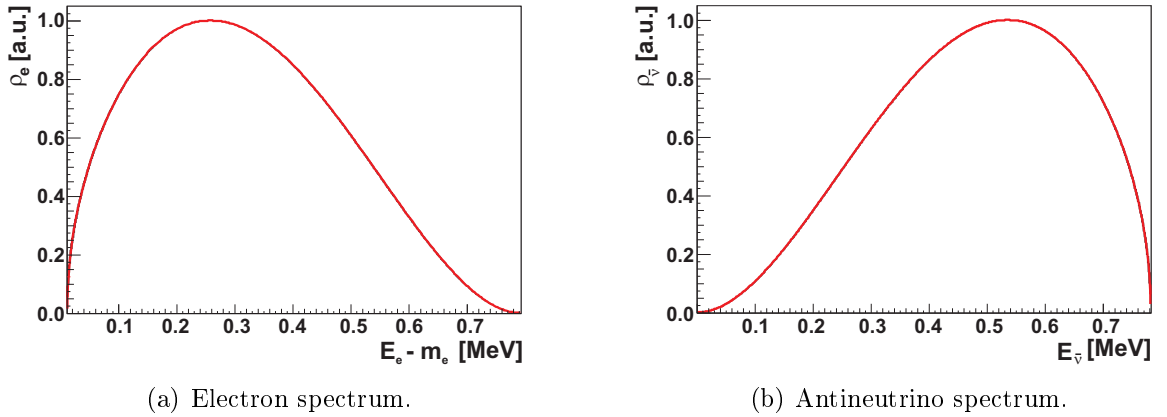
Figure 2.4: The kinetic energy spectra of electrons (left) and antineutrinos (right) from the decay of the free neutron (with $F(Z, E) = 1$).

2.3.2 Proton spectrum

A relativistic derivation of the proton recoil spectrum can be found in [23] (please note, that in that paper a sign error in the last line of eq.(4.5) was found by [43]). It is similar to the derivation of the electron spectrum described in the previous section. Again, the transition probability is a product of a phase space factor, the transition matrix element and a Coulomb correction factor. Neglecting the latter one, the kinetic energy spectrum

of the proton is calculated to be

$$
\mathrm{d}w(T) = \frac{\Sigma\Delta^3 G_V^2}{2^4\pi^3(1+2\delta)}\left(\frac{\sigma-x^2}{\sigma}\right)^2\sqrt{1-\sigma}\Bigg\{\left(1+\frac{x^2}{\sigma}-\sigma\right)-
$$
$$
-\frac{1}{3}\frac{\sigma-x^2}{\sigma}(1-\sigma)+\lambda^2\left[\left(1+\frac{x^2}{\sigma}+\sigma\right)-\frac{1}{3}\frac{\sigma-x^2}{\sigma}(1-\sigma)\right]\Bigg\}\mathrm{d}T \quad (2.39)
$$

with T being the kinetic energy of the proton, λ as introduced in eq. 2.14 and the quantities

$$
\begin{aligned}
\Delta &= m_n - m_p, & \Sigma &= m_n + m_p, \\
x &= m_e/\Delta, & \delta &= \Delta/\Sigma, \\
\sigma &= 1 - \frac{2m_n}{\Delta^2}T.
\end{aligned}
$$

Eq. 2.39 can be rewritten as function of the angular correlation coefficient a using eq. 2.24 [23]:

$$
\frac{\mathrm{d}w(T)}{\mathrm{d}T} \propto g_1(T) + ag_2(T) \quad (2.40)
$$

with $g_1(T)$ and $g_2(T)$ being known functions of the kinetic energy T of the proton:

$$
g_1 = \left(\frac{\sigma-x^2}{\sigma}\right)^2\sqrt{1-\sigma}\left[4\left(1+\frac{x^2}{\sigma}\right)-\frac{4}{3}\frac{\sigma-x^2}{\sigma}(1-\sigma)\right] \quad (2.41)
$$

$$
g_2 = \left(\frac{\sigma-x^2}{\sigma}\right)^2\sqrt{1-\sigma}\left[4\left(1+\frac{x^2}{\sigma}-2\sigma\right)-\frac{4}{3}\frac{\sigma-x^2}{\sigma}(1-\sigma)\right] \quad (2.42)
$$

The shape of the spectrum (without radiative and Coulomb corrections) is depicted in fig. 1.1.

3 Measurement of the correlation coefficient a

As introduced in chapter 1, the purpose of the aSPECT spectrometer is to measure the energy spectrum of protons in free neutron decay with high sensitivity. From this spectrum one can extract the angular correlation coefficient a of the emitted electron and electron-antineutrino. The present best experiments had an accuracy of $\frac{\delta a}{a} = 5\%$, according to measurements done by Stratowa *et al.* [2] and Byrne *et al.* [3]. The aim of aSPECT is to determine a with a relative error $<0.3\%$. I will focus in my thesis on the recent beam time in 2008. This chapter will give an introduction to the design of aSPECT, its measurement principle and the setup at the beamline.

3.1 The spectrometer aSPECT

The method implemented in aSPECT is based on a magnetic spectrometer with an electrostatic retardation potential. This spectrometer type is called MAC-E filter which stands for **M**agnetic **A**diabatic **C**ollimation combined with an **E**lectrostatic filter. It consists mainly of a set of electrodes and superconducting coils which produce various strong magnetic and electric fields. The technique of MAC-E filters was first used in electron spectroscopy [44], [45], [49]. And it was the essential idea for searches of the neutrino mass from tritium β-decay [50] in experiments performed at Troitsk and at Mainz as well as now for the new Karlsruhe Tritium Neutrino experiment KATRIN [51]. In the second section of this chapter the concept of a MAC-E filter and the technical realization in aSPECT will be described in detail. At first, the general principle of the measurement will be discussed:

3.1.1 Measurement principle

A sketch of the spectrometer is shown in fig. 3.1. Unpolarized neutrons coming from the cold[1] source of the reactor are guided via neutron guides to the experimental zone. After passing a set of diaphragms, the collimated beam enters the **Decay Volume** (DV)

---

[1]So called "cold" neutrons have energies of about 0.05 to 25 meV.
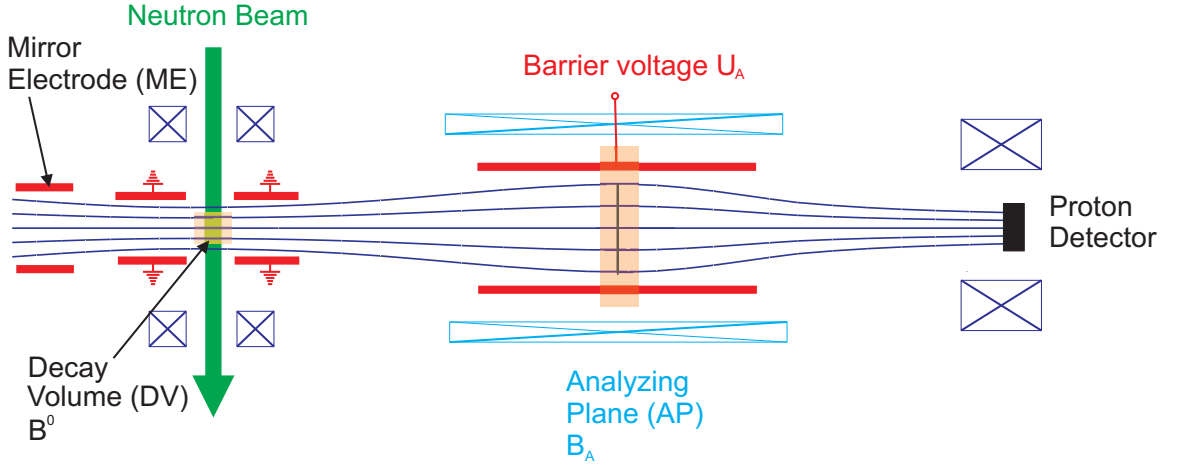
Figure 3.1: Scheme of the spectrometer aSPECT turned by 90 degrees. For details of the setup see text.

of the spectrometer in which a fraction of about 10^{-8} of the neutrons decays in flight. The neutron beam passes through the spectrometer and is finally blocked in a beam dumb downstream. In the DV, a strong magnetic field B_0 is applied which guides the decay protons along the field lines towards the detector (upper hemisphere) on top of the spectrometer. Protons emitted in the opposite direction (lower hemisphere) are reflected adiabatically by an electrostatic **Mirror Electrode** (ME) below the DV. Therefore the spectrometer achieves 4π acceptance for protons created in the DV.

The spectrometer aSPECT is a retardation spectrometer: In the so-called **Analyzing Plane** (AP) (between the DV and the detector position) we apply a variable barrier voltage U_A. Only protons with sufficient kinetic energy can pass and are accelerated onto the detector where they are counted. By setting the barrier voltage to different values, we obtain an integral information on the proton spectrum. Since the end point of the proton spectrum in free neutron decay is $T_{max,p}=751.4\,\text{eV}$ (fig. 1.1) higher voltage settings (we have chosen $U_A=780\,\text{V}$) allow for background investigation.

3.1.2 MAC-E filter

The central demand on a MAC-E filter is "adiabaticity". This sets strict limits on the arrangement of the electric and magnetic fields: The motion of a decay proton to the detector must fulfill the so called *adiabatic approximation* [Jac57], meaning that the relative change of the electromagnetic field during one gyration of the proton has to be small (i.e., $\Delta B/B \ll 1$ and $\Delta E/E \ll 1$).

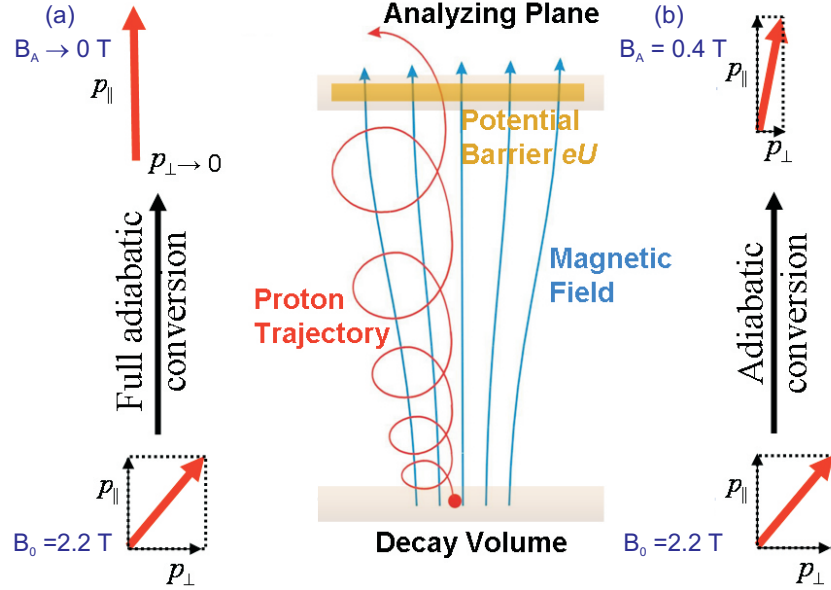Fig. 3.2 illustrates the motion of a proton from its origin in the DV to the AP. The

Figure 3.2: Scheme demonstrating the adiabatic magnetic collimation between the DV and the AP. The left side (a) shows the case of full transfer of transverse ($p_\perp$) to longitudinal ($p_{||}$) momentum: $p_{||} = p, p_\perp = 0$. On the right side (b), the situation is shown for the given magnetic field strengths of aSPECT.

momentum can be split into a longitudinal component $p_{||}$ and transverse component $p_\perp$ as shown by the red arrows in the lower part of fig. 3.2. The proton is magnetically guided along the spectrometer and performs a helical motion (red trajectory in the center of fig. 3.2) around the magnetic field lines (blue lines). The magnetic field strength in the AP (B_A) is much lower compared to the DV (B_0) and decreases adiabatically between both regions. This field gradient causes a transfer of transverse kinetic energy into longitudinal kinetic energy. This transfer is necessary, since the applied potential barrier analyzes only the longitudinal energy component. It has no sensitivity to a possibly remaining transversal energy component.

The helical motion (called cyclotron or gyration motion) is due to the Lorentz force that acts on charged particles (i.e., p^+ and e^-) in electromagnetic fields and is given by

$$\vec{F} = q(\vec{v} \times \vec{B}) + q\vec{E} \tag{3.1}$$

Here, $\vec{v}$ and q are the velocity and the charge of the particle, while $\vec{B}$ and $\vec{E}$ are the magnetic and electric fields. The gyration frequency ω can be derived to be

$$\omega = \frac{qB}{\gamma m} . \tag{3.2}$$

$\gamma = 1/\sqrt{1 - v^2/c^2}$ is the relativistic factor and m the rest mass of the charged particle. Due to adiabaticity, the magnetic flux Φ through the orbit of the gyrating particle with

$\Phi = B\pi r^2$ is a constant of motion, with r being the gyration radius. From Φ=const. several *adiabatic invariants* can be derived, like Br^2, $p_\perp^2/B$ and $\gamma\mu$. μ is the magnetic moment of the current loop of the charged particle which is defined by

$$\mu = I \cdot A = (e \cdot \nu)(\pi r^2) = \frac{e\omega r^2}{2} \tag{3.3}$$

We can rewrite this formula by using the adiabatic invariants and the definition of ω

$$\mu = \frac{p_\perp^2}{2mB} = \text{const.} \tag{3.4}$$

The relativistic factor γ is set to 1 due to the low proton velocities that occur in free neutron decay. The magnetic gradient forces $\vec{F} = -grad(-\vec{\mu} \cdot \vec{B})$ can be calculated using eq. 3.4.

The degree of momentum conversion ($p_\perp \rightarrow p_\parallel$) between DV and AP defines the energy resolution or sensitivity of MAC-E filter spectrometers. It depends on the ratio of the magnetic field strengths in the DV (B_0) and the AP (B_A):

$$r_B = \frac{B_A}{B_0}. \tag{3.5}$$

This ratio has to tend to zero ($r_B \rightarrow 0$) for achieving the ideal case of full energy conversion (left hand side (a) of fig. 3.2) and herewith maximal sensitivity. $r_B \rightarrow 0$ can hardly be realized since it requires a long distance between DV and AP and therefore a huge spectrometer size. As a compromise, a ratio of $r_B \approx 0.2$ was chosen for aSPECT which results in a reasonable spectrometer size. The scheme on the right hand side (b) of fig. 3.2 illustrates the situation for the given field strengths in aSPECT. As shown in [22], the energy resolution by this ratio is sufficient for our aimed accuracy in a. In comparison with a hypothetical spectrometer with $r_B \approx 0$ the loss in sensitivity is below 10% [26]. The deviations from the adiabatic approximation are also negligible for the magnetic and electric field performance realized in aSPECT.

The so called "magnetic adiabatic collimation" (also called "inverse magnetic mirror effect") is the fundamental principle of all MAC-E filter spectrometers and can be described by a **transmission function** $F_{tr}(T_0)$. The transmission function represents the probability of a proton with a given initial kinetic energy T_0 and emission angle (with respect to the magnetic field lines in the DV) to pass the AP where a variable barrier potential U_A is applied.

Analyzing $p_\parallel$ (or the longitudinal kinetic energy) of the decay protons by application of a retardation potential, the transmission function of a spectrometer with $r_B \rightarrow 0$ gets a simple step function:

$$F_{tr}(T_0) = \begin{cases} 1 & \text{for } T(p_\parallel) > e \cdot U_A \\ 0 & \text{else} \end{cases} \tag{3.6}$$

But also for $r_B \neq 0$, a transmission function can be calculated analytically in the adiabatic limit as discussed in the next section:

3.1.3 The transmission function

The following derivation of the transmission function is based on the references [22] and [25]. It assumes always adiabaticity along the particle´s trajectory. The kinetic energy of the protons can be split into a longitudinal ($T_{||}$) and a transversal component ($T_\perp$) with respect to the magnetic field lines (z-axis):

$$T_\perp = T \sin^2 \theta \tag{3.7}$$

$$T_{||} = T \cos^2 \theta \tag{3.8}$$

where θ is the angle between the z-axis and the proton momentum. In the adiabatic approximation the magnetic moment μ of the proton is an invariant (see eq. 3.4),

$$\mu = \frac{p_\perp^2}{2m_p B} = \frac{T \sin^2 \theta}{B} = \text{const.} \tag{3.9}$$

This equation is valid for all protons (with mass m_p) at any point of their trajectories from the DV to the AP. Therefore, also the following equation holds:

$$\frac{T_0 \sin^2 \theta_0}{B_0} = \frac{T \sin^2 \theta}{B} \tag{3.10}$$

where B_0 is the magnetic field strength in the DV. θ_0 and T_0 denote the initial angle and the initial kinetic energy of a proton at that position, respectively. B, θ and T are the magnetic field strength, angle and kinetic energy at any given point between DV and AP. Eq. 3.10 can be rewritten on $\sin^2\theta$:

$$\sin^2 \theta = \frac{B}{B_0} \frac{T_0}{T} \sin^2 \theta_0 \tag{3.11}$$

Using eq. 3.11 with eq. 3.8, the energy component $T_{||}$ of the proton can be expressed as:

$$T_{||} = T(1 - \sin^2 \theta) = T - \frac{B}{B_0} T_0 \sin^2 \theta_0 \tag{3.12}$$

$$\Leftrightarrow T = T_{||} + \frac{B}{B_0} T_0 \sin^2 \theta_0 \tag{3.13}$$

The total proton energy E is the sum of its kinetic (T) and potential (V) energy: $E = T + V$. All electrodes that surround the DV are grounded[2]. Therefore, the initial potential in which the proton is generated is set equal to zero (i.e., $V_0 = U_0 = 0$) and the proton

---

[2]See also section 3.2.3 and tab. 3.1.

holds only kinetic energy (i.e., $E_0 = T_0$). At any other point along its trajectory, where a positive electric potential is applied, the proton gains potential energy $V = e(U - U_0)$ and thus loses kinetic energy, implying $T = E - e(U - U_0)$. For reasons of total energy conservation, $E_0 = E$, we obtain the expression:

$$T_0 = T + e(U - U_0) \tag{3.14}$$

$$\Leftrightarrow T = T_0 - e(U - U_0) \tag{3.15}$$

By using the parametrization of T in eq. 3.13 with eq. 3.15, the longitudinal kinetic energy component of the proton can be written as:

$$T_{||} = T_0 - e(U - U_0) - \frac{B}{B_0} T_0 \sin^2 \theta_0 \tag{3.16}$$

$T_{||}$ must be positive along the complete particle trajectory, otherwise the proton is reflected. In the AP, protons reach their minimum of longitudinal kinetic energy. The applied barrier voltage U_A filters the protons by their longitudinal energy component $T_{||}$. We define T_{tr} as the minimum initial energy ($T_{0,min}$) to pass the AP, meaning $T_{||,A} \to 0$:

$$T_{tr} = \frac{e(U_A - U_0)}{1 - \frac{B_A}{B_0} \sin^2 \theta_0} \tag{3.17}$$

T_{tr} is a function of the emission angle θ_0 and $0° \leq \theta_0 \leq 180°$ with respect to the magnetic field lines (z-axis). For a fixed θ_0, the transmission function $F_{tr}(T_0, \theta_0)$ can be written as:

$$F_{tr}(T_0, \theta_0) = \begin{cases} 1 & \text{if } T_0 > \frac{e(U_A - U_0)}{1 - \frac{B_A}{B_0} \sin^2 \theta_0} \\ 0 & \text{otherwise} \end{cases} \tag{3.18}$$

As it is shown in fig. 3.3, the transmission energy T_{tr} has two minima at angles $\theta_0 = 0°$ and $\theta_0 = 180°$ and a maximum at $\theta_0 = 90°$:

$$T_{tr}^{min} = e(U_A - U_0), \qquad T_{tr}^{max} = \frac{T_{tr}^{min}}{1 - \frac{B_A}{B_0}} \tag{3.19}$$

Protons with an initial kinetic energy $T_0 < T_{tr}^{min}$ will be reflected totally by the potential barrier independent of their emission angle. Protons with energies higher than T_{tr}^{max} will pass the barrier voltage $U_A - U_0$, also regardless of their initial angle θ_0. However, in the intermediate energy range, $T_{tr}^{min} < T_0 < T_{tr}^{max}$, the transmission of protons is strongly dependent on their initial angle. To extract a value for this angular dependent transmission probability, the number of transmitted protons $\rho_{tr}(T_0)$ has to be divided by the total number of protons emitted in the same hemisphere pointing towards the detector $\rho_{total}(T_0)$ for a given initial kinetic energy T_0:

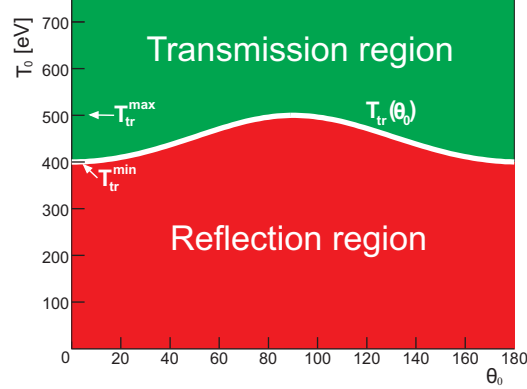$$\rho_{tr}(T_0) = \int_0^{2\pi} d\phi \int_0^{\theta_0^{max}} \sin \theta_0 d\theta_0 \omega(T_0) \tag{3.20}$$

Figure 3.3: Angular dependence of the transmission kinetic energy $T_{tr}(\theta_0)$ shown for a potential barrier $e(U_A - U_0) = 400eV$. T_{tr} is defined in eq. 3.17. Only protons with initial kinetic energy $T_0 > T_{tr}(\theta_0)$ will be transmitted. Notice that if the adiabatic transmission condition is fulfilled for $\theta_0 = 90°$, it is also fulfilled for any other value of θ_0.

and

$$\rho_{total}(T_0) = \int_0^{2\pi} d\phi \int_0^{\pi/2} \sin\theta_0 d\theta_0 \omega(T_0) \qquad (3.21)$$

For symmetry reasons, the transmission function for protons emitted into the lower hemisphere shows the same dependence. θ_0^{max} is defined as the maximum initial angle a proton of initial kinetic energy T_0 can have to pass the potential barrier. It can be derived from eq. 3.17 assuming $T_{tr} = T_0$ and thus it depends on four parameters: T_0, B_A, B_0 and $U_A - U_0$. $\omega(T_0)$ is the proton recoil spectrum (see section 2.3.2 and fig. 1.1) and does not depend on θ_0. Thus, the integration of eq. 3.20 becomes easier, resulting in

$$\rho_{tr}(T_0) = 2\pi\omega(T_0)(1 - \cos\theta_0^{max}) \qquad (3.22)$$

$$\rho_{total}(T_0) = 2\pi\omega(T_0) \qquad (3.23)$$

Finally, for $T_{tr}^{min} < T_0 < T_{tr}^{max}$ the transmission probability is given by:

$$\frac{\rho_{tr}(T_0)}{\rho_{total}(T_0)} = 1 - \cos\theta_0^{max} = 1 - c_{tr}(T_0) \qquad (3.24)$$

The transmission cosine function $c_{tr}(T_0)$ is defined by combining eq. 3.17 and 3.19:

$$c_{tr}(T_0) = \sqrt{1 - \frac{B_0}{B_A}\left(1 - \frac{T_{tr}^{min}}{T_0}\right)} = \sqrt{1 - \frac{B_0}{B_A}\left(1 - \frac{e(U_A - U_0)}{E}\right)} \qquad (3.25)$$

Finally, we can formulate the adiabatic transmission function $F_{tr}(T_0)$, which is plotted
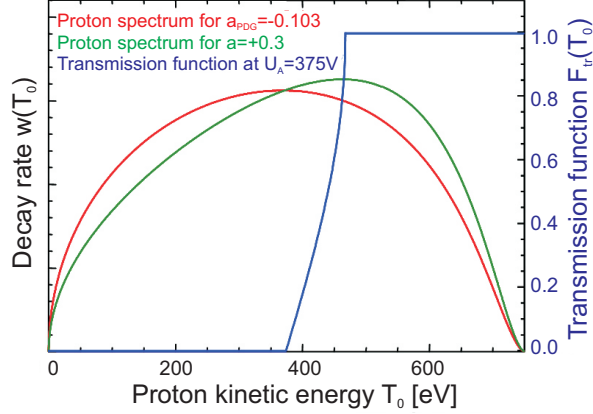
Figure 3.4: The blue curve represents the adiabatic transmission function defined in eq. 3.26 when applying a barrier voltage of 375 V. Two simulated proton spectra are shown for different values of a.

in fig. 3.4 (blue line):

$$F_{tr}(T_0) = \begin{cases} 0 & \text{if } E \leq eU \\ 1 - \sqrt{1 - \frac{B_0}{B_A}(1 - \frac{T_{tr}^{min}}{T_0})} & \text{otherwise} \\ 1 & \text{if } E \geq eU/(1 - B_A/B_0) \end{cases} \quad (3.26)$$

It is important to note, that the transmission function depends only on two parameters: The electrostatic potential difference, $e(U_A - U_0)$, and the ratio of the magnetic field strengths in the DV and in the AP, $r_B = (\frac{B_0}{B_A})^{-1}$. As long as the adiabatic conditions are fulfilled, the transmission function is independent of the explicit shape of the electromagnetic field. For a measurement of the coefficient a with an accuracy of $\delta a \approx 3 \times 10^{-4}$, r_B has to be known with an uncertainty of 10^{-4}, whereas the uncertainty of the potential difference $e(U_A - U_0)$ has to be 10 meV or smaller.

All protons that pass the electrostatic barrier are accelerated by a high negative electric potential towards the detector (see fig. 3.1, right) (e.g., U_{det}=-15 kV). For technical reasons and in order to reduce the impact of certain systematic effects (see section 3.5), the magnetic field increases strongly towards the detector. The resulting magnetic collimation focusses the proton beam onto the detector.

3.2 Technical properties and investigations

The setup as used in the FRM II beam time in 2005/ 2006 was proposed in [26] and is discussed in detail in [22] and [25]. This subsection only provides a summary of the technical setup and main investigations for the beam time at ILL in 2008:

3.2.1 Vacuum, cryogenic and mechanical setup

The aSPECT spectrometer was manufactured by Cryogenics Inc. and was delivered in February 2005 to Mainz. As shown in fig. 3.5, it has a cylindrical shape ($\varnothing$=0.76 m) and a total outer length of $\approx$3.30 m. The spectrometer has two separated vacuum sections: The first section surrounds the superconducting coils and insulates them from external heat load (called: "insulation vacuum"). Under operation, the pressure is about 10^{-4} mbar. The second section is defined by the volume in which the neutron decay takes place and is detected (called: "main vacuum") inside a cold bore tube. Ultra high vacuum (UHV) conditions are needed here to suppress scattering processes with residual gas ions inside the spectrometer, therefore a pressure better than 10^{-8} mbar was proposed in [22].

Six openings allow the access to the main vacuum section: Two side ports ($\varnothing$=150 mm) define the neutron beam axis (z=0, vertical axis). Two more side ports are needed for pumping and control of the vacuum conditions. Inside the cylindrical bore tube ($\varnothing$=200 mm) the decay protons are guided towards the detector. On top of the spectrometer, the detector mechanics can be installed. The electrode system can be inserted from below using the bottom flange which is closed during operation. Several small side ports in the bottom flange are necessary for supply and control of the electrode voltages and the vacuum properties. Additionally, the SAES getter pumps mounted at the electrode system are activated via theses ports. The main vacuum section is pumped simultaneously via the port on top and via one of the side ports. Both ports can be closed by gate valves.

For running the magnet at high current and to sustain the superconducting mode[3] a powerful cooling system is installed that stabilizes the coil temperatures. Two helium compressors provide liquid helium which is pumped by two cryocoolers (Sumitomo RDK408D) via helium flex lines to the spectrometer. The helium lines are thermally coupled at two positions by "cold fingers" to the spectrometer. Each cryocooler has a cooling power of 35 W at the first stage (about 70 K) and 1 W at the second stage (about 4.2 K). The first stage is coupled to the inner bore tube and the second stage to the superconducting coils. The temperature in the inner bore tube forces residual gas ions to freeze out on the surface, which increases the UHV in the main vacuum section. The operation pressure was about 8×10^{-9} mbar at ILL. More details concerning the pumping and cooling procedure are given in Appendix 1.

The mechanical fixation of aSPECT is done by a specially designed suspension. The spectrometer is fixed above its center of gravity by two massive shafts which allow rotation by 90°. This is important for transportation and mounting of the electrode system. The height of the side ports can be adapted to the height of the allocated neutron beam. For the beam time at ILL a new support made of Armco iron was designed [30] which simultaneously acts as antimagnetic screen. Thus, it reduces the strong magnetic stray

---

[3]Also called "persistent mode"

fields by a factor of 7 at a distance of 5.6 m. By this measure destructive interference with neighboring instrumentations is prevented.

3.2.2 Magnetic field performance

aSPECT consists of a set of thirteen axially symmetric coils (see fig. 3.6). The main coils are solenoids. The coil system provides the necessary variable magnetic field strength between DV, AP and detector. Simultaneously, the field homogeneities in the DV and AP are as requested in section 3.1.3. Nine of these coils are superconducting and made of NbTi (transition temperature $T_C \approx 9$ K). The external coils c10/ c11 and c12/ c13 were installed for correcting small deviations of the main magnetic field from its design values and also to perform systematic tests. They can be used for changing the ratio r_B and for shifting the position of the magnetic field maximum in the AP. The superconducting coils c5/ c6 were designed as trim coils to adjust the field maximum within the DV and they allow to apply a field gradient across the DV. c5/c6 can be powered independently and provide a field up to 1% of the main field. All superconducting coils except for c5/c6 are connected in series. This implies an important advantage since the ratio r_B is independent of the exact value of the current.

The critical current density of the used superconducting NbTi-wire (cross section of 0.39 mm^2) limits the applicable maximum current in the main coils I$_{main}$ to a value of about 100 A, which is a conservative approximation. At I$_{main}$=100 A, the magnetic field was calculated to be ≈ 3 T in the DV, ≈ 0.6 T in the AP and ≈ 6 T at the detector position. Fig. 3.5 shows on the right side the simulated magnetic field shape for this maximum current setting. Adiabaticity holds already at currents above 50 A (see [22]). Thus we have chosen a maximum current of 70 A, since the lower current also limits the heat load of the superconducting coils. The lower heat load also reduces the risk of an unwanted switch from superconductivity to a resistive state[4].

The magnetic field in the DV was designed in a way that it shows a maximum at z=0. Towards the AP and the mirror electrode (ME) e1 it decreases without showing any local minimums. Since the neutron density distribution in the DV is approximately symmetrical in height around z=0 (see sect. 3.4.3), half of the protons are emitted below z=0 towards the ME. Protons which are emitted almost perpendicular to the magnetic field axis can can be blocked by the magnetic field maximum in the DV due to the magnetic mirror effect. Thus, they are permanently trapped between the ME and the magnetic mirror. Calculations showed [22] that this effect can be minimized by a monotonously decreasing magnetic field in direction of the proton detector along the entire DV: The trim coils c5/ c6 were used to shift the field maximum inside the DV below the neutron beam to z= -8 cm. But the applied magnetic field gradient ΔB was chosen small enough that $\frac{\Delta B_0}{B_0} \approx 10^{-4}$. This limits the impact on the transmission condition eq. 3.26 (see section 3.1.3) on a
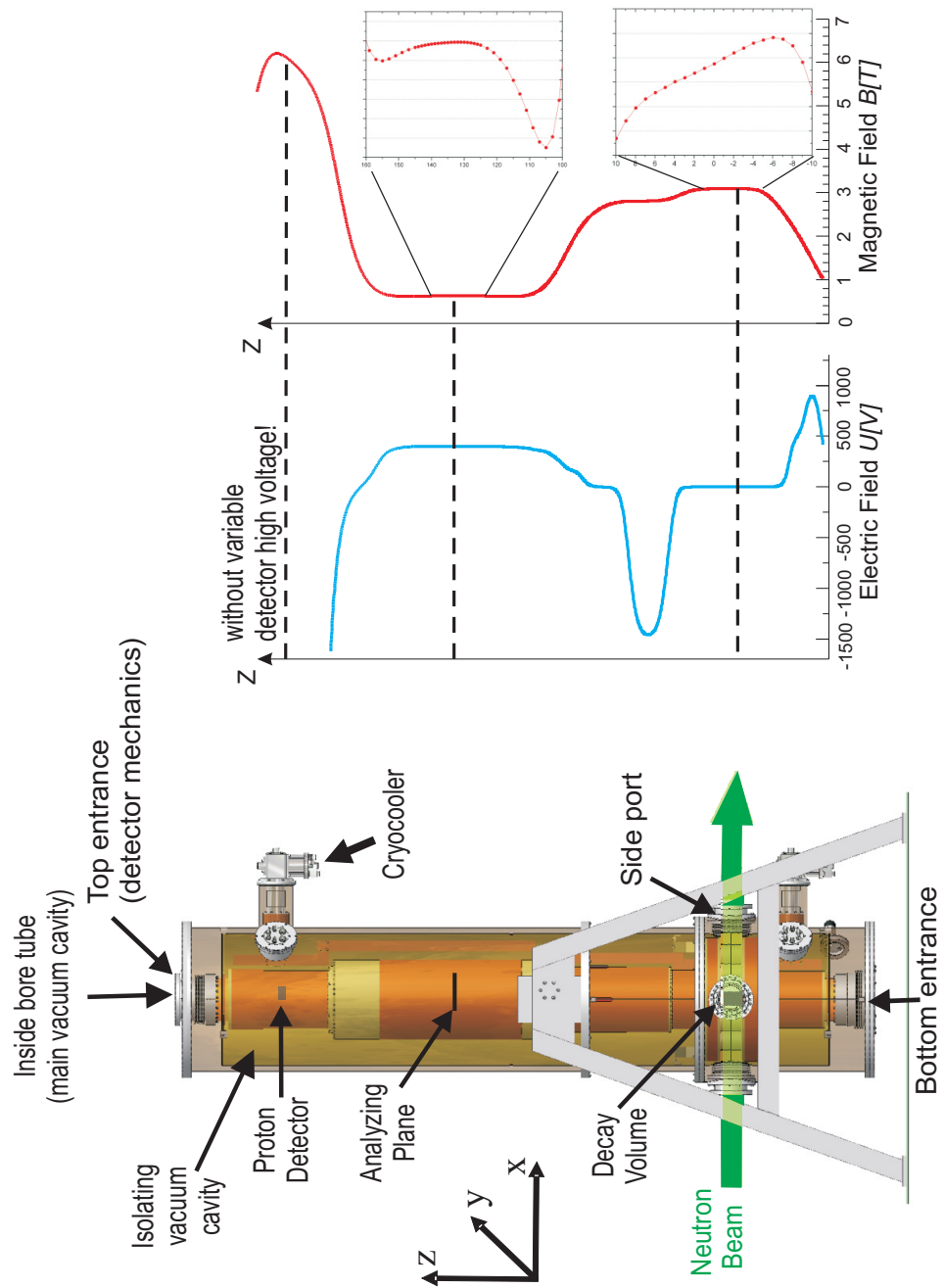
---

[4]Called "quench".

Figure 3.5: Sketch of the aSPECT spectrometer and the simulated electric (blue) and magnetic field shape (red) calculated for a maximum current I_{main}=100A.
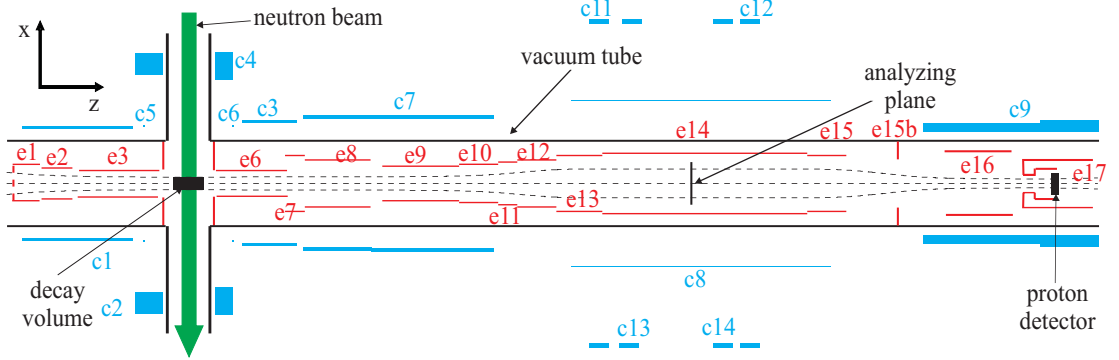
Figure 3.6: Scheme of magnetic field coils (c1-c14, blue) and electrodes (e1-e17, red).

admissible level with respect to our aimed accuracy in a.

In the center of the AP electrode e14, the magnetic field has a local maximum which is adjusted by the external coils c10/c11. Close to the AP, the electrostatic potential is nearly uniform, $U \approx U_A$. If the magnetic field would have a minimum there, its shape must be extremely flat in order to fulfill the transmission condition. By producing a small local maximum, the adiabatic transmission condition is automatically fulfilled [22]: The condition $T_{||}(T_{tr}) > 0$ (see eq. 3.15 and 3.16) requires

$$\frac{B_0 - B \sin^2 \theta_0}{B_0 - B_A \sin^2 \theta_0} > \frac{U - U_0}{U_A - U_0} \qquad (3.27)$$

U is maximal in the center of the AP and $U_A > U$ holds everywhere in the transmission region. Therefore the right-hand side of this equation is smaller than 1. For $B < B_A$ this equation is fulfilled as claimed. With the chosen settings, the achieved level of magnetic field homogeneity in the DV is sufficient for our aimed accuracy in a. As mentioned above, the magnetic field in the detector region is about a factor of 2 higher than in the DV. This has two positive effects: First, the flux tube is collimated towards the detector which enables us to use a smaller detector. Second, the strong magnetic mirror at the detector blocks electrons and reduces significantly the electron background. Protons overcome this mirror due to post-acceleration by the electrodes e16 and e17, which are held at high negative potential (-2 to -4 keV and -10 to -15 keV respectively).

3.2.3 Electric field performance

As discussed in sect. 3.1.3, the analytical calculation of the transmission function presumes adiabaticity of the electromagnetic fields along the proton trajectories. The simulation of the electric field shape was done by F. Glück [22]. The electrode system consists of a set 15 electrodes that are fixed to 4 long rods (e1-e15 in fig. 3.7). It is in-

serted into the bore tube of aSPECT via the bottom entrance. Two more electrodes (e16 an e17) are installed and powered independently from the top of the bore tube.
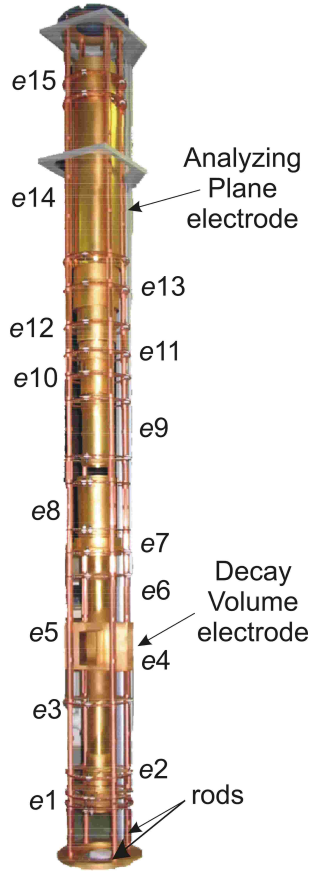
The electrodes of the electrode system (e1-e15) are all made of OFHC copper, which fulfills the UHV standards. In the DV and the AP, the potentials are requested to be strongly homogeneous. The aimed accuracy of 3×10^{-4} in a requires $e(U_A - U_0) \leq 10\,\mathrm{meV}$. The homogeneity of an electric potential depends on the work function at the electrode surface. This work function is strongly dependent on the crystal structure of the surface. Electrodes made from single crystals with a defined, uniform orientation would therefore provide the best potential homogeneity. But the production of such electrodes would be too expensive. And the manufacturing (e.g., bending and welding) of our electrodes produces mechanical stress, which degrades the surface conditions.

Cold coating of the OFHC copper leads to a more constant work function along the electrode surfaces. For reasons of adhesion, a thin layer of silver $(1\,\mu\mathrm{m})$ was coated between the copper substrate and the gold layer $(2\,\mu\mathrm{m})$. Investigations which will be discussed later resulted in a redesign and a new assembly of several electrodes (e.g., DV and AP). Those were coated differently with a $2\,\mu\mathrm{m}$ layer of silver and a $5\,\mu\mathrm{m}$ layer of gold since we discovered, that the gold surfaces looked dim after the cleaning procedure for UHV. The diameters of the electrodes were chosen in a way not to reach into the flux tube: All protons emitted in the

Figure 3.7: The electrode system.

DV and which could be imaged onto the detector should not be blocked by any electrode. Besides, electrons and ions might be produced at edges of electrodes (e.g., by field emission). These electrons and ions represent a source of background and should not be imaged onto the detector. Calculations done by G. Konrad [30] resulted in changes of several critical electrodes. The technical preparation and build-up of the electrode system is explained in [25]. I will summarize now successively the parts of the electrode system and will focus on their various usage, the modifications and the applied settings in the ILL beam time:

- *Electrostatic mirror electrodes (e1, e2):*
The electrostatic mirror was designed to reflect all decay protons which are emitted into the lower hemisphere of the spectrometer. The applied voltages at the ME are higher than the maximum kinetic energy of the decay protons. The mechanism of reflection has to fulfill the adiabatic condition. In this case, the protons are reflected by 180° without
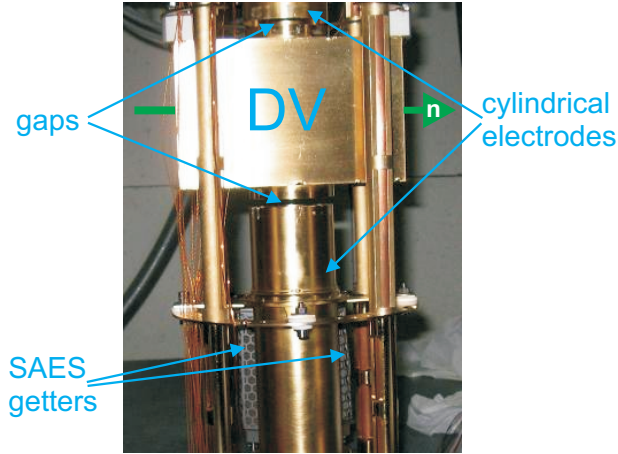
Figure 3.8: Side view of the DV electrode.

changing their kinetic energy and are kept on their trajectories relative to the magnetic field lines. The electrode e1 has cylindrical shape whereupon e2 is a quadrupole. e2 was planned for the usage with a calibration source installed via the bottom entrance of aSPECT. e2 could be used to shift the ion beam in x-y-direction by the application of asymmetric potentials. For our measurement of the coefficient a, the quadrupole e2 was always powered by an uniform voltage at all four parts. e1 and e2 provide a homogeneous potential at the position of the flux tube.

Without ME we would have to know very precisely, which protons are emitted in the upper hemisphere and get detected. The accuracy would be limited by the knowledge of the neutron beam profile in the DV (see sect. 3.4.3). Due to the ME, aSPECT has 4π-acceptance which reduces the impact of the neutron beam profile. Values of $+800$ to $+1000$ V are typical voltage settings. In order to improve the potential shape in the center of the ME, a grid electrode (grid distance 5 mm) was attached to e1 from the bottom (see Appendix 2, fig. 6.1).

- Decay volume electrode (e3 to e6):
Generally, the DV electrode shields the DV from electric field contributions of neighboring electrodes. In operation mode, the DV electrode is grounded. According to calculations, the penetration by neighboring potentials into the DV is <1 meV [22]. The DV electrode was rebuild for the beam time at ILL: It was segmented into 3 pieces with a total length of 60 cm. The central part of the electrode has rectangular shape (110×70 mm) and surrounds the neutron beam along its passage through the spectrometer (y-axis). Two adjacent cylindrical electrodes (e3 and e6) of 220 mm length with an inner diameter of 64 mm along the flux-tube (z-axis) are mounted above and below the DV. There is a small gap of 5 mm between the three parts of the DV electrode (see fig. 3.8). Calculations showed that the field penetration through these gaps is negligible. The diameter of the cylindrical electrodes restricts the maximum volume that can be imaged onto the detector.
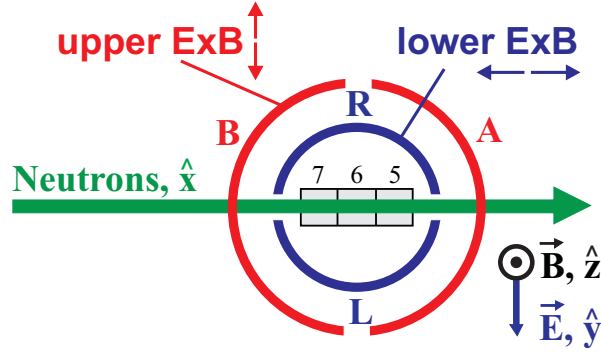
Figure 3.9: Scheme of the ExB-electrodes and their orientation with respect to the neutron beam direction and the detector pads.

All three pieces can be powered independently, which enables us to apply an electric gradient field along the DV. In this case, U_0 is position dependent. For example, the gradient field can be used for systematic investigations on the transmission function F_{tr}, since the potential difference $e(U_A - U_0)$ enters (see eq. 3.26). Another purpose of the gradient field will be discussed in sect. 3.6.1. It is related to hypothetical, local Penning traps close to the DV electrode surfaces. These traps could be generated by a variance of the work function between different positions on the electrode. In the ILL beam time, all measurements for the extraction of the coefficient a were done without application of a gradient field in the DV. We tested its influence only for a short time but for future beam times further investigations are planned. Another reconstruction was needed to make room for a NMR-type magnetic field probe, which will monitor the field ratio r_B and field drifts in our next beam times ([31]). It can be installed off-axis next to the backside of the DV electrode (at height z=0).

- Lower ExB electrode (e8):
Two half cylinders held at different negative potentials produce an electric dipole field perpendicular to the neutron beam axis (see fig. 3.9). Charged particles that pass the electrode are shifted in beam (or in opposite) direction. The lower ExB-drift electrode is mainly necessary to clean the Penning trap in the lower part of the spectrometer between AP and ME (see sect. 3.6.2, fig. 3.28): All protons without sufficient kinetic energy to pass the AP are normally trapped in between the ME and the AP electrode. Due to the lower ExB electrode they will drift towards the bore tube walls and are removed after a few oscillations in the trap. Calculations of proton trajectories through the drift region give upper limits on the acceptable strength of the dipole field [22]. Fig. 3.10a shows a picture of the lower ExB electrode.

- Analyzing Plane electrode (e14):
The AP electrode e14 provides the retardation potential U_A which is held on voltages

between 0 and +800 V. It is applied by a highly stabilized power supply to suppress field drifts. In order to shield the center of the AP from penetration by neighboring potentials, the AP electrode was designed as a long cylinder with a length of 620 mm. Due to the low magnetic field in the AP the flux-tube size is maximal here. Therefore, the AP electrode has also a maximal diameter of 140 mm. The electrodes e10 to e13 and e15 are electrically coupled with e14 and a defined fraction of U_A is applied (see tab. 3.1). The potentials from e10 to 14 increase in the adiabatic limit.

- Upper ExB electrode (e16):
The upper ExB drift electrode is needed for the post-acceleration of protons that pass the AP. It is necessary because the strong magnetic mirror effect towards the detector would otherwise reflect those protons. In addition, the upper ExB electrode can be used to shift the proton distribution in x-direction (see fig. 3.9) along the detector. Furthermore, the drift spatially separates electrons and protons of the very same decay neutron (called "coincidence events"). The separation also serves for systematic checks: For example, the coincidence time between electron and coincidence proton is influenced by the strength of the upper ExB drift (see sect. 4.8).

In the FRM II beam time, the upper ExB electrode consisted of two $10 \times 10 \, \text{cm}^2$ stainless steel plates oriented parallel to each other with a distance of 40 mm, 90 mm below the detector electrode. New electric field calculations showed that the chosen geometry gives rise to local Penning traps for certain potential settings. Therefore, the upper ExB electrode was reshaped and repositioned for the ILL beam time. It consists now of two half cylinders of 130 mm diameter and a length of 160 mm made. The upper edge of the electrode is positioned 37.5 mm below the detector electrode and 430.7 mm above the end of the AP electrode e14. The electrode e16 is made of stainless steel and not coated. The reason is that the homogeneity of the electric potentials at that position is of minor importance.

The electrodes are placed clearly outside the flux-tube. This means, that electrons produced by field emission on edges of the ExB electrode could not directly reach the detector. In addition, field emission was reduced by better polishing of the electrodes. Additionally, sharp edges (e.g., screws) were covered by insulators. The fastening of the electrodes is as well done by insulators made of ceramics (see white pieces in fig. 3.10, b). The voltage supply which is connected on the backside of the electrodes is shielded by glass on its complete length. The improved setup was tested to work up to a voltage difference of 20 kV without discharges (e.g., -10 kV on electrode A and -30 kV on electrode B. The settings will be denoted by "electrode A/ electrode B", i.e., -10/-30 kV). In the ILL beam time, a maximal voltage difference of 4 kV was applied (-4.2/-0.2 kV). But most of the time, we measured without using the electrode e16 as a drift electrode, meaning by a symmetric application of -2/-2 kV only for post-acceleration of the protons.

- Detector electrode (e17):
The detector is mounted on a UHV-feed-through in a cup-like electrode also made of stainless steel. The cup has an inner diameter of 45 mm and an outer diameter of 109.4 mm.
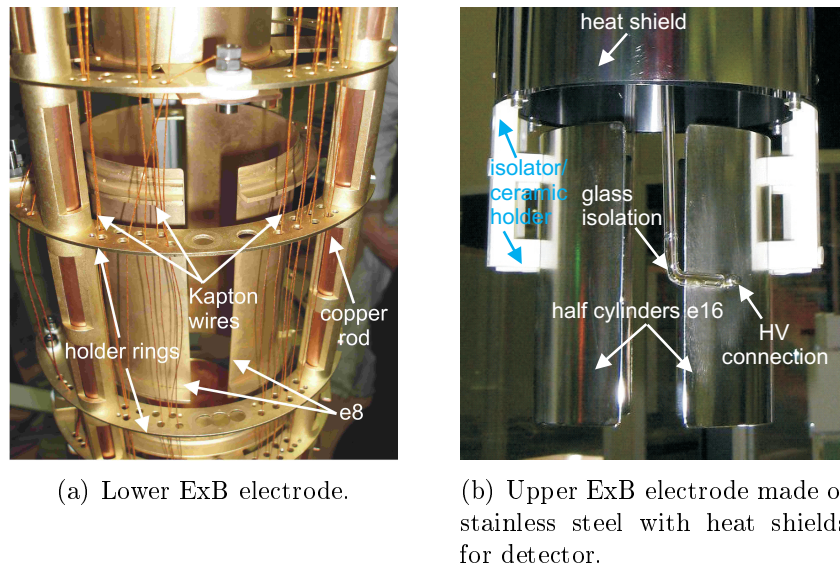
(a) Lower ExB electrode.

(b) Upper ExB electrode made of stainless steel with heat shields for detector.

Figure 3.10: The ExB drift electrodes. The lower ExB electrode (e8) is made of OFHC copper and integrated in the electrode system. The upper ExB electrode (e16) is made of stainless steel. It is inserted from the top into the bore tube.

This electrode was held on acceleration voltages between -10 kV and -15 kV (maximum). The surface of the electrode is electropolished and a long cylindrical tube covers all possible edges (e.g., screws) as can be seen in fig. 3.11. The inner vacuum system contains the preamplifier, the cables for signal processing and for high voltage application. A detailed description of the mechanical construction of the electrode system, the preparation for UHV, the mounting and wiring are presented in [25] and [31]. I will summarize the most important points: The electrodes e1 to e15 are mounted by ring holders on four rods of about 2.4 m length. A bottom and a top plate fix the rods and stabilize the electrodes positions. All holders and rods are kept on ground potential. Contrary to the FRM II beam time, all electrodes are double-wired by Kapton-insulated wires. These are mechanically more stable, which is important since cooling of the magnet contracts them. The double wiring safeguards, that in the case of one broken wire, the other one could still be used to apply the voltage to the electrode. Via two 19-pin feed-throughs, the voltages can be applied to the electrodes as well be controlled via PC. The voltage difference between AP and DV was measured with a calibrated Agilent 3458A multimeter, which has a temporal stability <5 mV when applying 1000 V. Tab. 3.1 summarizes the features of the main electrodes.

(a) Electrode e17 and mechanics (side view).

(b) View from below onto cup and detector.
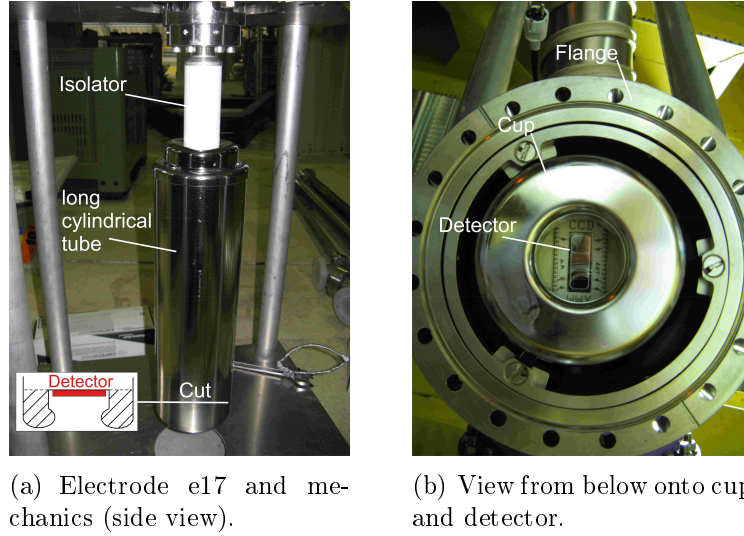
Figure 3.11: Detector electrode e17: The electrode with detector is movable in z-direction via an UHV bellows. Dimensions of detector cup: $\varnothing_{inner} = 45\,\text{mm}$, $\varnothing_{outer} = 109.4\,\text{mm}$

Electrode	Voltage [V]	Comments
e1	800	electrostatic mirror (new: grid on bottom side)
e2	1000/ 820	electrostatic mirror (quadrupole electrode)
e3 to e6	grounded (U_0=0 V)	DV electrodes (parts wired individually)
e7	grounded	useable for systematic checks
e8	mostly -1000/-50 or -200/ 0	lower $E \times B$ drift electrodes (two half cylinders)
e10	$0.4 \times U_A$	variable
e11	$0.7125 \times U_A$	variable
e12	$0.9 \times U_A$	variable
e13	$0.9925 \times U_A$	variable
e14	U_A	AP electrode; variable
e15	$0.9875 \times U_A$	variable
e16	mostly -2/ -2 or -3.7/ -4.2 [kV]	upper $E \times B$ drift electrodes (two half cylinders)
e17	-10/ -12/ -15 [kV]	detector HV

Table 3.1: Typical voltage settings at the electrodes.

(a) The ILL (left) and ESRF (right on top).

(b) View from top into the reactor core.
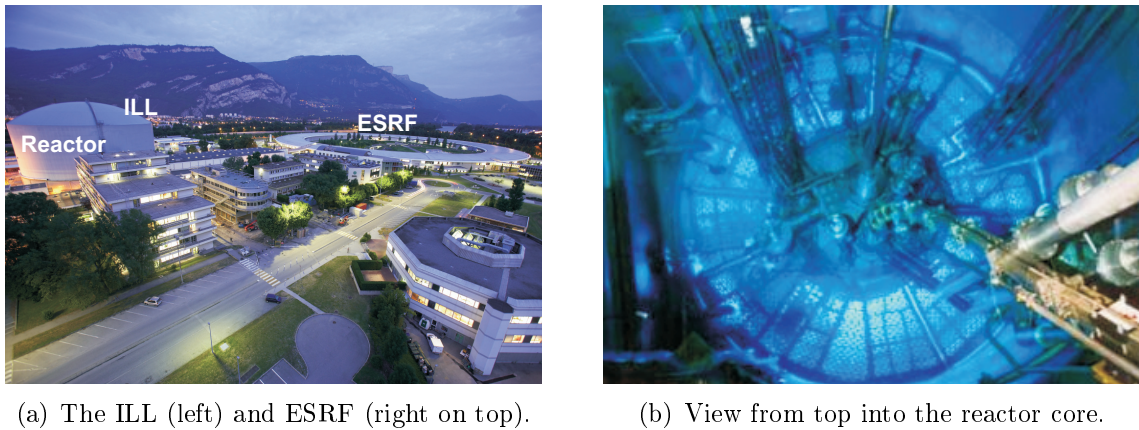
Figure 3.12: (a) Impressions from the ILL and ESRF site situated in Grenoble/ France at the junction of the rivers Drac and Isère in the French Alps. It provides one of the strongest cold neutron beams in the world. The vertical cold source is situated in the lower right corner in (b).

3.3 The cold neutron beam facility PF1B at ILL

The Institut Laue-Langevin (ILL), founded in January 1967 by the French Republic and the Federal Republic of Germany, is located in Grenoble/ France beside the ESRF synchrotron facility (see fig. 3.12). The ILL operates one of the most powerful scientific neutron sources in the world with a flux of $\phi = 1.5 \cdot 10^{15}\,\mathrm{cm^{-2}s^{-1}}$.

3.3.1 The ILL-reactor

The reactor provides a maximal thermal power of 58.3 MW which takes $1\,\mathrm{kg}$ of ^{235}U in 50 days of continues operation. The reactor power can be reduced, so each cycle is about 52 days long. 4 cycles per year are scheduled including shutdowns in between. The neutrons emitted in the fission process of ^{235}U have energies of several MeV and are therefore also called fast neutrons. They are moderated to thermal energies of about $25\,\mathrm{meV}$ by a heavy water ($\mathrm{D_20}$) tank surrounding the fuel elements. This energy corresponds to neutron velocities of $\mathrm{v} \approx 2200\,\mathrm{m\,s^{-1}}$. Since the number of neutrons decaying within a given volume (like the DV in aSPECT) is inversely proportional to their velocity, it is essential for gaining high statistics in the experiment to moderate the neutrons to even lower velocities. This happens in the "vertical cold source" in the reactor core which is mainly a spherical vessel filled with liquid deuterium at $25\,\mathrm{K}$ (see fig. 3.12b). It is situated close to a double neutron guide (H113) that extracts the neutrons. These "cold" neutrons have average velocities of $\mathrm{v} \approx 1000\,\mathrm{m\,s^{-1}}$.

3.3.2 The beam position PF1B

The ILL provides about 40 instruments: Most of them are appointed to condensed matter physics, chemistry, biology, solid state physics and materials science. In this scientific fields, the neutrons are mainly used as a probe. The instruments are different types of diffractometers, reflectometers, time-of-flight and high-resolution spectrometers.

We used the beam position PF1B, which is not an instrument in this respect. It is rather a free experimental space at the end of the neutron guide H113. It has an area of about $10 \times 3 \, \text{m}^2$ where users can build up their complete own experiment. Further more, at PF1B we have the necessary infrastructure as well as assistance in mechanical needs. PF1B is dedicated to fundamental nuclear and particle physics experiments and allocates one of the most powerful cold neutron beams in the world (beside MEPHISTO at FRM II in Garching). The capture flux is $\phi_c = 1.35 \cdot 10^{10} \, \text{cm}^{-2} \, \text{s}^{-1}$, measured by gold foil activation at the exit window of the neutron guide [52]. The capture flux is defined as the particle flux ϕ weighted with the velocity v ([53]):

$$\phi_c = \int_v \phi(v) \frac{v_0}{v} dv, \qquad (3.28)$$

using the thermal velocity $v_0 = 2200 \, \text{m} \, \text{s}^{-1}$. It is a more meaningful parameter for our experiment since the used neutron detector to monitor the neutron flux has a $\frac{1}{v}$-detection efficiency. And the neutron decay rate in our DV has as well a $\frac{1}{v}$-proportionality. The super-mirror neutron guide H113 has a profile of $60 \times 200 \, \text{mm}^2$, is 78 m long and ends in a concrete shielded casemate close to the experimental zone. Neutron guides are generally rectangular tubes of various dimensions covered by one or multiple layers of materials with high Fermi potential like in light optics. Standard guides are for example coated with one layer of ^{58}Ni. The neutrons are guided along these tubes by total reflections on the inner surfaces, therefore materials with high Fermi potential are mandatory. The potential step V_0 for a material surface is given by:

$$V_0 = \frac{2\pi\hbar^2}{m} \cdot N \cdot b_c \qquad (3.29)$$

where N is the number density of atoms and b_c the coherent scattering length of neutrons. From this equation one can estimate the critical angle γ_c of total reflection as:

$$\gamma_c \approx \lambda \cdot \left(\frac{N \cdot b_c}{\pi} \right)^{1/2}. \qquad (3.30)$$

Coatings with ^{58}Ni offer critical angles of reflection of $\gamma_c \, [°] \approx 0.1 \cdot \lambda [\mathring{A}]$. Since the neutron de Broglie wavelength is related to its velocity via

$$\lambda = \frac{3956}{v} [\mathring{A}], \qquad (3.31)$$

meaning a mean wavelength of $\overline{\lambda} \approx 4\mathring{A}$ for cold neutrons. Eq. 3.30 defines a limit for the divergence of the neutron beam at the end of the neutron guide. This divergence is an important input parameter for the simulation of a neutron collimation system (see sect. 3.4.2). In the H113 super-mirror, a coating of 100 double layers of nickel and titanium increases the critical angle by a factor of two and delivers very high neutron fluxes even after long distances [52]. The mean divergence for neutrons guided through H113 is of order $\pm 4 \times 10^{-3}$ rad for thermal and $\pm 8 \times 10^{-3}$ rad for cold neutrons [54]. The neutron guide is curved in its central part to block direct sight from the exit of the guide into the reactor core. This results in a neutron density distribution at the end of the guide which is not completely left-right symmetric. This fact will be discussed later in the evaluation of the beam profile measurements (see sect. 3.4.3.

For experiments with polarized cold neutrons (e.g., PERKEO, [52]) the casemate at the end of H113 contains a super-mirror polarizer. For our purpose, we had to bridge this area by a non-polarizing M2-guide of $50 \times 116 \, \text{mm}^2$ profile which we lend from the TU München. Due to the different profiles, we lost a certain amount of neutrons in the transition zone. However, the dimensions of the internal beam tubes in aSPECT are limiting for the usable beam profile: The neutron beam has to be collimated further to a size of $45 \times 70 \, \text{mm}^2$ for reasons of radiation protection. This is done directly behind the end of the neutron guide. We introduced a linear neutron shutter made of boron carbide between the two different neutron guides for systematic tests. This shutter can be automatically activated by the DAQ computer. In a tenth of a second the complete beam cross section could be blocked. The thick concrete and lead shielding surrounding the casemate made it the most recommendable place for the shutter. The first collimation stage was as well planned inside the casemate for reasons of radiation safety.

3.4 Experimental setup at PF1B

Our beam time at ILL was split into three main parts:

- November/ December 2007: Delivery and built up of the complete experimental setup at PF1B (i.e., alignment, radiation shielding, vacuum pumping, cooldown, first test measurements).

- Christmas 2007 to April 2008: Reactor shutdown (for changing the fuel elements and for reasons of preventive maintenance). Magnetic field measurements at PF1B inside of aSPECT.

- April to 23rd of May 2008: Data taking.

This section will give an overview on the experimental setup at PF1B, starting with the realization of the beamline (i.e., vacuum system, collimation, radiation shielding). I planned the beamline in consultation with the person in charge for PF1B, considering the

experiences made in the beam time at FRM II.

3.4.1 The beamline

The beamline configuration had to fulfill some general demands:
(1) A collimation system (i.e., an arrangement of several diaphragms) should produce a
defined neutron beam profile in the DV of aSPECT.
(2) This collimation system ought to keep the radiation on a low level to reduce beam
related background. It should as well prevent the spectrometer and all vacuum parts from
activation by the neutron beam.
(3) A sophisticated radiation shielding around the beamline and a beam dumb at its end
should limit the radiation in the experimental zone. This includes direct radiation by the
neutron beam as well as secondary radiation by the collimation system. An obligatory
vacuum system around the beamline was planned as well. The vacuum is necessary to
suppress neutron scattering and to increase the free mean path of the charged decay
products.
(4) The vacuum system has to satisfy the need of mechanical alignment of the beamline.

Monte-Carlo/(MC)-simulations were necessary for the design of the collimation sys-
tem (see sect. 3.4.2). These calculations resulted in the sizes and positions of the di-
aphragms (see tab. 3.2). The complete setup as it was built up at PF1B is shown schemat-
ically in fig. 3.13. It can be split up into three main parts:
(1) The entrance side is defined by a long beam tube with belows (brown color in fig. 3.13).
The tube begins inside the casemate (built of thick concrete walls) which comprises the
neutron guides and a neutron shutter. The beam tube contains three diaphragms (P0-P2)
to pre-shape the neutron beam.
(2) The internal beamline inside of aSPECT is separated by two windows from the en-
trance and the exit side. The internal beamline is under UHV-conditions.
(3) The exit side is connected with a bellows to aSPECT and ends in a beam dumb that
blocks the neutron beam. The beam dumb contains a neutron monitor at its center to
measure the flux.
These three parts will be discussed further in detail.

The entrance side:
The vacuum system: An ISO-KF tube followed by two bellows[5] with a total length of 2 m
and a diameter of 200 mm. The tube contains the end of an additional neutron guide. The
bellows are connected to the entrance port of aSPECT (see Appendix 2, fig. 6.2). They
are necessary for the alignment of the spectrometer. Inside the casemate, the vacuum
system is closed by an Al-window, on the spectrometer side we used a MgAl3Zn1 foil
with a thickness of 250 μm as entrance window . The pressure inside the entrance side
was $\mathcal{O}(10^{-2}\,\text{mbar})$.

---

[5]Thanks to the PERKEO collaboration!
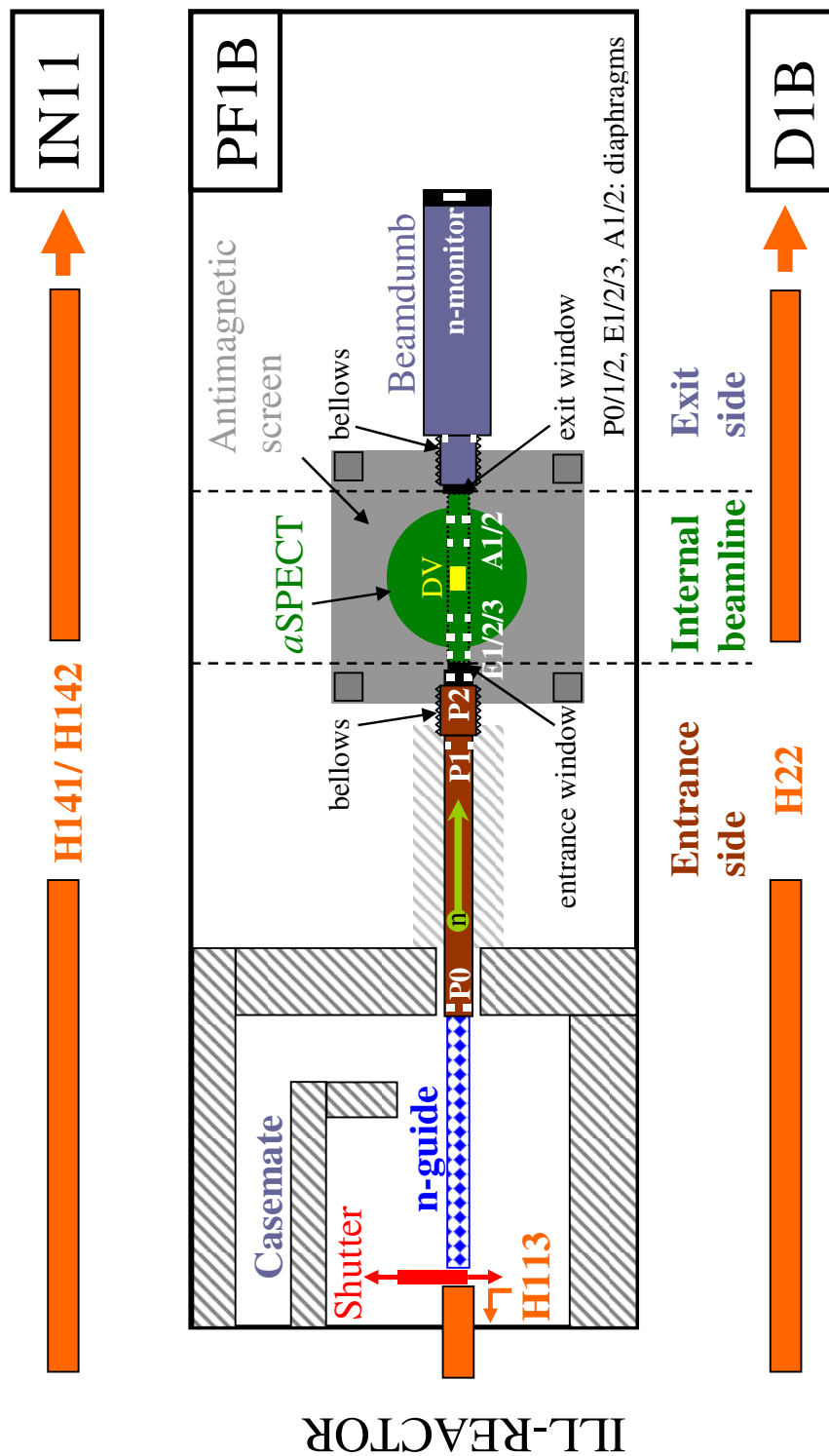
Figure 3.13: Sketch of the PF1B beamline at ILL.

(a) Halo-diaphragm P1, backside   (b) Diaphragm P2, front
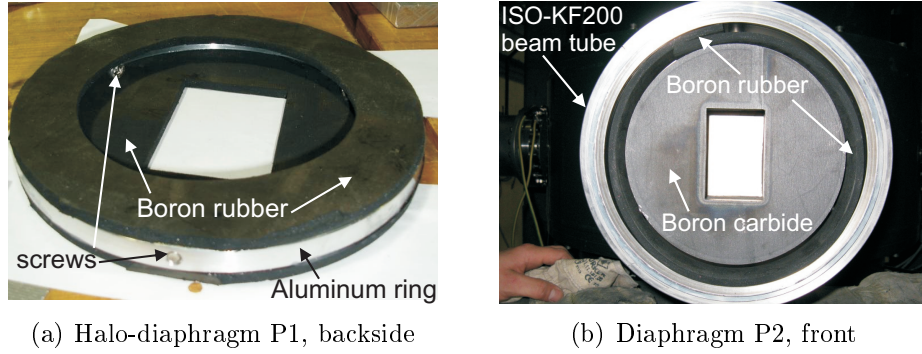
Figure 3.14: The diaphragms were held by 3 screws inside the beamline and were precisely aligned to the neutron beam axis using both a laser and a theodolit.

Collimation: At the entrance window of aSPECT, the neutron beam had to fulfill the following requirements: (a) Inside of aSPECT (internal beamline), the beam is collimated only minimally in order to reduce radiative background produced by the collimation itself. (b) Direct neutrons (scattering is neglected at that point) should not hit the inner walls of the spectrometer. This avoids activation and further radiation. (c) The beam should have a homogeneous spatial distribution across the DV.

The last requirement can only be fulfilled approximately due to the divergence of the neutron beam. A long flight distance and the use of three diaphragms helps to remove neutrons with high divergence: A small diaphragm $P0$ inside the casemate reduces the cross-section of the beam to an initial size of $45 \times 70 \, \mathrm{mm}^2$. This size is adapted to the dimensions of the DV electrode comprising a certain tolerance. A second, wider diaphragm $P1$ (see fig. 3.14a) at the end of the $2 \, \mathrm{m}$ long beam tube blocks the halo of the neutron beam. Right in front of the entrance window the beam size is reduced to $45 \times 70 \, \mathrm{mm}^2$ again by $P2$. $P0$ and $P2$ were made of $5 \, \mathrm{mm}$ thick boron carbide ($\mathrm{BC_4}$). Boron ($^{10}\mathrm{B}$) has a high absorption cross-section ($\sigma_{n,\alpha} = 3840 \, \mathrm{b}$ for neutrons at thermal velocities of $\mathrm{v_0} = 2200 \, \mathrm{m/s}$). $^{10}\mathrm{B}$ emits one photon per neutron absorption:

$$^{10}B + n \rightarrow^4 He +^7 Li + \gamma. \tag{3.32}$$

Therefore, the $\mathrm{BC_4}$ was glued on $50 \, \mathrm{mm}$ thick lead plates used for radiation shielding in neutron beam direction. $P1$ was made up of several layers of boron loaded rubber glued on an aluminium holder. Also the backside of this holder is covered by boron rubber (see fig. 3.14a). The outer shape of all diaphragms is cylindrical and is adapted to the beam tube.

Radiation shielding: On the one hand, there is direct radiation due to the neutron beam. On the other hand, there is γ-radiation induced by the collimation. To suppress radiation by neutrons in the experimental area (e.g., scattered neutrons), the inner surfaces of all beam tubes were covered with boron loaded rubber (see fig. 3.14b). An additional layer of $5 \, \mathrm{mm}$ boron loaded rubber was bend around the tubes from outside. Electrons and protons

from neutron decays are shielded by several layers of lead bricks and plates (total thickness of 10-15 cm) which are stacked all around the beamline (see appendix 2, fig. 6.3). The lead protects also the experimental area from γ-radiation (e.g., induced by the collimation and the neutron shielding). In addition, the diaphragm (P0) that blocks about 50 % of the neutrons is placed inside the casemate. It is surrounded by 1 m thick concrete walls and a 10 cm thick wall of lead bricks in beam direction.

The γ-radiation produced on the entrance side of the beamline should not disturb our measurement of a: The proton detector is about three meters away from diaphragm (P2) and only sees a very small solid angle. In addition, a solid stainless steel cup (see fig. 3.11) shields the detector. Charged particles (emitted outside the flux-tube) are "shielded" by the strong magnetic field of aSPECT and thus can not reach the detector. The experiences during the FRM II beamtime showed that γ-background is insignificant compared to other sources of background.

The internal beamline:
Vacuum system: As mentioned in the technical description of our spectrometer, the internal beamline is kept under UHV conditions. It is confined by an entrance and an exit window made of a 250 μm thick MgAl3Zn1 foil. The windows are indium sealed and have circular shape. The internal beam line has a total length of 125 cm.
Collimation: The internal collimation is divided into an entrance side (before the DV) and an exit side. Three diaphragms (E1 to E3) belong to the entrance, two to the exit side (A1, A2). The internal collimation mainly prevents primary neutrons from hitting the inner spectrometer walls. Only diaphragm E2 was designed to re-shape the beam to a size of 45×70 mm^2.

Boron loaded material is only used outside of the spectrometer, whereas the internal collimation is made of isotopically enriched ^{6}LiF. This choice was made for reasons of UHV requirements and of radiation shielding. An advantage of ^{6}Li compared to ^{10}B is, that neutrons are mainly absorbed in a spallation process eq. 3.33, but the (n,γ)-process eq. 3.34 is strongly suppressed:

$$^6Li + n \rightarrow\ ^4He +\ ^3H \qquad (\sigma \approx 945\,\text{b}) \tag{3.33}$$

$$^6Li + n \rightarrow\ ^7Li + \gamma \qquad (\sigma \approx 0.04\,\text{b}) \tag{3.34}$$
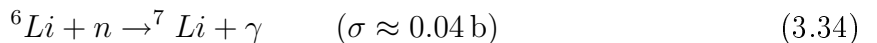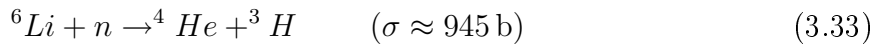
The cross-sections were taken from [55] for neutron energies of 20 meV. The absorption cross-section for neutrons of ^{6}LiF is about a factor of 4 lower compared to ^{10}B. But it is sufficient since the internal collimation absorbs only a small fraction of the neutron beam (about 5.2% compared to 79.8% on the entrance side). For the realization of the internal diaphragms, ^{6}LiF-stripes[6] were glued on holders made of boron loaded glass plates (8 mm thick) as shown in fig. 3.15. The holders fitted perfectly in the rectangular openings of aSPECT with some space left for alignment.

---

[6]Thanks to the PERKEO-collaboration for support in the production of the sintered LiF-plates. A pictured manual how to produce these plates is given in Appendix 13.
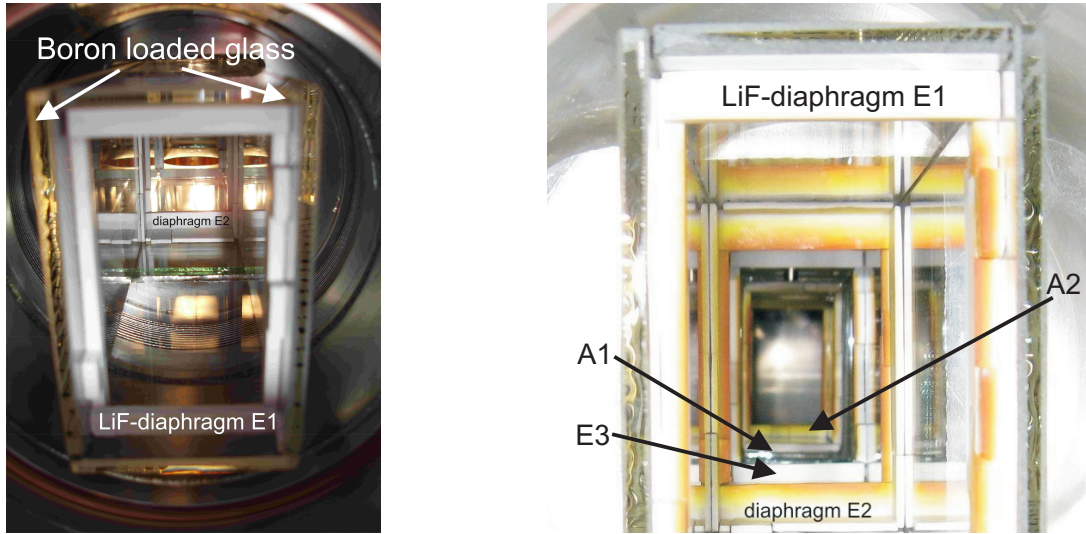
(a) View along the beam axis before the beam time. The pieces of LiF have still white color.

(b) LiF diaphragms after the beam time. The change in color indicates the strength of neutron absorption.

Figure 3.15: Internal collimation system. Pieces of isotopically enriched ^{6}LiF are glued on boron loaded glass.

Radiation shielding: The boron loaded glass plates that hold the diaphragms should absorb scattered and backscattered neutrons. Inside the entire internal beamline, additional boron loaded glass tubes were installed. γ-radiation produced by the entrance and exit window is shielded towards the detector by a great amount of lead bricks stacked around the side ports of aSPECT.

Diaphragms E2 and A2 have the highest neutron absorption of the internal diaphragms (see tab. 3.2). They were placed at predefined distances of about ± 280 mm to the DV. At these positions, the direct view between E2/ A2 and the proton detector is interrupted by lead pieces which are encapsulated in the insulation vacuum of aSPECT. The lead suppresses the radiative background at the detector position.

The beamdumb:
Behind the exit window an averaged capture flux of $\phi_c = 6.62{\cdot}10^{-9}$ n cm^{-2} s^{-1} for thermal neutrons was measured by gold foil activation in December 2007 at 58.25 MW reactor power. This corresponds to $\approx 15\%$ of the initial neutrons at the end of the neutron guide. A single diaphragm was used to collimated the beam into the aluminum box $(150 \times 50 \times 50$ cm$^3)$ of the beamdumb (see appendix 2, fig. 6.4). It is mainly a boron carbide plate at the backside wall of the box. Thick lead walls ($\varnothing$=10 cm) were stacked with a crane all around the aluminum box. Inside the beamdumb, boron loaded plastic and lead surrounded the beam tube. It was connected and aligned to the spectrometer by a bellows which contained boron loaded glass as well. A neutron counter was implemented

(a) Entrance side.

(b) Exit side with shielded beam dumb.
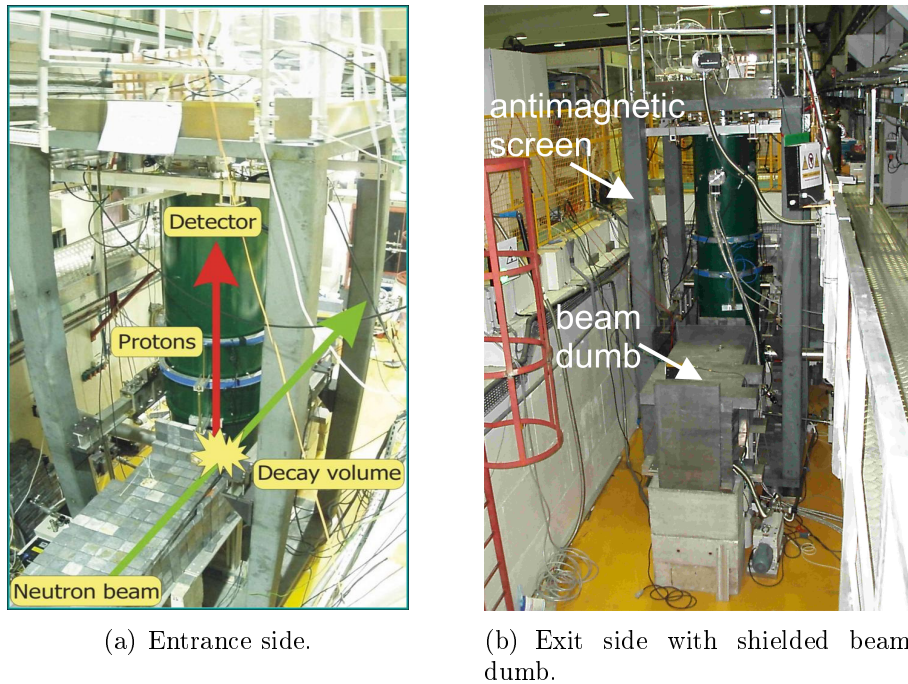
Figure 3.16: The complete *a*SPECT setup mounted at PF1B at ILL.

in the center of the beamdumb for in-situ monitoring of the neutron flux. The complete setup as it was built up at PF1B is shown in Figs. 3.13 and 3.16.

3.4.2 The collimation system: MC-calculations

For the simulation of the neutron beamline at PF1B, I used two independent programs both based on the Monte-Carlo method: Both programs simulate neutrons moving from the end of the neutron guide through the collimation system. The start parameters are the initial neutron density distribution and the initial emission angles and energies of the neutrons at the end of the neutron guide. Only straight trajectories are assumed, scattering and backscattering processes are not included in this calculations. All neutrons that hit diaphragms are absorbed and removed from the final neutron distribution. The outputs of both programs are neutron density distributions at any point of the beamline. Especially the beam profile in the DV is of interest here.

The difference between these two programs is the variability of the start parameters: The first program (a) (called "n-distributor"[7]) provides a homogeneous neutron distribution at the end of the neutron guide. The beam width and divergence can be chosen. In the second program (b)[8], several beam components can be superimposed. These components

---

[7]First-time implemented by Dr. S. Baeßler, a former Post-Doc of our group.
[8]Provided by Dr. T. Soldner at ILL.

Name	Width [mm]	Height [mm]	Distance to DV [mm]	Rel. absorption [%]
n-guide	50	116	3175	-
P0	45	70	3174	45.70
P1	50	75	1600	20.81
P2	45	70	690	13.27
Entrance window	Ø=110		625	
E1	48	80	480	0.31
E2	45	70	280	2.94
E3	48	80	120	0.08
DV			0	
A1	48	90	-120	0.78
A2	47	80	-280	1.10
Exit window	Ø=140		-625	
Beamdumb			-2270	15.01

Table 3.2: The collimation system at ILL: Positions, sizes and relative absorption of the diaphragms. 100% corresponds to the intensity at the end of the neutron guide.

can have different dimensions, intensities and divergences. It allows to simulate inhomogeneous neutron distributions at the end of the neutron guide. Program (a) was used for the construction of the diaphragms and their holders before the beam time. I expanded the program to our needs by implementation of various modifications. As mentioned in sect. 3.3.2, the neutron guide H113 is slightly bend. This results in an inhomogeneous density distribution at its end. Therefore, program (b) was used after the beam time to analytically reconstruct the conditions at PF1B: The simulations were adapted to the measured beam profiles.

My experiences with beamline simulations for the FRM II beam time ensured, that program (a) guarantees a sufficient accordance between simulation and attained beam profile. Two general concepts how to design the collimation system will be discussed in detail in Appendix 3. In order to suppress "edge effects", a beam profile with a broad, flat central part and sharp edges outside was chosen.

For technical reasons (e.g., geometrical constraints), the width of the neutron beam could not be increased any further. Fig. 3.15b shows the internal collimation system after the beam time. The color of the LiF diaphragms changed due to neutron absorption from white to yellow, orange and brown. The colored area comes already close to the side walls.- Tab. 3.2 lists the sizes and positions of the diaphragms in the final configuration of the collimation system.

3.4.3 The collimation system: B-n-scans

The knowledge of the neutron density distribution inside the DV is of great importance for the systematics of our experiment. Of major interest is the neutron distribution along the width of the DV (x-axis). It is needed for the calculation and correction of the so-called "edge effect" at the detector done in [30]. The edge effect will be discussed in detail in sect. 3.6.3. For precise calculations of proton trajectories and the magnetic mirror effect in the DV (see sect. 3.2.2), the neutron distribution along the height of the DV (z-axis) is as well needed. In addition, a map of the magnetic field strength is required for these calculations. After spectrometer and collimation system were aligned along the neutron beam (see Appendix 4), the resulting neutron beam profile was measured by means of copper foil activation. We performed several such measurements both in front of the entrance window and behind the exit window of aSPECT.

Neutron beam profiles: n-scan
The technique of copper foil activation is commonly used to determine the density distribution of a neutron beam in a precise way. A thin copper foil ($\approx 150\,\mu$m) is activated for about 80 minutes by neutrons. By neutron capture the unstable elements ^{64}Cu and ^{66}Cu are generated:

$$^{63}Cu + n \rightarrow^{64} Cu + \gamma(\tau = 12.7\,h) \tag{3.35}$$

$$^{65}Cu + n \rightarrow^{66} Cu + \gamma(\tau = 5.1\,min) \tag{3.36}$$
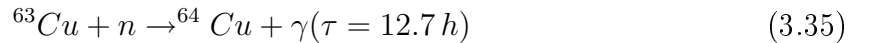
After activation, the foil stays untouched for about 2 h. After that waiting period, the influence from β-decays of the short-lived ^{66}Cu is negligible. The decay electrons of the meta-stable ^{64}Cu were detected by a PIN-diode[9]. Moved by a robotic arm, it scanned automatically the two-dimensional intensity profile in grid patterns (see fig. 3.17).

First, we performed several measurements to find the optimum activation time, waiting period and shielding of the diode: For background suppression, we shielded the diode with lead and kept a hole of Ø=3.5 mm open towards the copper foil. The diode was placed in the center of that hole, 35 mm above the surface of the Cu-foil. The size of the grid pattern and the measurement time at each pattern was arbitrary: A step size of 2.5 mm with an integration time of 5 sec/step were chosen as standard parameters (36×48 patterns). Each activated copper foil was scanned six times. After a single scan, the direction of scanning was reversed. The entire scanning sequence took about 2.5 h. The overall accuracy of the positioning of the copper foil in the beamline and in the scanner is 1 mm. The beam axis of the spectrometer (center of exit/ entrance flange) was marked on the foil and after scanning the foil several times, a small hole was drilled in the copper foil to see the center also in the scans.

Finally, 6 copper foil activations were performed as listed in tab. 3.3. The reproducibility was checked as well as the influence of the magnet cool down (index 1, 3): There is

---

[9]See also sect. 3.5 for an introduction to semiconductor detectors.
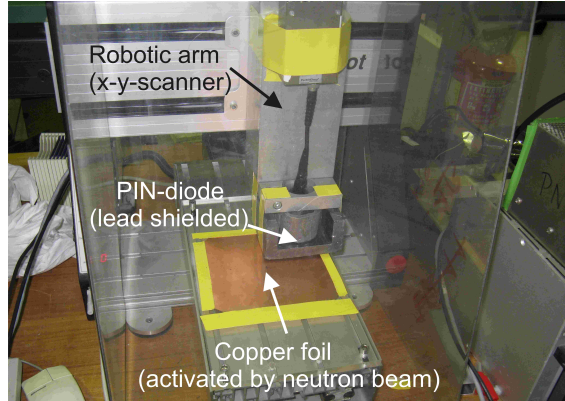
Figure 3.17: The activated copper foil was scanned in grid patterns along its surface using a PIN-diode moved by a robotic arm. The diode was situated inside a cup of lead (35 mm thick) above the activated copper foil surface.

Index	Foil position	Description
1	Exit window	Full beam (magnet warm)
2	Entrance window	Full beam (magnet warm)
3	Exit window	Full beam (magnet cold)
4	Exit window	Beam width (along x-axis) reduced to 5 mm in front of diaphragm P2
5	Entrance window	Beam width reduced to 20 mm in front of diaphragm P2
6	Exit window	Beam width reduced to 20 mm in front of diaphragm P2

Table 3.3: Copper foil activation measurements used for data analysis.

always a risk of loosening and dropping off of glued LiF-pieces from the internal collimation. The reason are the different heat expansion coefficients of the bonded materials. The variation of the neutron beam width by insertion of additional apertures (made of boron loaded rubber) (index 4-6) in front of the last external pre-collimator P2 was necessary to study edge effects.

The measured beam profiles in fig. 3.18 show an asymmetric shape. Final neutron simulations were done by using program (b): A sum of two Gaussian distributions turned out to be a suitable description for the neutron density distribution at the end of the neutron guide. The first distribution has the full dimensions of the neutron guide (i.e., 50x116 mm^2). The second distribution superimposes the first one on the right[10] half (i.e., 25x116 mm^2). Its intensity is half the intensity of the first component (i.e., $I_1 = 2 \times I_2$).

The focus of the simulation was set on the reproducibility of the central part of the profile which is imaged onto the proton detector. Uncertainties in the detector position, the proton gyration radii and the magnetic collimation onto the detector were taken

---

[10]View from the experimental zone onto the neutron guide, in direction to the reactor.
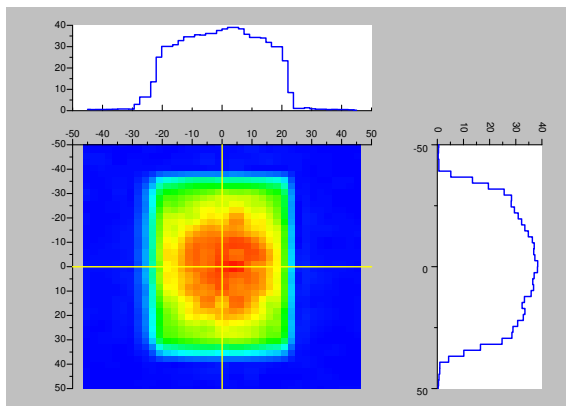
(a) Entrance window, full beam.
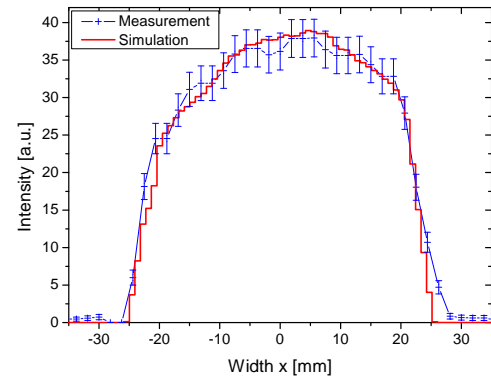
(b) Entrance window, full beam: Width (y=z=0).
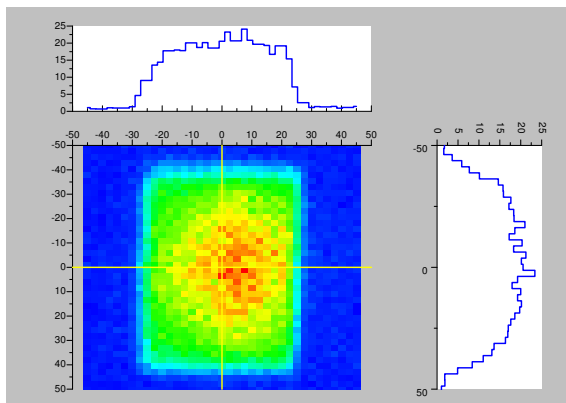
(c) Exit window, full beam.
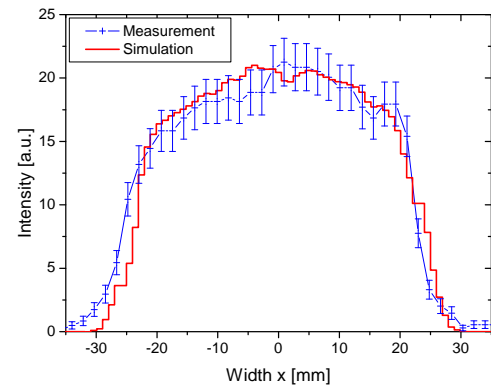
(d) Exit window, full beam: Width (y=z=0).
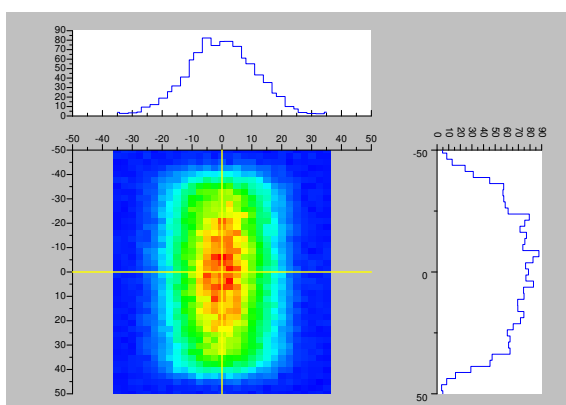
(e) Exit window, 20 mm beam width.
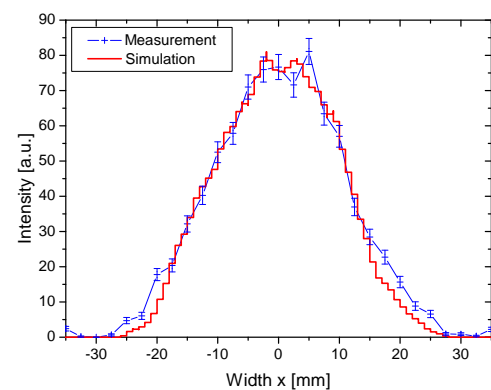
(f) Exit window, 20 mm beam width: Width (y=z=0).

Figure 3.18: Neutron beam profiles in front of the entrance window and behind the exit window. Left side: Measurements by copper foil activation. Right side: Cut along the x-axis (y=z=0) and comparison with simulated profiles calculated by superposition of 2 Gaussian distributions. The measurements are always plotted in blue and the simulations (using program (b)) in red color.
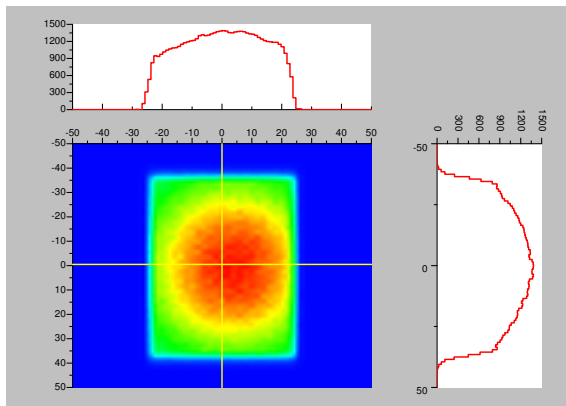
(a) DV, full beam.
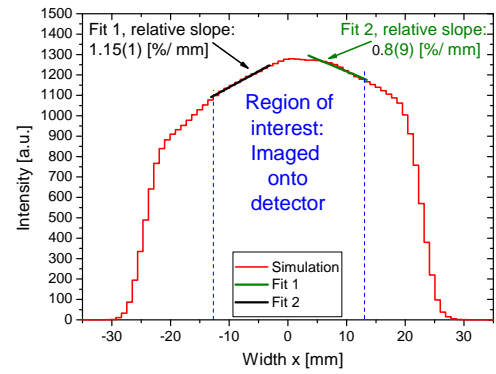
(b) DV, full beam: Width (y=z=0).
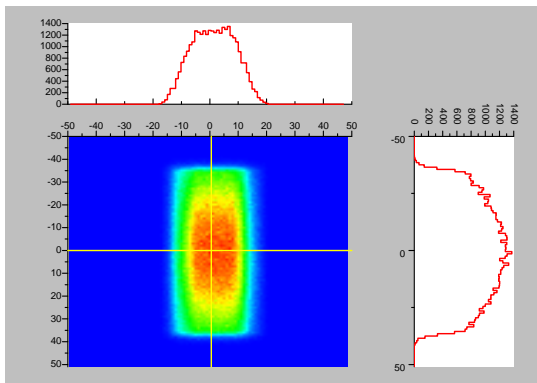
(c) DV, 20mm aperture.
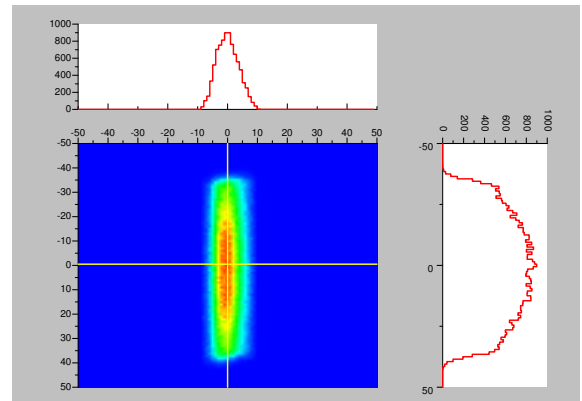
(d) DV, 5mm aperture.

Figure 3.19: Simulations of the beam profiles in the DV for three different beam widths. These profiles are used for edge effect calculations as well as for proton trajectories and magnetic mirror effect calculations. [30]

into account. It is of less importance, if the simulation fits the precise shape of the measured profile outside of the detector area. The adapted simulations are shown in fig. 3.18 together with the measured profiles. The model fits the measured profiles in the region of interest (along the central region from -12.5 mm to +12.5 mm, see sect. 3.6.3 concerning the "edge effect") both with and without apertures. The limited time for performing our experiment forced us to forgo beam profile measurements inside the DV. For the removal of the foil, aSPECT would have to be warmed up, vented, evacuated and cooled down again. The whole procedure would have taken about 10 days. Instead, I used the parameters of the simulation that fitted the measured profiles (at the entrance and exit window) to calculate the neutron density distribution in the DV. The result is shown in fig. 3.19 for different beam width. For the full beam (see (a) and (b)), the relative slope ($\frac{dI/dx}{I_{max}}$, with I being the intensity) of the proton density distribution is $1.15 \pm 0.01 \, [\%/\text{mm}]$ along one edge of the detector and $0.79 \pm 0.09 \, [\%/\text{mm}]$ along the other edge. Apart from the neutron density distribution, a precise knowledge of the magnetic field ratio $r_B = B_A/B_0$ is essential for the accurate extraction of a.

Magnetic field measurements at PF1B: B-scans

The magnetic field measurements followed several general aims:
(1) Investigations on the long and short term stabilities.
(2) Verification of reproducibility:
(a) Absolute field strength B for a given current I (B-I-calibration).
(b) Ratio $r_B = B_A/B_0$ after dismounting and remounting of the antimagnetic screen.
(3) Determination of the field ratio r_B with a sufficient accuracy $<10^{-4}$.
(4) Extraction of a longitudinal field map (along z-axis).
(5) Extraction of a radial field map (off-axis) in the DV and the AP.
The field maps (4) and (5) are required for adiabaticity calculations and simulations of particle trajectories.

In prior measurements at Mainz (2005 and 2007) and Munich (2005 and 2006) we proved that the magnetic field of aSPECT meets the demands: On the one hand, the magnetic field dependence along the z-axis (called "axial" field) always fulfills the adiabatic conditions. On the other hand, the axial and radial magnetic field gradients in the DV and the AP are below the critical limits necessary to reach the required sensitivity on a. In this context, the region of interest is defined by the dimensions of the proton flux-tube.

For our measurements at PF1B the construction of an antimagnetic screen was obligatory: Without screen, the stray field of our spectrometer would interfere destructively with neighboring experiments. The use of the screen involved further magnetic field measurements. At the beginning of 2007, we verified in Mainz the impact of the screen on the internal and external magnetic field which was calculated by G. Konrad ([30]): The internal field increases by about 2% in the AP and by about 7% in the DV. Thus, the ratio r_B changed minimally but the magnetic field shape between DV and AP stays in

the adiabatic limit. The external stray field in 5.6 m distance to the vertical spectrometer axis (z-axis) is reduced by a factor of 7 and satisfies our needs.

Various factors lead to the necessity to re-measure the magnetic field of aSPECT at PF1B: Unknown environmental conditions (e.g., external sources of magnetic fields) might change the internal magnetic field of aSPECT. In addition, the superconducting coils in the DV and the AP showed a hysteresis effect which was recognized in 2007. After ramping down the current to 0 A, a magnetic field of about 3 mT remains that produces a rather inhomogeneous field. The field disappears after warming up the coils above their critical temperature of $T_{crit} \approx 9$ K. Especially for NbTi-superconductors it is a known effect and was discussed for example in [57]: Persisting currents cause a small magnetic field once the superconducting coils were switched on before. This effect appears even at zero nominal current. Recent investigations showed that aSPECT provides a reproducible magnetic field after warming up above the critical temperature and cooling down again. To prevent any influence of hysteresis, we ramped up the main magnetic field of aSPECT (i.e., to operation conditions of 70 A) only once and kept it on that level during the entire beam time for the measurement of a. Details on the performance of the magnetic field measurements and their analysis are given in [27] and [31].

It should be mentioned, that a Hall probe of model MPT-141 manufactured by Group 3 Technologies was used for magnetic field measurements. The probe requires operation temperatures from 0 to 50 °C. To provide this conditions, an inverted dewar was designed that consists of a non-magnetic aluminum tube covered outside by a multitude of layers of super-insulation foil. The dewar fits the inner bore tube size and keeps the probe at room temperature. The use of several holders allows to measure on- and off-axis.

For the extraction of a, a reliable magnetic field ratio r_B is required. Its accuracy arises from the axial homogeneities in the DV and the AP. The plots of fig. 3.20 show the on-axis measurements taken in the DV and the AP to determine the field homogeneities. The relative gradient on-axis (z=-4...+4 cm) in the DV was:

$$\frac{B_{0,max} - B_{0,min}}{B_0} < 7 \times 10^{-4} \tag{3.37}$$

and the variation in the AP (z=+129...+132 cm) was found to be:

$$\frac{B_{A,max} - B_{A,min}}{B_A} < 1 \times 10^{-4} \tag{3.38}$$

The maximum of the magnetic field strength B_A in the AP was shifted minimally above the calculated maximum of the electric barrier potential eU_A. Therefore a region of 3 cm was used for the extraction of the homogeneity in eq. 3.38.

The uncertainty of r_B is given by the experimental accuracy of the Hall probe. For each point i with coordinates (x_i,y_i,z_i) inside the DV (especially inside the flux-tube region), one can determine a ratio $r_B(x_i,y_i,z_i)$ using the magnetic field maps. For the calculation

(a) DV, on-axis. (b) AP, on-axis.
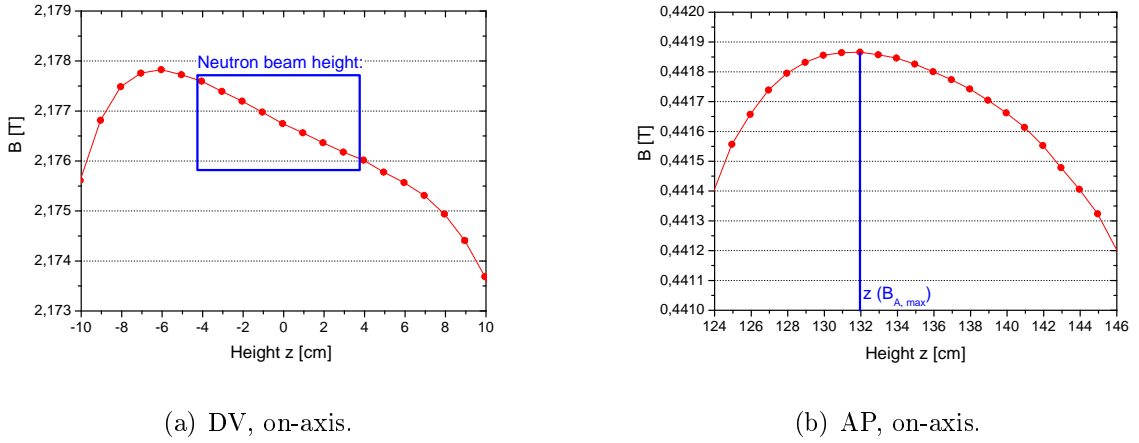
Figure 3.20: Magnetic field profiles measured on-axis with a coil current of 70 A. The maximum of the electric field potential in the AP was shifted minimally with respect to the maximum of the magnetic field. Therefore the gradient in the AP was extracted in a region ± 3 cm. The on-going analysis in [31] will extract a final value for the field gradient in the AP.

of an average r_B (necessary for the extraction of a), all ratios have to be weighted with the simulated 3-dimensional neutron beam profile in the DV (see projection in fig. 3.19a). The uncertainty of this simulation limits the accuracy of r_B. Precise calculations of an average ratio r_B can be found in [30] and [31]. An upper limit for the uncertainty of r_B can be estimated by using the measured field homogeneities in eq. 3.37 and eq. 3.38. The obtained average magnetic field ratio is r_B=0.20298(7). The detailed analysis of all magnetic field measurements is still on-going and will be part of the PhD thesis of F. Ayala [31].

However, in-situ measurements of the magnetic field during data taking would be more appropriate. One could monitor possible field drifts due to malfunctions or field changes due to environmental conditions. A first implementation of a nuclear magnetic resonance (NMR)-unit was developed in the PhD thesis of F. Ayala [31].

3.5 The detection system

3.5.1 A brief introduction on semiconductors

General introductions to the working principle of semiconductor detectors, used for detection of charged particles, can be found in common textbooks (e.g., [58], [59] or [60]). But some features should be mentioned to point out the differences between the detector type used in the FRM II beam time (Silicon (Si)-PIN-diode) and the ILL beam time (Silicon-drift-detector, SDD): Semiconductors are solid materials which show a small band gap

between the valance band and the conducting band of about $1\,\mathrm{eV}$ (in conductors the two bands overlap, in insulators they are separated by several eV). Electrons in the valence band can be excited by thermal vibrations to the conducting band at room temperature. Each excited electron leaves a hole in the valence band which is equivalent to the generation of a positive charge.

The electrical behaviour of an intrinsic semiconductor can be manipulated by the technique of doping, meaning the add-on of specific atomic impurities to the crystal. Atoms with one valence electron more (or less) than the semiconductor create an additional free electron (or hole). In the case of silicon, boron can be used to create holes (called "p-doped", where p stands for positive) or arsenic to create free electrons ("n-doped"). The energy to create electron hole pairs can not only come from thermal vibrations but also from other processes like optical excitation or penetration by charged particles. The specific energy loss $-\frac{dE}{dx}$ of a charged particle traveling through material (in x-direction) is described by the Bethe-Bloch formula [61], [62]:

$$-\frac{dE}{dx} = \frac{4\pi e^4 z^2}{m_e v^2} NZB, \tag{3.39}$$

where v is the velocity of the particle and ze is its charge. N and Z are the number density and the atomic number of the penetrated material, m_e is the rest mass of the electron. B is a rather complicated expression depending on the energy of the particle as well as on the excitation and ionization energy of the absorber. The maximal energy transfer of an incoming particle to an electron (by central elastic collision) is limited to $4E\frac{m_e}{M}$ for kinematic reasons, with E and M being the energy and mass of the incoming particle, respectively. Protons can transfer about 0.2% of their energy per collision. Therefore protons undergo many scattering processes on their way through the detector until getting stuck. This statistical process results in a smearing of the deposited energy and therefore a broadening of the measured energy distribution.

3.5.2 The Si-PIN-Diode used at FRM II

In our beam time at FRM II we used segmented Si-PIN-diodes for detection of the decay protons. PIN-diodes are the common type of semiconductor detectors: Their "PN"-structure[11] is separated by an intrinsic layer "I" to increase the active volume of the detector. Their specific characteristics and the corresponding DAQ-electronics are well described in [25], [28] and [29]. Hence I will focus on the special features that forced us to choose another type of detector for our recent beam time at ILL.

As explained in section 3.2.3, the protons have to be accelerated towards the detector to overcome the magnetic mirror and to gain sufficient impact energy to be registered in the active layers of the detector. These are covered by a thin dead layer for protection

---

[11]"PN" denotes a layer of p-doped material connected with a layer of n-doped material.
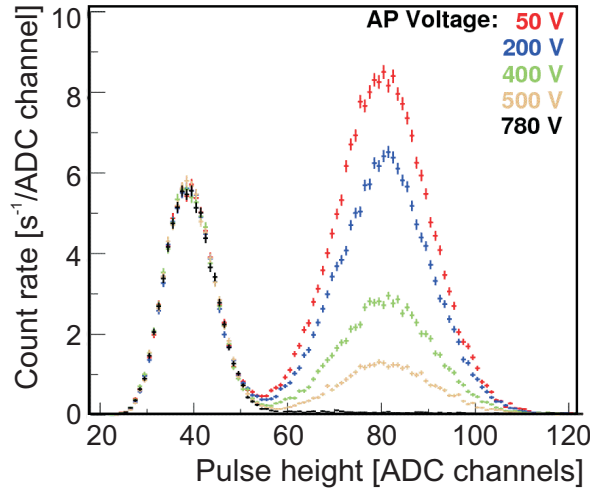
Figure 3.21: Pulse height spectrum measured in the beam time in 2006 at FRM II. The left peak represents the electronic noise and the right peak the protons. By increasing the APV the amount of detected protons decreases.

(67 nm thickness in the case of the Si-PIN-diode). Protons with a kinetic energy of 30.4 keV were found to lose 5.8 ± 0.9 keV in the dead layer. The remaining energy is deposited in the active layers and produces a pulse. The corresponding pulse height has to be higher than the pulse height of electronic noise signals in order to separate them. The disadvantage of Si-PIN-diodes (for our demands) relies on the fact, that the thermal noise of this detector type is proportional to its active area. Even though the active area of the PIN-diode used at FRM II was divided into 25 single stripes with separated readouts, the noise level was still too high: Fig. 3.21 shows such a pulse height spectrum recorded in 2006 at FRM II with a Si-PIN-diode kept at -30 kV. The peak on the left side of the plot represents the electronic noise, the right peaks correspond to protons for different settings of the AP voltages (APV-settings). It is obvious that both peaks are not well separated from each other. The analysis showed, that the overlap at the left tail of the proton peak increases the uncertainty of the extracted value of the coefficient a. Therefore, the reduction of electronic noise was one consequence of the FRM II beam time. In principle, this can be achieved by effective cooling of the pre-amplifier. A second consequence would be to increase the detector HV in order to shift the proton peak to higher pulse heights.

But already the chosen detector HV of -30 kV caused some instabilities: Phases of increased field emission currents were correlated to the detection of an uncontrollable source of background [25]. Even without recognizable discharges, the production of electrons in the detector region (e.g., by field emission at the detector cup) seemed to induce secondary effects (e.g., residual gas ionization). The impact of these effects was demonstrated in 2006 by various systematic tests. Even background contributions at the position of the proton peak were found in the pulse height spectra. Their amount depended on the APV what
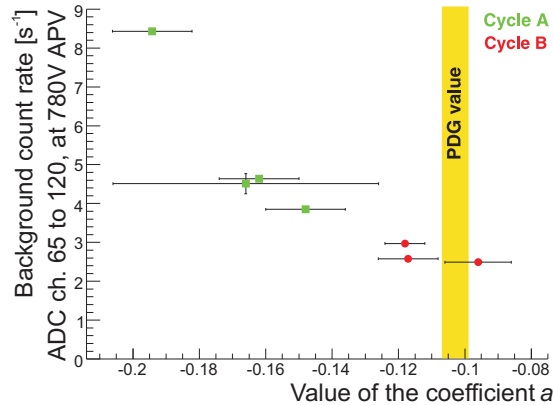
Figure 3.22: The average background count rate at 780 V APV integrated from ADC ch. 65 to 120 (see fig. 3.21) related to the extracted value of the coefficient a for measurements from different cycles. An increased background results in a strong variation in a.

causes the major problems: The only way to measure the total background in our experiment is the measurement at 780 V APV (see sect. 3.6.2). All decay protons are reflected by the potential barrier and the background is measured. This method presumes, that the AP potential does not influence the background or produces any other contributions (i.e., the background at all other APV-settings is constant and corresponds to the value measured at 780 V). Measurements with neutron beam switched "off" showed an obvious AP dependence of this background. However, these measurements can not deliver the absolute numbers for the background with neutron beam "on". Since the amount of the APV-dependent background in the beam times at FRM II was high and very unstable, it caused an uncorrectable systematic error on the coefficient a (see fig. 3.22). Further investigations done at Mainz in 2007 reproduced the APV-dependence of the background. These measurements approved that the background was correlated to phases of increased field emission currents at the detector electrode. In [1] and [25], possible production mechanisms are outlined, a detailed discussion will follow in section 3.6.2.

Three main conclusions were drawn from the FRM II beam time: (1) A better separation of electronic noise and proton peak is needed.
This requires (a) an increment of the detector HV, (b) a reduction of electronic noise by cooling of the electronics and/ or (c) the use of another type of detector which might produce less electronic noise.
(2) The APV-dependent background has to be reduced.
This could be achieved by (a) improving the surface conditions, geometry and positioning of several electrodes. (b) By reducing the detector HV (requires also another type of detector which works at lower detector HV). (c) By improving the vacuum conditions. The probability for residual gas ionization depends on the pressure (see sect. 3.6.1 and 3.6.2.)
(3) The APV-dependent background has to be investigated during data taking.

We employed a fast neutron shutter (opening and closing time $< 0.5\,$ms) for the measurements at ILL. It helps to study the rise and the decay of background contributions and to estimate their impact on a.

As a consequence, I adapted the geometry and positioning of the upper ExB-electrode e16 and we improved the shape and polishing of the detector cup e17. In addition, an insulating transformer was used for the voltage supply to the detector and its electronics. The new setup was tested in 2007 to allow for a simultaneous application of -35 kV to the detector cup (e17) and -35/ -20 kV to the upper ExB electrode (e16) without discharges. At the same time, our collaborators from TU München/ E18 sought out and tested a different type of semiconductor detector [63]. It emerged to solve both the HV problematics and the separation of the proton peak from the electronic noise peak.

3.5.3 The Silicon-drift-detector (SDD) used at ILL

The principle of SDDs was first described by E. Gatti and P. Rehak in 1984 [65]. Classical semiconductor detectors typically consist of a thin silicon wafer with a continuous n-doped layer on one side and p-doped strips on the other side. An electric field in reverse bias mode is used both for depleting the detector and creating the field gradient to collect charges created by particle impact, whereas the SDD-concept is based on the principle of sidewards depletion. Instead of using a single field for depletion as well as for charge separation, two separate fields are applied. This principle is shown in fig. 3.23. The bulk material of the detector is n-doped silicon. On one side of the SDD a smooth p^+ layer is implemented, whereas the other side has a structure of concentric p^+ rings ("+" refers to a strong degree of doping, "-" would indicate a minor degree).

The detector which we used at ILL was manufactured by the MPI Halbleiterlabor [66] in cooperation with PNSensor GmbH [67]. It consists of a set of three Si-drift-detectors implemented in a row on one silicon chip as shown in fig. 3.24. In the following, the complete set will be called "detector" and the single parts "pads". The pads will be enumerated by the corresponding channels of the ADC[12] readout (channel 5, 6 and 7). Each pad provides an active area of $1\,$cm^2 with a thickness of $450\,\mu$m, covered by a thin entrance window of $30\,$nm aluminum.

Fig. 3.25 shows a proton spectrum measured with the Si-PIN-diode (left side, at -30 kV detector HV) used in the FRM II beam time in direct comparison with corresponding spectra using the new SDD type proton detector (right side, at -10, -12 and -14 kV detector HV). In difference to PIN-diodes, the thermal noise (one component of the electronic noise peak) of a SDD is decoupled from its active area. Accessory, the first amplification stage is integrated in the detector itself which helps to reduce thermal noise: The detector and the first amplification stage is inserted in the cold bore of the spectrometer and therefore sufficiently cooled. Also the reception of environmental noise is suppressed: The

---

[12]See sect. 3.5.4.
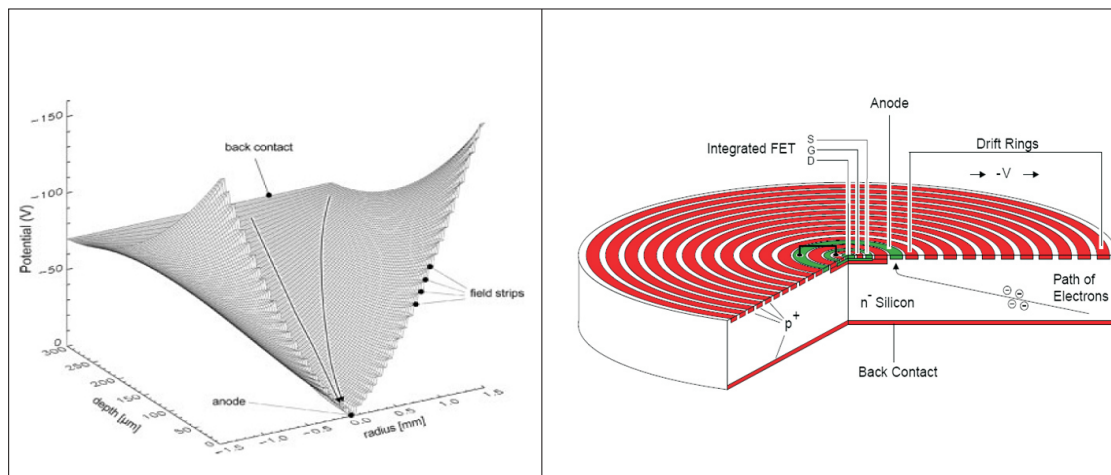
Figure 3.23: The principle of a Silicon-drift-detector (SDD). The left picture was taken from [64] and shows the drift potential from cathode to anode in the center. The right picture was taken from [63]. The gate (G) of the integrated FET is connected to the anode and represents the first amplification stage which reduces the pick-up of noise by wires.
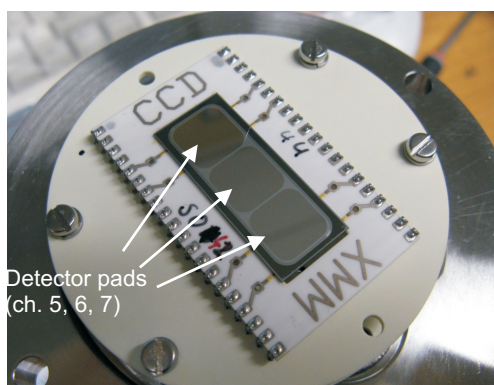
(a) The 3 detector pads.
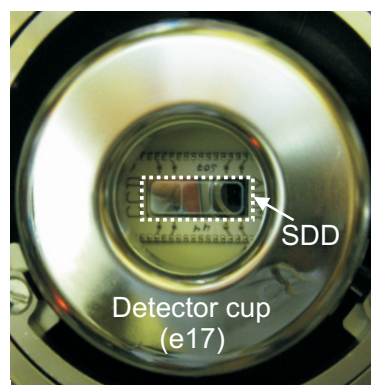
(b) SDD mounted inside the detector cup.

Figure 3.24: The SDD detector used at ILL. Each pad (denoted as ch. 5, 6, 7) provides an active area of $1\,\mathrm{cm}^2$.

signal is pre-amplified by a field effect transistor (FET) before environmental noise can be launched by the wiring between detector and amplifier. The improved separation of electronic noise and proton peak is obvious. Furthermore, the spectra demonstrate the possibility of reducing the detector voltages by a factor of 2 (e.g., to -15 kV).
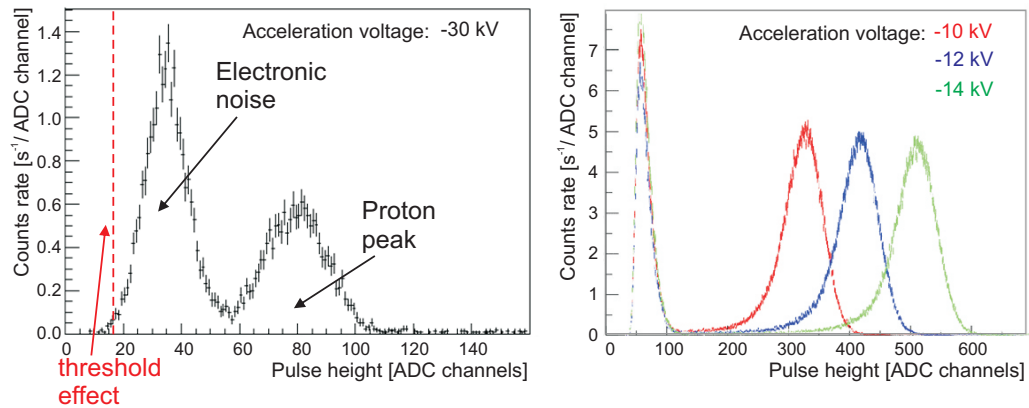
Figure 3.25: Comparison of pulse height spectra. Left: Measured with Si-PIN-diode (used at FRM II) at -30 kV detector HV. Right: Measured with SDD (used at ILL) at -10, -12, -14 kV detector HV.

The mechanical setup:
The detector is inserted from the top side of *a*SPECT into the cold bore tube. It is placed in the high magnetic field that guides and focuses the protons. For reasons of maintenance (e.g., HV-discharges might damage the detector) it is necessary to provide fast access to the detector. Therefore a separated vacuum system (called "detector vacuum"), was implemented that can be separated and removed from the main vacuum system of *a*SPECT by a gate valve without breaking the main vacuum. The exchange of a detector takes about 24 hours. It is limited by the pumping speed until the pressure in the detector vacuum section is similar to the main vacuum and the gate valve can be re-opened. It should be mentioned that we managed to measure the complete ILL beam time with just one detector.

3.5.4 Signal processing electronics

The amplification boards:
The preamplifier board is directly connected with a 50 pin SUB-D connector to the detector feed-through to prevent pickup noise (e.g., HF-noise) by long cables. Three Amptek A250 chips (one per detector channel) followed by an Analog Devices AD 8024 chip amplify incoming signals from each detector pad. Afterwards, the signals are transferred by

three coaxial cables out of the spectrometer: The digital part of the detector electronics could not be placed inside the cryostat since it needs too much space and generates too much heat load. Therefore, above the spectrometer on top of the antimagnetic screen (see fig. 3.16), an aluminium box covers the digital electronics for reasons of electrical shielding. In turn, this box is embedded in a bigger perspex box for safety since all the electronics is at HV.

The signals coming from the preamplifier are fed into an adapter board (called "shaper"). This board shapes the signals and distributes them to the ADC (**A**nalogue to **D**igital **C**onverter). The shape of raw signals from the detector consists of a steep rising part and a long exponentially falling tail. The shaper is mostly sensitive to the rising part and shortens the pulse, so it can be treated by the digital electronics. The shaping is done by a chain of two Analog Devices AD 847N and one AD 8138 chip for each channel. Furthermore, a readout circuit for the temperature diode on the detector chip is implemented on this board. The various voltages needed for operation are also applied by these cables. The voltages are fed to the preamplifier board by a 16 pole ribbon cable [32]. The cables to connect the two parts of the electronics (in and outside of the cryostat) are contained in a acrylic glass tube in order to shield the high voltage.

Digital electronics and trigger algorithm:
The ADC board is capable of processing signals from up to 32 channels simultaneously, because it was already used with the Si-PIN-diode (25 channels). Only three channels were used now for analyzing the signals of the SDD-detector pads and one for the readout of a temperature diode on the detector chip. The 12-bit-ADC digitizes the signals coming from the preamplifier with a sampling frequency of 20 MHz. This results in time bins of 50 ns length, which is a reasonable partition: The length of a typical proton event is about $4\mu s$ (see fig. 3.26). Besides, this sampling rate keeps the data volume on an acceptable level. After digitalization the signals are treated by two Xilinx Virtex-II 1000 field programmable gate arrays (FPGA). Each FPGA provides data buffering and processing for 16 channels. The full amount of data sampled by the ADC (≈ 28.6 MB/s per channel) would exceed the storage capacity of a conventional personal computer. Thus, signals are discriminated by the FPGAs applying an on-line trigger algorithm: The incoming data is steadily shifted through a register and discarded in absence of events.

The general algorithm is based on the comparison of two sliding time windows within the register. If the mean values of the two windows differ by more than a given threshold set, the trigger condition is fulfilled. As you can see in fig. 3.26, window $w1$ is used to determine the baseline, whereas $w2$ is separated from $w1$ by an arbitrary window distance. Another parameter called "delay" was implemented which specifies how many times in a row the trigger conditions have to be fulfilled before a trigger decision is made. This feature helps to suppress triggers on noise events. A trigger buffer ensures, that a sufficient amount of data before the rising tail of an event is stored. This information is needed in order to determine the baseline value in off-line data analysis (see fig. 3.26).
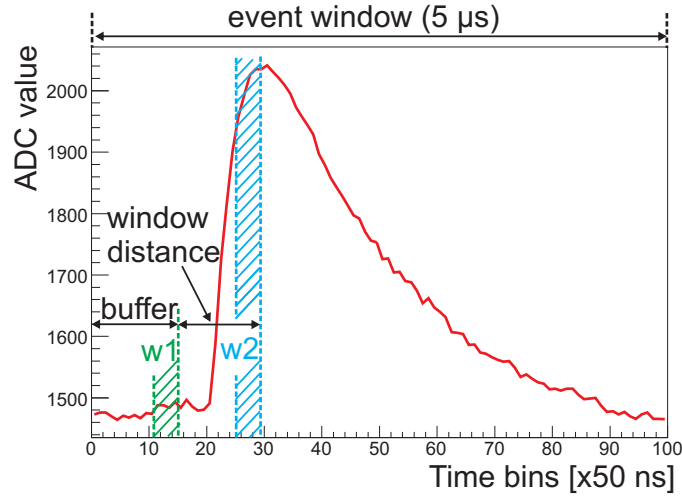
Figure 3.26: Overview on the trigger algorithm: The shown signal shape (red line) is typical for a proton event. The ADC values integrated in two windows $w1$ and $w2$ are compared with respect to a threshold set. The window distance can be chosen as well. The event window (also: "event size") was chosen to be $5\,\mu$s. A buffer of 15 time bins is stored before the triggered pulse for determination of the baseline value.

The window distance was fixed to 16 time bins ($0.8\,\mu$s) in our experiment, the other parameters could be set by a control program. For most of the measurements in the ILL beam time, $w1$ and $w2$ were set to a length of 4 time bins with a delay of 3 time bins. The trigger buffer had a length of 15 time bins and the total event window was chosen to be 100 time bins ($5\,\mu$s). In case of a trigger, the data from each channel is stored in a buffer on the ADC board. It can store up to 1024 ADC values and operates on the first in - first out (FIFO) principle. The data is send via a HOTLINK interface (i.e., an optical data transfer standard using fibre optics) from the FPGAs to the DAQ computer. The optical connection allows for operating of the digital electronics on the detector HV whereas the DAQ computer stays on ground potential. A detailed description of the technical realization of the data processing electronics is given in [32]. Also the structure of the raw data is explicitly discussed there. The raw data was decoded in-situ into a processable format. For each single measurement a file was stored that consists of several parameters which were filled into a ROOT-tree (ROOT is an object-oriented data analysis framework developed at CERN, see [68]). These parameters contain information about the pulse height, timing and the typification of events.

The characterization of the detector, its electronics and the DAQ-system, as well as the construction of the mechanical detector setup, were central tasks in the PhD thesis of our collaboration partner M. Simson from the TU München [32].

3.6 Systematic effects

A good knowledge of the systematics is important for any kind of experiment but essential for high precision measurements such as aSPECT. When the design of the spectrometer was proposed in 2000, several systematic effects were considered in [26] and discussed in [22]. To achieve the final goal of aSPECT that is to measure the coefficient a with an accuracy of $\frac{\delta a}{a} \approx 3 \times 10^{-3}$, the impact of each systematic effect on a should be $\delta a < 10^{-4}$.

3.6.1 Effects regarding the transmission function

The discussion in this subsection is based on the publications of our collaborators O. Zimmer *et al.* [26] and F. Glück *et al.* [22] describing the design of the aSPECT-spectrometer as well as its electromagnetic design including systematic effects. The transmission function F_{tr} was expressed in eq. 3.26 by terms of the potential difference $e(U_A - U_0)$ and the magnetic field ratio $r_B = B_A/B_0$:

$$F_{tr}(E) = \begin{cases} 0 & \text{if } E \leq eU \\ 1 - \sqrt{1 - 1/r_B(1 - e(U_A - U_0)/E)} & \text{otherwise} \\ 1 & \text{if } E \geq eU/(1 - 1/r_B) \end{cases} \qquad (3.40)$$

where E refers to the initial proton kinetic energy and e denotes the unit charge.

The field ratio r_B:
The impact of the uncertainty of r_B on the uncertainty of a can be expressed as ([26]):

$$\delta r_B = c(U, r_B) \times \delta a \qquad (3.41)$$

For a given r_B, the function c(U, r_B) is < 1 and is monotonically increasing with U. As discussed at the end of sect. 3.4.3, r_B can be extracted precisely from the magnetic field measurements at any chosen position inside the DV. But the calculation of an average ratio r_B is limited by the accuracy of the (simulated) 3-dimensional neutron density distribution in the DV. With the preliminary value of r_B=0.20298(7), an accuracy of $\frac{\Delta a}{a} < 0.37\%$ can be achieved. Please note, that the uncertainty of r_B is a worst case approximation. The on-going analysis of the magnetic field measurements in [31] and trajectory calculations in [30] might deliver decreased errors in r_B and a, accordingly.

The electric potential difference $e(U_A - U_0)$:
Some general demands were made on the potentials in the DV and the AP:
(1) The electrodes themselves must provide uniform electric potentials across the flux-tube region. This requires certain dimensions of the electrodes and a good preparation of

their surfaces (e.g., mechanical construction, polishing and coating; see sect. 3.2.3).
(2) Field penetration by neighboring electrodes must be minimized.
(3) Additional effects that may change the potentials should be suppressed, for example variations of the electrodes´ work function (e.g., due to surface charges by adhesion of negative charged particles).

Several measures were taken to meet this requirements, partly discussed in sect. 3.2.3: The surfaces of all electrodes were polished and gold coated. The central DV electrodes (e4, e5) and the AP electrode (e14) have big diameters. In this configuration, small work function differences along the electrodes surfaces can average out in the flux-tube region. In addition, field penetration by neighboring electrodes was restricted by setting the electrodes e3/e6 next to the DV on the same potential as e4/e5. The electrodes e13/e15 next to the AP were set on similar potentials as e14.

To reach the goal of $\frac{\delta a}{a} < 3 \times 10^{-3}$, the potential difference $e(U_A - U_0)$ has to be known with an absolute accuracy of 10 meV. Local differences of work functions might have a dominant impact on the uniformity of the potentials. They can be caused by impurities and defects in the crystal structure of the electrode surface. A Kelvin Probe was used to determine work function differences along an electrode surface. First measurements at an electrode, which was polished and coated as in the FRM II beam time, showed variations of up to 150 meV. The more sophisticated polishing and coating for the ILL beam time might reduce the work function variations. An uncertainty of ± 75 meV on the potential difference $e(U_A - U_0)$ would prevent an absolute precision in a of better than 1.13%. The previous measurements showed, that the surface conditions have to be improved: For future beam times, we test different materials, better surface preparation and different coatings combined with Kelvin Probe measurements. For details on the measurements of various electrodes see [30].

An additional way how to determine the potential difference $e(U_A - U_0)$ would be by using a mono-energetic calibration ion source. It could be installed below the bottom flange of aSPECT or directly inside the DV. In the latter case, the source could be used to measure the transmission function F_{tr}. During my PhD thesis, I designed and tested a prototype ion source which will be described in Appendix 12.

Apart from their influence on the potential difference $e(U_A - U_0)$, local potential differences (due to variations of the work function) can create Penning traps (e.g., for protons emitted with minimal initial longitudinal energy close to the surface of the DV electrode). The applied small magnetic field gradient in the DV reduces the impact of this effect (see sect. 3.2.2).

Non-adiabatic proton motion:
Contributions of non-adiabatic proton motion should be negligible to first order since it was an essential requirement in the design of the aSPECT spectrometer following the calculations of F. Glück [22]. As the analytical calculation of the transmission function

B_0	3 T	1.5 T	1.2 T	0.9 T	0.6 T
δa	10^{-6}	$4 \cdot 10^{-5}$	$5 \cdot 10^{-4}$	$4 \cdot 10^{-3}$	$2 \cdot 10^{-2}$

Table 3.4: Calculated dependence of the systematic uncertainty δa due to non-adiabatic proton motion for different magnetic field values B_0 in the DV. The dipole potential in the lower ExB-drift electrode was fixed on -3 keV in this calculations. It was calculated to be an upper limit for the drift potential. For the lower drift potential used during the ILL beam time the effect even reduces.

is only valid in the adiabatic limit, the impact of non-adiabatic contributions has to be considered nonetheless. By using calculated electric field maps and the magnetic field within the flux tube, an optimization procedure for suppression of non-adiabatic effects down to the required level was established in [22].

A central statement in the derivation of the transmission function in sect. 3.1.3 was the invariance of the orbital magnetic momentum $\mu = \frac{T_\perp}{B}$. Sophisticated calculations of proton trajectories showed that the adiabaticity conditions are fulfilled in aSPECT although the protons pass an inhomogeneous electric field between DV and AP. As described in [22] and [69], charged particles show some kind of "memory" when moving from one region of high homogeneity (DV) to another one (AP): The charged particle "remembers" its original orbital magnetic moment.

The influence of non-adiabaticity effects is more severe for protons trapped between AP and ME than for transmitted protons. Protons with insufficient energy to pass the AP perform axial oscillations between both potential wells (see fig. 3.28). The impact of non-adiabatic changes of the angle and of the orbital magnetic momentum increases with the number of oscillations. This would result in an uncertainty in the transmission function and the measured spectra. Therefore, the dipole field produced by the lower ExB drift electrode (e8) was provided to remove trapped protons after a few oscillations, e.g., 5-6 oscillations when applying an electric field gradient of 3 keV (from calculations done by F. Glück [22]). On the one hand, the efficiency of the lower ExB drift increases with the strength of the applied gradient field. But on the other hand, it also amplifies the impact of non-adiabatic effects: The electric field gradient causes acceleration of the protons and an increased gyration length. With regard to the adiabatic conditions, appropriate parameter settings were calculated to suppress both errors from trapping and non-adiabaticity effects. They showed a breakdown of the adiabatic approximation at an upper limit of -3 kV at e8 [22]. In the ILL beam time, we applied even lower voltage settings at the lower ExB drift electrode: -1000 V / -50 V was used most of the time (i.e., an electric field gradient of 950 eV and an averaged potential of -525 eV (on-axis)). Furthermore, even lower settings of -200 V / 0 V were applied for some time for systematic tests. Recent simulations and the experiences made in the FRM II beam time showed that these settings are reasonable. In both cases, the impact on non-adiabaticity effects is negligible. The dependence of a on the magnetic field in the DV (B_0) was calculated in [22] for a given dipole field of -3 kV: Above

$B_0 = 1.5\,\mathrm{T}$, the systematic effect on a is negligible, but below $1\,\mathrm{T}$ it becomes substantial [22]. Tab. 3.4 shows the results of these calculations. All measurements in the ILL beam time, which are used for the extraction of a, were taken at $B_0 = 2.2\,\mathrm{T}$. Therefore non-adiabatic influences are negligibly small at the considered level of accuracy. Nevertheless, we performed supplementary systematic tests with $B_0 \approx 0.94\,\mathrm{T}$ to verify the impact of a low magnetic field strength on a (see sect. 4.10.2).

Interactions with residual gas atoms:
Residual gas atoms can interact with decay protons by different types of collisions: Elastic and inelastic scattering as well as charge exchange collisions are possible mechanisms. These processes can induce changes in the kinetic energy or the pitch angle θ between the proton momentum and the magnetic field and result in variations of the transmission properties. The collision probability is proportional to the residual gas density and therefore to the pressure. The aim is that protons with an initial kinetic energy higher than the potential barrier ($T_0 > T_{tr}$) should reach the detector without collisions. Therefore calculations in consideration of the critical pressure p_{cr} were performed in [22]. p_{cr} denotes the vacuum limit from which on a certain type of collision introduces a systematic error of $\delta a = 10^{-4}$.

I will summarize these results with respect to our vacuum conditions in the ILL beam time of $p_{main} = 8 \times 10^{-9}\,\mathrm{mbar}$. Please note, that the pressure was monitored at the end of a $2\,\mathrm{m}$ long tube (at room temperature) outside the antimagnetic screen. This is necessary during magnet operation for calibration issues of the used IKR vacuum gauge. We expect the vacuum between DV and AP to be better due to the four getter pumps inserted there and the freezing out of residual gases at the cold bore tube walls.

1) Elastic scattering:
Elastic scattering affects mainly the pitch angle θ. The scattering probability is proportional to the path length and therefore to the time a proton spends within the flux tube. Accordingly, the effect is more severe for trapped protons since they perform several oscillations before they are removed by the lower ExB-drift electrode (e8). Without this ExB-drift, the path length would be large and the impact of elastic scattering might cause a strong systematic effect.

For the calculation of critical pressures, tabulated values of differential cross-sections for elastic p-H_2 collisions were used (see [22] and [70]). Tab. 3.5 presents three critical pressures for different voltage settings (U_8) at the lower ExB-drift electrode e8. As discussed in the last section, the adiabatic approximation is fulfilled up to a drift potential of $3\,\mathrm{keV}$. We applied a drift potential of $0.95\,\mathrm{keV}$ during the ILL beam time. With the given vacuum conditions ($p_{main} = 8 \times 10^{-9}\,\mathrm{mbar}$), an error of $\delta a < 10^{-4}$ can be calculated due to elastic scattering on residual gases.

2) Inelastic scattering:
Inelastic p-H_2 collisions mainly result in energy losses due to large cross sections for rotational and vibrational excitations, while electronic excitation and ionization are negligible

U$_8$ [kV]	p$_{cr}$ [mbar]
-3	$5 \cdot 10^{-8}$
-0.3	10^{-8}
-0.03	$1.4 \cdot 10^{-9}$

Table 3.5: Calculated critical pressure values p$_{cr}$ for elastic p-H$_2$ collisions for different voltages U$_8$ applied to the lower ExB drift electrode e8. Please note, that these are only partial pressures for H$_2$ which is the main residual gas. p-H$_2$ gives only an upper limit.

Gas	p$_{cr}$ [mbar]
H$_2$	$2 \cdot 10^{-8}$
Ar	10^{-8}
N$_2$	$2 \cdot 10^{-8}$
O$_2$	$4 \cdot 10^{-8}$
He	10^{-6}

Table 3.6: Calculated critical pressure values p$_{cr}$ of the charge exchange process for different gases.

for protons below $1 \, \mathrm{keV}$ [22]. Changes of the pitch angle θ are insignificant in comparison with elastic scattering. The energy losses are in the range of 50 to $1000 \, \mathrm{meV}$. Vibrational excitation turned out to be the crucial factor for inelastic scattering. The calculations determined a limit of p$_{cr} = 4 \times 10^{-8} \, \mathrm{mbar}$ for H$_2$. Therefore, the achieved vacuum conditions meet the demands for suppression of inelastic scattering effects.

3) Charge exchange:
Possible electron capture processes from gas molecules by decay protons would result in neutral hydrogen atoms and positive molecular ions with very low energy: p + M $\rightarrow$ H + M$^+$. The M$^+$-ions would be blocked by the potential barrier and the neutral hydrogen atoms would stay undetected as well. Simulations concerning the critical pressures p$_{cr}$ for several gases are presented in [22]. Tab. 3.6 shows the calculated limits. The vacuum conditions during our data taking at ILL are slightly below the limits given here.

3.6.2 Background

The examination of systematic effects had the major priority in the ILL beam time. We focussed on studies of background effects as a consequence of the observations made during the FRM II beam time: Unstable and uncorrectable background conditions prevented us from extracting a value for the coefficient a with a reasonable systematic
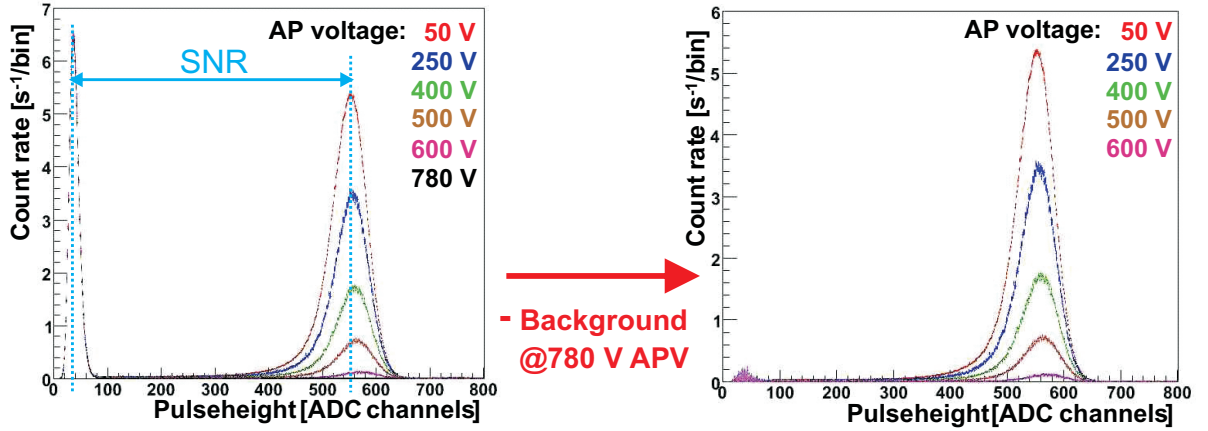
Figure 3.27: The strategy of background subtraction. Left: Pulse height spectra measured
at -15 keV detector potential at ILL. An average SNR of 10:1 can be deter-
mined by the pulse height ratio of the proton peaks to the noise peak. Right:
Pure proton spectra after subtraction of background spectrum (black line in
left picture) measured at 780 V APV.

error. With neutron beam "off", we found a background contribution that depended on
the APV. After a general introduction to background in our experiment, I will focus on
the mechanisms producing this APV-dependent background.

Background classification:
The background measured in our experiment can be classified either as (1) APV-
independent or as (2) APV-dependent. As mentioned before, we determine the
background (1) by applying $+780$ V APV. The resulting barrier potential is above the
maximum kinetic energy of protons from free neutron decay of $E_{p,max}=751.4$ eV (see
fig. 1.1) and reflects all decay protons. The measured background is subtracted in data
analysis from spectra at different APV settings (see fig. 3.27). Without APV-dependent
background (2), this method delivers the pure proton count rates. An APV-dependent
background constituent (2) was found first in the FRM II beam times with neutron beam
"off" and by variation of the APV. We investigated, that APV-dependent background is
produced and influenced by various processes. The most important is field emission at
HV-electrodes. Our aim was to reduce field emission and to suppress hereby as well the
APV-dependent background below a critical level. If its contribution is negligible, the
subtraction of background measured at 780 V APV is sufficient for the determination of a.
Only some assumptions can be made from investigations on parts of the APV-dependent
background in measurements with neutron beam "off": In the ILL beam time, we used a
fast neutron shutter to block the neutron beam upstream. This allows to study, how the
APV-dependent background behaves when the neutron beam is closed or opened. But

this can only be an approach to the amount of APV-dependent background with neutron beam on.

Background sources:
Background is mainly produced by the neutron beam and the environmental conditions (e.g., neighboring experiments, cosmic rays). For example, its constituents are decay electrons, gammas, high-energy electrons created as a secondary process of neutron capture (n,γ) and by cosmic rays (electron shower). γ-radiation is suppressed by the small opening angle to the detector. Charged particles from outside the spectrometer are "shielded" by the strong magnetic field of aSPECT. Therefore, they can not intrude into the flux-tube and can not be imaged onto the detector. Cosmic rays make only a small contribution to the spectra. Ionization of residual gas in the flux-tube produces very low energetic ions of several eV. They will be detected for APV-settings of $U_A \approx 0$ V. But they can be blocked easily by applying a low AP potential if their origin is below the AP. Therefore, data was taken down to $U_A = 50$ V, only.

Model of the production mechanism of APV-dependent background:
The destructive impact of the APV-dependent background registered in our first beam times was already pointed out and is discussed in detail in [25]. For an understanding of the previously described technical improvements, a quantitative explanation of the complex production mechanism is helpful. The production mechanism of APV-dependent background is a multiple-stage process (see fig. 3.28):
(1) The electrodes e17 (-30 kV) and e16 (e.g., -2/-4 kV) produce primary electrons by field emission.
(2) These electrons follow the magnetic field lines and can hit electrode surfaces (e.g., e14) producing secondary electrons of lower energy. Secondary electrons possess a higher cross section for residual gas ionization. They can drift into the flux-tube due to ExB-field gradients (e.g., at edges of electrodes).
(3) Primary electrons leave the spectrometer mainly to the bottom whereas secondary electrons can be trapped (green regions in fig. 3.28), for example, between e8 and e16. The Penning traps increase the probability of residual gas ionization induced by secondary electrons.
(4) Ions produced above the center of the AP can reach the detector, ions produced below will be reflected and trapped between the AP and the ME. We expect the ionization of residual gas by secondary electrons to be the main mechanism in the production of APV-dependent background. In addition, Penning discharges induced by primary electrons can intensify this production. Penning discharges are a well known source of background in MAC-E-type spectrometers.
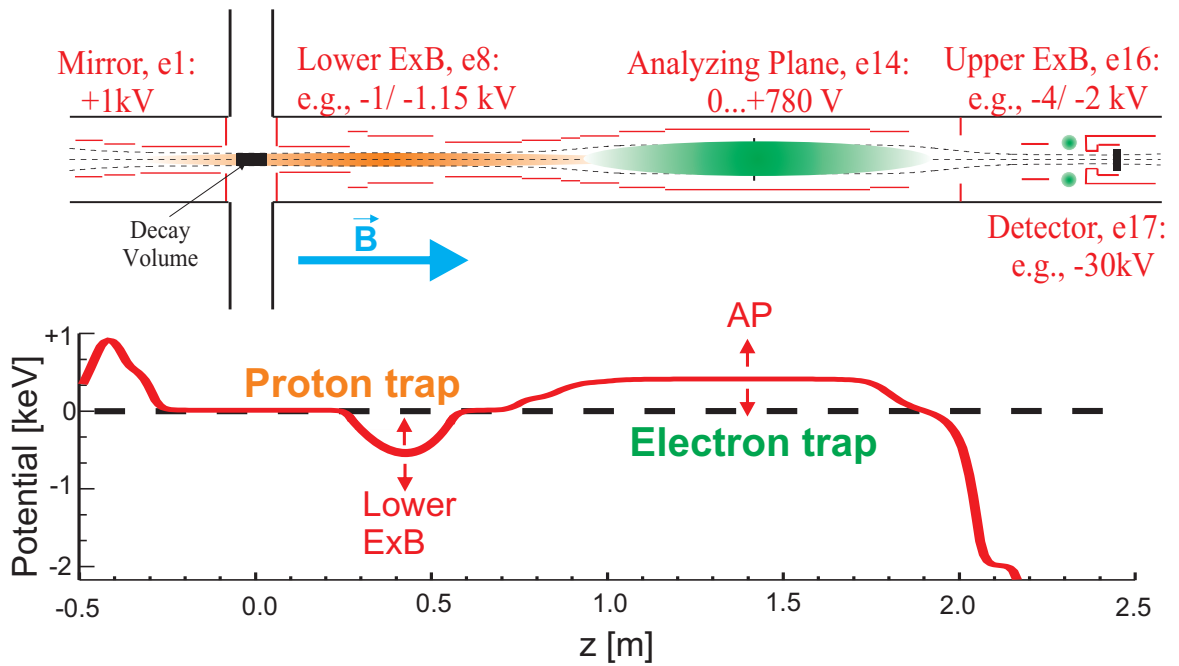
Figure 3.28: Illustrations concerning the production mechanism of APV-dependent background at FRM II.
Top: The electrode system of *a*SPECT with respect to traps for positive (orange region) and negative (green region) charged particles. Exclusively the most relevant electrodes are named and common settings are included.
Bottom: Schematic shape of the electric potential in the regions of interest. The trapping region is marked orange for protons and green for electrons. Both regions overlap between lower ExB (e8) and AP (e14).
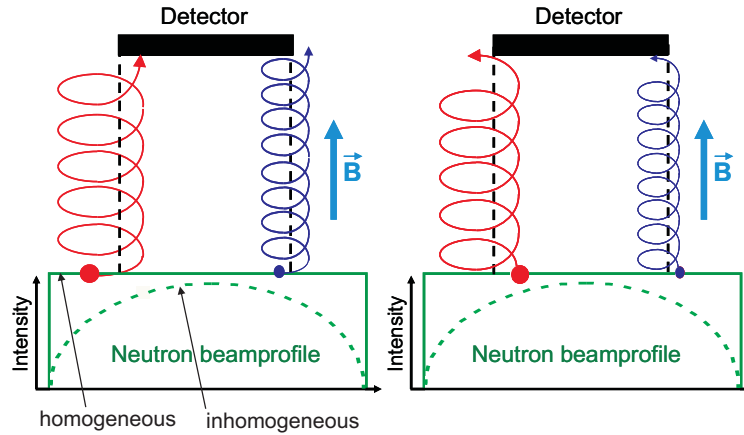
Figure 3.29: Influence of the gyration motion of decay protons on the flux-tube: In the case
of a homogeneous beam profile the effect cancels out but not in the case of an
inhomogeneous beam profile. The edge effect is caused by an APV-dependent
distribution of gyration radii for protons at the detector. The focusing by
magnetic collimation onto the detector is not included in this sketch!

3.6.3 Edge effect

The "edge effect" (in aSPECT) describes the systematic impact of an inhomogeneous
beam profile on the coefficient a. Generally, it is caused by the energy dependence of the
proton gyration radius, $r_g \propto \sqrt{T_\perp}$: The neutron beam passing through the spectrometer
is wider than the area of the detector (see fig. 3.19b). Therefore, only a fraction of the
decay protons actually hits the active area of the detector. The magnetic field projects the
shape of the neutron beam via the decay protons onto the detector. Due to the gyration
radius, the beam width that is "seen" by the detector depends on the kinetic energy of
the protons. Fig. 3.29 illustrates the dependence on the beam profile: On the one hand,
some protons may miss the detector due to the gyration motion although they were
emitted inside the flux-tube. On the other hand, protons from outside the flux-tube may
be detected instead. This effect would be balanced in the case of a perfectly homogeneous
neutron beam profile (green line). For an inhomogeneous beam profile (dashed green line),
this becomes an important systematic effect on a: The probabilities of losing or gaining a
proton are no longer the same and depend on the kinetic energy.

In aSPECT, the protons are post-accelerated by the detector potential (e.g., -15 keV).
Therefore, the small variance of the proton kinetic energy at the detector produces only
a 2nd-order effect and is negligible. But the distribution of gyration radii is influenced by
the angular distribution above the AP. This is the transmission function: Gyration radii

can be calculated by

$$r_g = \frac{m \cdot v_\perp}{e \cdot B_{det}} = \frac{\sqrt{2T_\perp \cdot m}}{e \cdot B_{det}} \qquad (3.42)$$

with e being the unit charge and $T_\perp = \sin^2\theta \cdot T_{p,det}$ being the transversal component of the proton kinetic energy at the detector. The angular distribution of protons that passed the AP potential depends on the initial kinetic energy in the DV. In addition, it is affected by the the transmission function. The transversal kinetic energy component $T_\perp$ in eq. 3.42 depends on the angle θ and therefore on the initial kinetic energy. This induces an APV-dependent distribution of gyration radii which is the main source for the edge effect in our experiment. Detailed calculations of this edge effect are part of the PhD thesis of G. Konrad [30]. Input parameters are the 3-dimensional neutron beam profile in the DV, the calculated electric field map and the measured magnetic field map in aSPECT.

3.6.4 Doppler effect due to neutron motion

The motion of the decaying neutron may have an impact on the transmission function since it influences the observed energies of the emitted protons relative to the energies in the center-of-mass system (CMS). An appraisal of the effect was done in [22]: Neutrons from a cold neutron beam have an average kinetic energy of $\overline{T}_n \approx 5$ meV. Assuming protons of CMS-energy $T_{CMS}=400$ eV emitted in flight direction of the neutrons, the protons gain energy in the laboratory system of $\delta T = 2\sqrt{\overline{T}_n \cdot T_{CMS}} \approx 2.8$ eV, with $T_{LAB} = T_{CMS} + \delta T$. With respect to the aimed 10 meV-accuracy of the proton CMS energy, this would have an enormous impact: Due to the distribution of neutron velocities ($T_n \neq \overline{T}_n$) the proton energy spectrum would get smeared out.

In aSPECT, the magnetic field is transverse to the neutron flight direction. The influence of the Doppler effect results in a distortion of the angular distribution at the AP after the conversion by the magnetic adiabatic collimation. The angular distribution has an important impact on the transmission probability if T_{kin} is minimally higher than the AP potential eU_A. Due to the finite width of the transmission function, the effect which is generated by the left half-space in neutron decay (opposite to the neutron flight direction) compensates approximately the effect generated by the right half-space. The integration over the entire solid angle results in a suppression of this Doppler effect in the geometry of aSPECT: The influence on the coefficient a was calculated in [22] for different settings of the AP voltage to be smaller than 10^{-4}.

3.6.5 Detector effects and properties

This last subsection is dedicated to the introduction of some important detector properties. Some of these properties lead to additional systematic effects and can be summarized by the expression "detection efficiency". For more I refer [32].

Backscattering:
A fraction of the protons that hit the detector will be backscattered. This means, a proton enters the detector, is scattered several times inside the detector and finally leaves it again without having fully deposited its energy. Due to the negative acceleration voltage, the proton can not escape and will hit the detector again with the same energy and pitch angle as it was backscattered before. The time difference between the two hits is rather short ($\approx 0.5\,\mu$s), thus it is not possible that one backscattered proton is counted as two events. The probability for Rutherford backscattering of protons in the entrance window ($\approx$30 nm thick aluminum layer) of the detector depends on the impact energy ($T_{det,p}$: 15 to 15.75 keV, in our case),

$$\sigma_{Rutherford} \propto \frac{1}{(T_{det,p})^2} \tag{3.43}$$

and therefore leads to a slight distortion of the measured spectra to lower pulse heights.

Additionally, the impact angle (0 to $\approx 18°$, as calculated by M. Simson [32]) affects the path lengths of protons in the (insensitive) entrance window (dead layer) on a level of $\approx 5\,\%$. Furthermore, the angular distribution is influenced by the applied AP potential. Simulations performed by M. Simson [32] using SRIM 2006[13] predict an amount of $\approx 1.8\,\%$ backscattered protons at -10 kV and $\approx 1.0\,\%$ at -15 kV detector voltage.

Energy calibration and energy loss:
The energy calibration was done by M. Simson in [32] with a ^{133}Ba source and by performing proton simulations. The combination of both methods results in an energy calibration of 65$\pm$2 ADC ch./ keV. In our measurements, the peak position of the proton peak for -15 keV detector potential was found at ADC channel $\approx$550 and for -10 keV at ADC channel $\approx$330. This corresponds to energy depositions of about 8.7 and 5.2 keV or energy losses in the dead layer of 6.3 and 4.8 keV for 15 and 10 keV protons, respectively. Simulations with SRIM for 15 keV protons in a 30 nm aluminum entrance window showed comparable values.

Position dependence:
In September 2008, M. Simson and me performed first tests with the SDD at the proton accelerator *paff* at the TU München. *paff* produces protons from neutral hydrogen molecules in an extractor type ion source (see [71] and [32] for detailed descriptions). We scanned one detector pad longitudinally (see fig. 3.30): The proton beam was fixed and focused onto a small aperture with a diameter of $\approx$0.13(1) mm. The detector was moved linearly to the beam behind that aperture. The obtained count rates for different detector positions are shown in fig. 3.31.

The fluctuations at the left edge (position around 13 mm) and the small decrement of count rates along the plateau of the pad are due to the instabilities of the accelerator: During the measurements, the hydrogen pressure in the source part of the accelerator decreased (quite fast at the beginning and more slowly later on). At the edges of the

---

[13]A program which simulates the stopping and range of ions in matter. See: http//:www.srim.org
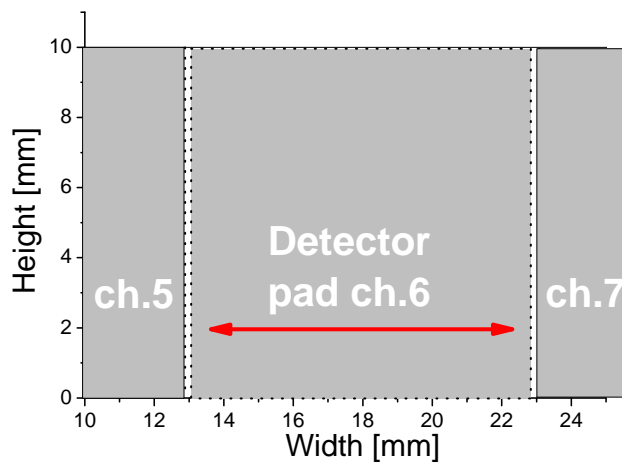
Figure 3.30: Scheme concerning the scan of the detector pad.
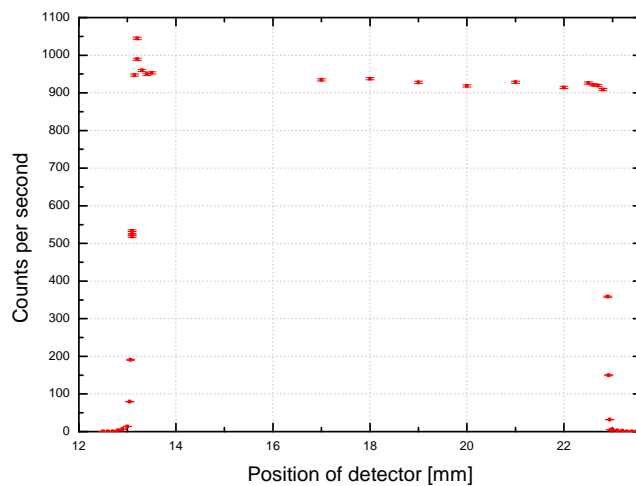
Figure 3.31: One dimensional scan of a detector pad. The values on the x-axis refer to the reading on the micrometer screw of the linear motion feed-through.

detector pad, the measured count rate rises steeply. In reality, the edge of the detector is not a sharp line, but there will be a region where the detection probability of the protons drops from the maximum to zero. Given the geometric expectancy of $0.13(2)$ mm, an upper limit of about $40\,\mu$m can be deducted for the width of the edge (see [32]) (i.e., $<2 \cdot 10^{-5}$ of the detector area is involved). For the calculation of the detector edge effect, the decreasing count rates at the edges should be negligible.
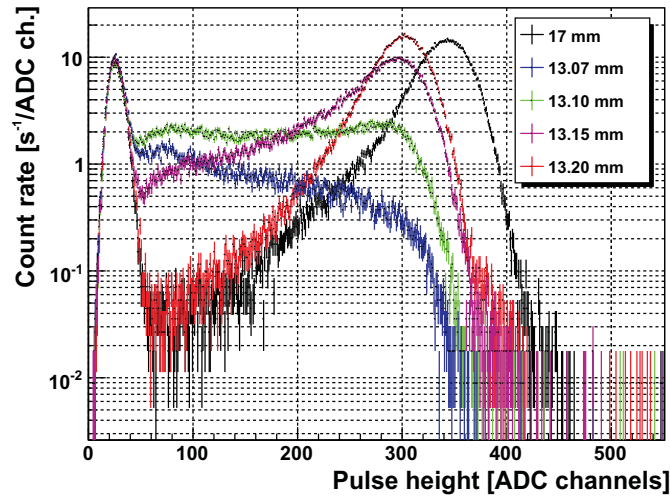
(a) Left edge.
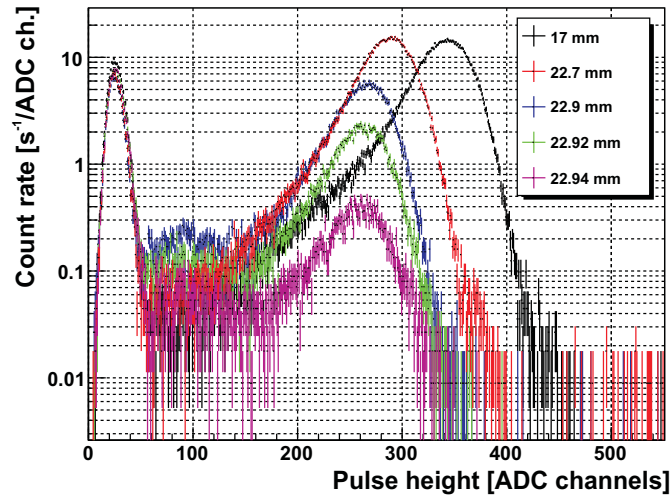
(b) Right edge.

Figure 3.32: Proton spectra obtained on the left (a) and right (b) edge of the detector. The spectra at 17 mm were determined in the center of the detector. They show nearly no count rates at ADC channels <100.
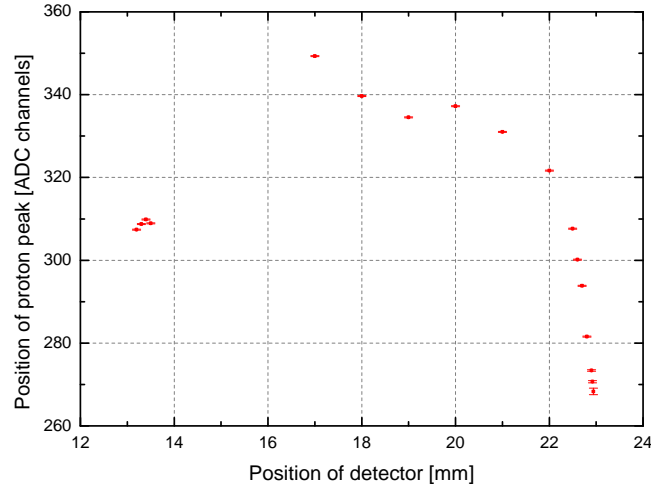
Figure 3.33: The position of the proton peak (ADC channel) depending on its impact position along the detector pad.

Another interesting effect was discovered in the analysis of these measurements: The shape of the pulse height spectrum changes significantly along the detector. As you can see in the spectra in fig. 3.32, the average pulse height of the protons is reduced close to the edges of the detector. Furthermore, the peak structure changes at the edges. On the right edge (fig. 3.32b, 22.94 to 22.9 mm), only some more protons appear at very low pulse heights between ADC channel 100 and 200. On the left edge (fig. 3.32a, 13.07 to 13.10 mm), the main proton peak disappears completely at a detector position of about 13.10 mm. The count rates are nearly uniformly distributed between ADC 80 to 300. It is uncertain, if this effect appears all along the outer edges of the detector or if it is localized to a small region around the point which was measured with the linear motion feed-through. A local effect could be caused by some dust particles on the surface of the detector at that point. Another possibility is, that the protons are scattered from a bond that runs close to the measured point. The dependence of the proton peak maximum on the position along the detector pad is summarized in fig. 3.33. Due to the distortion of the spectra at the edges of the detector, more protons might be detected at lower ADC channels and could get superimposed by electronic noise. Because of the small detector area that is involved, this effect is as well negligible.

Dead time losses:
According to the fact, that each detector pad of the SDD has a detection area of about $100\,\text{mm}^2$ compared to one stripe of the Si-PIN-diode used at FRM II of about $25\,\text{mm}^2$, dead time losses play a more crucial role. The probability that two events occur in the same pad at the same time is higher for the SDD. Different sources of dead time losses have

to be considered in this context: First of all, each energy deposition by a charged particle in the depletion volume involves a dead time, in which the secondary charges can drain off and the depletion is recovered. This recovery time is in the order of several nanoseconds and completely negligible with respect to the statistical time difference between two events of about 1.4 ms (for a maximal count rate of ≈ 700 /s at 0 V APV). Second, each event has an event length (due to the shaper board and the trigger algorithm as explained in section 3.4.2.) of $5 \, \mu s$ and is processed in $0.2 \, \mu s$ by the detector electronics to the DAQ computer. Thus, only one event per $5.2 \, \mu s$ can be registered. A first order dead time correction is implemented by (see [72]):

$$\text{corrected count rate} = \frac{\text{measured count rate}}{1 - \text{measured count rate} \cdot 5.2 \mu s} \tag{3.44}$$

For a given proton count rate of $500 \, [1/\text{s}]$, the count rate loss due to dead time losses would be $\approx 1.3 \, [1/\text{s}]$. It depends on the APV-settings because of the differences in the measured proton count rates and therefore it produces an error on the coefficient a: The APV-dependent count rate loss shifts the coefficient a relatively by $\frac{\Delta a}{a} < 4\%$. This shift is correctable on a permille level but requires an accurate knowlegde of the dead time: An uncertainty of $\delta \tau = \pm 0.2 \, \mu s$ results in an error $\frac{\delta a}{a} < 0.04\%$. If the dead time would be $6 \, \mu s$ instead of $5.2 \, \mu s$, the resulting systemtatic error would be $\frac{\delta a}{a} = 0.2\%$.

One class of events is detected with a shorter time difference than given by pure statistics: Coincidence (correlated) events (see sect. 4.8). These are electrons and protons from the same neutron decay. Their minimal coincidence time was calculated by to be about $6 \, \mu s$. This means, coincidence events do never occur in the same event window of $5.2 \mu s$. And they never get lost due to dead time losses described here. Therefore, the dead time losses discussed here should only affect uncorrelated events (from different neutron decays).

4 Data analysis

The aSPECT spectrometer was installed from December 2007 to Mai 2008 at the PF1B beam line of the ILL reactor in Grenoble. The first aim of the beam time was to overcome the major problems which occurred in the FRM II beam time in 2005/ 2006. The problems were already discussed in detail in the last chapter (see sect. 3.5 and 3.6.2) as well as the newly implemented modifications in our experimental setup (see sect. 3.2 and 3.5.2). The analysis of the data taken in the FRM II beam time is the subject of the PhD thesis of R. Muñoz Horta [25] and was published partly in EPJ [1]. Our second aim was the extraction of a from the data taken with an overall error of $\frac{\Delta a}{a} < 2\%$, i.e. much less than the accuracy from previous experiments, $\frac{\Delta a}{a} \cong 5\%$.

For the extraction of a, several steps of analysis had to be done:

- Decoding of the raw data to a processable format (see [32]).

- Exclusion of phases of instable measurement conditions (e.g., discharges, drifts, etc.).

- Event analysis (e.g., treatment of special events, discrimination of noise events), determination of the pulse heights of events and creation of pulse height spectra.

- Background treatment (e.g., types, stability, etc.) and subtraction from spectra.

- Determination of the pure proton count rates in a defined region.

- Studies on systematics.

4.1 Data acquisition procedure

4.1.1 Measurement structures

The data acquisition (DAQ) system was introduced in section 3.5. For details on the structure of the recorded raw data and the DAQ hardware I refer to [32]. Furthermore, the on-line trigger algorithm was discussed (see fig. 3.26) and the necessity of stable measurement conditions was pointed out. Generally, the data taking sequence for extracting a with a minimal statistical error in a given time would necessarily consist of at least three different APV-settings: (1) Measurements at 780 V are required to detect the background count rate. (2) For extracting a, the intensity of the integral proton spectrum is needed:

The direct determination of the intensity via the APV set to 0 V may be incorrect due to low energy residual gas ions (energies of several eV) as introduced in sect. 3.6. Therefore, measurements at, e.g., 50 V minimum APV-settings are used. (3) Finally, at least another APV-setting is required at which the proton spectrum (see fig. 1.1) is highly sensitive on a (e.g., 200 V).

For reasons of systematic studies, the sequence of APV-settings was chosen as shown in the upper part of fig. 4.1. The measurement time at each APV was chosen with respect to the proton count rates and the number of repetitions. Each measurement is separated by the neutron shutter cycle in 5 parts (lower part of fig. 4.1). Data is taken continuously at each of the 5 shutter states (green boxes). 0 V APV is only applied for opening frequently the trap between AP and ME.

4.1.2 Stabilities

The stability of the APV, the detector HV, the upper ExB voltages and the neutron flux were monitored to find and to exclude periods of instabilities from the data analysis for the extraction of a. Electric instabilities introduced non-statistical fluctuations of the proton and electron count rates at the beginning of the beam time. They were probably caused by insufficiently defined ground potentials and malfunctions at some power supplies. Therefore, the most reliable data with stable conditions was taken from the 15th of May to the end of the beam time.

AP voltage:
The applied APV-settings were found to be stable on a level of 5 mV monitored by a calibrated Agilent 3458A multimeter. The procedure of ramping and stabilization of the APV is described in detail in appendix 5.

High voltage settings at e16/ e17:
Using the new SDD detector, the maximal applied voltages were -15 kV for e17 and -4.2 kV for e16. The analysis of the stored log files showed no voltage breakdowns or discharges during data taking, neither for the detector electrode nor for the upper ExB-electrode. The relative stability of the detector HV was determined to be $6.5 \times 10^{-5} \leq (\delta U / U_{e17}) \leq 2.3 \times 10^{-4}$ and $3 \times 10^{-4} \leq (\delta U / U_{e16}) \leq 4 \times 10^{-3}$ for the upper ExB-electrode. Only during phases of ramping, increased leakage currents at the upper ExB-electrode and small discharges occurred.

Neutron counter:
For monitoring fluctuations of the neutron flux in our experiment, a ^{6}Li neutron counter was installed in the center of the beam dumb. The expected intensity at that position was calculated to be below the saturation limit of the neutron counter. The monitoring of the neutron count rate is important for normalization of the count rate of the decay protons. It may change due to drifts, for example, by changing conditions of the neutron
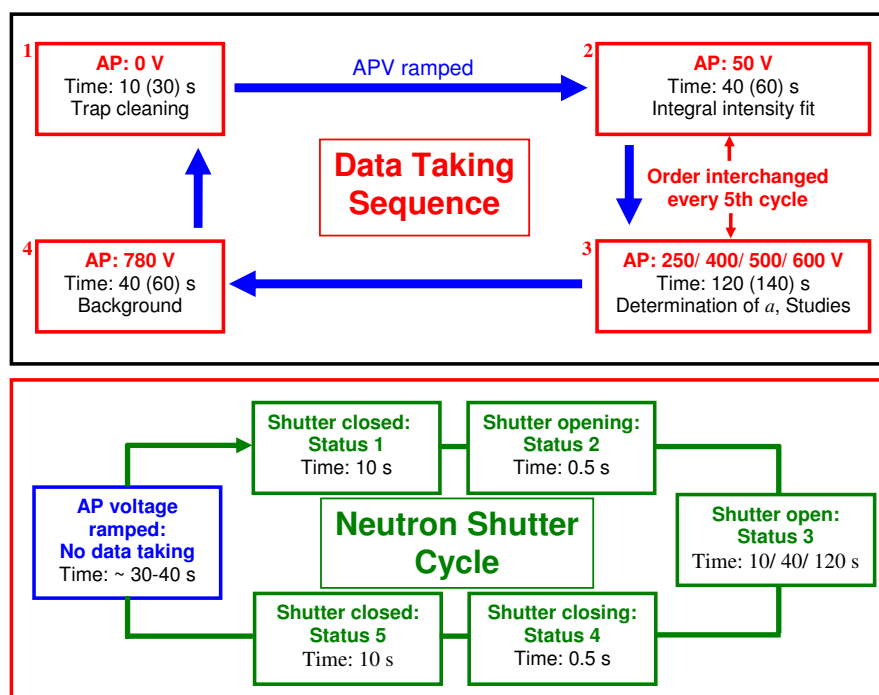
Figure 4.1: Top: The data taking sequence. At each step (red boxes 1-5), data with neutron beam "on" was taken for a measurement time given before the brackets. Each step is subdivided into 5 phases with closed and open neutron shutter depicted in the neutron shutter cycle below (green boxes). The total measurement time is given in brackets. Bottom: The neutron shutter cycle. At each APV we took first data for 10 s with closed shutter (status 1), opened the shutter (status 2), measured for a given time (10 s, 40 s or 120 s, dependent on the count rate at the chosen APV) with neutron beam "on" (status 3), closed the shutter (status 4) and measured for 10 s with closed shutter (status 5). Afterwards the APV was ramped (i.e., next step in the data taking sequence). In all measurement, the neutron count rate is monitored for the same measurement times (synchronized to the proton detection).

guide or the reactor power. Unfortunately, the neutron counter did not run stable in the
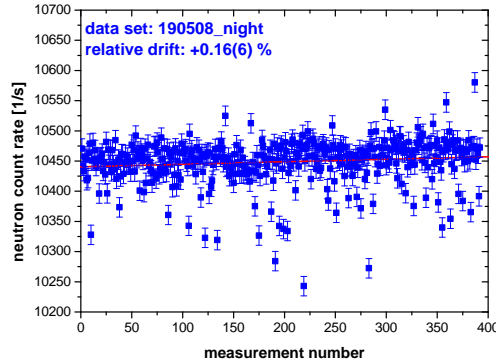
Figure 4.2: Neutron count rate during data set "190508_night". A small positive drift (fitted red line) is visible. The count rates are non-statistically fluctuating. A possible explanation is an insufficient synchronization between the trigger of the neutron counter and the internal clock of the DAQ system. It might have caused problems during the readout by wrong normalization of the recorded neutron counts.

beginning of the data taking period but showed a strong drift which was uncorrelated to the reactor power monitored by ILL (see appendix 6.6, fig. 6.7 and 6.8). There are good reasons to believe, that this drift was induced by a bad reference voltage or ground potential. It was found that the synchronization between n-counter and proton detector DAQ was not working properly (i.e., the start/ stop signals that were sent by the DAQ computer to the proton detector were insufficiently synchronized to the start/ stop signal sent to the neutron counter). The neutron counter worked more stable from the 16th of May to the end of the beam time. An example is shown in fig. 4.2 for the data set "190508_night": A small drift (fitted red line) is still visible. The error bar of each data point is purely statistical given by $\sqrt{N}/T$ (N: neutron counts, T: integration time). It does not include any calibration accuracy of the neutron detector. The relative error of a single measurement is in the order of 0.1-0.15 % (about $400000\pm\sqrt{400000}$ neutrons counted in 40 s). This statistical accuracy would be sufficient to correct fluctuations in the proton count rates: The maximum statistical accuracy of a single proton measurement is about 0.7% (about $20000\pm\sqrt{20000}$ protons counted in 40 s measurement time at 50 V APV). But as shown in fig. 4.2, non-statistical fluctuations in the neutron count rate were observed. They reached a level of 1-2 %. If the neutron counter data can be used for normalization of the proton count rates will be analysed in sect. 4.4.

4.2 Event analysis

The event analysis contains the following tasks:

- The extraction of the pulse heights of measured events to produce pulse height spectra. A way to distinguish between different event types (electrons, protons, electronic noise) is designated.

- The examination of unexpected or anomalous events adverting to systematic effects of the measurement itself (e.g., due to correlated events of short time difference to each other that may influence the dead time) or impacts by the DAQ-electronics (e.g., phases of increased noise).

- The exclusion of additional systematic uncertainties implemented by the method of extracting the pulse height.

4.2.1 Event types

The shaper board (see sect. 3.5.4) transformed all detected signals into characteristic pulse shapes which were stored and are available in an off-line analysis. Each of these signals will be called "event" in the following chapters. Due to the shaping, an incoming electron and a proton that deposited the same energy in the detector will have identical pulse shapes and can not be distinguished this way. Despite that fact, several parameters can be defined that help to suppress noise and to separate event types in an off-line analysis: The baseline (y_0) and the pulse height maximum ($HistMax$), which determine the pulse height $ph = HistMax - y_0$. Further parameters are the starting point of the pulse (x_0) and the time when it reaches its maximum ($MaxBin$).

Single proton and electron events:
Apart from a small amount of background events produced by, for example, γ-radiation from the beam or cosmic rays, most events in the pulse height spectra are proton and electron events. Proton events are typically shaped as shown in fig. 4.3a and electron events as shown in fig. 4.3b. The shape of about 90 % of the electron events is deformed due to saturation effects (electrons $< 40\,\mathrm{keV}$ produce pulse shapes comparable to those of protons). After amplification and shaping, the resulting pulse height excesses the maximal range of ADC channels. The values of the baseline y_0, x_0 and $MaxBin$ vary only minimally between (a) and (b) and will be discussed in detail later.

Coincidence proton and electron events:
A coincidence (or "correlated") event is defined as an electron and a proton from one and the same neutron decay detected in coincidence. Fig. 4.4a gives an example for a proton (event 2) after a non-saturating electron (event 1). The baseline of event 1 (green line) is slightly higher ($<$50 ADC ch.) than the baseline of event 2 (green dotted line).

(a) Proton event of typical pulse height.

(b) Electron event of typical pulse height.
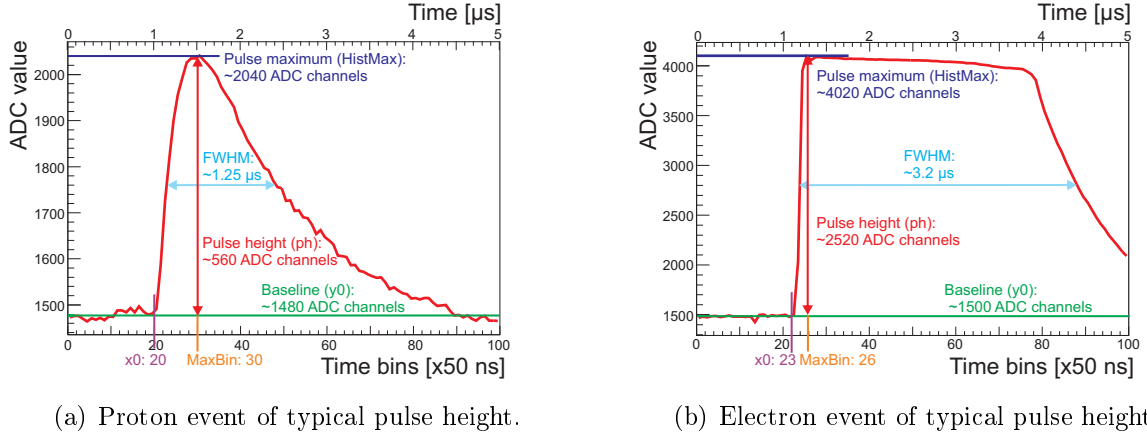
Figure 4.3: Typical pulse shapes of (a) proton events and (b) electron events saturating the shaper board. The parameters $y0$ (baseline), $x0$ (start of pulse), ph (pulse height), $MaxBin$ (time when pulse maximum is reached) and $HistMax$ ($HistMax = y_0 + ph$) are defined and will be used in the development of a pulse height determination method. The FWHM of a proton pulse was about twice as big compared to the FRM II beam time mainly caused by an increased amplification factor. This also leads to the saturation effect (e.g. in (b)) above a pulse height of about 2500 ADC channels (i.e., $HistMax \approx 4000$ ADC ch. for an average baseline value $y_0{=}1500$ ADC ch.).

As a consequence of saturation by an electron, the baseline drops down below its initial value and drifts slowly back as shown in fig. 4.4, (b). Depending on the strength (i.e., the duration) of the saturation, the baseline needs about 20-30 μs to recover. In the case of correlated electron-proton events in fig. 4.4, (c), the proton can reach the detector while the baseline is still decreasing (from 1500 ADC ch. for event 1 to about 1300 ADC ch. for event 2). This influences the trigger efficiency for proton events with low pulse heights (e.g., due to backscattering). Further investigations and simulations concerning the trigger efficiency will be discussed in sect. 4.8.- The characteristic shape of the proton events changes with respect to the trigger algorithm: The trigger condition (see sect. 3.5.4) is fulfilled later for a decreasing baseline. Therefore, the pulse shape parameters x_0 and $MaxBin$ are different for these type of correlated proton events like in fig. 4.4, (d).

The pulse height determination method had to be adapted to this behaviour. A further requirement was a good separation between noise and protons. This implies the need for noise suppression and a way of discrimination of events in the overlapping pulse height region:

Noise events:
Thermal noise (as one component of the electronic noise) is a purely statistical process and depends on the operation temperature of the electronic components. That is the

(a) Non-saturating electron and coincidence proton pulse.

(b) A saturating electron pulse: The baseline y_0 falls below its initial value (green line) afterwards and needs about 20-30 μs to recover completely.

(c) Saturating electron and coincidence proton pulse.

(d) Coincidence proton pulse.
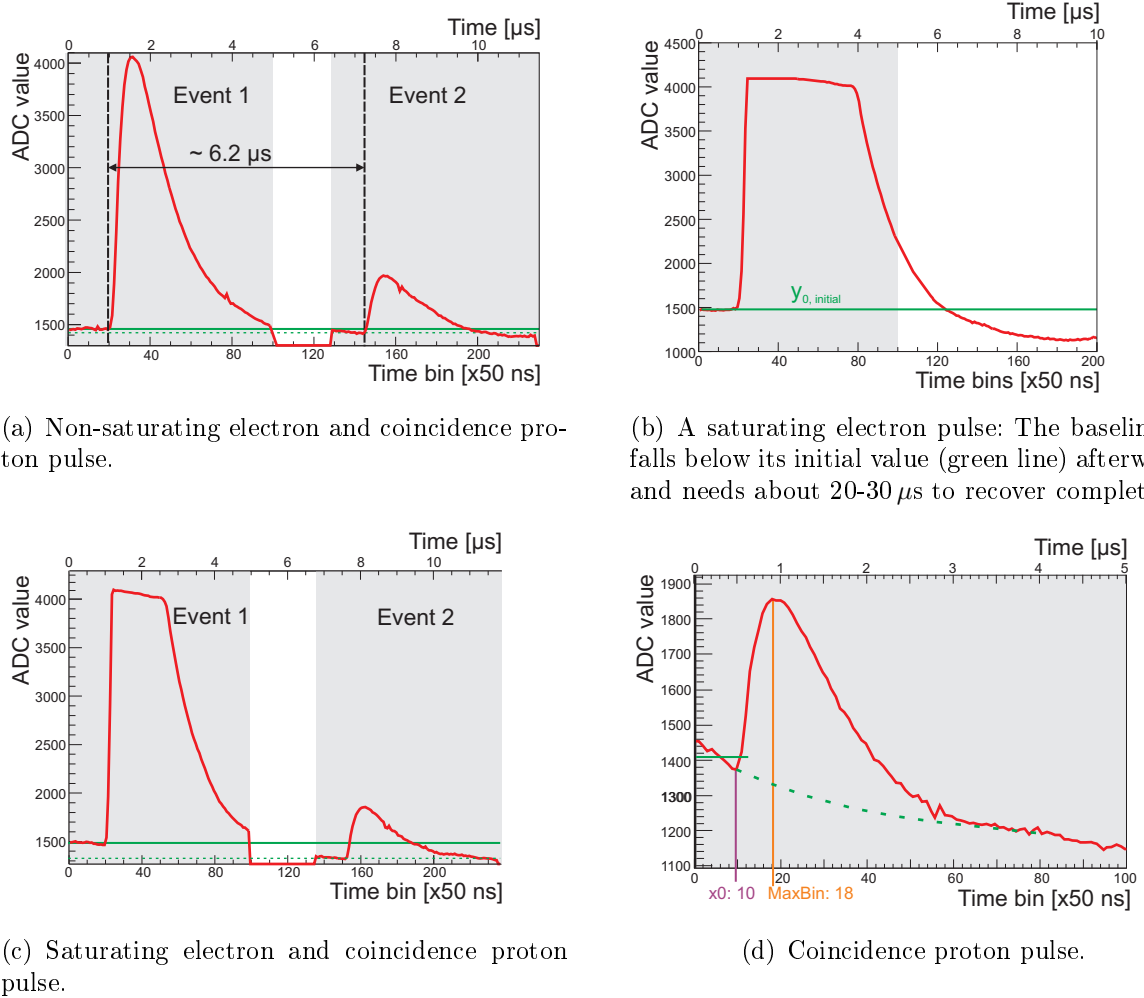
Figure 4.4: (a) Gives an example for a coincidence proton pulse detected after a non-saturating electron pulse. The time difference (6.2μs) is close to the calculated minimal flight-time difference of about 6 μs. The baseline y_0 of the proton (event 2, dashed green line) falls only minimally under the initial value of the electron (event 1, green line). In (b), a saturating electron pulse is shown. The baseline falls clearly below its initial value. (c) shows an example for a coincidence proton pulse following shortly in time after a saturating electron pulse: Obviously, the baseline of the proton (event 2) is strongly reduced. (d) shows only a proton event that followed a saturating electron: The parameters x_0 and $MaxBin$ are shifted to lower time bins due to the prior saturation. This is due to the trigger condition (see section 3.5.4) that is fulfilled later for a decreasing baseline.
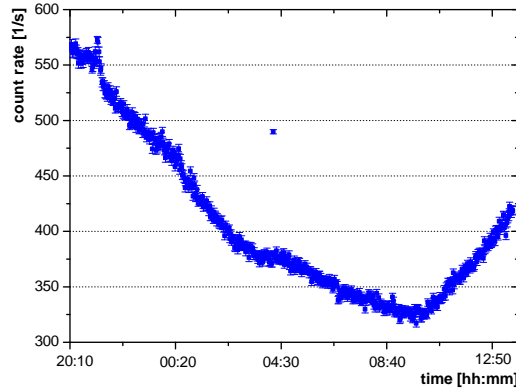
Figure 4.5: Dependence of the count rate of the electronic noise (0...150 ADC channels) on temperature variations (day and night in the experimental zone). The count rates were extracted from measurements with neutron beam "off" (data set "190408_night").

reason why the recorded noise events do not have a characteristic pulse shape and the parameters x_0, y_0 and $MaxBin$ vary strongly. We tried to stabilize the temperature of the preamplifier board and the ADC-board by blowing continuously dry, pressured air on them. But the temperature variations between day and night in the experimental zone were still visible in the noise count rates (see fig. 4.5).

Multiple events:
If several pulses appear in one and the same event window of $5\,\mu s$ we called it a "multiple event" (i.e., each pulse would have caused a trigger if it appeared individually). The occurrence of multiple events depends on the total count rate and therefore on the APV-setting (maximal at 0 V APV). For the realization of a reliable and easy dead time correction (as introduced in sect. 3.6.5), the treatment of multiple events is essential: Only the pulse, that initially released the trigger should be considered in data analysis. In that case, a dead time of $5.2\,\mu s$ can be assigned to each event. The appearance of multiple events in a $5.2\,\mu s$ time window is strongly suppressed at our measured count rates of maximal $\approx 700\,[1/\text{s}]$ (at 0 V APV). The probability of double events can be calculated by Poisson statistics: In about $2\,\%_0$ of all measured events, double events are expected to occur. The statistical loss of (uncorrelated) events can be corrected using eq. 3.44, coincidence proton events can not get lost this way as explained there: They do not appear as multiple events.

Some double events, as shown for example in fig. 4.6a, could be counted separately in the off-line analysis. Other events could not: For example, pulses which do not reach their maximum pulse height in the event window (see fig. 4.6b). In those cases, one can not determine the pulse height of the second event. In order to circumvent this problem, the proposed treatment of multiple events seems reasonable: Only the first event is counted

(a) Double event of protons.

(b) Double event of a proton and a non-identifiable second event.
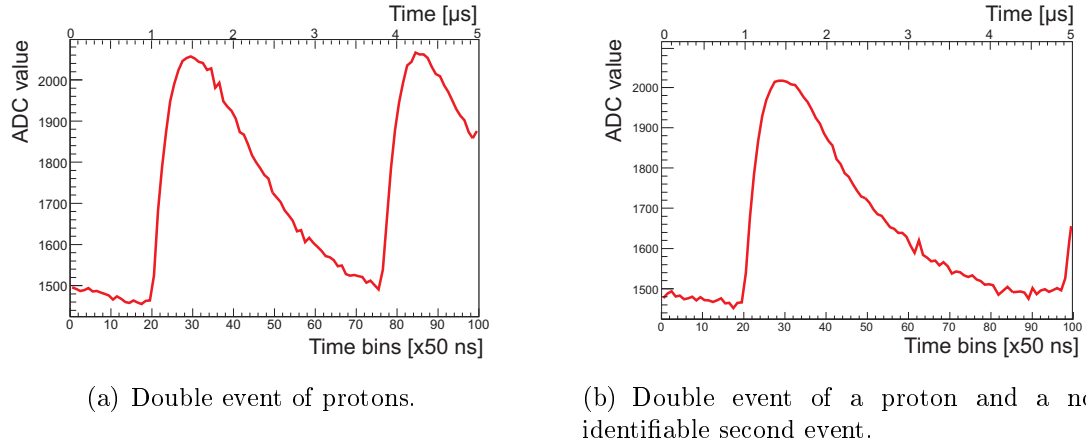
Figure 4.6: Examples for two pulses by protons in the same event window called "double event". If both are separated and reach the maximum as in (a) the pulse height of both events could be extracted. In the case of example (b) the pulse height of the second event is not extractable.

and a dead time correction is applied afterwards.

If two events overlap partly or completely, we speak of "pile-up" events. Two examples for pile-up events are drawn in fig. 4.7. In both cases, only one event shall be counted. The two events in fig. 4.7 (b) can hardly be separated by automatic pulse height determination: The parameter values of x_0 and $MaxBin$ are still in the limit of a single pulse. But the pulse height of the pile-up event is increased. For the extraction of the proton count rate for a given APV-setting (i.e., by integration over the pulse height spectrum), protons are discriminated by their pulse height from higher energetic background events (e.g., saturating electrons). Therefore, one has to find an appropriate upper (and lower) integration limit: The maximal proton pulse height is limited by the endpoint of the proton kinetic energy (about 751 eV) and the post-acceleration by -15 keV detector potential. Typical proton pulses have pulse heights between 500 and 600 ADC channels. Thus, the maximum pulse height of a pile up event will be ≤1200 ADC ch. To include all pile-up events in the determination of the proton count rate (see sect. 4.3 and 4.6.1), the upper pulse height limit was chosen to be 1200 ADC channels.

4.2.2 Pulse shape parameters

The baseline value y_0:
We determined the baseline before a pulse by averaging over a certain amount of time bins due to the characteristic pulse shape (i.e., from the first $1\,\mu$s stored by the trigger buffer, see fig. 3.26). The baseline distribution in fig. 4.8a for a typical data set (e.g., "190508_night") has a peak around 1490 ADC ch. with a FWHM of about 45 ADC ch.

(a) Partly separated.   (b) Fully overlapping.
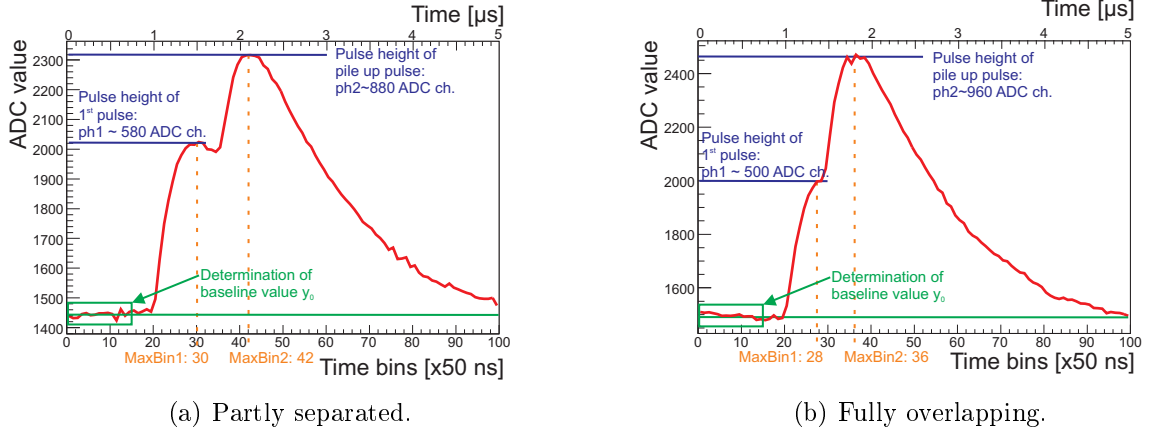
Figure 4.7: Pile-up events of two protons. In (a) the second event is partly separated from
the first event and reaches its maximum at a higher value $MaxBin2{=}42$ time
bins than single events. These types of pile-ups could be discriminated by auto-
matic pulse height determination methods. In (b) the two pulses are overlapping
strongly and $MaxBin2{=}36$ time bins is in the region of single events.

Affected by the falling baseline after saturating electron events, the distribution shows a
tail to lower ADC values. There is a small dependence on the size of the time window
in which the baseline is averaged as shown in fig. 4.8b. By using less time bins closer to
the pulse starting point x_0, the baseline shifts minimally to higher values since it is less
sensitive on drifts.

Pulse start x_0:

(a) Baseline distribution.   (b) Dependence on window size.
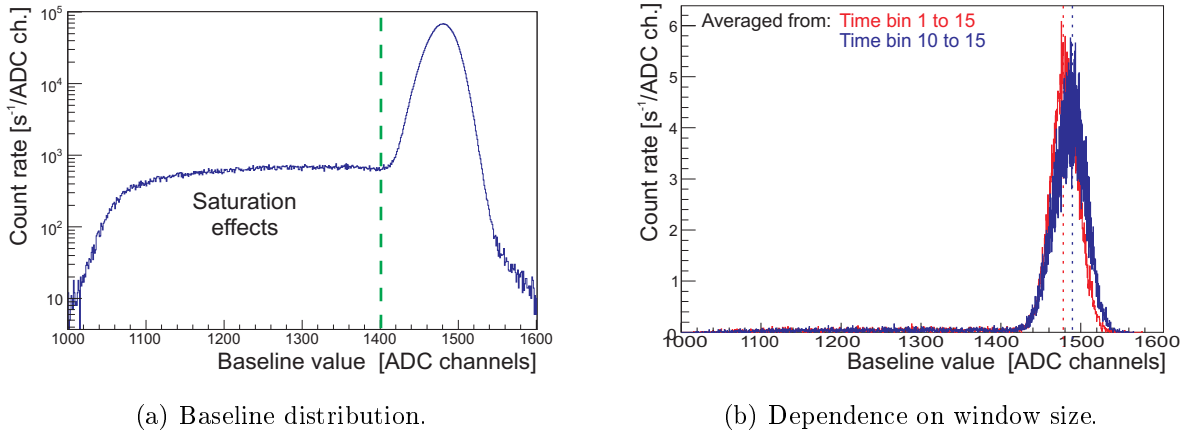
Figure 4.8: Distribution of the baseline values y_0. Most events have baselines > 1400 ADC
ch. as shown in (a). Caused by saturations effects the baseline can decrease
down to channel 1000. By extracting the baseline in less time bins (from time
bin 10 to 15) the baseline shifts minimally to higher values (b).
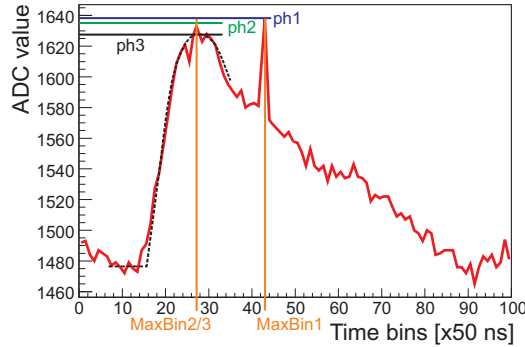
Figure 4.9: Spikes of thermal noise influence the pulse maximum $HistMax$ as well as its position $MaxBin$. Especially low pulse heights are distorted. The black dotted line represents a theoretical fit to the pulse shape. The fit parameters will be discussed in detail in the next section. The fit suppresses the influence of electronic noise on the parameters $MaxBin$ and $HistMax$.

The starting point of a pulse x_0 can only be defined for electron and proton events by the sharp rise of the pulses. For the description of randomly fluctuating pulses (e.g., electronic noise) the parameter x_0 is useless. x_0 has a distribution around 20 time bins ($1\mu s$) under normal conditions. Some coincidence proton pulses (see fig. 4.4d) shift the distribution to lower values of x_0 and may have lower x_0-values down to 10 time bins ($0.5\mu s$), (see sect. 4.8).

Pulse maximum $HistMax$ and its position $MaxBin$:
The parameters $HistMax$ and $MaxBin$ are influenced by the superposition of proton events and electronic noise. $MaxBin$ can vary by some units of time bins due to noise spikes as shown for example in fig. 4.9: Here, the maximal pulse height is reached at $MaxBin1$=43 time bins, but the proper proton pulse reaches its maximum already earlier at $MaxBin2/3$=28 time bins. An upper limit for the distribution of $MaxBin$ of pure proton events can be set at 35 time bins. The value of $HistMax$ is shifted to higher pulse heights due to electronic noise. To suppress the influence of electronic noise on the parameters $MaxBin$ and $HistMax$, the pulse is fitted (black dotted line in fig. 4.9) by using a theoretical fit function which will be initialized in detail in the next section.

4.2.3 Pulse height spectra

General discussion:
Fig. 4.10 (a) shows a typical pulse height spectrum extracted from the recorded pulses of an entire data set ($\approx$8 h measurement time). The uncertainty of each point in the spectra with N counts (per ADC channel) is given by $\sqrt{N}/T$ (statistical error). Some general remarks may help to explain the spectral shape: Filtered by the threshold of the

trigger algorithm (sliding windows, see fig. 3.26), the electronic noise distribution is cut at low pulse heights and a "peak" appears in the spectrum. The proton distribution can be described by a superposition of a Gaussian and an inverted Landau distribution. The tail towards lower ADC channels can be explained by the distribution of energy losses in the insensitive entrance window of the detector after several scattering processes (see [32]). Therefore, the tail of the proton peak is produced by protons which deposit only small energy in the active area of the detector. This tail reaches to low ADC channels even below the electronic noise peak. The upper end of the proton peak is defined by protons which deposit their maximum energy of 15.75 keV impact energy (for -15 kV detector HV).

Due to the discussed saturation by an energy deposition >40 keV, a peak rises in the spectrum around ADC ch. 2500. It is mainly produced by decay electrons (also cosmic rays are included). Fig. 4.10b and (c) show zooms to the single peaks: The average electronic noise peaks (b, left) and electron peaks (c). For both APV-settings (50 V, 780 V) the peaks overlap. The proton distribution for 50 V APV in (b) shows an unexpected second ("satellite") peak (in logarithmic scale) at its right tail around ADC ch. 740. It is about three orders of magnitude smaller than the main proton peak. Detector tests in sect. 3.6.5 showed a dependence of the peak position from the impact position on the detector which might be an explanation. The impact of the satellite peak on the determination of a will be discussed in detail in sect. 4.6.1.

Pulse height extraction:
M. Simson and me adapted three methods of extracting the pulse heights from the raw data. This provided the possibility of cross-checks to exclude errors produced by the pulse height determination method. The method of fitting the pulses turned out to be the most reliable. Additionally, it suppresses electronic noise and helps to filter special kinds of pulse shapes. The other two methods are outlined in appendix 7.

The pulse fitting routine:
Our former collaborator Dr. G. Petzoldt evolved already in 2007 in his PhD-Thesis [29] a first fit routine for the FRM II data. But the bad signal-to-noise ratio (2:1) undid the possibility of distinguishing noise from proton events and averted to use it. In the ILL data the increased SNR (10:1) allows the advantage of fitting the pulses. M. Simson re-implemented the fitting routine in his PhD-thesis [32]. We applied together several additional conditions and requirements arising from the event analysis and the extracted parameter distributions. Both, the shape of a proton pulse as well as the shape of a non-saturating electron pulse (e.g., see fig. 4.11 (a)) can be described by a function with 6 parameters:

$$y(x) = \begin{cases} y_0 & ; \text{ for x} \leq x_0 \\ y_0 + A\left(1 - e^{-\frac{x-x_0}{t_2}}\right)^p \left(e^{-\frac{x-x_0}{t_1}}\right) & ; \text{ for x} > x_0 \end{cases} \tag{4.1}$$

where the new parameters t_1 and t_2 denote the rise and decay time of the pulse, respectively. p influences the shape of the pulse. t_1, t_2 and p are defined by the amplification
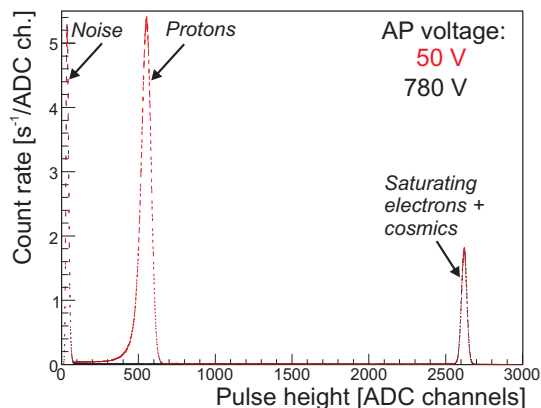
(a) Full spectrum.
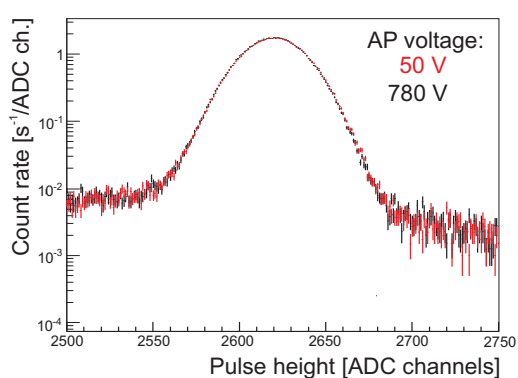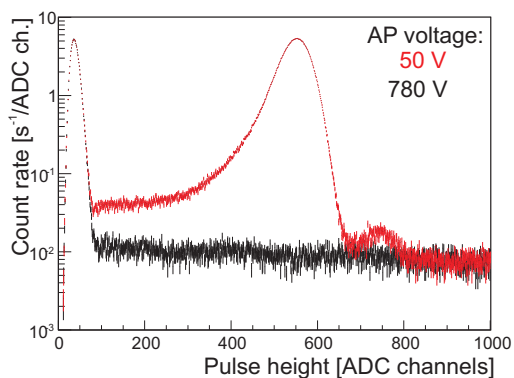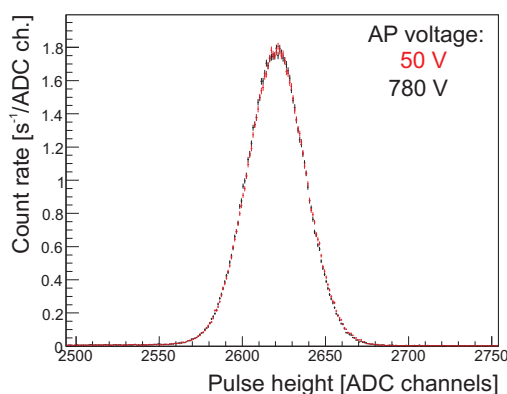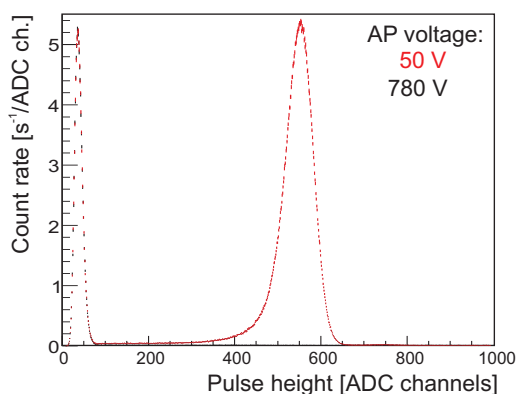
(b) 50 V APV: Noise and proton peak. 780V APV: Background (i.e., mainly noise and electron events).

(c) Electron peak.

Figure 4.10: (a): Pulse height spectrum measured for -15 kV detector HV in May 2008. The two distributions represent the average over all measurements at 50 V (red) and 780 V (black) APV of the data set "190508_night". (b) The zoom shows the noise peak between ADC channels 0 and 80 for both 50 V and 780 V APV. For 50 V the proton peak appears around 550 ADC channels. The measurement at 780 V determines mainly the electron background below the proton peak. (c) Electron peaks (due to saturation effects by high energetic electrons) for different APV-settings. The lower plots of (b) and (c) are both drawn on logarithmic scale. They focus on the differences between 50 V and 780 V APV. A second peak arises in (b) beside the proton peak. It will be called "satellite" peak. Its impact on a will be discussed in sect. 4.6.1.

parameter	lower limit	upper limit	unit
y_0	800	2000	ADC channels
x_0	13	23.5	time bins [x50ns]
t_1	77.49	77.49	time bins [x50ns]
t_2	10.47	10.47	time bins [x50ns]
p	0.394	0.394	-
A	1	$2 \cdot 10^5$	ADC channels

Table 4.1: Limits of the fit parameters.
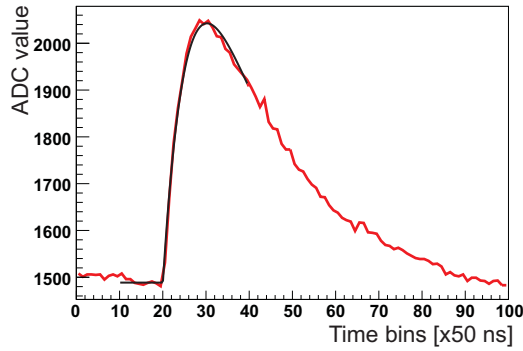
Figure 4.11: Example for a fitted proton pulse (black line) taken from data set "170508_night2".

and shaping chain of the detector electronics. They are practically constant and therefore fixed in the fit. A is proportional to the pulse height and can take only positive values. The start point x_0 is restricted to a certain range as well as the baseline y_0. Tab. 4.1 shows the limits of the fit parameters.

Pulses are only fitted from time bin 10 to 40 which significantly reduces the computing time. An example for a fitted proton event is shown in fig. 4.11. According to the fit result, events are classified as different types (Fit Status 0 to 7). The fit states depend on the fitted pulse height ph as well as the χ^2-value and the convergence of the fit. The fit states help to distinguish between electronic noise, proton and saturating electron events and serve for systematic tests: Noise and saturating electrons have pulse shapes which can not be described by the fit function eq. 4.1. Therefore, these fits have a bad χ^2 and do not converge. Also pile-up events can be separated by the fit routine. All details concerning the fit routine are explained in [32] and in appendix 8.

Fig. 4.12 shows a comparison of fitted and non-fitted spectra (see caption and appendix 7 for details). The separation of noise and proton peak is obviously much better with the fit. For that reason, the fit routine was applied in the analysis to determine the pulse
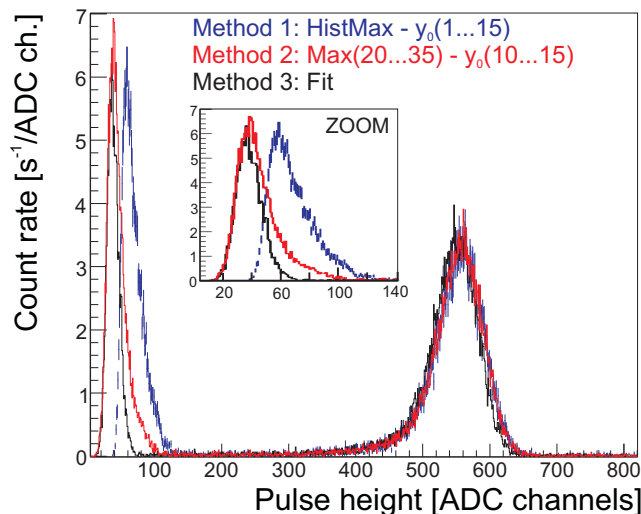
(a) 3 methods of pulse height determination for a 50 V APV measurement.
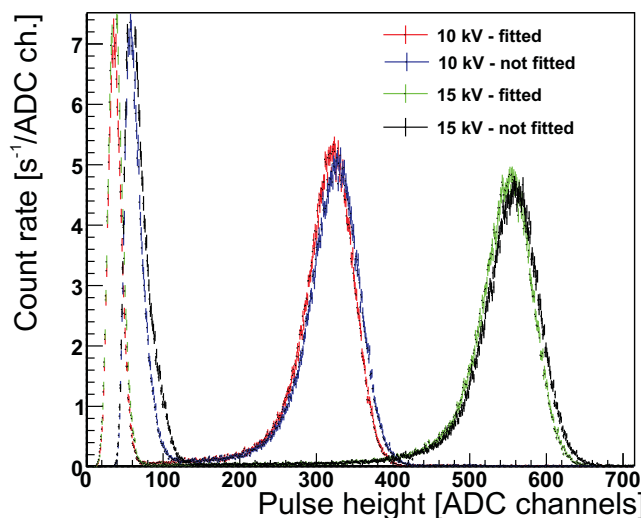
(b) Fitted and not fitted spectra measured at 50 V APV for -10 and -15 kV detector voltage.

Figure 4.12: (a) Comparison of 3 different methods of pulse height determination. Method 1: The baseline y_0 is averaged from time bin 1 to 15. The parameter $HistMax$ extracts the highest ADC-entry in an event window. The pulse height is determined by subtraction. Method 2: The baseline is averaged from time bin 10 to 15. The maximum (Max) of a pulse is determined only between time bin 20 and 35 (see appendix 7). Method 3: The fit routine described in the last section.- The zoom shows the advantage of the fit routine: The noise peak is shifted to lower ADC channels and therefore the separation from the proton peak is better. (b) Spectrum for -10 and -15 kV detector HV from data set "150508_rampHV". Methods 1 and 3 were used here. The noise peak is always clearly shifted to lower ADC channels in the fitted spectra. The proton peak is only slightly shifted to lower ADC channels in the fitted spectra. This shift is due to suppression of noise spikes on proton pulses.
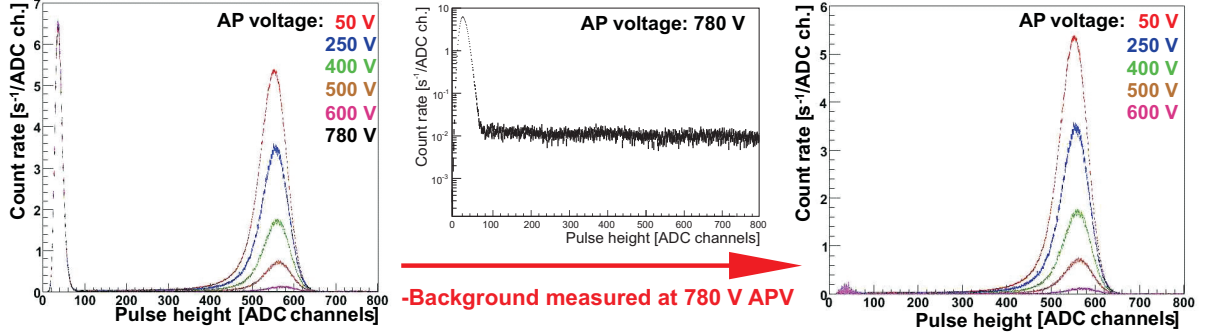
Figure 4.13: Left: Pulse height spectra for different APV-settings measured at -15 keV detector potential (data set: "190508_night"). The plot shows the electronic noise peak (around ADC ch. 40) and the proton peaks (around ADC ch. 560). Center: Background spectrum measured at 780 V APV (mainly noise and electron events). Please note, that this spectrum is drawn in logarithmic scale. Right: Pure proton spectra after subtraction of background measured at 780 V APV.

heights of all measured pulses. The resulting pulse height spectra are now used to extract the proton count rates for each APV-setting.

4.3 Extraction of the coefficient a

The subtraction of background in our experiment was already introduced in sect. 3.6.2 and is summarized in fig. 4.13. The integration in a defined pulse height region (e.g., from ADC ch. 80 to 1200) gives the sum of proton and background count rates for each APV, U_A. The pure background count rate is determined by measurements at 780 V APV in the same pulse height region. The subtraction of both count rate values determines the pure proton count rate. The integral spectrum fig. 4.14 shows integrated proton count rates for 50 V (red circle) to 600 V (purple circle) after background subtraction. The proton count rate $N_p(U_A)$ at a given APV can be described by (see [1]):

$$N_p(U_A) = N_{p,0} \int_0^{T_{max}} F_{tr}(T)w_p(T)dT \qquad (4.2)$$

with T being the kinetic energy of the decay protons, F_{tr} being the transmission function defined in eq. 3.26 and $w_p(T)$ being the differential proton spectrum. Without Coulomb correction (taking into account the electromagnetic interaction between electron and proton) and radiative corrections (taking into account bremsstrahlung), $w_p(T)$ is given by $w_p(T) = g_1(T) + a \cdot g_2(T)$ (with $g_1(T)$, $g_2(T)$ as defined in eq. 2.42). The Coulomb and radiative corrections on $w_p(T)$ were calculated in [24]. In our experiment, we extract a from a fit to $N_p(U_A)$ ([1]). Coulomb and radiative corrections are included in this fit. They have been extrapolated from the tabulated values in [24].
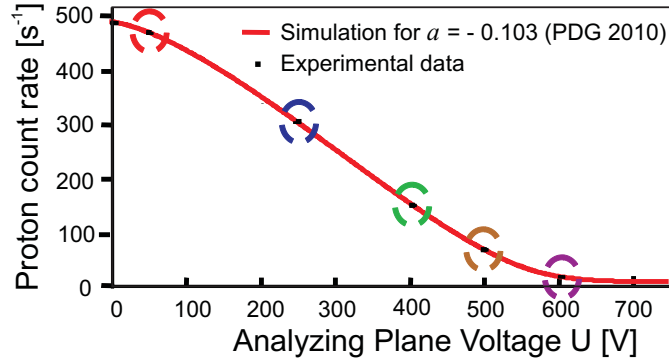
Figure 4.14: Integral spectrum extracted from the data set "190508_night". Each point represents the averaged proton count rate for a given APV-setting extracted from pulse height spectra (fig. 4.13 (right)). The integration was done from ADC ch. 80 to 1200 for different APV-settings. The red line shows the APV-dependence of eq. 4.2 as expected by taking the PDG-value of a=0.103. Note: The aimed accuracy of our experiment is sensitive to shifts in the integral spectrum which are smaller than the line width!

The red line in fig. 4.14 shows a simulated spectrum for a=-0.103 (PDG 2010). The expected APV-dependence of the integral proton count rates in eq. 4.2 seems to be reproduced to first order. This indicates, that the way how the background is determined and subtracted in our experiment is maintainable also to first order. But the line width of the simulated spectrum involves a relative accuracy $\left(\frac{\delta a}{a}\right)$ in the order of several %. For our aimed level of accuracy $\frac{\delta a}{a} < 2\,\%$, the background subtraction has to be analysed in more detail. Especially, the characteristics of background components that depend on the APV-settings is of importance. As introduced in sect. 3.5.2, APV-dependent background was discovered first in the FRM II beam time and induced a relative error up to $\frac{\delta a}{a} \approx 100\,\%$ (see fig. 3.22 and [25]). I refer to sect. 3.6.2 for a general introduction to background in our experiment. A model of the production mechanism of APV-dependent background in the FRM II beam time is presented there as well.

The sensitivity of a to APV-dependent background can be pointed out by assuming a hypothetical APV-dependence as shown in fig. 4.15: First, an APV-independent background component (1) with a count rate of $10\,\mathrm{s}^{-1}$ is assumed[1]. Second, we assume a linearly increasing APV-dependent background component (2). It is by $+0.5\,\mathrm{s}^{-1}$ higher at $780\,\mathrm{V}$ APV compared to $0\,\mathrm{V}$ APV (slope of the fit: $\approx 6.4 * 10^{-4} * \mathrm{APV}\,[s^{-1}]$) and superimposes the constant background component (1). The pure proton count rates for each APV are now extracted in two ways: (A) only the background count rate measured at

---

[1]The count rate is in the order of the background count rate extracted from measurements at $780\,\mathrm{V}$ APV between ADC ch. 80 and 1200.
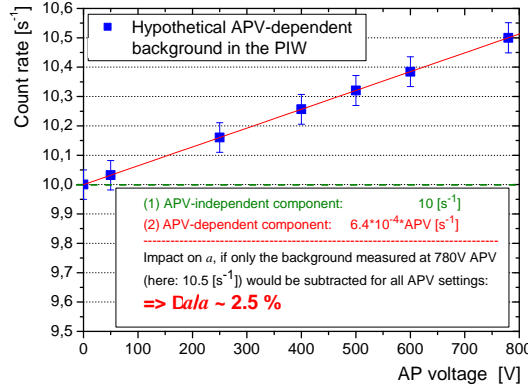
Figure 4.15: Hypothetical APV-dependence of background: This functionality is used to derive a sensitivity of a to an APV-dependent background component.

780 V is subtracted (i.e., -10.5 s^{-1}) from count rates[2] measured at different APV-settings. This means, the extracted proton count rates will be lower than the actual proton count rates (e.g., -0.5 s^{-1} at 0 V APV) and therefore, the APV-dependence shifts the proton spectrum to higher kinetic energies. (B) The background count rates as given in fig. 4.15 are subtracted from the count rates measured at each APV-setting in the PIW. This method extracts the actual proton count rates. For both cases (A) and (B), the coefficient a is now extracted: The value of a is shifted by $\frac{\Delta a}{a} \approx +2.5\,\%$ from (B) to (A). This means, without knowing the APV-dependence sufficiently, the subtraction of background measured at 780 V APV would result in a systematic error of $\frac{\delta a}{a} \approx +2.5\,\%$.

The high sensitivity of a on APV-dependent background motivated various background studies in the ILL beam time. As introduced in sect. 3.6.2, only some assumptions can be made from investigations on parts of the APV-dependent background studied with neutron beam "off" (shutter status 1 and 5). Section 4.5 will focus on these studies and the impact of APV-dependent background on the extracted value of a in the ILL beam time. The investigations on the origin and characteristics of APV-dependent background in aSPECT are presented in detail in appendix 6.10. First, the stability of background count rates measured at 780 V APV with neutron beam "on" will be discussed in the next section since it determines the background to first order.

---

[2]i.e., proton + background count rate in the PIW.

4.4 Background measured at 780 V APV

For the further discussion, the measured pulse height spectra in fig. 4.16 are subdivided into 3 integration windows:

(I)   ADC channel 0 to 80 (mainly electronic noise).

(II) ADC channel 1200 to 4000, called: "**E**lectron **I**ntegration **W**indow" (**EIW**).

(III) ADC channel 80 to 1200, called: "**P**roton **I**ntegration **W**indow" (**PIW**).
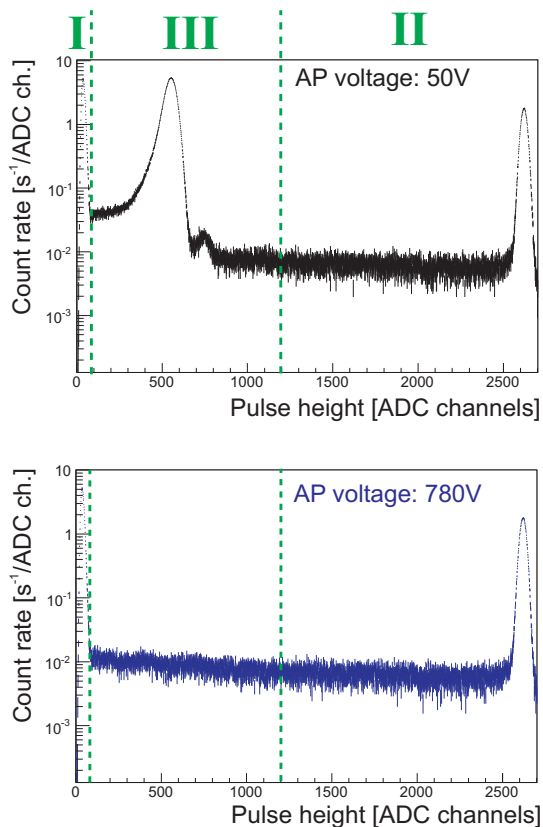
Figure 4.16: (Top) Pulse height spectrum measured at 50 V APV. (Bottom) Pulse height spectrum measured at 780 V APV. The spectra are subdivided in 3 main integration windows: (I) ADC ch. 0...80, contains mainly electronic noise events. (II) ADC ch. 1200...4000 (EIW), contains mainly electron events. (III) ADC ch. 80...1200 (PIW), contains the proton peak for all APV-settings except for 780 V. The electron spectrum superimposes continuously the pulse height region of the proton peak for all APV-settings. In first order background subtraction, spectrum (b) is subtracted from spectrum (a). This determines the proton count rate for 50 V APV.

In this section, all presented measurements were performed with neutron beam

switched "on". The magnetic field as well as the detector HV were set on standard parameter settings (B_0=2.177 T, U_{det}=-15 kV). The decay protons were always reflected by application of 780 V APV and the background was determined. Two observables are of interest: The background stability during one data set[3] (several hours) as well as the stability of averaged background count rates of different data sets (several days). The background

(a) Count rates of data set "190508_night".

(b) Average count rates.
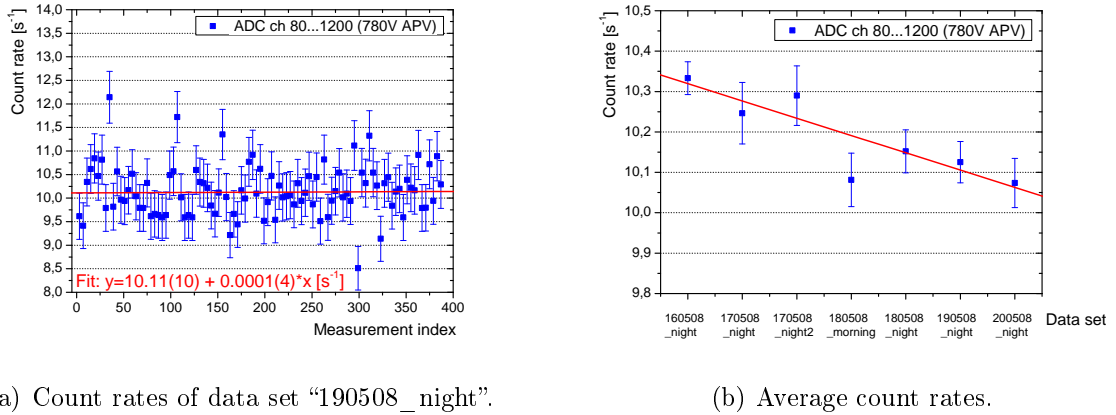
Figure 4.17: Measurements in the PIW at 780 V APV. (a) Background determination for an exemplary data set. Each data point represents the average count rate in 40 s measurement time. The linear fit (red line) indicates no drift during the data set. (b) The average background count rate determined from different data sets decreases during the last days of the beam time: From 16th to 20th of May 2008, the count rate decreases by $\approx -0.25 s^{-1}$. Obviously, the background count rate must be affected by changed parameter settings (e.g., ExB drift potentials switched off or changed, ME "off") in between those data sets.

stability in the PIW during a typical data set ("190508_night", ≈ 7.5 hours) is depicted in fig. 4.17a. It is exemplary for all data sets at standard settings from 16th to 20th of May 2008 (see tab. 4.2). The background count rate shows no drift but is non-statistically fluctuating on a low level ($1 \leq \chi^2 \leq 1.65$). Fig. 4.17b shows the average background count rate in the PIW for different data sets in the last 5 days of the beam time. The count rate decreases by $\approx -0.25 s^{-1}$ from 16th to 20th of May 2008. The background count rates in the EIW behaved similar to the PIW as shown in fig. 4.18: (a) The count rates during a single data set showed no significant drift. But the average count rates (b) were decreasing. The averaged count rates in the PIW and EIW are listed in tab. 4.3. No significant drifts of the background count rates were observed during single data sets. Therefore, it seems reasonable that the decrease in background count rates during the last 5 days of the beam time was probably affected by changed parameter settings in between these data sets. In our beam time at ILL systematic tests were performed during daytime, whereas

---

[3]A data set consists of several hundred single measurements of 40-120 s measurement time with neutron beam switched "on" (see also fig. 4.1).

(a) Count rates of data set "190508_night".   (b) Average count rates.
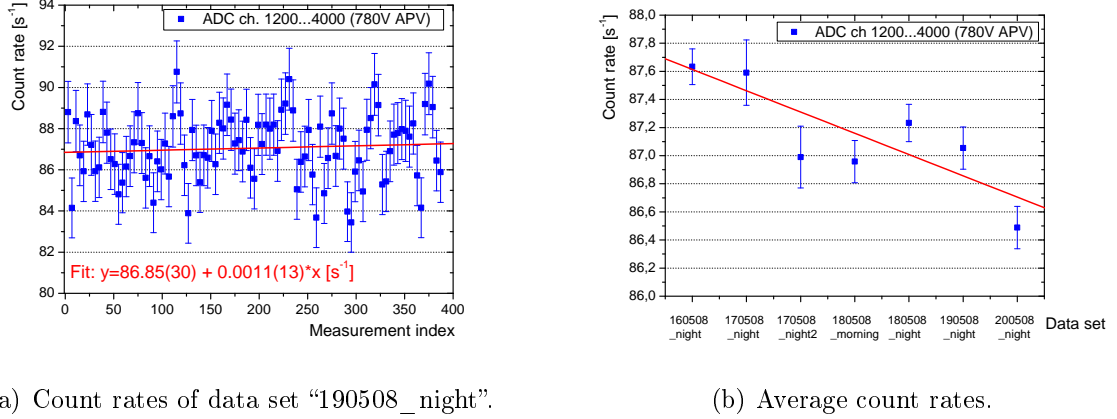
Figure 4.18: Background count rates in the EIW (ADC ch. 1200 to 4000) measured at 780 V APV. (a) The count rates during a single data set ("190508_night") show no drift. (b) The average background count rates determined from different data sets decrease during the last days of the beam time.

Data set	Lower ExB voltages (left / right) [V]	Upper ExB voltages (A / B) [kV]	ME voltages (quadrupole / grid) [V]	Comment
160508_night	-200 / 0	-3.7 / -4.2	820 / 800	
170508_night	-1000 / -50	-3.7 / -4.2	1000 / 800	
170508_night2	-1000 / -50	-2 / -2	1000 / 800	
180508_morning	-1000 / -50	-4.2 / -0.2	1000 / 800	
180508_night	-1000 / -50	-2 / -2	1000 / 800	
190508_night	-1000 / -50	-2 / -2	1000 / 800	
200508_lunch	-1000 / -50	-2 / -2	820 / 800	
200508_night	-1000 / -50	-2 / -2	820 / 800	$r_B = 0.2049$

Table 4.2: Parameter settings of the data sets taken at standard parameter settings (-15 kV detector HV and magnetic field switched "on", i.e., B_0=2.177 T) and during the phase of a reliable electronic performance at the end of the beam time. Each data set represents about 6 to 12 hours of measurement time.

Integration window [ADC channels]	Count rate [s^{-1}]	Neutron beam on/ off
80...1200 (PIW)	10.18(4)	on
1200...4000 (EIW)	87.00(5)	on

Table 4.3: Average background count rates measured at 780 V APV with standard parameter settings (see tab. 4.2).

measurements at standard parameter settings for the determination of the coefficient a were mainly done during night. For systematic tests, the electrode potentials had to be changed. Field emission and Penning discharges depend both on the electric potential settings and the surface conditions of the electrodes. The latter one can change in time and by variation of the applied potentials. Both effects were discussed in sect. 3.6.2 as possible mechanisms for the production of APV-dependent background. Another feasible explanation for the decreasing background count rate at 780 V APV would be a steadily decreasing neutron flux at the beam line PF1B: A fuel element of the ILL reactor has a length of about 70 cm. During 52 days of a reactor cycle, the barycenter of nuclear burning shifts to some extent relatively to the cold source that feeds the PF1B beam line. Therefore, the neutron flux at the beam place might decrease in the end of a reactor cycle. This was experienced by prior experiments as our collaborator Dr. T. Soldner[4] confirmed. However, this decrease was not registered in our neutron counter (see fig. 4.19 (b)). For that reason, the normalization of count rates on the neutron flux (as proposed in sect. 4.1.3) was not applied in the present analysis (see discussion in the caption of fig. 4.19).

To study the non-statistical fluctuations of background in the PIW observed in fig. 4.17 (a), we changed the integration interval by increasing the lower ADC channel (see fig. 4.20). The different data points correspond to four independent measurements at 780 V APV of the data set "200508_night". The red stars (corresponding to the right scale) represent the χ^2-values for the calculation of the mean value. $\chi^2 \to 1$ points out that the count rates are distributed statistically above ADC channel 480. This is an indication that the non-statistical fluctuations of the background emerge from the lower energetic part of the spectrum (<480 ADC ch.).

The following conclusions can be drawn from the background measurements at 780 V APV:
(1) No count rate drift during a data set was observed. Therefore, the background count rate in the PIW is averaged for each data set in the analysis. The averaged background is subtracted from the averaged count rates in the PIW at different APV-settings to determine the pure proton count rates.
(2) The neutron counter can not be used for normalization of the proton count rates.
(3) Non-statistical contributions to the background count rate at 780 V APV emerge in

---

[4]Beam line responsible of PF1B in our beam time.
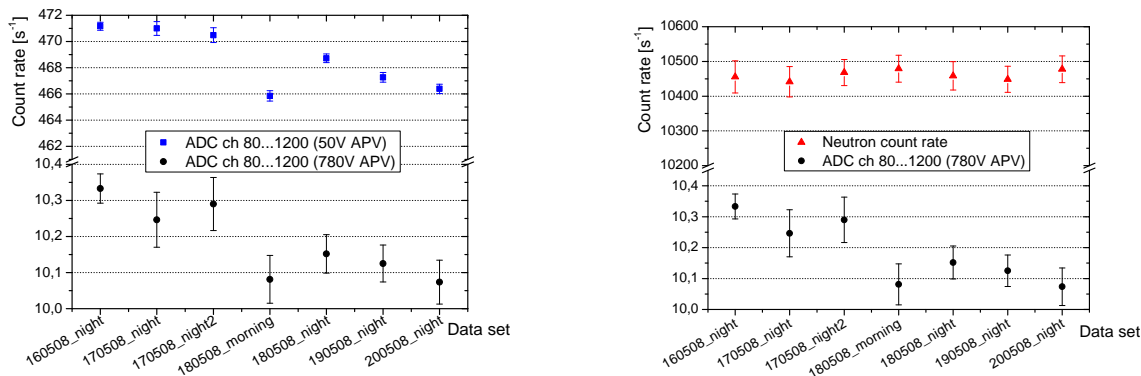
(a) Decrease of proton count rates (50 V APV) as well as background count rates (780 V APV) at the end of the beam time. A correlation is observable.

(b) Background and neutron count rates at the end of the beam time. There is no obvious time correlation.
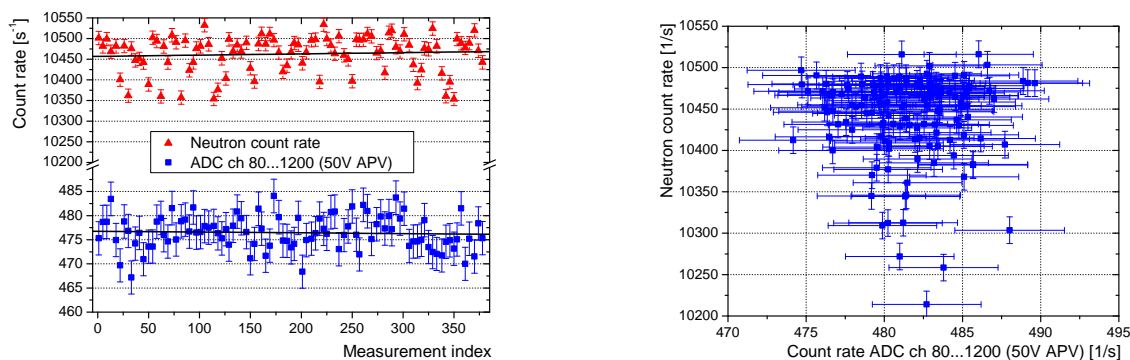
(c) Proton and neutron count rates during the data set "200508_night".

(d) Correlation plot: Neutron vs. proton count rates of data set "160508_night". There is no obvious time correlation.

Figure 4.19: Illustrations concerning the non-coherence between drifts/ fluctuations of the neutron counter and the background/ proton count rates. (a) shows the decrease of the background and the proton count rates at the end of the beam time (both extracted in the PIW) (b) shows the average neutron count rate compared to the average background count rate at 780 V APV in the PIW. There is no common time dependence observable. (c) Neutron and proton count rate (50 V APV) during a typical data set "200508_night". The neutron count rates show a small positive drift. But the proton count rates show a small negative drift. (d) Correlation plot: The neutron and proton count rates (50 V APV, PIW) show no correlation.- Conclusion: Obviously, the neutron counter cannot be used for normalization of the proton count rates, since there is no similar time dependence. The background rates must not necessarily coincide with the neutron count rates. But we observe a similar time dependence of proton and background count rates in (a). The reason can be that part of the background consists of decay electrons, which naturally have a 1:1 correlation to the proton count rates.
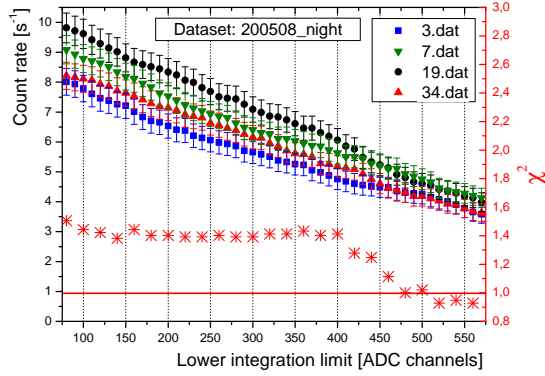
Figure 4.20: Dependence of the background count rate (at 780 V AP) on the lower integration limit of individual measurement runs (left scale). The upper integration limit was fixed to ADC ch. 1200. The examples are taken from data set "200508_night". The diagram indicates non-statistical fluctuations (i.e., $\chi^2 > 1$), e.g., by background below ADC ch. 480.

the region <480 ADC ch. and have to be studied (see next section).

Data set	Lower ExB voltages (left/right) [V]	Upper ExB voltages (A/B) [kV]	ME voltages (e2/e1) [V]	Detector HV [kV] + comments
060508_night	-1000/-50	-4.2/-0.2	1000/800	-10
				2 detector pads
090508_Mirror_Off	-1000/-50	-4.2/-0.2	0/0	-10
150508_night	-200/0	-2/-2	820/800	-15
				20 mm beam width
190508_lExB1	-2.4/0	-2/-2	820/800	-15
190508_lExB2	-10.6/0	-2/-2	820/800	-15
210508_night	-1000/-50	-2/-2	820/800	-15
				30 A main current

Table 4.4: Parameter settings of data sets for systematic tests.
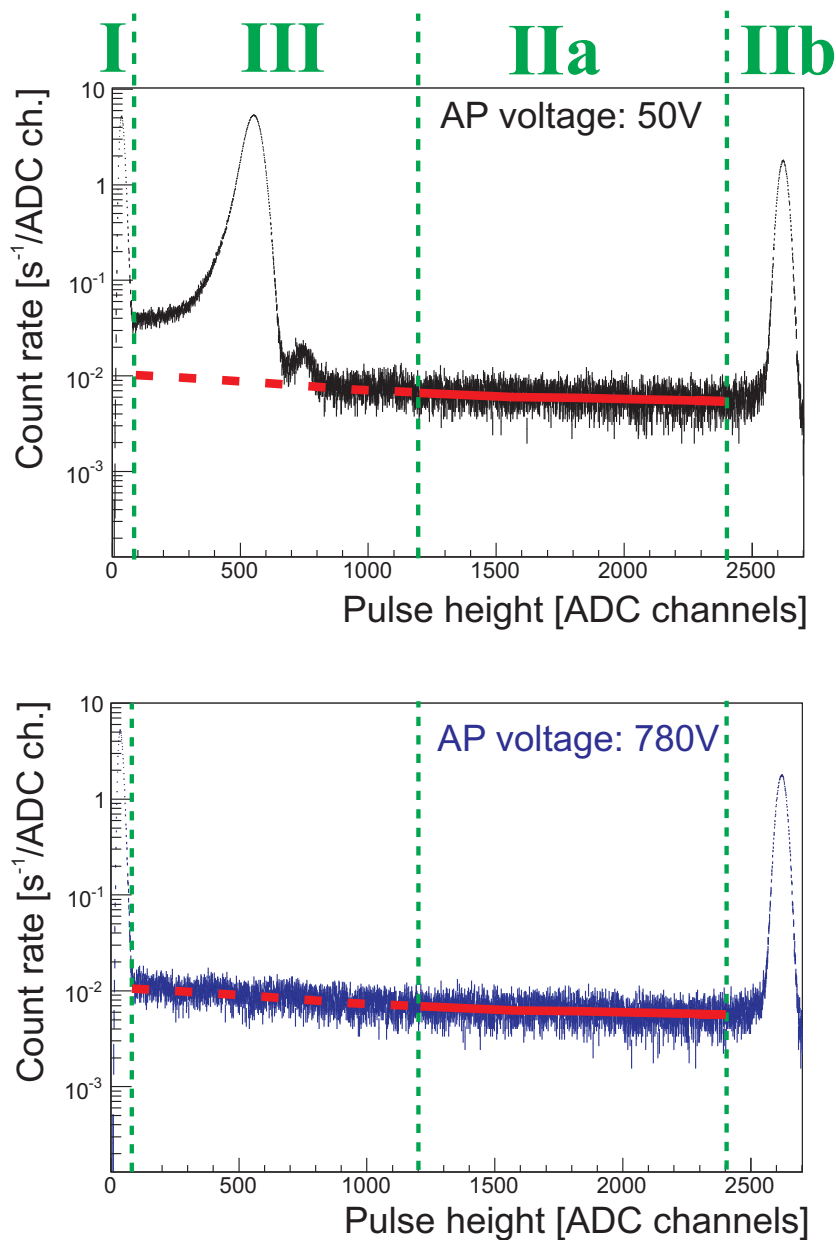
Figure 4.21: (Top) Pulse height spectrum measured at 50 V APV. (Bottom) Pulse height spectrum measured at 780 V APV. The spectra are subdivided in 3 main integration windows: (I) ADC ch. 0...80, contains mainly electronic noise events. (II) ADC ch. 1200...4000, contains mainly electron events. It is split up in two sub-windows: IIa (ADC ch. 1200...2400) is used to fit (red line) and to extrapolate (dashed red line) the electron background. IIb (ADC ch. 2400...4000) contains mainly saturating electron events. (III) ADC ch. 80...1200, contains the proton peak for all APV-settings except for 780 V. The continues electron spectrum superimposes the proton peak for all APV-settings. The red line is a 2nd order polynomial fit done with ROOT: The average count rate difference between the fit and the measurement is $< 0.5(1)\,[1/s]$ in the PIW for all data sets.

4.5 APV-dependent background

As introduced in sect. 3.6.2, the background measured at 780 V APV consist of several
components:
(1) Electronic noise (between ADC channel 0 to 80),
(2) Decay electrons (superimposing the entire pulse height spectrum, above ADC ch.
1200 mainly electrons contribute to the spectrum),
(3) Environmental background (e.g., cosmic rays),
(4) Residual background (a possible APV-dependence has to be studied).

   Fig.4.21 shows two pulse height spectra measured at 50 V APV (top) and at 780 V
APV (bottom). The spectra are subdivided in 4 pulse height regions: (I) ADC ch. 0 to 80,
(IIa) ADC ch. 1200 to 2400, (IIb) ADC ch. 2400 to 4000 and (III) ADC ch. 80 to 1200.
The APV-dependence of background will be studied in each of these regions starting with
the electronic noise (I): Fig. 4.22a shows the temporal dependence of the electronic noise
count rates for different APV-settings (about 10 h measurement time during night). The
count rates are decreasing with time due to a decreasing temperature in the experimental
area. Fig. 4.22b shows the mean electronic noise count rates for different APV-settings.
No clear dependence on the APV was observed.
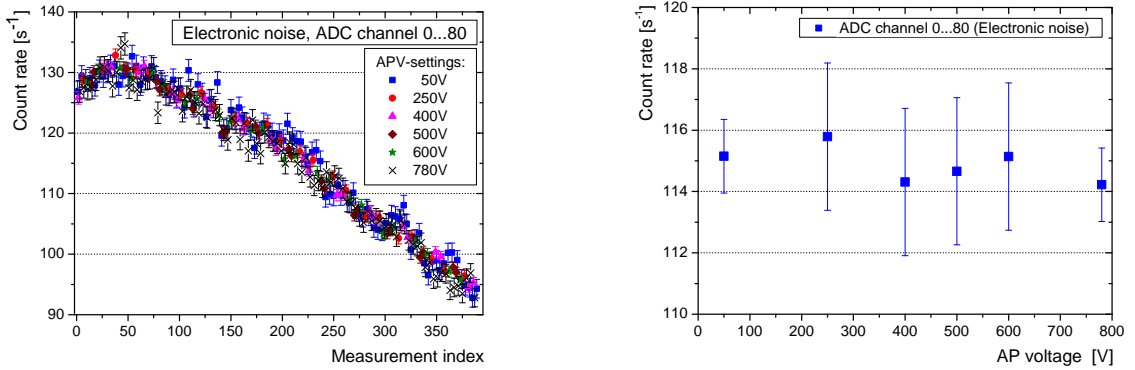
(a) Temporal dependence of the electronic noise
count rate (ADC ch. 0 to 80).

(b) Mean electronic noise count rate vs. APV-
settings.

Figure 4.22: Data set: "190508_night". (a) The electronic noise count rates (ADC ch. 0
to 80) are correlated to the temperature in the experimental area. Data set
"190508_night" was measured over night and therefore the count rate de-
creases. (b) The mean electronic noise count rate shows no APV-dependence.

   The average background count rates in the pulse height regions (IIa) and (IIb) are
shown in fig. 4.23 for different APV-settings. Mainly decay electrons contribute to this

pulse height regions. Obviously, no APV-dependence was observed in both regions. Therefore, the pulse height region (IIa) can be used to extrapolate the continuous electron background in the pulse height region (III), ADC ch. 80 to 1200 (PIW): Background spectra measured at 780 V APV (for standard parameter settings) were fitted by 2nd order polynomial fits (see fig. 4.21, $\chi^2 \approx 1$). At 780 V APV mainly electrons contribute to the pulse height region (III). The comparison of the measured background count rates (extracted from pulse height spectra) and the extrapolated background count rates (from the polynomial fit) gives an upper limit of $\leq 0.5\,\mathrm{s}^{-1}$ for the average count rate generated by residual background in the PIW (pulse height region (III)) at 780 V APV. This residual background might depend on the APV-settings and needs to be studied. APV-dependent
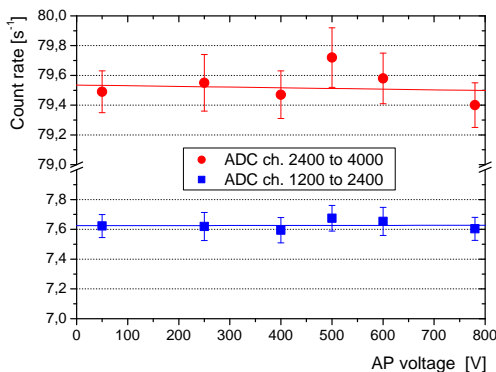
Figure 4.23: Average background count rate in the integration windows (IIa) ADC ch. 1200 to 2400 and (IIb) ADC ch. 2400 to 4000. No APV-dependence is observed.

background in the PIW can not be measured with neutron beam "on" since the proton spectrum superimposes the background spectrum for all APV-settings except for 780 V. But it can be partly measured with neutron beam "off":

4.5.1 General analysis: FRM II vs. ILL beam time

A main aim of the beam time at ILL was the reduction of background that depends systematically on the APV-settings. This additional background was observed for the first time during the measurements at FRM II ([25]). Further systematic tests in Mainz showed that it is coupled to the settings and changes of HV-electrode potentials (see sect. 3.6.2). The mechanical modifications on several electrodes, a lower detector HV (-15 kV instead of -30 kV) and the improved vacuum conditions were already discussed in sect. 3.1. They were crucial for achieving the aim of reducing the APV-dependent background produced mainly by ionization of residual gas atoms. The outcome of all our efforts is presented in fig. 4.24a. It shows the comparison of the background measured with neutron beam "off" in the FRM II beam time (blue rectangles) and in the ILL beam time (red dots, shutter
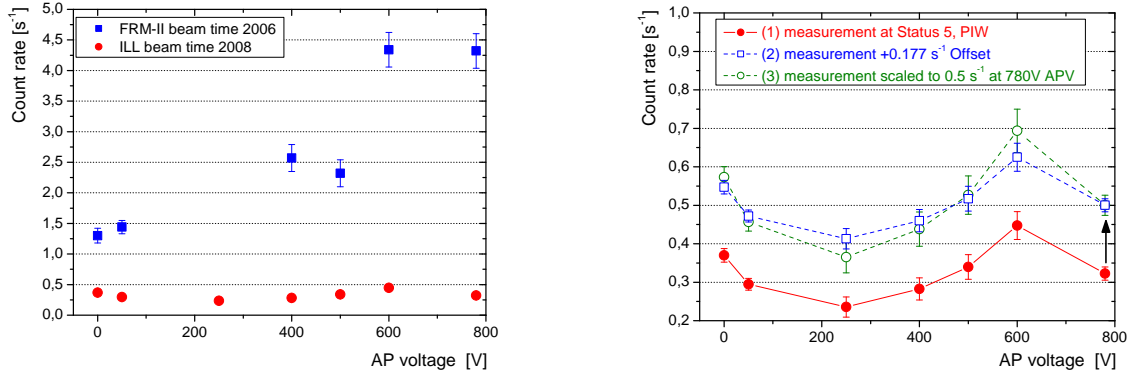
(a) APV-dependent background measured with neutron beam "off": FRM II vs. ILL beam time (Data set "160508_night").

(b) APV-dependent background measured with neutron beam "off" in the ILL beam time (Data set "160508_night").

Figure 4.24: (a) Comparison of the background measured with neutron beam "off" for the FRM II beam time (blue squares) ([25]) and the recent ILL beam time (red dots) (shutter status 5, average count rates of data set "160508_night"). The PIW (pulse height region (III)) was used for extracting the count rates. We achieved our aim to reduce the APV-dependent background. (b) (1) Background measured with neutron beam "off" (status 5) in the ILL beam time (red dots) for a typical data set "160508_night". The background count rate measured at $780\,\mathrm{V}$ APV is $0.323(17)\,\mathrm{s}^{-1}$ in this data set. This count rate is in the order of the upper limit for residual background of 0.5^{-1} with neutron beam "on" at $780\,\mathrm{V}$ APV approximated by polynomial fits (see fig. 4.21). Therefore, the measured integral spectrum (1) is normalized in two ways to a count rate of $0.5\,\mathrm{s}^{-1}$ at $780\,\mathrm{V}$ APV: (2) The count rate difference of about $0.177\,\mathrm{s}^{-1}$ is added as an offset for all APV-settings (blue squares).(3) The background is scaled by the count rate ratio ($\frac{0.5\,s^{-1}}{0.323\,s^{-1}}$) for all APV-settings (green circles).

status 5, average count rates of data set "160508_night"). At 780 V APV, the background was reduced by a factor of 10, at 50 V by a factor of 5. The background of the ILL beam time shows no strong dependence on the APV in the PIW. The count rate at 780 V APV is $0.323(17)\,\mathrm{s}^{-1}$ which is in the order of the upper limit for residual background of 0.5^{-1} approximated by polynomial fits (see fig. 4.21). The count rate difference of about $0.177\,\mathrm{s}^{-1}$ between the measurement with neutron beam "off" and the approximation with neutron beam "on" is used in fig. 4.24b to normalize the measured integral spectrum in two ways: For spectrum (2), an offset of $+0.177\,\mathrm{s}^{-1}$ was added for all APV-settings (blue squares). For spectrum (3), the background was scaled by the count rate ratio $\left(\frac{0.5\,s^{-1}}{0.323\,s^{-1}}\right)$ for all APV-settings (green circles).

We can use the count rate differences between background measurements at 780 V and at other APV-settings to calculate the influence of the APV-dependent background in fig. 4.24b on the coefficient a in four analysis steps (see sect. 4.3):
(0) Background measured at 780 V APV with neutron beam "on" is subtracted from the count rates at different APV-settings (standard background subtraction procedure).
(1) The pure proton count rate at each APV-setting is corrected on the APV-dependent background measured with neutron beam "off" (spectrum (1) in fig. 4.24b, red dots). The count rate difference to the background count rate measured at 780 V APV has to be subtracted from the proton count rates: #(780 V)-#(X V) (e.g., the background measured at 50 V APV was by about $-0.03\,\mathrm{s}^{-1}$ lower than at 780 V. Therefore, the proton count rate at 50 V APV has to be corrected by $+0.03\,\mathrm{s}^{-1}$).
(2) The pure proton count rate at each APV-setting is corrected on the APV-dependent background measured with neutron beam "off" with an additional offset of $+0.177\,\mathrm{s}^{-1}$(spectrum (2) in fig. 4.24b, blue squares).
(3) The pure proton count rate at each APV-setting is corrected on the APV-dependent background measured with neutron beam "off" which was scaled to the upper count rate limit of $0.5\,\mathrm{s}^{-1}$ at 780 V APV (spectrum (3) in fig. 4.24b, green circles).

For each analysis step (0) to (3), the coefficient a was extracted from the resulting proton count rates. The value of a extracted in step (0) was used as the reference value. Please note, that the coefficient a is only influenced by the APV-dependent background component. This means, the count rate differences of background at 780 V APV to background at different APV-settings determines the impact on a (see sect. 4.3). Therefore, a constant offset in (2) does not change the impact on a and analysis step (1) and (2) deliver the same value for the coefficient a. The APV-dependent background causes a shift[5] of a. In the case of the analysis steps (1) and (2), a shifts by $\frac{\Delta a_1}{a_0} = \frac{\Delta a_2}{a_0} = -0.53\%$. In the case of analysis step (3), the shift is even stronger: $\frac{\Delta a_3}{a_0} = -0.93\%$. The mean shift induced by the APV-dependent background correction for data set "160508_night" is therefore given by $\frac{\Delta a}{a} = -0.73 \pm 0.20\%$. The extracted value of the coefficient a can be corrected by inversion of this shift. The error of this correction is therefore given by the uncertainties

---

[5]e.g., $\frac{\Delta a_1}{a_0} = \frac{a_1 - a_0}{a_0}$.

(e.g., $\pm0.2\%$) of the measured and approximated APV-dependences (analysis steps (1) and (3)). I will come back to this correction on APV-dependent background after a short discussion of the background spectra measured with neutron beam switched "off".

4.5.2 Background spectra measured with neutron beam "off"

The better energy resolution of the silicon drift detector used in the ILL beam time (compared to the Si-PIN diode used in the FRM II beam time) allows for a more sophisticated analysis of the APV-dependent background constitution. In addition, the statistical accuracy of the measurements with neutron beam "off" was increased: We performed more than 4800 single measurements (in total about 13.4 hours of measurement time) with the neutron beam switched "off" (for standard parameter settings). In the FRM II beam time, the contribution of APV-dependent background was visible as a clear peak in the pulse height spectrum of single measurements at 780 V (with neutron beam "on" and "off"). In contrast, the APV-dependent background can only be observed now by summing up the measurements of a complete data set (for a given APV-setting). The spectra measured with neutron beam "off" (shutter status 5) are shown in fig. 4.25. Two peaks are visible: There is one peak between ADC ch. 300 and 450 (called "peak1"). The second peak appears between ADC ch. 500 and 600 (called "peak2"). Both peaks show different characteristics: Peak1 is detected for all APV-settings. The maximum of peak1 shifts to higher ADC channels for increased APV (40.6 ± 4.6 ADC ch/kV) as shown in fig. 4.26 and the intensity of peak1 increases minimally with the APV. Peak2 is only detected at 0 V and 50 V APV and its intensity is decreasing from 0 V to 50 V APV. In spectra for shutter status 1[6], the peak structure is even less obvious: One can only guess an accumulation of signals in the pulse height region ADC ch. 300 to 450. By re-binning[7] a faint peak structure is visible. Therefore I omitted a plot for shutter status 1.

It is reasonable to split up the PIW (pulse height region (III)) in four smaller parts: (IIIa) ADC ch. 80 to 300, (IIIb) ADC ch. 300 to 450 (peak1), (IIIc) ADC ch. 500 to 600 (peak2) and (IIId) ADC ch. 600 to 1200. The background in the pulse height regions (IIIa) and (IIId) is discussed in appendix 6.9.5 and shows no APV-dependence. Fig. 4.27 shows the APV-dependences of the mean background count rates in the pulse height regions of the two background peaks, (IIIb) and (IIIc). The count rates were extracted from all data sets measured at standard parameter settings. The APV-dependence induced by peak1 varies for different data sets and results in shifts of the coefficient a of $-0.15\% \leq \frac{\Delta a}{a} \leq -2\%$. The variation can be explained by changed parameter settings (e.g., electrode potentials) between these data sets. Obviously, the APV-dependent background is sensitive to these parameter settings. **The average correction on background peak1** (as introduced at the end of the sect. 4.5.1) **was calculated to be** $\frac{\Delta a}{a} = -1.14 \pm 0.3\%$. The correction of

---

[6]Neutron beam "off" before opening the shutter.

[7]"Re-binning": ROOT is reducing the number of bins (ADC channels) by summing up neighboring channels.

(a) Full spectrum for shutter status 5.

(b) Zoomed and re-binned spectrum with Gaussian fits.
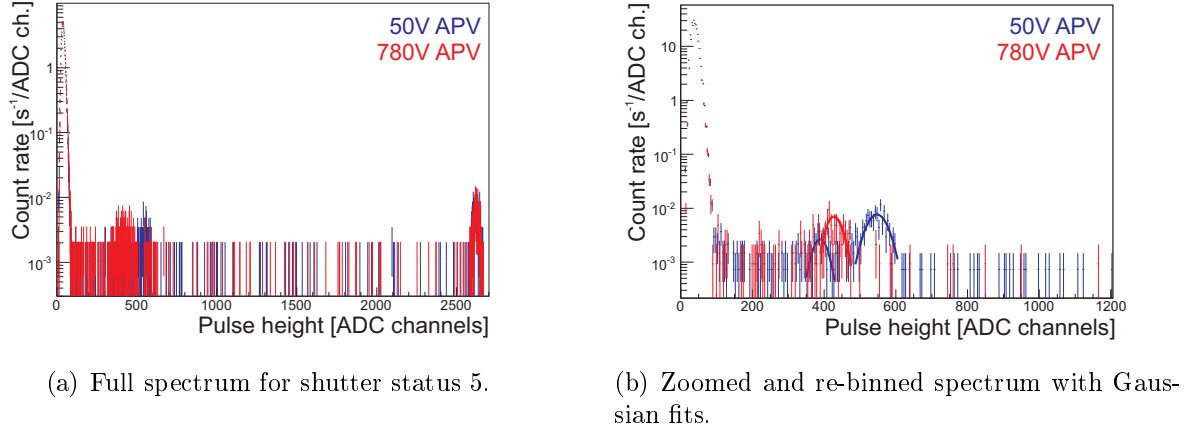
Figure 4.25: Pulse height spectra for shutter status 5 at 50 V and 780 V APV. (a) Complete spectrum up to the electron peak at ≈2600 ADC ch. Two background peaks between ADC ch. 300 and 600 are clearly visible. (b) Zoom into the spectrum (PIW) which is re-binned by a factor of 5. The intensity of peak1 (between ADC ch. 300 and 450) increases from 50 to 780 V APV. Peak2 (between ADC ch. 500 and 60) is only visible for 50 V APV.
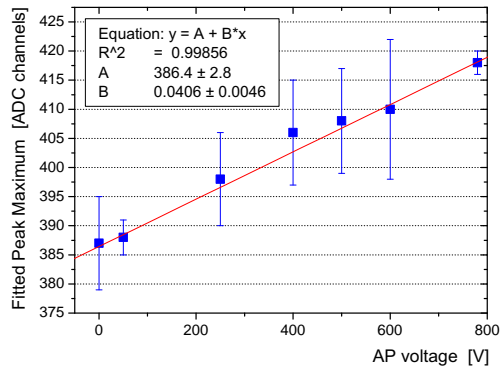
Figure 4.26: Peak position of background peak1 which appears in the spectrum at all APV-settings. The position shifts by 31.7±4.6 ADC channels from 0 to 780 V APV. The shift of the peak and the energy gain indicates that the source of the APV-dependent background might be situated above the center of the AP electrode.

(a) Status 1, all files.   (b) Status 5, all files.
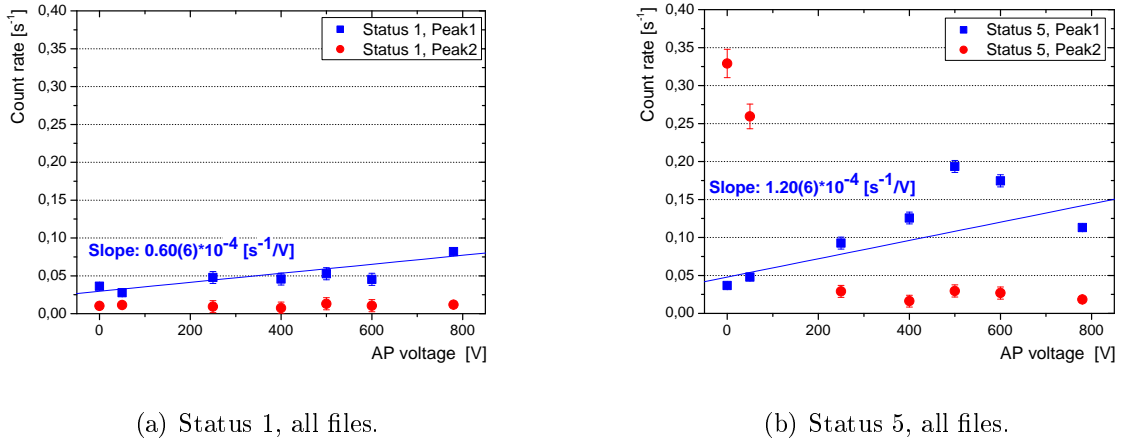
Figure 4.27: Background count rates measured with neutron beam "off" (status 1 and 5) averaged for all data sets with standard parameter settings. (a) shows the count rates integrated in the pulse height regions of peak1 (ADC ch. 300 to 450) and peak2 (ADC ch. 500 to 600) at shutter status 1. (b) shows the integral spectra measured at shutter status 5.

peak2 will be discussed later after some investigations on the nature of both background peaks.

Fig. 4.28 shows the temporal dependence of the background count rate for different APV-settings. The measurements started at t=0 s, about 0.5 s after the neutron beam was switched "off". To reduce the statistical error, all measurements at a certain shutter status and a given APV were summed up. The following observations were made:
Peak1: The count rates fluctuate for status 1 (a) and status 5 (b) without any obvious drift. The temporal dependence of the count rates measured at 780 V APV is similar for all other APV-settings. Only the relative strength varies.
Peak2: (c) The count rate is on a low level for status 1. (d) 0.5 s after the neutron shutter was closed (status 5), the background count rates of peak2 decay exponentially. The decay can be observed only at 0 V and 50 V APV. For all other APV-settings we see no drift or exponential dependence. Obviously, peak2 is beam related and correlated to trapped particles with regard to the observed decay.

The decay of peak2 can be fitted by an exponential function as shown in fig. 4.29. In these plots, t=0 s denotes the time when the neutron shutter was closed. The initial amplitude at t=0 s can be extrapolated via the fit. It will be further used as a good approximation for the average amount of APV-dependent background count rate with neutron beam "on" (at 50 V APV) represented by peak2. The mean amplitude of all data sets is $0.37(6)\,s^{-1}$ at 50 V APV. The average time constant of the decay is 2-3 s.

The amount of trapped particles in a Penning trap is determined by the mechanisms
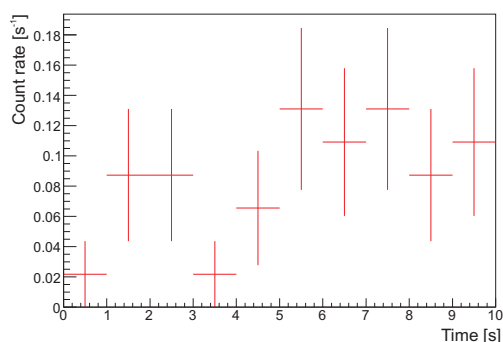
(a) Status 1, 780 V.
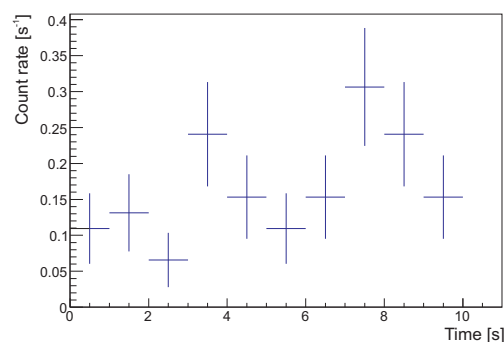
(b) Status 5, 780 V.
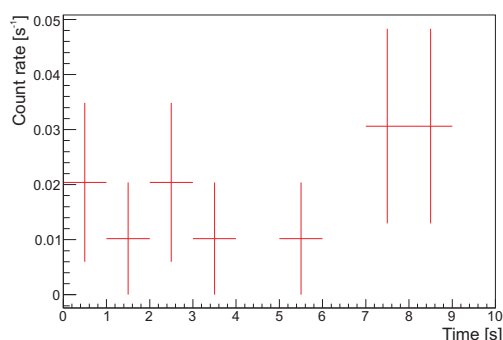
(c) Status 1, 50 V.
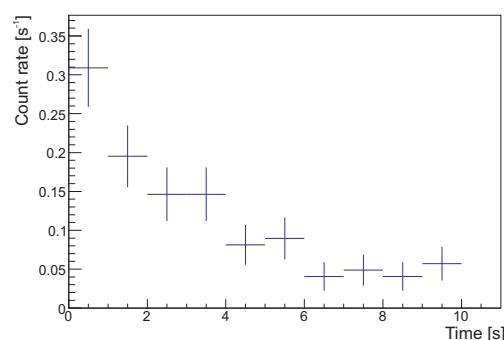
(d) Status 5, 50 V.

Figure 4.28: Data set: "170508_night2". Time dependence of the average count rate for all measurements with neutron beam "off". The measurement started at t=0 s, 0.5 s after the neutron shutter was closed. (a), (b): Pulse height region (IIIb) of peak1 (ADC ch. 300...450) at 780 V APV for shutter states 1 and 5. Similar temporal dependences are observed for all the other APV-settings, too. The count rates fluctuate randomly and show no obvious drift. In (a), the average count rate level is lower for status 1 than for status 5 in (b). (c), (d): Pulse height region (IIIc) of peak2 (ADC ch. 500...600). The count rates fluctuate randomly at status 1 but show no obvious drift. At shutter status 5 the count rates decay exponentially. For all the other APV-settings, the count rates of peak2 fluctuate around an average value.

(a) "180508_night".
(b) "190508_night".
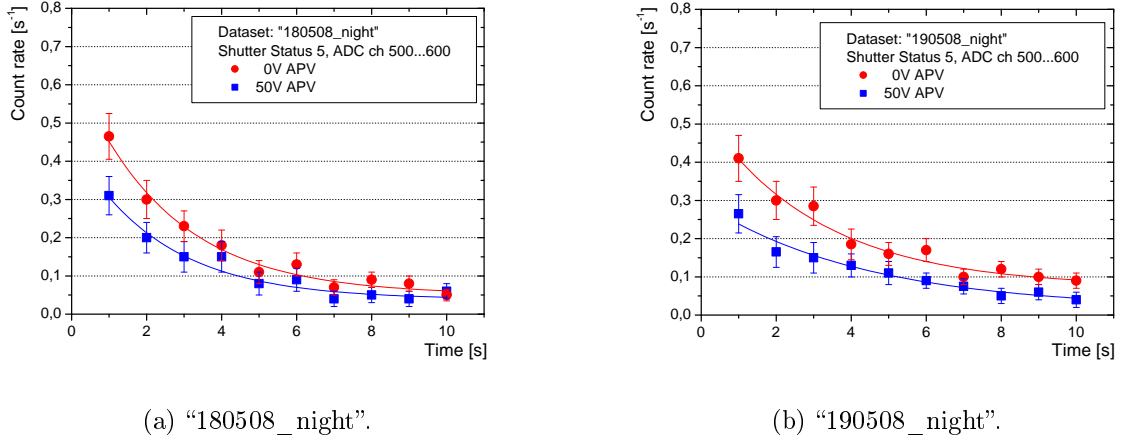
Figure 4.29: Examples for the count rate decay of peak2 at shutter status 5 for $0\,\mathrm{V}$ and $50\,\mathrm{V}$ APV. t=0 s denotes the time when the neutron shutter was closed. The decay is fitted exponentially: The averaged initial amplitude for all data sets is $0.54(8)\,s^{-1}$ for $0\,$V and $0.37(6)\,s^{-1}$ for $50\,$V APV.

that fill the trap and that empty the trap. In the case of the particle trap between AP electrode and Mirror electrode (ME) in aSPECT (see fig. 3.28), two terms for the filling process $F1$, $F2$ and two for the emptying process $E1$, $E2$ will be discussed:
($E1$) Emptying by the applied lower ExB-drift potential (at rate Γ_{E1}).
($E2$) Emptying via transmission of the AP potential towards the detector (at rate Γ_{E1}; e.g., by collisions).
From the comparison of measurements with standard parameter settings (e.g., "190508_night") and measurements with insufficient drift potential in the lower ExB electrode (e.g., "190508_lExB") we can conclude, that process $E1$ is dominant (please see appendix 6.10.1 for details). The terms that describe the process of filling the trap are:
($F1$) Filling by decay protons which do not cross the AP potential (at rate Γ_{F1}).
($F2$) Filling by ionized residual gas atoms (at rate Γ_{F2}).
The ionization process for peak2 is also beam related and depends on the amount of electrons in the spectrometer: Only low-energetic, secondary electrons can be trapped in the electron trap between lower and upper ExB-electrode (see also sect. 3.6.2). The density is highly increased. Trapped secondary electrons have a longer interaction time compared to decay electrons passing the spectrometer. Therefore, secondary electrons are assumed to play a crucial role for the rate Γ_{F2}.

The time constants c extracted from exponential fits of type $A * e^{-t/c}$ to the decay of peak2 (see fig. 4.29) were in the order of 1-4 s. This is far above the expected storage time for protons: When the neutron shutter is closed, the mean flight time for cold neutrons from the shutter to the DV is in the order of a view milliseconds. The storage time for decay protons between AP and ME, which have not passed the AP barrier, is also in that

order due to the applied lower ExB-drift potential. Measurements at shutter status 5 start about 500 ms after the shutter is closed. Due to that fact, no decay protons should be left in the trap. But low energetic electrons can be stored for about a few seconds. After that time they would lose their energy by synchrotron radiation (taken from calculations by F. Glück). Or they lose their energy before by inelastic scattering with residual gas ions that can be detected. When the neutron shutter gets closed, $\Gamma_{F1} = 0$ immediately. However, the ionization rate of residual gas atoms, Γ_{F2}, still continues for some seconds. Therefore, the observed decay of peak2 at 50 V is coupled to the vanishing filling rate Γ_{F2}.

A correction on the additional background count rate of peak2 (extrapolated for 50 V APV) was implemented as well: As for background peak1, the background count rate of peak2 measured at 780 V APV is subtracted from the background count rates measured at other APV-settings. For 50 V APV, the extrapolated count rate is used. The count rate difference is subtracted from the proton count rates at each APV. Only the proton count rates measured at 50 V APV (with neutron beam "on") are really influenced (reduced) by this correction. For example, the average count rate difference #(50 V APV)-#(780 V APV) is about $+0.3\,\text{s}^{-1}$ in the pulse height region of peak2. Therefore, the proton count rate at 50 V APV is reduced by $-0.3\,\text{s}^{-1}$ in this correction. This generates a shift of the coefficient a which is stronger than the shift induced by peak1: **The average correction on background peak2 was calculated to be** $\frac{\Delta a}{a} = +2.07 \pm 0.31\%$. The background count rate with neutron beam "on" was extrapolated individually for each data set. The uncertainty of the fit defines the error of this correction.

In addition to the discussed measurements with neutron beam "off", we studied the nature of the observed APV-dependent background in various measurements, in which specific parameter settings (e.g., electric potentials, magnetic field strength, neutron beam width) were varied. Table 4.5 lists these parameter settings and the regarded types of background. These measurements are discussed in detail in the appendix: Appendix 9.1 and 9.2 present that neither environmental background nor background produced by beam related γ-radiation show an APV-dependence. As analyzed in appendix 9.3, the background count rate of decay electrons in the PIW (pulse height region (III)) is also APV-independent. It is also shown there, that the two observed background peaks must be due to ionized residual gas ions. Appendix 10 presents five background studies with non-standard parameter settings. The observations and conclusions of all background studies will be summarized in the next sub-section:

4.5.3 Results of the studies on APV-dependent background:

From background analysis a central conclusion can be drawn:
Despite the fact, that we determined a non-vanishing APV-dependent background in the ILL beam time, a big improvement was made: In the FRM II beam time, the count rates of APV-dependent background were by a factor of 5-10 higher and the resulting impact on a was up to $\frac{\delta a}{a}=100\%$ (worst case). For the data taken at the ILL beam time,

Section	Type of background contribution	Parameter settings
4.4	Beam related background (A) (mainly decay electrons; only directly measurable at 780 V APV)	Neutron beam: on Detector HV: on Magnetic field: on **APV: +780 V**
4.5	APV-dependent background (A)	**Neutron beam: off** Detector HV: on Magnetic field: on **APV: 0...+780 V**
appendix 10	APV-dependent background (B): (studied by variation of various parameter settings)	**Neutron beam: off** Detector HV: on Magnetic field: on APV: 0...+780 V Mirror voltage: on/ off Lower and upper ExB: varying
(see also 4.5)	Electronic/ thermal noise (detector and preamplifier)	Neutron beam: off Detector HV: on/ off Magnetic field: on/ off
appendix 9.1	Environmental background (e.g., cosmic rays)	**Neutron beam: off** **Detector HV: off** **Magnetic field: off** **APV: 0...+780 V**
appendix 9.2	Beam related background (B) (mainly due to gamma radiation)	Neutron beam: on **Detector HV: off** **Magnetic field: off** **APV: 0...+780 V**
appendix 9.3	Beam related background (C) (mainly decay electrons; measurable at all APV-settings since protons are not detected)	Neutron beam: on **Detector HV: off** Magnetic field: on **APV: 0...+780 V**

Table 4.5: Parameter settings for different background studies. The APV-dependent background is confined in the list since it was previously unexpected.

the APV-dependence was investigated for the entire pulse height spectrum. Only two regions showed APV-dependent background which could be studied in measurements with neutron beam "off": (a) ADC ch. 300 to 450 (peak1) and (b) ADC ch. 500 to 600 (peak2). The average shift induced by the APV-dependent background peak1 on the coefficient a is $\frac{\Delta a}{a}$=-1.14$\pm$0.30%. The average shift induced by the background peak2 is $\frac{\Delta a}{a}$=+2.07$\pm$0.31%. The coefficient can be corrected by inversion of that shifts, both corrections together induce a systematic error of $\frac{\delta a}{a}$ =0.61%. This is the result from all data sets with standard parameter settings. The observed characteristics of the two background peaks will be summarized in itemized style. Some of the conclusions are drawn from investigations discussed in detail in the appendix (9 and 10).

(1) Background peak1 (between ADC ch. 300 to 450 at -15 kV detector HV):

- Appears for all APV-settings with neutron beam "off" (status 1 and 5) (see sect. 4.5.2).

- Observable at low (-10 kV) and high (-15 kV) detector HV (see appendix 6.10.3).

- The count rate is fluctuating randomly (see fig. 4.28a and c. Appendix 6.10.1 and appendix 6.10.4, fig. 6.39 provide additional studies).

- The production mechanism is strongly coupled to the electron trap between the lower and the upper ExB drift electrodes. This was shown by various systematic tests (e.g., see appendix 6.10.4).

- The shift of the peak position with increased APV-settings to higher ADC channels (see fig. 4.26) indicates that the source of background peak1 might be allocated above the maximum of the AP potential.

(2) Background peak2 (between ADC ch. 500 to 600 at -15 kV detector HV):

- Appears only clearly as a peak in the pulse height spectrum for 0 and 50 V APV (see fig. 4.25).

- Appears only in measurements, when the neutron beam was "on" before (status 5) (e.g., see appendix 6.9.4).

- Its intensity decreases from 0 to 50 V APV (e.g., see fig. 4.27b).

- It is only observed at -15 kV detector HV (see appendix 6.10.3): The mechanism might be influenced by the detector HV since it is not detected at -10 kV. Possible mechanisms (e.g., reduced field emission at -10 kV) were discussed in sect. 3.6.2.

- Clearly beam related. Its origin might be allocated below the AP since peak2 disappears for APV-settings $\geq$250 V.

- Decays exponentially with an average time constant c of 2-3 seconds for 50 V APV (see fig. 4.29).

- The long time constant indicates that the production mechanism is coupled with trapped secondary electrons and/or radiation induced electrons (e.g., (n,γ)-processes due to the collimation, see appendix 6.10.2). These electrons produce low energetic residual gas ions or interact by collisions with trapped protons.

- The observations of measurements at 780 V APV with reduced lower ExB-drift potential indicate, that the effect fluctuates non-statistically and appears randomly also when the neutron beam is "on" (see appendix 6.10.1).

A last remark should be made on the type of ions that may cause the two background peaks: $^1H^+$, $^4He^+$, $^{14}N^+$ and $^{16}O^+$ are possible candidates for residual gas ions. M. Simson calculated the energy loss of different residual gas ions in the detector at incident energy of 15 keV. Fig. 4.30 shows the results. Unfortunately these results are not conclusive [32]: Whereas protons or helium ions might be the constituents of peak 2 (ADC ch. 500 to 600), heavier residual gas ions, like oxygen and nitrogen, are expected only at pulse heights below 300 ADC ch, whereas peak1 shows up between ADC ch. 300 and 450.
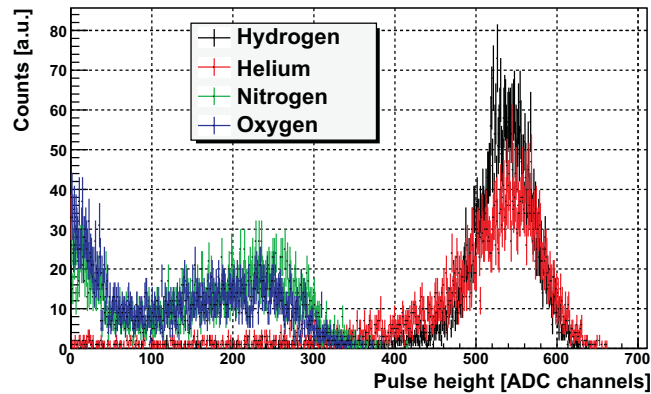
Figure 4.30: Spectra simulated by M. Simson for different residual gas ions hitting the detector with 15 keV kinetic energy. Picture courtesy of M. Simson [32].

For future beam times, I propose three independent measures for a further reduction of the impact of APV-dependent background on a: (1) The vacuum conditions in aSPECT should be further improved since the probability of residual gas ionization depends on the pressure (see sect. 3.6). For example, additional SAES getter pumps could be installed at the side-ports of aSPECT (see fig. 3.5). (2) A background study with reduced neutron beam width showed, that the production of both background peaks is clearly coupled to radiation induced secondary electrons (see appendix 6.10.2). Therefore, the width of the neutron beam should be reduced gradually below a size, where both background peaks disappear in the background spectra measured with neutron beam "off". This could be done by the implementation of a retractable diaphragm in front of the entrance window. (3) One should determine the lowest APV-setting, where the background peak2 disappears.

This APV should to be used as lowest APV-setting (instead of 50 V) in the measurement of the integral signal intensity as a function of the APV.

4.6 Integration limits of proton signal

In the next section, the selection of the upper and lower pulse height limit (so far chosen from ADC channel 80 to 1200) will be discussed. The dependence of the coefficient a on a variation of the upper limit (see sect. 4.6.1) and the lower limit (see sect. 4.6.2) will be investigated. As will be shown, an unexpected dependence on the lower integration limit was found that motivated studies on the detection efficiency (see sect. 4.7) and on time-of-flight/(TOF)-spectra (see sect. 4.8).

IMPORTANT NOTE:
All systematical dependences were investigated by performing a "blind analysis":
The routine that extracts the coefficient a from the integrated proton count rates
was manipulated/ cheated by a collaborator who was not involved in the data analysis.
The "cheat" algorithm stayed secret until the analysis was finished. The only known information
was, that the cheating does not change the way a behaves on the physical impact of parameter
manipulations. This means, that the relative errors are comparable:
$$\Delta a \approx \Delta a_{cheated}.$$
From this section on, first plots will be discussed that show the dependence of the
"uncheated" value of the coefficient a on various parameters. The values for a and the
error bars include only some systematic corrections: Dead time correction, subtraction of
background measured at 780 V APV and radiative corrections. The error bars are mainly statistical.
Further corrections are NOT included yet (e.g., edge effect correction, trigger efficiency, the
discussed corrections on APV-dependent background will be applied in chapter 5).

4.6.1 Upper integration limit

The right tail of the proton pulse height spectrum in fig. 4.31 is Gaussian distributed ($e^{(x-x_0)^2/2\sigma^2}$) with $x_0 \approx 550$ ADC ch. Therefore, a 4σ (99.994 %) limit for the upper integration limit can be chosen. σ can be defined via the FWHM:

$$\sigma \approx \frac{\text{FWHM}}{2.3548} \approx 34\,\text{ADC channels} \tag{4.3}$$

Thus, 4σ corresponds to 136 ADC channels which results in an upper limit of 686 ADC channels.
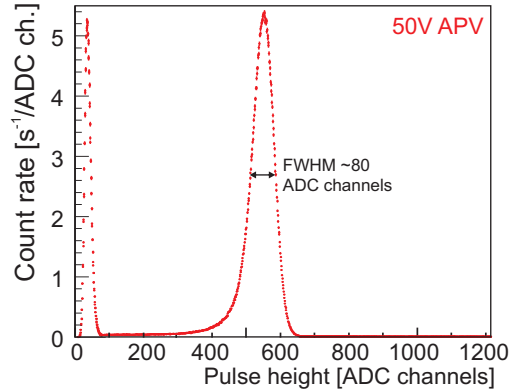
Figure 4.31: Pulse height spectrum measured at 50 V APV in data set "190508_night".

The proton spectrum (e.g., fig. 4.21(top)) however showed a "satellite" peak besides the right tail of the proton peak. It is only visible in logarithmic plot and by summing up several measurements for a given APV-setting. The peak is located between ADC ch. 675 and 850 (i.e., at pulse heights >686 ADC ch.). In addition, this peak shifts with the detector HV like the proton peak, too (e.g., see background study in appendix 6.10, fig. 6.33). Therefore the particles which may create such a peak must have positive electric charge. In the background measurements at 780 V APV with neutron beam "on" and for all APV-settings with neutron beam "off", no extra peak-like contributions are observed in that pulse height region.

The influence of the "satellite" peak on the extracted value of the coefficient a was studied: The lower integration limit was fixed to ADC ch. 80 and the upper integration limit was increased gradually above the region of interest (ADC ch. 500 to 1000). For each limit, the proton count rates were determined and a was extracted in a similar way as shown in fig. 4.13 (see sect. 4.3). Fig. 4.32 shows the result starting from an upper limit of 500 ADC channels up to 1000. The red points represent the values of a (corresponding to the left scale), the blue spectrum was inserted for orientation where the main peak ends and the "satellite" peak starts (right logarithmic scale).

The value of a varies by $\frac{\Delta a}{a} = \pm 0.30\%$ in the pulse height region of the "satellite" peak but stabilizes to higher limits (>850 ADC ch.). Efforts to explore the origin for that peak were partly successful: The measurements at a proton source presented in sect. 3.6.5 showed, that the position of the proton peak in the pulse height spectrum depends among others on the hit position of the proton on the detector. The integral spectra[8] extracted from the main proton peak and the "satellite" peak do not differ significantly. In sect. 4.7.2, a time-of-flight plot (fig.4.43) will be presented which also indicates that decay protons are the source of the "satellite" peak. To take pile-up events into account as discussed in sect. 4.2.1, the upper integration limit was finally fixed to ADC ch. 1200.

---

[8]Proton count rates integrated in the pulse height regions of the "satellite" peak and the main proton peak plotted vs. the APV-settings, e.g., see fig. 4.14.
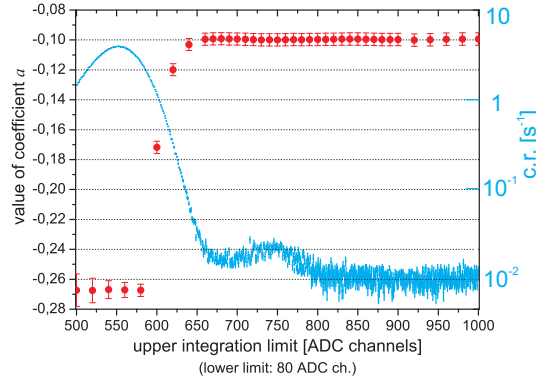
Figure 4.32: Values of the correlation coefficient a (red dots, corresponding to the left scale) extracted from data set "190508_night" by variation of the upper integration limit. The lower limit was fixed to 80 ADC channels. The blue points (corresponding to the right logarithmic scale) represent a cutout of the pulse height spectrum measured at 50 V APV with the "satellite" peak between ADC ch. 675 and 850. Obviously, a stabilizes above ADC ch. 660. The maximal variation between ADC ch. 750 (center of the "satellite" peak) to 1000 is $\frac{\Delta a}{a} = \pm 0.30\%$. Please note, that the error bars of the plotted a-values are strongly correlated!
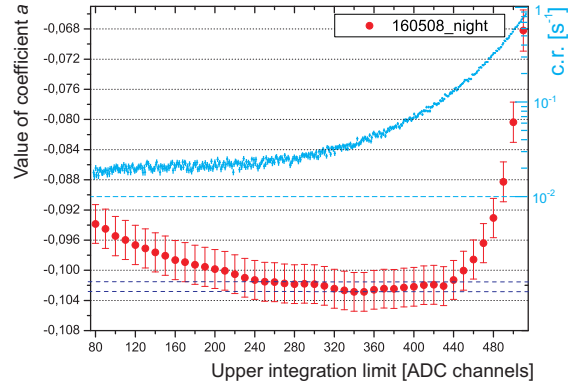
Figure 4.33: Values of the coefficient a extracted from data set "160508_night" by varying the lower integration limit (red dots, left scale). The upper limit was fixed to ADC ch. 1200. The relevant tail of the proton pulse height spectrum is plotted in blue (right scale).- The value of a seems to stabilize between ADC ch. 440 to 250 but increases strongly towards lower channels. The relative increase of a from ADC ch. 250 to 100 is $\frac{\Delta a}{a} = +6.4\%$. This region will be used as a reference for further comparisons with different data sets. The strong increase of a at the right side is explained by the dependence of the proton peak position on the applied APV. That is why the chosen upper and lower integration limits always have to cover the whole proton peak. Please note, that the error bars of the plotted a-values are strongly correlated!

4.6.2 Lower integration limit

Now, the coefficient a was extracted also for a fixed upper integration limit (to 1200 ADC channels) by gradually decreasing the lower integration limit from ADC ch. 80 to 540. The result is shown in fig. 4.33. The drift of a (red dots) to more positive values on the right side (>440 ADC ch.) was expected and can easily be understood: The position of the proton peak in the pulse height spectrum shifts due to the AP potential that cuts away the low energy part of the proton spectrum (see fig. 4.34a). For example, at 50 V
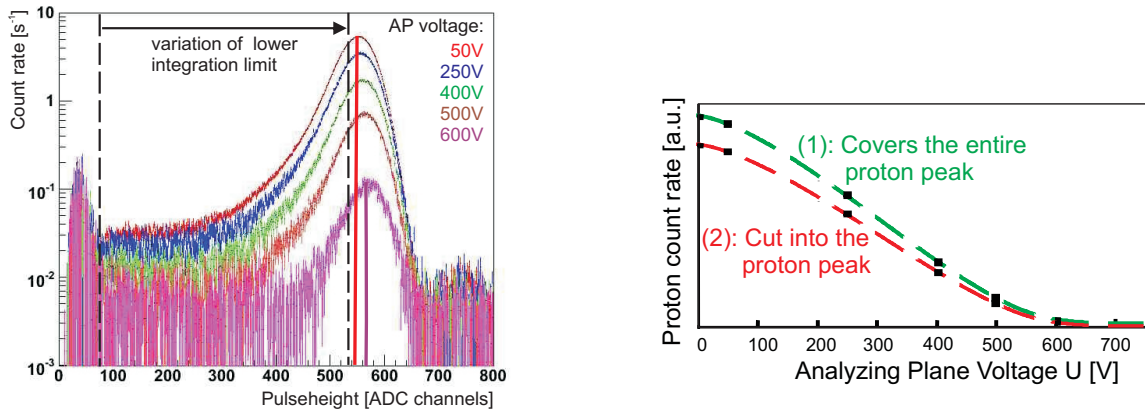
(a) Pulse height spectra after background sub-traction.

(b) Hypothetical integral spectra: Proton count rates vs. APV-settings.

Figure 4.34: (a) Pulse height spectra measured at different APV-settings (background measured at 780 V APV is subtracted). The red and purple lines mark the center of the proton peak at 50 V and 600 V APV, respectively. Due to the AP potential, the peak center shifts by 20 ADC ch. The blacked lines mark the region in which the lower integration limit was varied in the analysis. (b) Hypothetical integral spectra: The count rates in spectrum (1) are assumed to be extracted by integration over the whole proton peak. (2) shows a corresponding spectrum for an integration limit that might cut into the proton peak. The a-values extracted from both spectra would differ and a would be shifted to more positive values for spectrum (2).

APV and -15 kV detector HV, the protons' energy spectrum is distributed between 15.05 and 15.75 keV (peak center: 550±1 ADC channels), for an APV-setting of 600 V only between 15.6 and 15.75 keV (peak center: 570±2 ADC channels). Therefore, the center shifts to higher channels with higher APV-settings. This means, for integrations limits that cut in the proton peak, a different dependence of the proton count rate on the APV-settings is measured than for integration limits that cover the entire proton peak. For a fixed integration limit for all APV-settings, one cuts away more proton events for lower APV-settings than for higher ones.

Since the value of the coefficient a is extracted from integral spectra as shown in

fig. 4.34b by a fit, the pulse height cut results in an increased value of a (shifted to more positive values) compared to integration limits that cover the entire proton peak. Without an APV-dependence of the proton peak position one could chose arbitrary integration limits. M. Simson [32] used simulated spectral shapes for each APV-setting to calculate adapted integration limits and to correct the APV-dependent position of the proton peak. Fig. 4.35 shows the result of this correction (red points). The strong shift between ADC ch. 440 and 540 (see also fig. 4.33) can be corrected. The uncertainties of the correction increases the error of the coefficient a (e.g., clearly visible above ADC ch. 500).
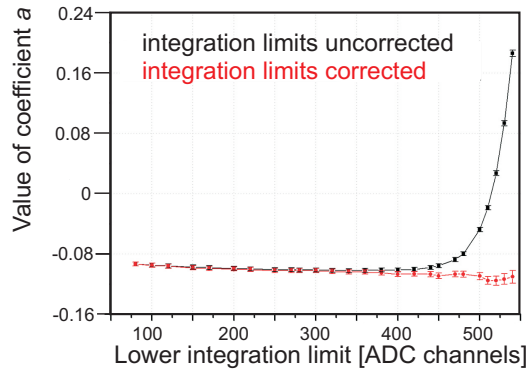
Figure 4.35: Dependence of the coefficient a on the lower integration limit. The red points are corrected values by M. Simson [32]. He calculated the spectral shape of the detected proton peak for different APV-settings and adapted the integration limits for each APV-setting. The uncertainties of these calculations increase the error of the coefficient a (e.g., clearly visible above ADC ch. 500). Obviously, the correction works in the central part of the peak. The increase on the left side is not affected. Picture courtesy of M. Simson [32].

But the strong shift of a for low pulse heights can not be explained by the shift of the proton spectrum: The relative increase of a from ADC ch. 250 to 100 is $\frac{\Delta a}{a} = 6.4\,\%$. An extraction of a only from the pulse height region of ADC ch. 100 to 250 (called a') results in a value of $a'_{100-250} = +0.414 \pm 0.046$. This value is far too high and must be generated by an additional mechanism that depends strongly on the APV. Although the amount of protons with low pulse heights is relatively small ($<2\%$), the high positive value of a' shifts clearly the value of a extracted in the integration limits ADC ch. 250 to 1200. This influence can be shown by a short calculation. The measured value of $a' = +0.414$ is used for the pulse height region ADC ch. 100 to 250 and the PDG-value $a_{DPG} = -0.103$ is assumed for the integration region ADC ch. 250 to 1200. A value of a for the complete pulse height region ADC ch. 100 to 1200 can be calculated via the following equation:

$$a = x \cdot a' + (1 - x) \cdot a_{PDG} \qquad (4.4)$$

a' and a_{PDG} are scaled by the relative amount of protons in the two pulse height regions (e.g., 1.5% and 98.5%). Using x=0.015, eq. 4.4 results in a=-0.095 which is about the

value we extracted from our measurement for a lower integration limit of ADC ch. 100 (see fig. 4.33).

APV-dependent background can be excluded as an explanation for the shift of the value of the coefficient a: The background spectra measured with neutron beam "off" showed no peak structure between ADC ch. 100 and 250. The measured background count rate was about $0.10(3)\,\mathrm{s}^{-1}$ and no APV-dependence was observed. This is far below the count rates necessary to explain a shift of $>6\%$ in a. For example, a loss[9] of $1.2\,\mathrm{s}^{-1}$ proton count rate at 50 V APV would be needed to induce such a shift.

Further investigations on the lower pulse height region were needed to figure out the reason for the shift of a: In the simulations done by M. Simson with SRIM [32], a discrepancy to the measured shape of the proton peak at lower ADC channels occurred. The measured count rates between ADC ch. 200 and 300 exceeded the simulations by about 40% for 50 V APV, i.e., $\approx 1.5\,\mathrm{s}^{-1}$. The enhancement of the detected count rates in the lower ADC channels was conspicuous. It is known that backscattering in the detector shifts proton signals to lower ADC channels in the pulse height spectrum. But even by changing the input parameters, which are used for the calculation of the backscattering process (e.g., thickness of the dead layer of the detector, proton impact angle and its energy distribution), in reasonable limits, the excess of measured count rates at low ADC channels could not be explained. Also the shift of the pulse height spectra observed at the edges of the detector (see sect. 3.6.5) is not sufficient as an explanation, since this edge area of the detector is negligible.

Finally, possible malfunctions of the trigger algorithm or effects of the detector response could give a reasonable explanation for the shift of a: In sect. 4.2.1, baseline drifts were briefly discussed which were observed directly after saturating electron events. It was figured out there, that the saturation effects could influence coincidence events: They reach the detector shortly separated in time with a minimal time difference of about 6 μs. This hypothesis can be tested by exclusion of coincidence events from the data analysis. I implemented an artificial dead time of 20 μs after each saturating electron event. This means, after a saturating electron pulse (pulse height >2500 ADC ch.), all pulses recorded within a time difference of 20 μs ("artificial dead time") are excluded from the pulse height spectra. These artificially modified pulse height spectra were used to determine the proton count rates for different lower integration limits. From the integral spectra the value of the coefficient a was extracted again. Fig. 4.36 shows that the shift of a between the lower integration limits ADC ch. 100 and 250 is reduced from $+6.4\%$ (blue squares) to $+1.5\%$ (red dots) for an artificial dead time of 20 μs. This result gives first evidence that the shift of a for lower ADC channels is influenced by the loss of coincidence events.

The next section focuses on investigations on the baseline drifts after saturating electron events. These analyses were done in collaboration with M. Simson [32]. A general

---

[9]i.e., an APV-dependent background component which is by $1.2\,\mathrm{s}^{-1}$ higher at 780 V APV than at 50 V APV must be subtracted.
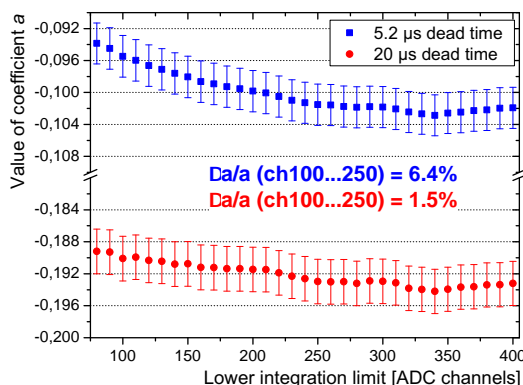
Figure 4.36: Impact of an artificially increased dead time on the dependence of the coefficient a on the lower integration limit (data set: "160508_night"). The application of $20\,\mu$s dead time reduces the relative shift between ADC ch. 100 and 250 from 6.4% (blue squares) to 1.5% (red dots). The exclusion of coincidence events (cut at $20\,\mu$s in the time-of-flight-spectrum, see sect. 4.8) means a strong cut in the proton spectrum and changes heavily the absolute value of a.

introduction to the impact of coincidence events and time-of-flight spectra will be handed in later in sect. 4.8.

4.7 Baseline drifts

As discussed in sect. 4.2.1, high energetic electrons which saturate the detector electronics (i.e, shaper and/or preamplifier board) create pulse shapes which show a plateau, followed by a tail towards the original baseline value. However, this baseline is not reached immediately. First, a baseline drift towards lower values is observed before the detector signal relaxes back to the original baseline value (see fig. 4.4b). Typically, the baseline height is at about 1500 ADC channels and can drop temporary to 1000 ADC channels after a saturating electron pulse (see fig. 4.8). When a coincidence proton pulse is detected shortly after the saturating electron pulse, there is a finite probability that it will be detected on the falling tail of the decaying electron pulse. Fig. 4.37 shows a typical example for coincidence events.

Although the pulse height of such events can be extracted by a pulse fit routine (see sect. 4.2.3), this behavior caused two effects that influence the result of our measurement:

(1) The on-line trigger efficiency of the sliding windows $w1$ and $w2$ (see fig. 3.26 for details on the trigger algorithm) is altered for protons sitting on the tail of a saturating
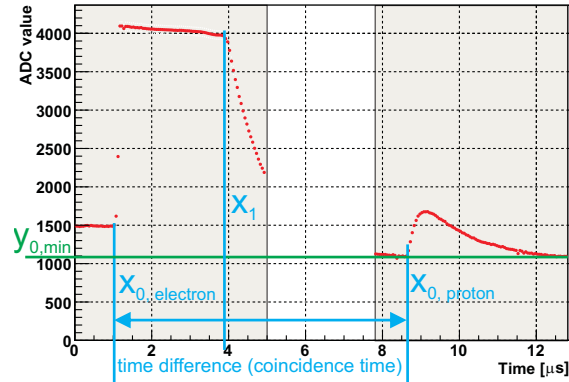
Figure 4.37: Saturating electron pulse followed by a coincidence proton pulse. The preceding electron event ($x_{0,electron}$=1 μs) saturates the detector electronics and is therefore cut off at a height of about 4000 ADC ch. The saturation ends at $x_1 \approx 3.8\mu$s. After the electron pulse, the baseline drops to about $y_{0,min}$=1100 ADC channels. The coincident proton pulse ($x_{0,proton}$=8.7 μs) sits on a lower and still drifting baseline. The time difference between the two pulses (called "coincidence time") is calculated from the rise parameter, x_0, of both pulses (7.7 μs) (see sect. 4.2.3).

electron pulse. Due to the baseline drift, the value of window $w1$ is shifted to higher values compared to the value at the position of window $w2$. As a result, a proton event will be lost if it has (a) a rather low pulse height and/ or (b) if the baseline drift and thus the shift between $w1$ and $w2$ is too high.

(2) A second effect was explored during the investigations on the trigger efficiency. It turned out that it makes the dominant impact: Pulse height spectra of coincident protons were extracted for different cuts in the coincidence time window. In the coincidence time interval of 8-15 μs (defined in fig. 4.37) after a saturating electron pulse, more proton events (relative) with low pulse heights were detected than in pulse height spectra at a longer time distance to the electron (see blue spectrum in fig. 4.38). Obviously, the saturation effects of the preceding electron pulse causes a reduced gain in signal amplification shortly afterwards (falling tail of the electron pulse) and thus shifts the proton spectrum to lower ADC channels. This explains also the discrepancy of the measured and simulated spectral shapes of the proton peak for low pulse heights (see end of sect. 4.6.1).

The coincidence time pulse height spectra in fig. 4.38 contain the evidence for both effects. All measurements at 50 V APV from data set "200508_night" entered. The background measured at 780 V APV was subtracted for each spectrum. The spectra were normalized to their count rates between pulse height 500 and 600 ADC ch. in order to study the deformation of the spectral shape. For events that were detected less than 8 μs after a saturating electron pulse (black symbols), almost no events with pulse heights below 200 ADC channels were detected. This is mainly due to effect (1), i.e., the alter-
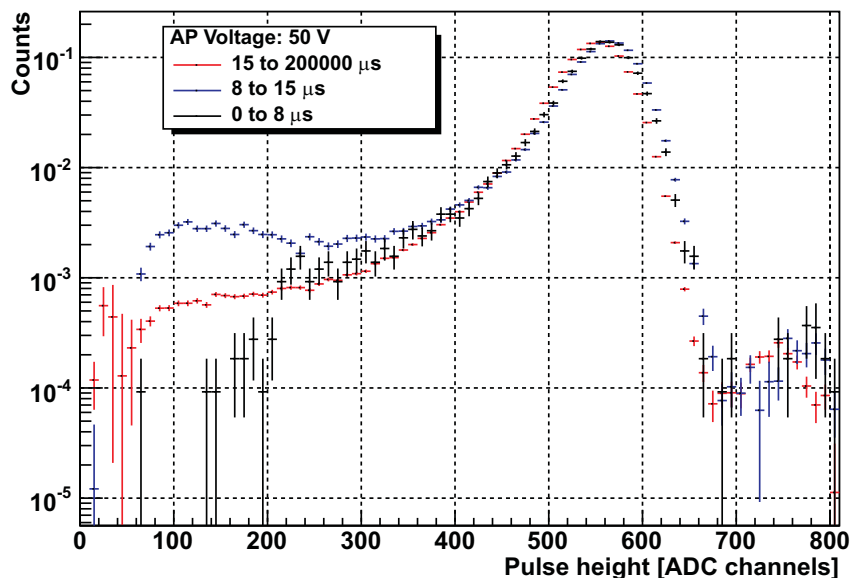
Figure 4.38: Pulse height spectra for protons detected in various time differences (defined in fig. 4.37) after a saturating electron pulse. The red spectrum contains proton events with time difference from $15\,\mu$s up to 0.2 s (i.e., also uncorrelated proton events). It represents the spectral shape as expected from simulations. The spectra are normalized to the region of 500 to 600 ADC channels to better focus on the changes in the spectral shape. The black spectrum (coincidence times up to $8\,\mu$s) provides evidence for the losses by effect (1), i.e., the trigger efficiency: Practically no events with pulse heights <200 ADC channels are detected. The blue spectrum mainly is influenced by effect (2): There is an excessive amount of proton events in the lower pulse height channels for protons detected 8-15 μs after a saturating electron pulse. The events are shifted from the main proton peak to lower channels. Some might be shifted as well below the electronic noise peak or stayed completely un-triggered. Effect (2) might also be effective for shorter time differences ($<8\,\mu$s) and increases the amount of lost particles for ADC ch. <200. Picture courtesy of M. Simson [32].

ation in the trigger efficiency. On the other hand, between 8 and 15 μs after a saturating electron pulse (blue symbols), there are more events with low pulse heights than in the spectrum for longer coincidence time (red symbols). The shape of the red spectrum is in accordance with the expectation from simulations done by M. Simson [32]. The effect (2) could also affect shorter time differences: Proton events would be shifted to lower pulse heights and get lost due to effect (1).

4.7.1 Trigger efficiency

The effect of the reduced trigger efficiency shortly after saturating electron pulses was simulated by M. Simson [32] with a program that creates artificial coincidence events of electrons and protons. The same trigger algorithm is applied to these artificial pulses, as it was done by the ADC-board in the experiment (see sect. 3.5.4). This method allows to freely choose the different parameters which are important for the trigger conditions. Besides the settings of the trigger algorithm, the parameters introduced in fig. 4.37 were used: The end point of the saturation x_1, the time difference between electron and proton pulse, the minimal baseline value $y_{0,min}$ of the tail after the saturating electron pulse as well as the pulse height of the proton. Moreover, artificial noise can be added to the signals to get a more realistic result. Fig. 4.39 shows two such events. In both pictures, the baseline drops to 1200 ADC channels, the saturation ends at x_1=4.25 μs and the pulse height of the proton was chosen to be 250 ADC channels. For the usual trigger settings with the sliding windows, the proton pulse would be triggered if it occurs 6 μs after the electron (a), but not if it occurs only 5.5 μs after the electron (b).

(a) Time difference 6.0 μs   (b) Time difference 5.5 μs
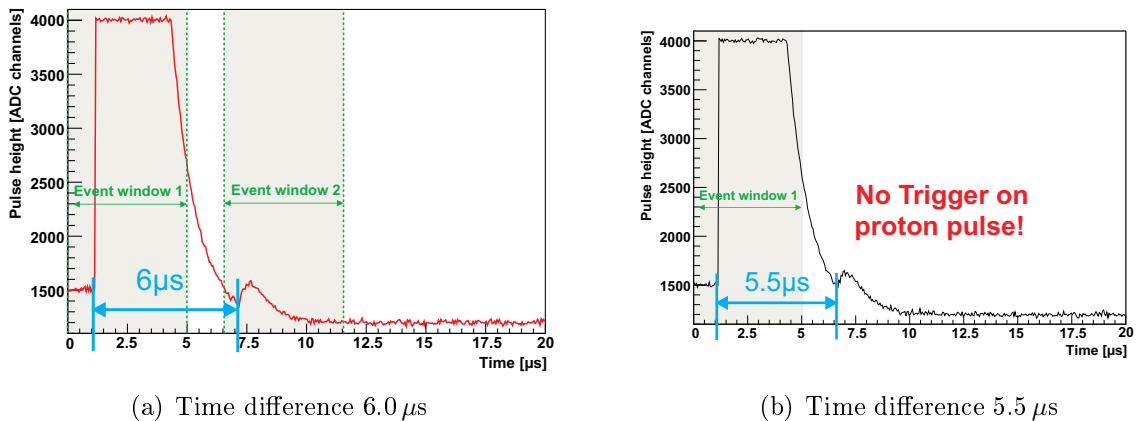
Figure 4.39: Two simulated coincidence events where the baseline drops after a saturating electron pulse to 1200 ADC ch. The proton sits on the tail of this pulse and was chosen to have a pulse height of 250 ADC ch. In case (a), the proton pulse is triggered 6 μs after the electron pulse. In case (b), the proton pulse is supposed to occur 5.5 μs after the electron pulse and is not triggered.

All contemplated parameters were varied within their physical limits to extract their functional impact on the trigger decision. As an example, fig. 4.40 shows the proton pulse height plotted vs. the time difference to the prior electron event. The baseline drift was set to ADC ch. 1000, which was the lowest measured baseline value (see fig. 4.8). 3 values for the end point of the saturation x_1 (4, 4.25 and 4.5 μs) were applied. The 3 colored areas allocate the lower trigger level for each value of x_1. The influence of the trigger efficiency on the coefficient a can now be estimated by using fig. 4.40: It tells if a proton pulse of a given pulse height that occurs in a defined coincidence time after a saturating electron pulse is detected or not. The coincidence time distribution[10] can be simulated and was measured: The spectra (discussed in detail in sect. 4.8) have an APV-dependent shape and intensity. They can be used in combination with fig. 4.40 to estimate the expected count rate loss for each APV (e.g., about $0.15\,\mathrm{s}^{-1}$ at 50 V APV). The losses are too small to explain the observed shift of the coefficient a. The trigger efficiency causes only a shift of $\frac{\Delta a}{a} \approx 0.2\,\%$ on the coefficient a.
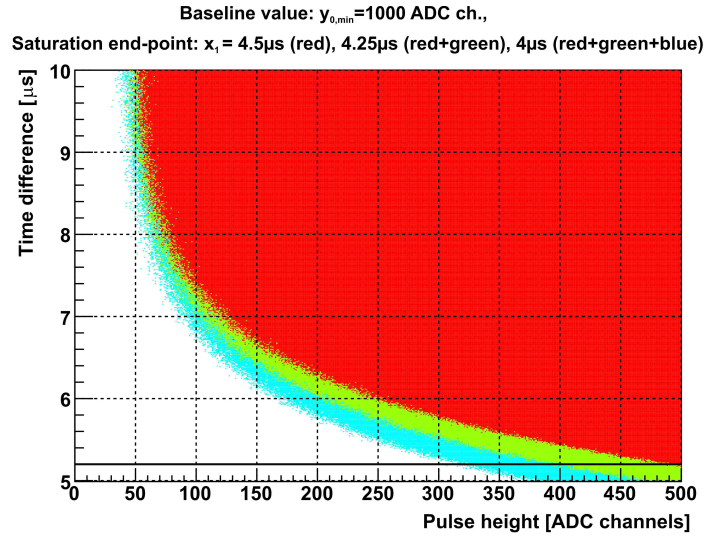
Figure 4.40: Relation of the proton pulse height and the time difference to a prior electron event for 3 saturation end points x_1 (4, 4.25 and 4.5 μs). The baseline drift was set to ADC ch. 1000, which was the lowest measured baseline value (see fig. 4.8). Protons belonging to the colored areas would be triggered, protons in the white area get lost: red area (x_1=4.5 μs), green+red area (x_1=4.25 μs), blue+green+red area (x_1=4 μs). Picture courtesy of M. Simson [32].

4.7.2 Saturation effects

As explained in sect. 3.5.3, detector signals are amplified, shaped and finally digitized. The cut-off of the events seen in the pulse shapes is due to a saturation of the shaper. But

---
[10]i.e., time difference vs. count rate.

for very high energetic events also the preamplifier may saturate. The principle is shown
in fig. 4.41: The original pulse given by the detector consists of a steep rising part with a
rise time of typically 150 ns and a long decay with a decay time of about 70 μs, (a). Hence,
any event that follows after a short time will sit on the shoulder of the previous pulse,
(b). If a first electron event deposits so much energy in the detector that the preamplifier
comes close to saturation, (c), the second event will drive the preamplifier into saturation
and thus the second peak will be cut off, (d). The shaper shortens the signal and is
mostly sensitive to the rising edge of the signal. The height of the pulse after the shaper
is proportional to the pulse height before the shaper, (e). After the shaper, the peak of
the second event will have a lower pulse height as well, (f). If the second pulse releases
the on-line trigger, the event would be recorded with a reduced pulse height of course.
Therefore, it might fall into the pulse height region of the electronic noise peak and could
get lost. If the second pulse falls below the pulse height threshold of the trigger it would
not be recorded at all.
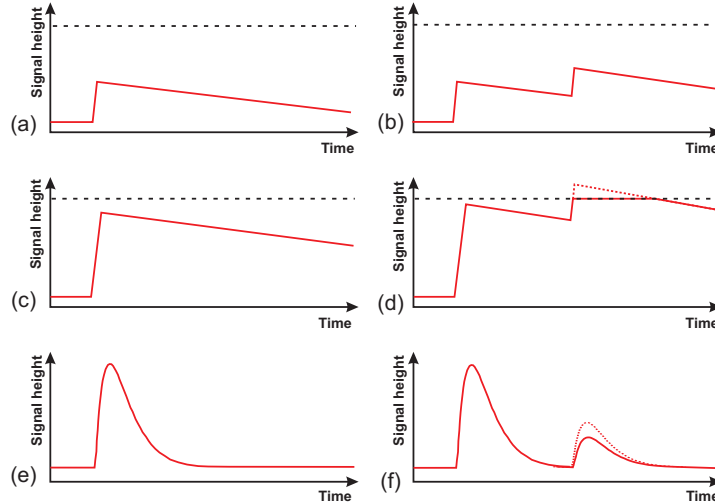
Figure 4.41: Scheme illustrating the preamplifier saturation. For explanations of (a)-(f),
see text.

The data analysis and simulations affirmed that the shift to lower pulse heights ap-
pears only after electrons that saturate the electronics for a finite time ($x_1 > 4\,\mu$s). This
fact is pointed out in fig. 4.42: The proton pulse height is plotted here vs. the satura-
tion end-point (x_1) of the prior electron event. For $x_1 < 1.6\mu$s nearly no coincidences were
found: The reason is, that triggered pulses rise around $x_0 \approx 1\mu$s and the pulse maximums
are distributed around $1.5\,\mu$s (see sect. 4.2.2). Mainly backscattered proton events belong
to region 1 because they deposit only part of their energy in the active detector layer
and thus give rise to lower pulse heights. Region 2 is obviously coupled to the saturation
end point x_1. Above a level of about $4\,\mu$s the distribution strongly distorts to lower pulse
heights. For $x_1 > 4.5\,\mu$s, nearly no pulses with low pulse heights < 400 ADC ch. are detected

anymore: Due to the saturation effects, the pulse height of the coincidence proton event was reduced below the trigger level and was lost in the data acquisition. In region 3 it
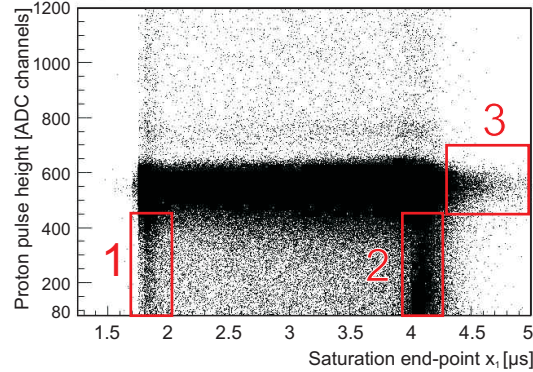
Figure 4.42: Data set: 160508_night, 50 V APV. The pulse height of the coincidence proton is plotted versus the measured saturation end-point of the preceding electron pulse.

looks like, as if electron pulses with a saturation end-point $x_1 > 4.5\,\mu$s correspond to coincidence proton pulses with pulse heights >400 ADC ch. This results mainly from an error induced by the analysis routine that produced this plot: First, the routine searches for an electron pulse (pulse height >2500 ADC ch.). Second, it searches for the next detected proton pulse (pulse height between ADC ch. 80 and 1200) and assigns it as "coincident" to the preceding electron pulse. If the coincidence proton was not detected due to the saturation effects, the next but one detected (uncorrelated) proton pulse is assigned by the analysis as "coincident". This generates the observed "false" coincidences in region 3.

Also the proton pulse height plotted vs. the coincidence time difference to the prior electron event in fig. 4.43 shows the behavior that was indicated by the time-cuts in fig. 4.38. Some more diagrams could be shown which all confirm the saturation effect of the preamplifier as assumed in fig. 4.41. A central conclusion on the loss mechanism should be memorized: **The saturation effect of the preamplifier shifts a fraction of coincidence proton events to lower pulse heights in the spectrum. Below a certain limit, which is defined by the trigger efficiency (see sect.4.7.1), the proton events get lost.**

4.7.3 Electronics test setup

M. Simson tested experimentally the behavior of the detector electronics ([32]). For that a waveform generator was used: The freely programmable waveform generated by this device was fed through the detector electronics and read out with an oscilloscope before and after the preamplifier as well as after the shaper.

(a) Full scale.   (b) Zoom.
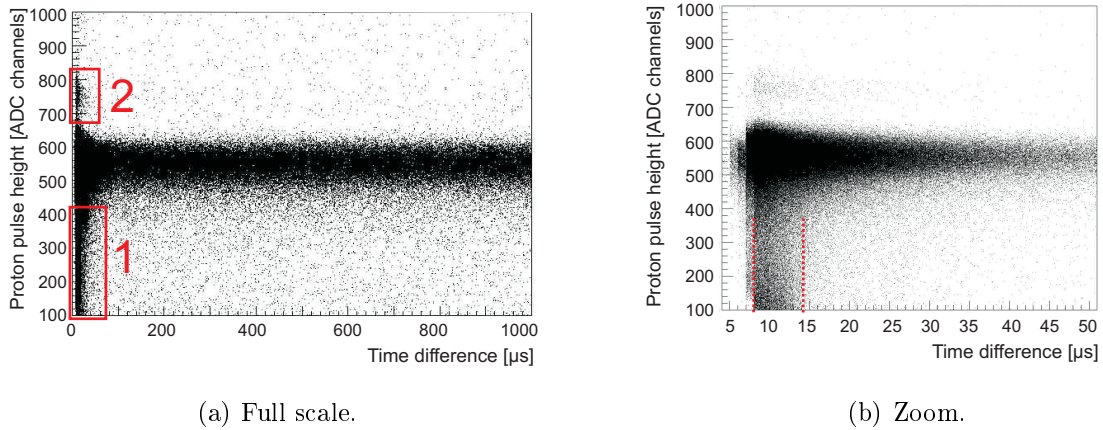
Figure 4.43: Data set: 160508_night, 50 V APV. Proton pulse height vs. time difference
to prior electron events. (a) Obviously, the main change in pulse heights co-
incides with time differences below 20 μs (region 1). Region 2 is marked as an
additional hint, that the "satellite" peak (see sect. 4.6.1) is due to decay pro-
tons. In (b), only the short time differences are picked out: The tail towards
lower pulse heights starts below 15 μs. The distribution from 8-15 μs for low
pulse heights (<400 ADC ch.) has a local maximum between ADC ch. 100
and 200. The loss of protons below 8 μs is visible again for low pulse heights.

To figure out the correct waveform, the detector was connected to the electronics
and the signals produced by cosmic rays were read out with the oscilloscope. Then, the
waveform of the generator was adjusted to reproduce the signals of the cosmic rays as
precise as possible. This is of crucial importance as the input waveform also determines the
shape of the signal after the shaper and thus influences the performance of the triggering
algorithm [32].

This waveform was used to investigate the effect of a high pulse followed by a low
pulse after a short time as shown in fig. 4.44. The results are presented in [32] and confirm
the assumed saturation behavior. A minimum kinetic energy of about T_e=400$\pm$20 [keV]
has to be deposited by the electron to saturate the preamplifier. Calculations showed that
only a small fraction of the electrons from neutron β-decay (maximum energy of about
780 keV) deposits more than 400 keV [32].

4.8 Coincidence events

At aSPECT, the fraction of decay electrons which are detected in coincidence with their
proton is small ($\approx$1/7). These electrons can be separated into two groups as shown by
the simplified schemes in fig. 4.45: (1) Electrons from the DV emitted into the upper
hemisphere of the spectrometer within a range of emission angles to the detector (called:
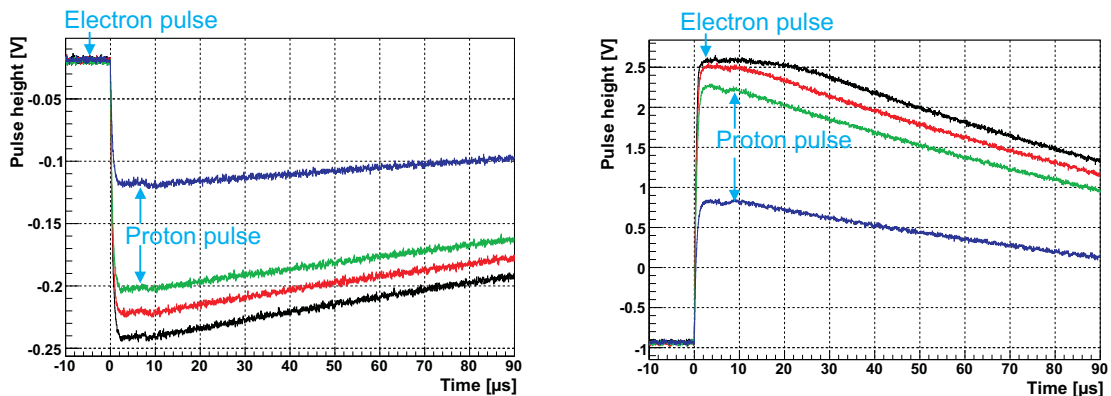
(a) Input signal of the waveform generator ("elec-
tron" pulse followed by a "proton" pulse).

(b) Corresponding signals after the preamplifier...
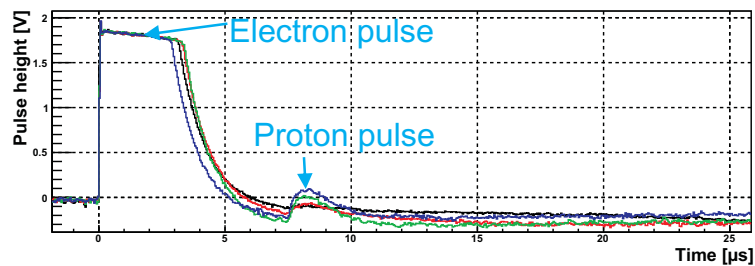
(c) ...and after the shaper.

Figure 4.44: A high, electron-like pulse followed by a low, proton-like pulse with a time difference of $7\,\mu$s. The graphs show the input waveform at different amplitudes (a), the waveforms after the preamplifier (b) and after the shaper (c). Please note the different time-scale in (c). The investigated behavior of the detector electronics corresponds to the proposed saturation scheme. In the case of short saturation (green and red curve) the proton pulse height is decreased. Above a certain limit of long saturation (black curve) the "proton" pulse disappears in (c). Picture courtesy of M. Simson [32].

"direct electrons"). About 14.7% of the total number of decay electrons belong to this first group (see [32]). According to simulations done by M. Simson [32], the finite detection efficiency for electrons reduces this amount by about 0.1% mainly due to backscattering from the detector. However, most of these electrons deposit enough energy in the detector and are detected. A count rate of $\approx 72 \pm 2\,\mathrm{s}^{-1}$ direct electrons can be approximated by calculations. (2) Electrons emitted into the lower hemisphere and which are reflected onto the detector (e.g., by reflection on the surface of electrodes or the bottom flange of aSPECT) (called: "backscattered electrons"). Their amount is difficult to predict but can theoretically be estimated to be up to 15% of the decay electrons as calculated by G. Konrad [30]. As it will be shown later, the angular and energy distribution of backscattered electrons can not be calculated yet with a sufficient accuracy to fit the measured

TOF-spectra. The experiment showed average electron count rates of 97.5 ± 0.8 $^{-1}$ (from ADC ch. 80 to 4000) for standard settings. This number is by 25.5 ± 2.2 $^{-1}$ higher than the estimated count rate for direct electrons (see above). This discrepancy confirms the incidence of backscattered electrons.
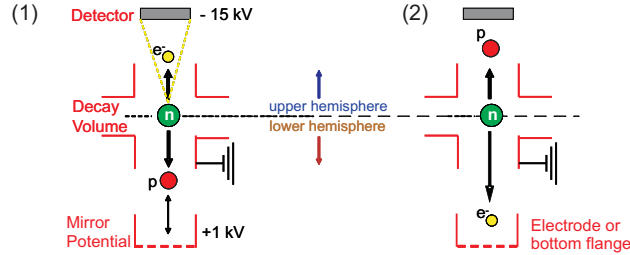
Figure 4.45: (1) Direct electrons, emitted into the upper hemisphere in a defined solid angle ($\approx 1/7$ of the decay electrons). One distinguishes three cases of coincidence proton events: (a) Most electron-proton coincidences belong to the case that protons are emitted to the lower hemisphere and are reflected by the ME. (b) The magnetic field gradient in the DV can reflect as well a minor amount of protons, i.e., those who are emitted almost $90°$ to the magnetic filed lines in the DV (see sect. 3.2.2 and fig. 6.37). (c) A small fraction of protons is emitted together with the electron into the upper hemisphere under a very steep angle. The initial angular and energy distributions of the coincidence decay electron and proton are theoretically known and can be used for simulations of TOF-spectra. (2) Backscattered electrons: The solid state potentials of the different materials (e.g., copper, gold, stainless steel) can backscatter electrons to the detector. The expected amount of electrons by these processes is hard to predict. Also the angular and energy distributions can not be calculated with a sufficient accuracy to fit the measured TOF-spectra.

Decay electrons, in general, have much higher energies than the decay protons (see fig. 2.4, left). Hence, the decay electron is always detected first. Compared to the flight time of the proton, the electron flight time is negligibly small. Therefore, the time difference between an electron and its coincidence proton is almost equivalent to the time of flight (TOF) of the proton from the DV to detector. The shortest TOF was calculated before the beam time to be about $6\,\mu$s. To avoid timing problems, the event size for a triggered event was set on $5\,\mu$s. Therefore, all correlated events should be detectable as separated, single events.

First, it should be defined how the TOF-spectra are extracted from the recorded data: The event that starts the TOF is an electron. Therefore we set as lower pulse height limit 1200 ADC ch. The second particle in coincidence is a proton. Thus all events in the PIW were used. The coincidence time difference is extracted from the difference of the rise time parameters x_0 as introduced in fig. 4.37. After an electron event was found in the

data file, the search algorithm looked for the coincident proton pulse. By doing so, the total amount of events in a TOF-spectrum reaches always the electron count rate. Due to the AP potential, not all electrons hitting the detector are detected together with their correlated proton. Uncorrelated events distribute the TOF-spectra for all time differences. Their average time difference is defined by Poisson statistics and comparably long. Their influence on the TOF-spectra is negligible for short time differences.
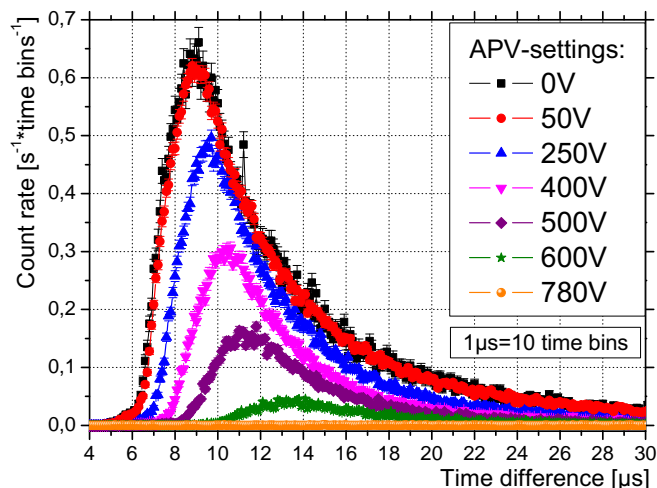
Figure 4.46: TOF-spectra for all APV-settings of data set "190508_night". The plots depict the distribution of time differences of proton events to prior, coincident electron events. The starting point of the TOF-spectra and the position of the maximum shifts with the APV to higher time differences. The amount of coincidence events decreases due to the AP potential.

In contrast to electrons, protons are retarded by the AP potential which has an essential impact on the TOF: At 50 V APV, the protons have shorter flight times than for 600 V as illustrated by fig. 4.46. Therefore, time dependent loss mechanisms, such as the observed saturation effects, have a stronger influence on 50 V APV measurements than on measurements at different APV-settings. This APV-dependent loss results in a shift of the coefficient a to more positive values as we observed it in sect. 4.6.2 (e.g., fig. 4.33).

Additionally, the settings of the ExB-drifts influence the trajectories and herewith the TOF of protons. Appendix 6.11 presents some details on the measured dependences of TOF-spectra on the main electrode settings (upper and lower ExB-settings and mirror voltage). A short overview will be given as well here: The drift potentials spatially separate coincidence protons from electrons. In some cases, coincidence events can get lost at the edges of the detector. Please note, that the total proton count rate for different ExB-settings stays nearly constant (see appendix 6.11, fig. 6.42): Although some coincident

protons get lost, some other (non-coincident) protons are shifted by the ExB-drift into the flux-tube and are detected instead. The separation of coincident pulses reduces the impact of the saturation effect on the coefficient a as shown in fig. 4.47: In the data set "160508_night" (see also in fig. 4.33) the upper ExB-settings were -3.7/-4.2 kV. This means, only a small drift potential was applied and the mean acceleration potential was about -4 keV. The coefficient a drifted by $\left|\frac{\Delta a}{a}\right|$=6.4% between lower integration limits of 100 to 250 ADC ch. Data set "180508_morning" was measured with higher upper ExB-settings of -4.2/-0.2 kV, i.e., a strong drift potential was applied and the mean acceleration potential was about -2 keV. This data set shows the smallest variation of a with the lower integration limit: $\left|\frac{\Delta a}{a}\right|$=3.7% (between 100 and 250 ADC ch.).
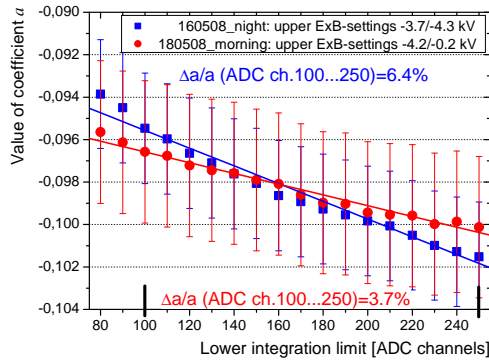
Figure 4.47: Dependence of the coefficient a on the lower integration limit for different settings of the upper ExB-voltages. Red points: -3.7/-4.2 kV. Drift of a between ADC ch. 100 and 250: $\left|\frac{\Delta a}{a}\right|$=6.4% (data set "160508_night"). Blue squares: -4.2/-0.2 kV. Drift of a between ADC ch. 100 and 250: $\left|\frac{\Delta a}{a}\right|$=3.7% (data set "180508_morning"). Obviously, the strong drift potential reduces the impact of the saturation effect.

In the sections 4.7 and 4.8, the APV-dependent loss effect was investigated that generates the observed dependence of a on the lower integration limit: **The time-dependent saturation effect of the preamplifier (see sect.4.7.2) shifts a fraction of coincidence proton events to lower pulse heights in the spectrum. Below a certain limit, which is defined by the trigger efficiency (see sect.4.7.1), the proton events get lost. This trigger efficiency depends strongly on the coincidence time. The APV-dependent TOF-distribution (see fig.4.46) induces an APV-dependent loss and shifts the value of a.**

4.9 Correction on saturation effects

The essential question is if the experimental data can be corrected afterwards in spite of the saturation effects. The idea is to reconstruct the amount of lost proton events from simulated TOF-spectra. First TOF-simulations were performed by G. Konrad for proton trajectories in the center of the flux-tube. They did not yet include the ExB-drift potentials and used averaged potentials instead. The results are shown in fig. 4.48. The simulated spectrum (blue) is normalized to the right tail of the measured spectrum (red). Deviations for the shortest time differences ($<7.5\mu$s) and for the maximum amplitude around 9μs are clearly visible and will be further discussed in this section. Latest, more sophisticated simulations will be part of the PhD thesis of G. Konrad [30].
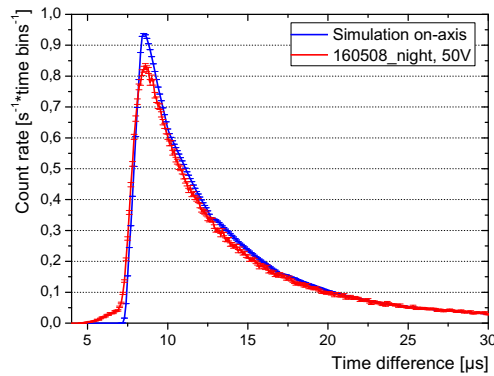
Figure 4.48: Comparison of first on-axis simulations with a measured TOF-spectrum for data set "160508_night". Because of the small lower (-200/ 0 V) and upper (-3.7/ -4.3 kV) ExB drift, it comes closest to the idealized conditions of the simulation which includes no drift potentials. The simulation is normalized to the right tail of the measurement. The deviations for short time differences ($<7.5\mu$s) and in the maximum of the spectra are clearly visible.

The saturation effects influence only coincidence proton events which occur within a certain coincidence time of up to $\approx 15\,\mu$s (see sect. 4.7) after a preceding saturating electron event. For higher coincidence times, the losses in the measured TOF-spectra (see sect. 4.8 and appendix 6.11) are negligibly small. A reconstruction of the actual proton count rates in our experiment is possible in three steps:

(1) Exclude all measured coincident proton events that were detected in coincidence times $<15\,\mu$s from the analysis (i.e., a cut in the TOF-spectra at $15\,\mu$s is performed).

(2) Extract the residual proton count rate (i.e., without the excluded coincidence protons) from pulse height spectra.

(3) Extract the count rate of coincidence proton events up to $15\,\mu$s coincidence time from simulated TOF-spectra.

The steps (1) and (2) can easily be implemented. For step (3), the initial angular- and energy-distributions in the DV of decay electrons and protons are requested. The main type of coincidences (type (1)a in fig. 4.45) in our experiment belong to "direct" electrons emitted into the upper hemisphere towards the detector and protons emitted into the lower hemisphere. Those protons are reflected by the electrostatic mirror electrode towards the detector. For this type of coincidences, the initial angular and energy distributions of the involved electrons and protons are known (e.g., see fig. 4.49). These distributions are used to answer several important questions for the reconstruction of the measured TOF-spectra:

(a) Which decay electrons are detected in coincidence to their decay proton? This means, how is the angular and energy distribution of the electrons correlated to the angular and energy distribution of the protons? The angular and energy distribution of the protons is needed to calculate the influence of the transmission function on the detected (APV-dependent) proton count rate.

(b) What is the angular and energy distribution of protons that coincide with decay electrons that saturate the preamplifier (an energy deposition of ≥ 400 keV was approximated by M. Simson [32] as a lower limit for the saturation of the preamplifier by decay electrons)?

Fig. 4.49 depicts theoretical Dalitz plots calculated by G. Konrad [30]. Obviously, these plots show the strong systematic dependence between the angular and energy distributions of decay electrons and decay protons: (a) shows how the initial kinetic energies of decay electrons and decay protons are coupled in aSPECT. (b) shows the coherence between the initial polar angles of electrons and protons (in the DV). (c) shows the coherence between the electron energy and the time difference to the coincidence proton for 0 V APV and (d) for 400 V APV.

The same questions have to be answered for backscattered electrons which are detected in coincidence with their proton (type (2) in fig. 4.45). Their angular- and energy-distribution is hard to predict. And the accurate count rate of backscattered electrons is not known as well. A count rate of $25.5 \pm 2.2\,\mathrm{s}^{-1}$ was estimated in sect. 4.8 (see also the TOF-spectra of backscattered electrons in appendix 6.11.2). The backscattering probability of electrons is strongly energy dependent. For example, it can have values between 40% (for low electron energies) and 25% (for high electron energies) at the surface of the grid electrode (e1) (see fig. 3.1) as calculations by G. Konrad show [30]. Electrons are backscattered on different materials (e.g., stain-less steel, copper, gold) in aSPECT, which possess different backscattering probabilities. Therefore, the accuracy of the TOF-simulations is critically limited by the insufficient knowledge of the energy and angular distribution of backscattered electrons.

More informations on backscattered electron events can be achieved by an additional analysis of the dependence of the coefficient a on coincidence proton events. The idea
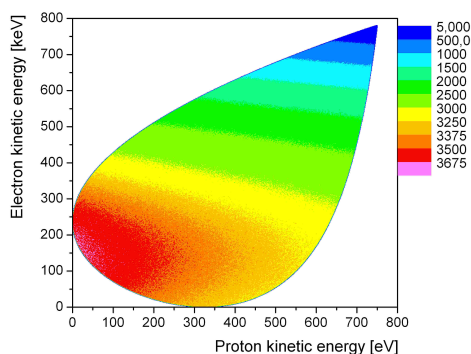
(a) Energy dependence.
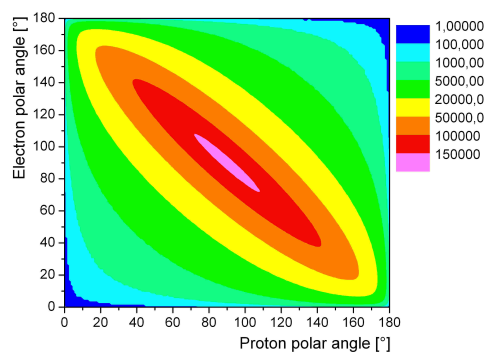
(b) Polar angle dependence.
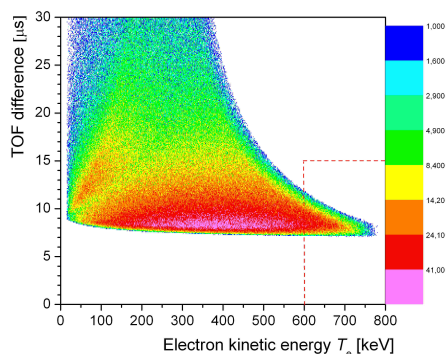
(c) T_e vs. TOF, 0 V APV.
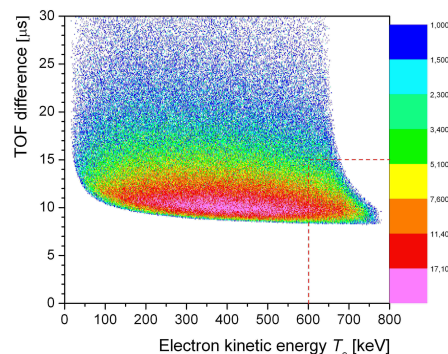
(d) T_e vs. TOF, 400 V APV.

Figure 4.49: (a) and (b) Dalitz plots for electron and proton kinetic energies and polar angles, respectively. (c) and (d) show the coherence of the proton coincidence time difference with the kinetic energy of the electron (T_e) for 0 V and 400 V APV. This dependence varies with the APV. These plots show clearly the necessity to know the energy- and angular-distribution of backscattered electrons to be able to derive the energy- and angular-distribution of coincidence protons. Picture courtesy of G. Konrad [30]

is to exclude step-wise coincidence proton events from the determination of the proton count rates which are used to extract a. For example, all coincidence proton events (pulse heights between 80 to 1200 ADC ch.) which were detected after a preceding electron event (pulse height $>$1200 ADC ch.)[11] in a coincidence time interval 0 to 8 μs, 0 to 10 μs, 0 to 12 μs... are excluded. The exclusion can be done by assigning an artificial dead time of 8μs, 10μs, 12μs... to each electron event (i.e., even if a proton event was detected in the measurement in this time span, it will be rejected in the analysis). The increasing artificial dead time increases the amount of coincidence protons which are excluded from the count rate determination. Since the backscattered electrons affect the measured TOF-spectra, they will as well affect the dependence of a on coincidence proton events.

The analysis can be subdivided in five main steps:
(1) Extraction of the dead time (coincidence time) dependence of a for different lower integration limits (e.g., 80, 300, 400 ADC ch.) for different parameter settings (ExB-settings, detector HV, etc.) from the measured data.
(2) Simulation of TOF-spectra that contain only coincidence protons which correspond to direct electrons. The dead time dependence induced by these spectra is different to the measured influence on a in step 1.
(3) Backscattered electrons are included in the simulation of TOF-spectra: Different possible (but hypothetical) angular and energy distributions are applied. The amount of backscattered electrons is also varied.
(4) Different energetic limits (e.g., 400 keV, 600 keV, etc.) for saturating electrons are applied to step 2 and 3. The simulations are done as well for the same lower integration limits and parameter settings as applied in the measurements in step 1.
(5) The parameters in analysis step 3 and 4 have to be adapted in a way, that the simulated and measured dependences of a on coincidence proton events are in accordance.

I took responsibility for the analysis of the measured dead time dependences (step 1). The simulations (step 2-5) were done by G. Konrad [30]. Fig. 4.50 shows a result for data set "200508_night". Fig. 4.50a/b show the absolute dependence of the coefficient a (y-axis) on an artificial dead time (x-axis). Fig. 4.50c shows the relative dependence $\frac{\Delta a}{a}$, normalized to a dead time of 5.2 μs (as defined in sect. 3.6.5)[12].

Fig. 4.51 presents similar plots for different data sets measured with the same upper and lower ExB-settings: Both show the dependence of the relative error $\frac{\Delta a}{a}$ on an artificial dead time between 0 to 30 μs. Fig. 4.51a for a lower integration limit of 80 ADC ch. and fig. 4.51b for a lower integration limit of 300 ADC ch. The dependences of these data

---

[11]The precise energetic limit for saturation of the preamplifier by electrons is not known yet. The proposed energy limit is easier to reconstruct in the simulation.

[12]Please note, that the data points in the plots of fig. 4.50 to fig. 4.51 are strongly correlated to each other: For a fixed lower integration limit, the data sets are only reduced by a certain amount of events with increasing dead time. This means, that the data points for different integration limits (80, 300, 400 ADC ch.) contain to some amount the same events at a given dead time. Therefore, overlapping error bars are not an evidence of equality.
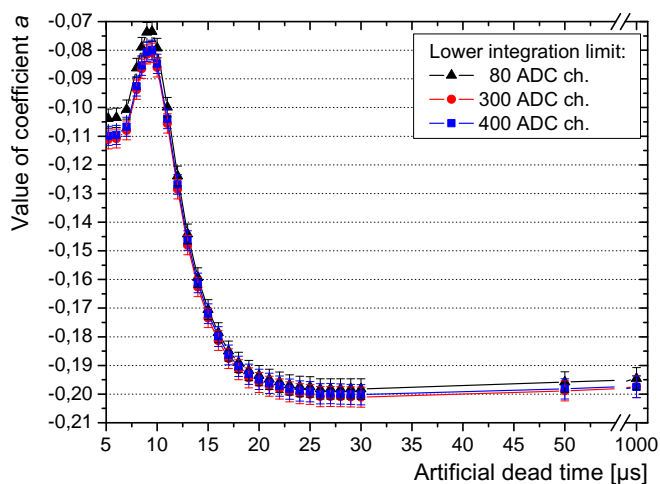
(a) Absolute dependence.
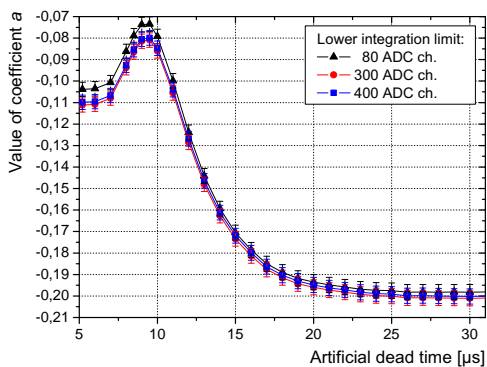
(b) Absolute dependence, zoom.
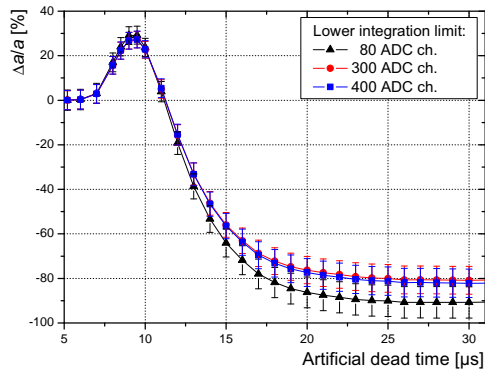
(c) Relative dependence, zoom.

Figure 4.50: Data set: "200508_night": (a) Absolute dependence of a on an artificial dead time after electrons for 3 lower integration limits. The dependence on the dead time can be explained by cuts in the energy and angular distribution of the decay protons. (b)/(c) Zoom to the absolute and relative dependences.

sets are comparable within their error bars. The analysis of measurements with different ExB-settings shows slightly different dependences.
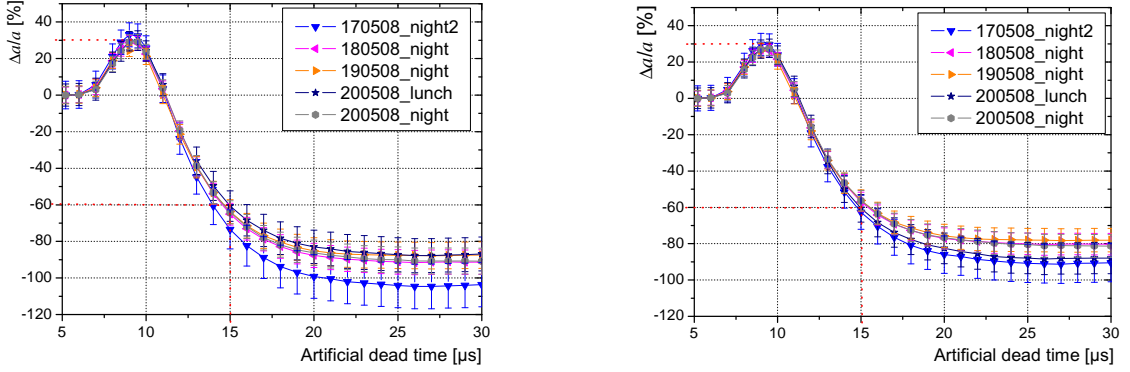
(a) Lower limit 80.

(b) Lower Limit 300.

Figure 4.51: Dependence of $\frac{\Delta a}{a}$ on an artificial dead time after electrons for data sets with same parameter settings: upper ExB -2/-2 kV, lower ExB -1000/-50 V.

Calculations done by G. Konrad [30] result in curves which show a comparable behavior (see fig. 4.52). Their shapes depend strongly on the input parameters:
(1) The amount of backscattered electrons.
(2) The energy and angular distribution of backscattered electrons.
(3) The correlated distributions of the coincidence protons.
(4) The lower energetic limit for the saturation of the preamplifier by decay electrons.
(5) The influence by parameter settings, e.g., the ExB-settings and the detector HV.
Several combinations of these input parameters have comparable results. And the dependences extracted from measurements with different ExB-settings (5) can not be reconstructed yet by using the same input parameters (1) to (4). Obviously, it was not possible to restrict the input parameters of the simulation sufficiently by the dependences extracted from the measured data sets. Thus, the amount of coincidence proton events which were lost by the saturation effects could not be reliably reconstructed.

An upper and a lower limit for the error induced by the saturation effects can be extracted from the measured dependences for lower integration limits of 80 ADC channels (e.g., see fig. 4.51a): The saturation effects influence coincidence events with coincidence times up to 15 μs. The average dependence $\frac{\Delta a}{a}$ (for all data sets with standard parameter settings) varies between $+30\%$ (around 9 μs) and -60% (around 15 μs). These are the upper and lower limits if all coincidence events up to a given coincidence time would have got lost in our experiment. In reality, the impact will be smaller (in this limits) since only a small fraction of coincidence proton events was lost in the measurement. However, we did not succeed in characterizing the saturation effects quantitatively. Therefore, we can
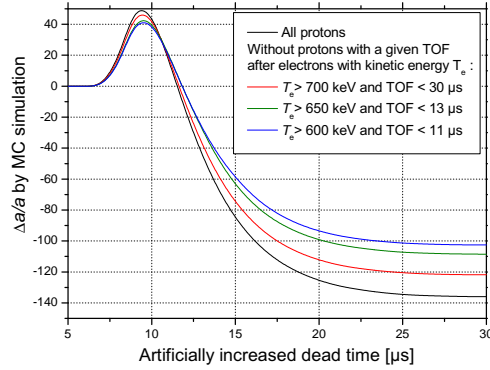
Figure 4.52: Example for calculated dependencies on an artificial dead time. Apart from the electron kinetic energy T_e and the time difference between electron and proton, other parameters like the amount of backscattered electrons and their angular and energetic distribution can be varied. Picture courtesy of G. Konrad [30].

neither correct the influence of this effect on the coefficient a nor give a reliable error. The destructive impact of the saturation effects frustrated our aim to extract the coefficient a with an error $\frac{\delta a}{a} < 2\%$.

For future beam times, the saturation effects can be suppressed by progressive reduction of the amplification of the detector electronics. The amplitudes of high energetic electrons have to be decreased below the saturation limit.

4.10 Magnetic field tests

4.10.1 Different ratio r_B

An additional magnetic field was applied in data set "200508_night" in order to test the influence of a changed magnetic field ratio r_B on a. With external Helmholtz coils c12/c13 (see sect. 3.2.2) the field in the AP was slightly increased. The ratio was changed from $r_B = 0.2030(1)$ to $r_B = 0.2049(1)$. Fig. 4.53 shows a comparison with data set "200508_lunch" measured at $r_B = 0.2030(1)$. Both data sets give the same result on a within the statistical errors. Analyzing the data set "200508_night" with the standard value of $r_B = 0.203$ instead, the value of the coefficient a differs by about 12 % from the data set "200508_lunch". The comparison shows, that the impact of r_B on the calculated transmission function is understood and that the way, how a is extracted, is reliable.
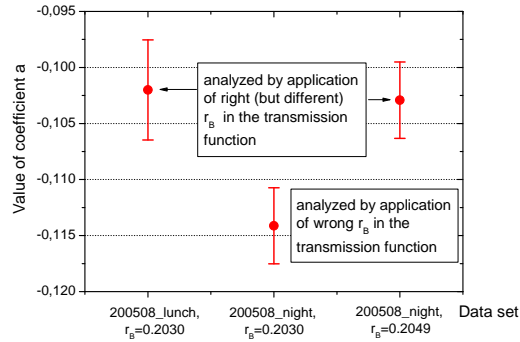
Figure 4.53: Influence of the magnetic field ratio r_B on a: By analyzing the data set "200508_night" with the standard value of $r_B = 0.2030(1)$ the a-value differs by about 12 % from the data set "200508_lunch". Applying the right ratio $r_B = 0.2049(1)$ the a-values are consistent within their statistical error bars.

4.10.2 Reduced main field (non-adiabatic effects)

A measurement with a reduced magnetic field was performed in order to study non-adiabatic effects. In data set "210508_night" the current in the superconducting coils was set to 30 A instead of 70 A. The field value obtained were typically $B_0 \approx 0.933$ T in the DV and $B_A \approx 0.189$ T in the AP. It was calculated in [22] that the reduced field strength will increase the uncertainty in a to $\frac{\delta a}{a} > 4 \cdot 10^{-3}$ (see tab. 3.4) due to the fact that the adiabatic approximation does no longer hold. The a-value extracted from the measurement is a=-0.070(4). From the preceding measurement "200508_lunch" (at standard magnetic field strength) a value a=-0.100(4) was extracted. This means a shift of $\frac{\Delta a}{a} > 3 \cdot 10^{-1}$ induced by the reduced magnetic field strength. It should be noted that the imaging of the beam profile in the DV onto the detector changes as well by reducing the magnetic field strength. Therefore the edge effect correction might have a stronger impact. Obviously, the influence by non-adiabatic proton motions is stronger for 30 A main current as previously calculated in [22] (see tab. 3.4). Thus, new calculations are recommended to clarify the discrepancy.

5 Summary and conclusion

During this PhD thesis, the neutron decay spectrometer aSPECT was completed and initially tested in Mainz. First data was taken in beam times from July 2005 to end of May 2006 at the Forschungsneutronenquelle Heinz Maier-Leibnitz (FRM II) which resulted in various modifications and technical improvements from May 2006 to November 2007. In December 2007, aSPECT was set up at the Institut Laue-Langevin in Grenoble/ France. The goal was to achieve an increased accuracy of the angular correlation coefficient a compared to existing results, i.e., $\frac{\delta a}{a} < 5\%$.

Experimental improvements of the ILL beam time in 2008 were made: We managed to reduce the background count rate by a factor of 5 to 10 (see sect. 4.5). Its destructive influence on the extracted value of the coefficient a was as well resolved. Furthermore, the background components could be systematically studied and two peaks with different characteristics (APV-dependence) were discovered. The filling and emptying of traps and the nature of the two background peaks were investigated on several studies (see appendix 6.10).

Unfortunately, saturation effects (see sect. 4.7) induced by high energetic decay electrons prevented us to extract a value for the coefficient a with a reduced absolute error (compared to previous measurements, [2] and [3]). These effects influenced the detection probability of certain electron-proton coincidence events. The effects depended on the coincidence time and influenced the trigger efficiency (see sect. 4.7.1). The impact of these effects was investigated (sect. 4.7.2 and sect. 4.8) but could not be corrected in the off-line data analysis (see sect. 4.9). Therefore, I could only extract upper and lower limits for the impact of the saturation effects on a. These limits were extracted from measured data sets (e.g., see fig. 4.51) in combination with simulations done by G. Konrad [30]. The relative errors are $+30\% \leq \frac{\delta a}{a} \leq$ -60%. Further simulations are required to extract reliable error limits which are lower. These simulations are on-going and will probably be part of the PhD thesis of G. Konrad [30]. Nevertheless, the limit of $\frac{\delta a}{a} < 5\%$ cannot be reached.

Tab. 5.1 lists the impact of the systematic effects on the coefficient a which were investigated in my thesis. The theses of my collaborators G. Konrad [30], M. Simson [32] and F. Ayala [31] will include additional details: For example, [30] presents further simulations concerning a theoretical correction of the saturation effect with respect to backscattering and the TOF-spectra. Particle trajectory calculations will be included as well for an edge effect correction. The 3-dimensional neutron beam profiles (see sect. 3.4.3) are used in this calculations in combination with the magnetic field map. The analysis of

Type of correction	Relative correction $\frac{\Delta a}{a}$ [%]	Relative error $\frac{\delta a}{a}$ [%]
(1) Magnetic field ratio r_b	-	< 0.37
(2) Potentials U_0, U_A	-	< 1.1
(3) Dead time	< 4	< 0.04
(4) Average Background 1 (lin.)	-1.14	0.30
(5) Average Background 2 (exp.)	+2.07	0.31
(6) Proton simulation	0.13	0.09
(7) Saturation effects	$^{+30}_{-60}$	$^{+30}_{-60}$
(8) Edge effect	calculations ongoing (see [30])	calculations ongoing (see [30])

Table 5.1: Summary of relative shifts $\frac{\Delta a}{a}$ and errors $\frac{\delta a}{a}$ by systematic effects and the applied corrections. The destructive influence of the saturation effects is dominant. Remarks on (1): Worst case approximation which is calculated from the error of the averaged value of r_B (see sect. 3.6.1). On (2): Limit estimated for potential variations of 150 meV. This work function differences was measured along the surface of a test electrode. On (3): Depends on the total count rate. On (4) and (5): See sect. 4.5. On (6): Correction done by M. Simson [32] on expected protons (due to backscattering) below the integration limit of 80 ADC ch. The error bar is dominated by the statistics of the proton simulations and thus can be lowered. On (8): I approximated the impact on a to be $<1.2\%$ by using a model developed by G.Konrad in 2007: The neutron beam profile in the DV is projected onto the x-axis (2-dimensional). The slope of the proton density distribution along the detector edges is used to estimate the edge effect. The variance of the transmission function due to the variance of r_B along the beam width (in DV and AP) is also included in this approximation. But the influence of the ExB drift electrodes was not included in this calculations. Therefore, 3-dimensional calculations are required to calculate the edge effect with high accuracy. These 3-dimensional calculations are on-going and will be part of the PhD thesis of G. Konrad [30].

different magnetic field measurements is part of [31]. Simulations and detector effects are presented in [32].

To give a preliminary value for the coefficient a, its lower integration limit dependence has to be taken into account: (a) For a lower integration limit ADC ch. 80, and (b) for an intermediate lower limit ADC ch. 300. Both are influenced by the observed saturation effects and the investigated background peaks. The correction for both background peaks is applied and the resulting a-values for data sets are presented in fig. 5.1a and b.
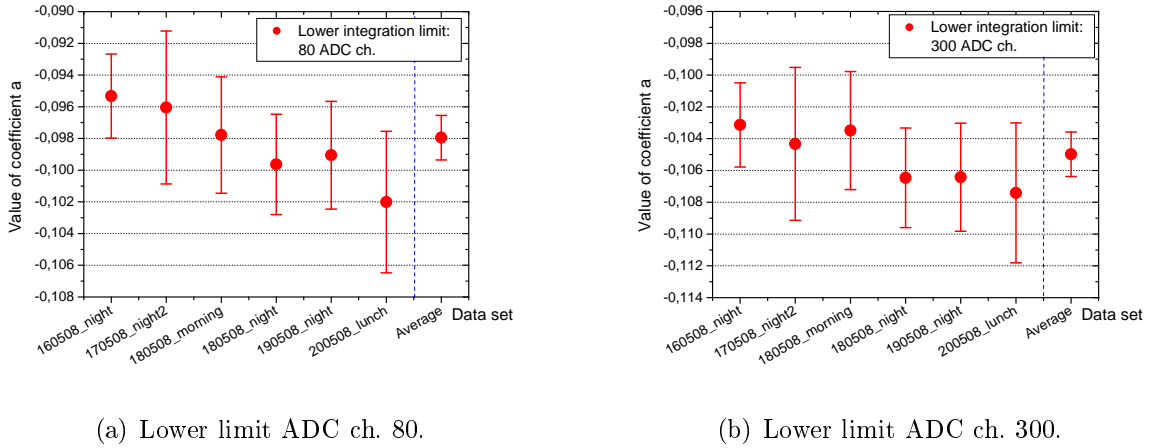
(a) Lower limit ADC ch. 80.

(b) Lower limit ADC ch. 300.

Figure 5.1: Values for the coefficient a extracted for different integration limits. The averaged value is shown on the right side (beyond the dashed blue line). The error limits extracted for the saturation effects are not included in these plots.

The averaged values for the angular correlation coefficient a are:

$$a = -0.0980 \pm 0.0014^{\text{(stat.)}} {}^{+0.0316,\,\text{(syst.)}}_{-0.0610,\,\text{(syst.)}}; \text{ lower limit}: \text{ 80 ADC ch.} \tag{5.1}$$

$$a = -0.1050 \pm 0.0014^{\text{(stat.)}} {}^{+0.0338,\,\text{(syst.)}}_{-0.0657,\,\text{(syst.)}}; \text{ lower limit}: \text{ 300 ADC ch.} \tag{5.2}$$

Please note, that the edge effect correction is not included in the given systematical errors. The influence of the saturation effects are worst case scenarios. They might be calculated in [30] and [31] to be well below the values given here. The statistical error is in the region of $\frac{\Delta a}{a} \approx 1.4\,\%$ and can easily be reduced below $1\,\%$ in the next beam time. More beam time could be scheduled on measurements with standard parameter settings and a less time on systematics.

After a long time of strong efforts on finding a way how to correct the dependence of a on the lower integration limit, our collaboration decided to perform another measurement in 2011. To stop the proton losses due to saturation effects, gain factors of the preamplifier have to be reduced such that a detector electronics does not saturate even for high energy electron pulses. Tests with generated pulses could be done in advance to study the proper

functioning of the detector [32]. By preventing these effects, also the knowledge on the distribution of backscattered electrons is not necessarily needed anymore.

Of course, the reduced amplification will affect the pulse heights of proton events and therefore the separation from noise. But the amount of protons expected in the low energetic tail of the proton peak should not critically change a as calculated in tab. 5.1, (6).

From the background analysis (see sect. 4.5), I drew several conclusions for future beam times: (1) Longer measurements with closed shutter are necessary to study the APV-dependence of the background peaks, especially of peak1. In addition, the lowest APV-setting has to be determined from which on peak2 disappears. This limit should be used instead of the lowest APV-setting of 50 V used before to fit the spectral intensity. Therefore, the DAQ-cycle (see fig. 4.1 has to be adapted (measurement times and APV-sequences). (2) Generally, the vacuum conditions should be further improved since all background effects are strongly correlated to the residual gas pressures. Possible modifications will help to reduce the pressure, e.g., additional SAES getter pumps, which could be mounted at one of the side ports of aSPECT.

6 Appendix

6.1 Appendix 1: Pumping and cooling procedure

For achieving UHV conditions, we generally start pumping with two 40 liters roughing pumps for some hours until the pressure reaches about 10^{-1} mbar in the main vacuum section. Presuming no vacuum leaks, continuing pumping with two turbo molecular pumps for about six days provides at least a pressure better than 10^{-7} mbar. One of the pumps is directly installed on top of aSPECT and can be separated from the main vacuum section by a CF150 gate valve to be able to install the detector mechanics later on. The other one (CF100) is mounted to a side port of aSPECT at the end of a 1 m CF150 tube. It can be separated by a CF100 gate valve. By four internal getter pumps (SAES Getters "CapaciTorr D400-2"), the vacuum is decreased furthermore to 6×10^{-8} mbar. The insulating vacuum that surrounds the superconducting coils and thermally insulates the main vacuum from external heat load, has to be pumped with a roughing pump and a small turbo pump until it reaches a value of about 5×10^{-3} mbar before starting to cool the magnet.

The spectrometer is cooled by liquid helium which is compressed and pumped by two cryocoolers (Sumitomo RDK408D). Each cryocooler has a cooling power of 35 W at the first stage (about 70 K) and 1 W at the second stage (about 4.2 K). The temperatures at the different stages are controlled by 20 sensors which are continuously but successively read out. The walls of the inner bore tube are cooled down to about 60 K. After cooling, the pressure decreased to $<5 \times 10^{-4}$ mbar in the insulating vacuum and to 8×10^{-9} mbar in the main vacuum.

A complete cool down cycle takes about 5 days. By using in addition liquid nitrogen in the first 36 hours of cooling, the total time can be reduced to 3.5 days. A tube that spirals around the superconducting coils inside the insulating vacuum is used to introduce the nitrogen. The in- and outlets (KF16 flanges) are on top of the magnet. When the temperature of liquid nitrogen is reached, this tube has to be evacuated to a pressure in the order of 10^{-2} mbar. Warming up lasts between 2 days (in an emergency case by filling in several times warm nitrogen gas in the vacuum system) and 7 days (under normal warm up conditions).
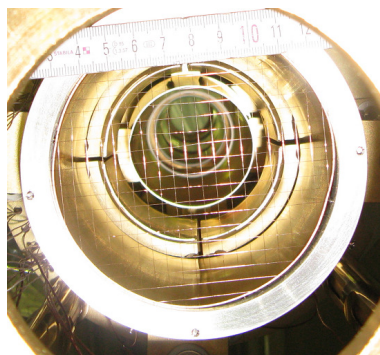
Figure 6.1: Grid electrode on the bottom side of the ME (e1). It is winded by μm^2 copper wire and has a grid distance of 5 mm.

6.2 Appendix 2: Additional pictures of the setup
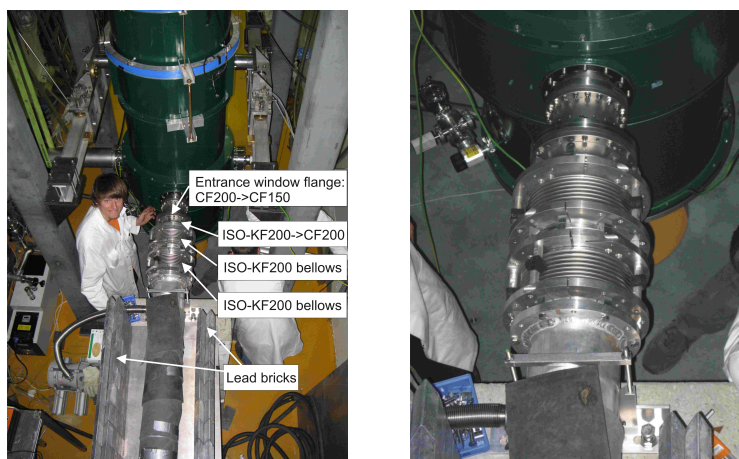
(a) Overview.

(b) The bellows for alignment.

Figure 6.2: The vacuum system of the beamline at the entrance side of aSPECT with 2 ISO-KF200 bellows for alignment (and transitions to CF150).

(a) Boron shielding.

(b) Lead shielding.
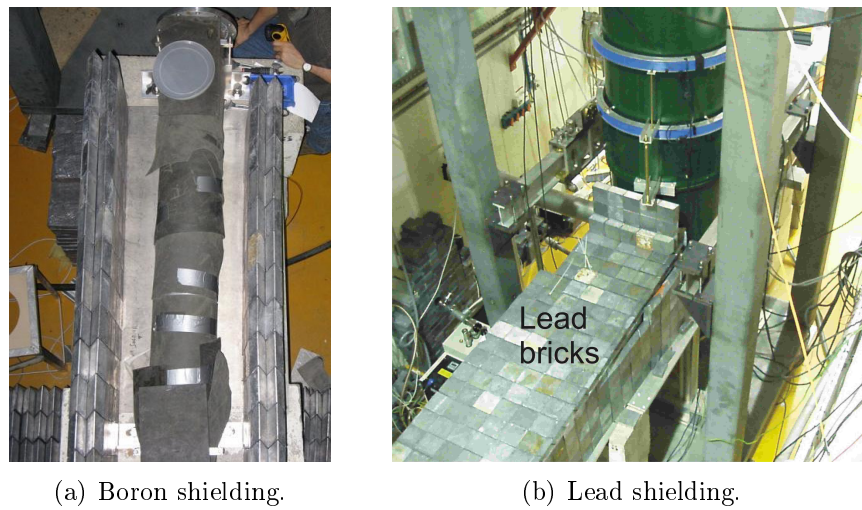
Figure 6.3: Radiation shielding at the entrance side of the beam line.

(a) The exit window.

(b) The unshielded beamdumb box.
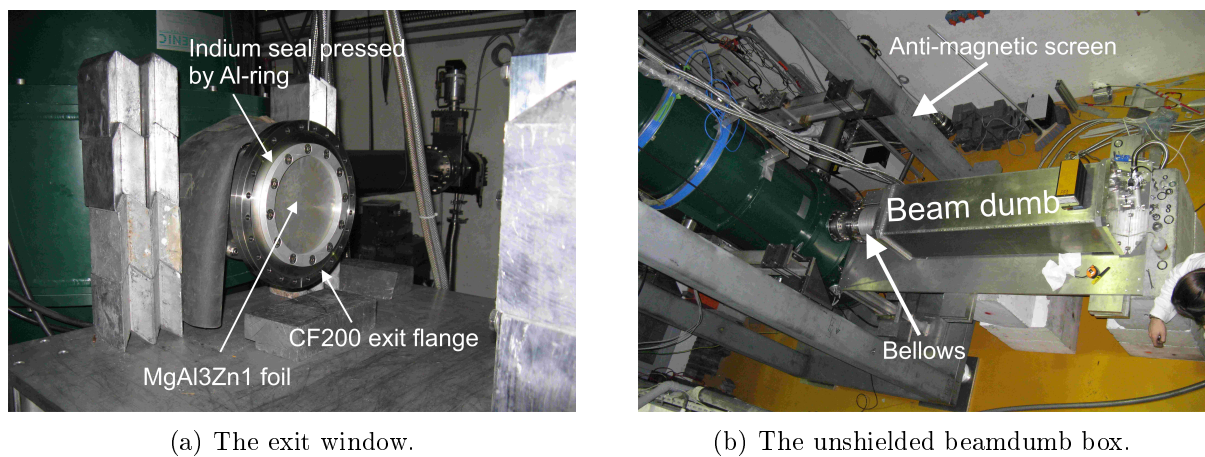
Figure 6.4: Exit side of the aSPECT-Setup at PF1B.
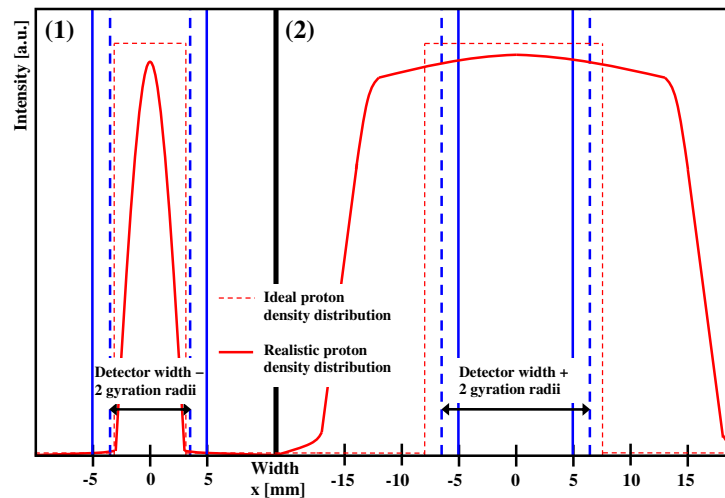
Figure 6.5: Illustration of the two theoretical concepts for reducing the detector´s edge effect. Concept (1) makes an edge effect correction dispensable but the count rate is reduced critically. Concept (2) was favoured in our experiment. The ideal profiles would imply the absence of convergence.

6.3 Appendix 3: Concepts for the neutron collimation.

An essential demand on the collimation system was only introduced generally: The shape of the neutron density distribution in the DV should limit the impact of edge effects which occur at electrodes and at the detector borders (see sect. 3.6.3). Two general strategies, illustrated in fig. 6.5, exist for the reduction of these effects:

(1) Limitation of the beam width to a small size: All decay protons emitted inside the DV are imaged onto the proton detector.

- Advantages:

(a) Corrections due to a non-symmetric neutron distribution are negligible.

(b) The risk of activation of the spectrometer walls is minimized.

(c) The knowledge about the neutron distribution in the DV and therefore the needed precision of its determinations is of minor importance.

- Disadvantage: Loss of count rate that results in

(a) reduced achievable statistical accuracy in the available time.

(b) reduced signal-to-noise-ratio (SNR) especially for higher barrier voltages and therefore reduced systematical accuracy.

(2) Expansion of the beam to a maximum width to provide a beam profile that is maximally homogeneous and symmetric but with a sharp drop down at the sides.

- Advantage: Gain of count rate that results in

(a) better statistical accuracy achievable in the available time.

(b) better SNR and increased systematical accuracy.

- Disadvantages:
(a) Precise knowledge of the neutron density distribution in the DV required for correction of remaining edge effects.
(b) Risk of activation is higher and increased radiative background.

The width of the used SDD-detector (10 mm per pad) was the critical criteria to choose option (2) because the expected proton count rate for a narrow beam would have been to low for performing systematic tests with high statistical accuracy.

6.4 Appendix 4: Alignment of aSPECT

The technical realization of the essential components of the beam line was discussed in sect. 3.4.2. Now, I want to complete this description by an overview of the alignment procedure: Each diaphragm has its predefined position on the beam axis but is itself mechanically coupled to the vacuum system (e.g., the beamline inside of aSPECT). Since the distance from the end of the neutron guide to the center of the DV is about 3.2 meters, a misalignment by 0.1° would cause a theoretical shift of 5 mm in the DV. The pre-collimation limits the extent of this shift by reducing the beam directly in front of the entrance window. The alignment requires seven steps:

1st step: Alignment of the beam tube behind the neutron guide by a laser (rough) and a theodolith (fine). The position and height of the theodolith were adjusted by a laser diode which is permanently mounted on the backside wall of the experimental zone of PF1B. It is pointing onto the center of the neutron guide.
2nd step: Alignment of the diaphragms P0 and P1 inside that beam tube by using the theodolith.
3rd step: Mechanical adjustment of the spectrometer inside the antimagnetic screen by setting up uniform distances to the four pillars.
4th step: Alignment of the beam ports of aSPECT relative to P1. Therefore, the entire antimagnetic screen has to be moved by four air-cushions[1] since the overall weight of about 11 tons exceeds the approved load of the crane. The height is corrected by shimming with aluminum plates below the feet. For angular alignment the theodolith is used.
5th step: Alignment of the internal diaphragms E1 to A2.
6th step: Magnetic adjustment of the spectrometer inside its antimagnetic screen: This is an important procedure because of the forces that are effective between the superconducting coils and the solid iron parts (pillars and plates) of the antimagnetic screen. An insufficient adjustment could result either in an uncorrectable distortion of the magnetic field shape inside the spectrometer or in the worst case in a breakaway of coils. The design of the antimagnetic screen and the construction of a support capable of three-dimensional adjustment and fixation was part of the PhD thesis of G. Konrad [30]. Various magnetic field measurements confirmed that the field distortion by the antimagnetic screen is not critical if a magnetic adjustment is proceeded. While the magnetic adjustment, the spectrometer is in operation mode hanging on a crane inside the screen. By slowly increasing the magnetic field strength the spectrometer intents to move out of the center which is defined by the maximum of the magnetic forces to all pillars. By using the provided stoppers for x-y-movement the position of the force maximum can be localized. The best height can easily be determined by a balance hanging between the spectrometer and the crane. In addition to the stoppers at the support the spectrometer is fixed in position by blocks around its top. The spectrometer

---

[1]Supplied by 10 bar of compressed air. Thanks to the PERKEO-collaboration!

position after the magnetic adjustment was comparable to the pre-positioning in the 3rd step. Frequently controls during the beam time verified the concept of the fixations. It should be remarked, that it would be better to accomplish the 6th step before the 4th one. But this means to warm up and to vent the magnet in order to have access to the diaphragms. In combination with re-evacuation and re-cooling this procedure takes in minimum 10 days. Time forced us to change the order and to hazard the consequences of possible misalignment for the beam time in December 2007. In January 2007 we opened the magnet for small reconstructions and controlled the internal collimation. The traces of neutron absorption on the LiF (see fig. 3.15) showed that the alignment had been effective.

7th step: Alignment of the beamstop with the laser diode.
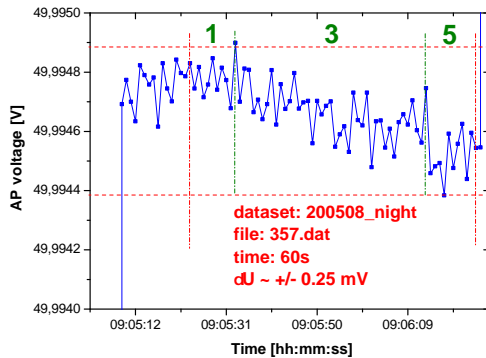
(a) 50 V.
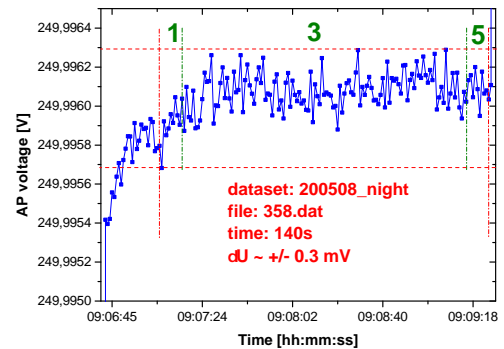
(b) 250 V.
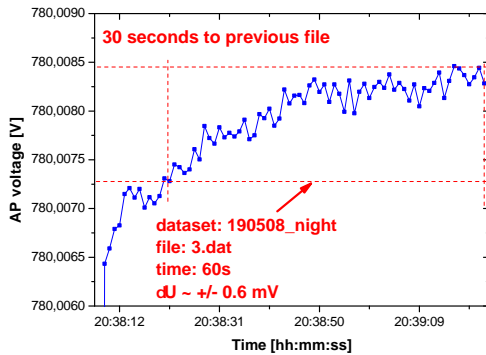
(c) 780 V for 30 s ramping time.
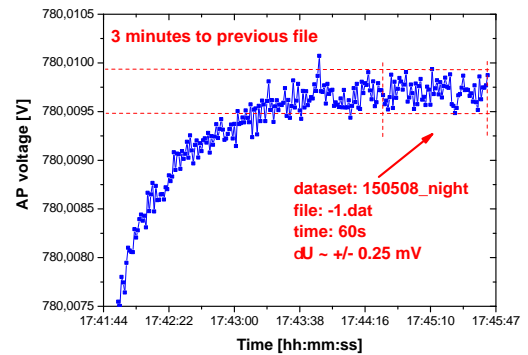
(d) 780 V for 30 s ramping time +150 s waiting time.

Figure 6.6: Ramping of the APV. Plots (c) and (d) are taken from different datasets and show the increased stability for 780 V APV after longer waiting time.

6.5 Appendix 5: Ramping of AP potential

The time for ramping the APV took 30 to 40 s. The speed depended on the voltage difference to the foregoing APV-setting. The process consisted of four steps: A rough ramping in about 8 s to 97-99 % of the selected APV, 5 s exposure time. Afterwards, 10-12 s of slowly ramping to the selected voltage and 5-17 s for stabilization. The voltage fluctuations were in the order of $< \pm 1$ mV which is below the absolute calibration of the multimeter. Measurements with longer waiting time after ramping (fig. 6.6c and d) showed that the APV still stabilizes for some minutes. Nevertheless, the achieved level of APV-stability after ≈ 30 s total ramping time is acceptable since other effects limit our accuracy. Fig. 6.6 shows several ramping processes to give an impression on the stability.
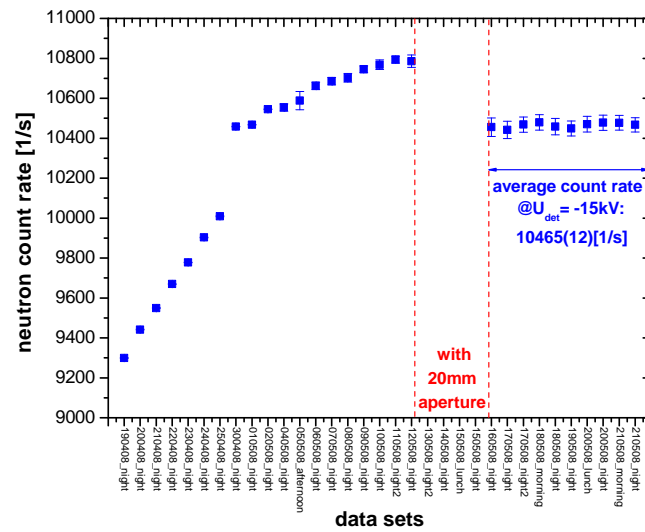
Figure 6.7: Instabilities of the neutron counter in the beginning of the beam time and its stabilization in the end. Three days of measurements with a reduced beam width (20 mm) are excluded since the total neutron intensity was reduced hereby and is not comparable.

6.6 Appendix 6: Neutron count rates for entire beam time

Fig. 6.7 and fig. 6.8 show the drift of the neutron counter (in the beginning of the beam time) which is uncorrelated to the reactor power monitored by the ILL. Although the count rates look stable from the 16th of May on, it was found that the counter can not be used for normalization of the proton count rates.
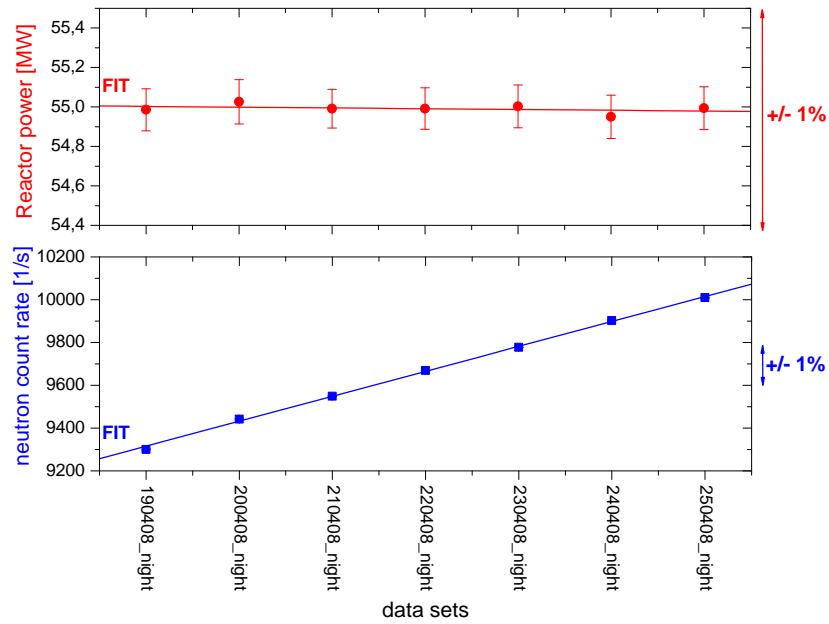
(a) Period of highest drift from 19th to 25th of April.
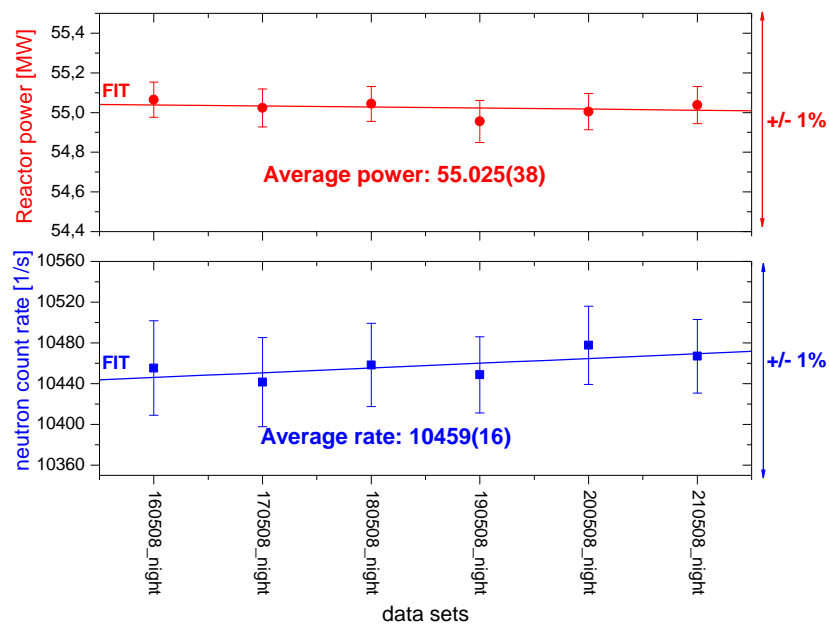
(b) More stable conditions from 16th to 21st of May.

Figure 6.8: Drifts of the neutron counter in the beginning (+1.4% per day) (a) and the end (b) of the beam time in comparison to the reactor power monitored by the ILL.

6.7 Appendix 7: Pulse height extraction methods

Method 1) Method of FRM-II beam time: The baseline is averaged in the first 15 time bins of an event. The parameter $HistMax$ is used as the amplitude of the pulses ($ph = HistMax - y_0$).

Method 2) This method uses several additional conditions to extract the pulse height only of the event that released the trigger. Therefore, the proposed dead time correction can be used with this method. The baseline is determined from time bim 10 to 15 and the maximum of the pulse between time bin 20 and 35 is extracted. For proton events shortly in time after saturating electrons, the determination of the baseline and the pulse maximum is shifted to lower time bins. The method and all required conditions are implemented in the function "PH()" (used by "PH_File()" and "PH Day()") and is embedded in the C^{++}-routine "mbo2.C".

Status	Description
0	events with good χ^2
1	events with bad χ^2 and $ph_{fit} \geq 80$
2	events with bad χ^2 and $ph_{fit} < 80$
3	high energy events
4	fit failed
5	refitted status 1 events
6	refitted status 2 events
7	events with different shape

Table 6.1: Overview of the different fit states.

6.8 Appendix 8: The pulse fit routine

This introduction to the fit routine is mainly taken from [32] by courtesy of M. Simson: According to the fit result, all events are classified as different types. Tab. 6.1 gives an overview of the different fit states.

Only non-saturating events (ADC value < 3500 before time bin 30) are fitted, the others are assigned as status 3. The exact pulse height of status 3 events is of minor importance in the data analysis since they are energetically well separated from the proton peak. Events where the fit did not converge are assigned status 4, events with converging fits are classified according to their pulse height and the χ^2 of the fit. Events with $\chi^2/(ph_{fit} \cdot NDF) < 0.00741$, with NDF being the number of degrees of freedom of the fit, get status 0. If the fit result has a bad χ^2 (e.g., $\chi^2/(ph_{fit} \cdot NDF) \geq 0.00741$) the event is classified according to its pulse height: Noise events ($ph_{fit} < 80$ ADC ch.) are status 2, the other events are status 1. Some examples for status 1 events are shown in fig. 6.9, status 2 events in fig. 6.10. Electronic malfunctions and bugs as in fig. 6.9b should be excluded from pulse height spectra but still taken into account for dead time calculation. Pulses with status 1 and 2 are fitted again to extract for example pile-up events and other incorrectly sorted events. Pulses with status 4 (fit not converged) are fitted again with the improved fit routine of ROOT and, if the fit still does not converge, the pulse is re-binned to even out short spikes in the electronic noise and re-fitted. With this technique practically all events can be fitted. The improved fit routine of ROOT uses the integral values of the fit function instead of the value at the centre of the bin. This method gives more precise results but needs more computing time.

Unfortunately not all events are sorted correctly by the standard fit routine. Especially in two cases events are sorted as status 1 or 2, although they are valid proton events:

- *Pile-up events:* When two proton pulses arise close to each other the fit does not work,
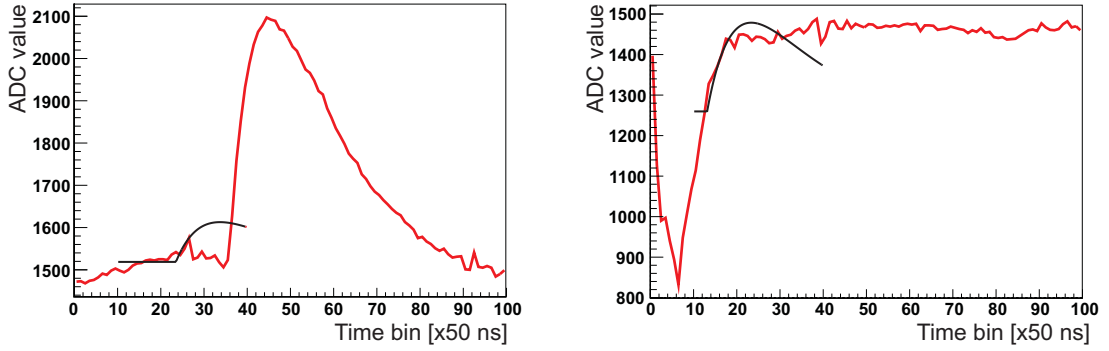
(a) Event 3045: $ph_{fit} = 94.1$ ADC ch., $ph_{nofit} =$ 594.6 ADC ch.

(b) Event 16866: $ph_{fit} = 219.0$ ADC ch., $ph_{nofit} = 394.1$ ADC ch.

Figure 6.9: Fit status 1 events. (a) shows an event where the trigger was caused by electronic noise followed by a proton pulse. (b) shows an examples for an unclassifiable event.
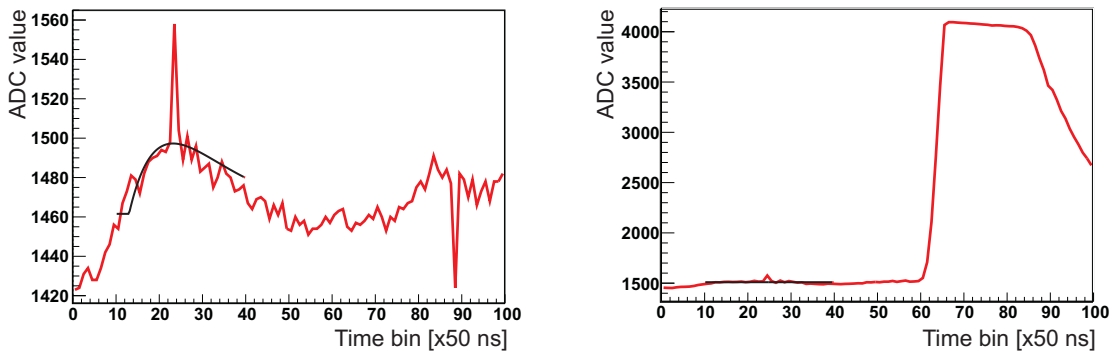
(a) Event 297: $ph_{fit} = 35.7$ ADC ch., $ph_{nofit} =$ 108.1 ADC ch.

(b) Event 9783: $ph_{fit} = 0.02$ ADC ch., $ph_{nofit} =$ 2612.7 ADC ch.

Figure 6.10: Fit status 2 events. (a) noise event with positive spike, (b) noise followed by an electron.

(a) Event 7688.

(b) Event 7033.
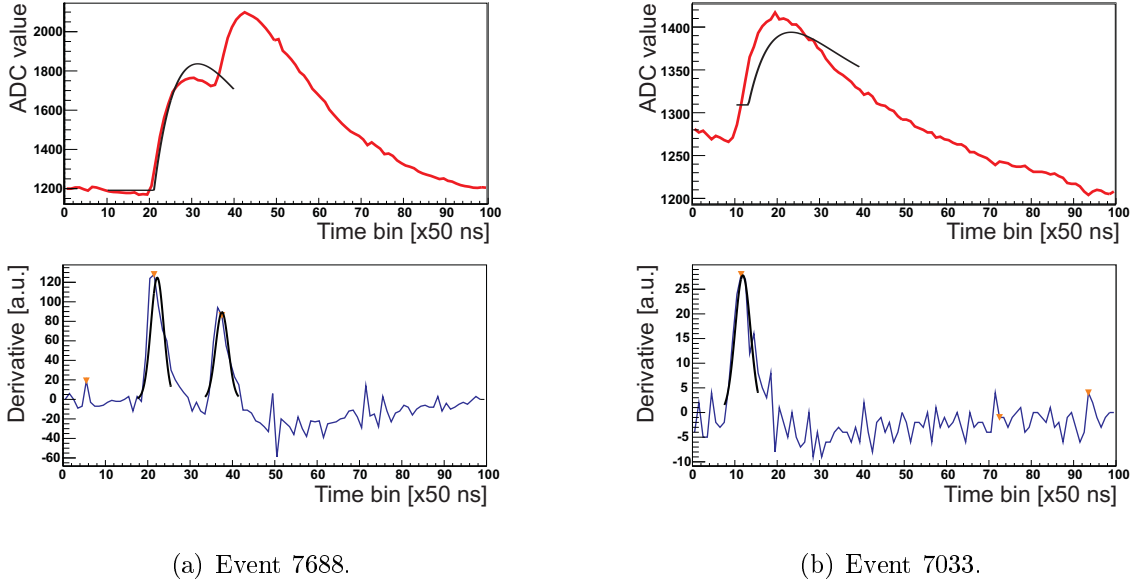
Figure 6.11: Top: The shown events were incorrectly sorted into fit status 1 because of a bad χ^2. Bottom: To separate these events from unwanted noise events the "derivative" of the event is investigated. The peak candidates found by the peak find algorithm are shown as orange triangles, the thick black line shows the Gaussian fits to the relevant peak candidates.

as the shape of the signal is altered by the rising edge of the second proton. Since the standard fit goes from bin 10 to bin 40 this happens when the second proton peak starts before bin 40 in the recoded event window. Fig. 6.11(a) (top) shows such an event.

- Correlated proton events: As shown in Fig. 4.4b, the start point x_0 is shifted and the proton sits on the exponentially decaying edge of the electron event. Therefore the fit fails as shown in fig. 6.11b (top). To identify and separate these events from the correctly sorted ones the "derivative" of the event shape is calculated. This means, a new histogram is created from the ADC values $h(i)$ of the event shape histogram with the derived values $d(i)$:

$$d(i) = h(i) - h(i-1). \tag{6.1}$$

Although it may not be mathematically correct, this type of histogram will be called the "derivative" of the signal further on. Two examples are shown in fig. 6.11 (bottom). The steep rise of the signals cause distinctive peaks in the derivative, from the number and position of those peaks the two above mentioned cases can be identified. Pile-up events cause two peaks in the derivative, the first one around time bin 23, the second one between time bin 25 and 40. Correlated proton events show one single peak at low bin numbers (below bin 14). To automatize the process, the `TSpectrum::Search` peak finding routine is used. It returns the position of possible peaks in the derivative. Between time bin 5
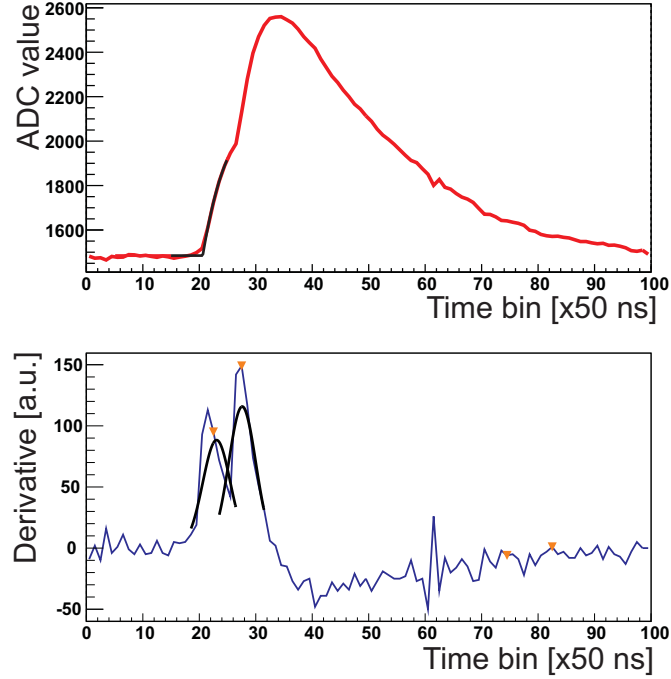
Figure 6.12: An example for a pile-up event with a very short time difference of only about 4.5 time bins $\hat{=}$ 225 ns (event 10071, file 9). In the derivative the two peaks can be separated and limits for the fit can be set. Although only the rising part of the event is fitted, the result gives a reasonable pulse height of 572.5 ADC channels.

to 45, the algorithm returns one or two peak candidates, only those are used for further investigation. Although the exact shape of the derivative follows a quite complicated function (the derivative of eq. (4.1)), a simple Gaussian fit can be used to get the needed information about the peaks. The event gets classified as a pile-up, if there are two peaks whereas the first peak is beyond time bin 10. Both derivative peaks must have amplitudes > 10 and widths between 0.5 and 4 time bins. In this case, the pulse is re-fitted with the standard fit function eq. (4.1) but with changed limits of the fit. The fit starts now at time bin 5 and ends at the position of the second Gaussian peak x_{G2} minus the width σ_{G2} of the peak:

$$x_{end} = x_{G2} - \sigma_{G2}. \tag{6.2}$$

This method works to time differences of the two pile-up events down to about $0.2\,\mu$s (fig. 6.12). A comparison of the result of the standard fit and the adapted fit is given in fig. 6.13. All re-fitted events of status 1 are assigned status 5 afterwards. A correlated proton is identified via a Gaussian peak in the derivative before time bin 13.5 with an amplitude > 10 and a width of at least 0.8 time bins. A special fit function is used to
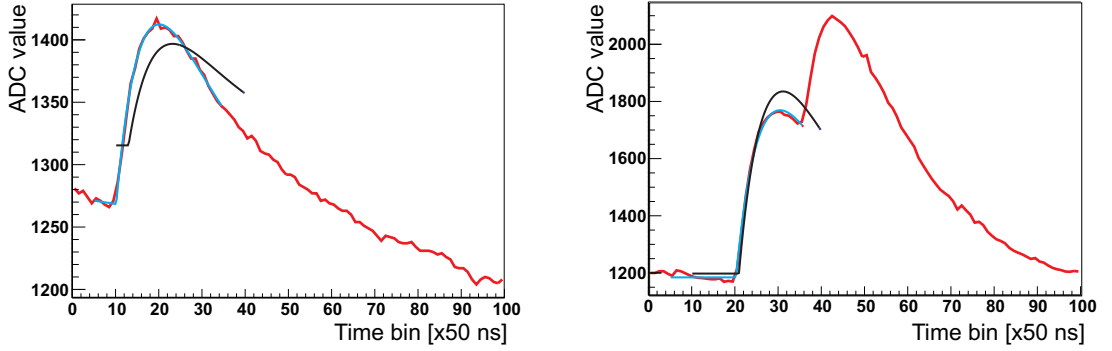
(a) Event 7033: $ph_{fit} = 151.5$ ADC ch., $ph_{nofit} =$ 115.9 ADC ch.

(b) Event 7688: $ph_{fit} = 584.8$ ADC ch., $ph_{nofit} =$ 906.2 ADC ch.

Figure 6.13: Fit status 5 events. The results of the standard fit and the adapted fit are shown in black and cyan, respectively.

re-fit those events:

$$y_{PaE}(x) = y_{Fit} + e^{x_1 + p_1 x} - 1, \qquad (6.3)$$

where y_{Fit} is the standard fit function eq. (4.1). x_1 and p_1 are the parameters of the additional exponential decay. A comparison of the result of the standard fit and the adapted fit is given in fig. 6.13. The pulse height of the event is then calculated from the parameters of the standard fit y_{Fit}, which means the pulse height the event would have if it was sitting on a flat baseline is used for the further analysis. Some events have a slightly different shape in the rising part of the pulse, the rising edge is not as steep as for the "common" events and the maximum of the pulse is shifted to higher time bins. These events are treated with the same fit as the other events, but instead of fitting mostly the rising edge of the pulse, like the standard bin 10 to 40 method does, the fit focuses on the falling edge of the pulse from time bin 30 to 90. Furthermore the x_0-restriction is now widened from bin 13 to bin 25. Fig. 6.14 displays such an event type.
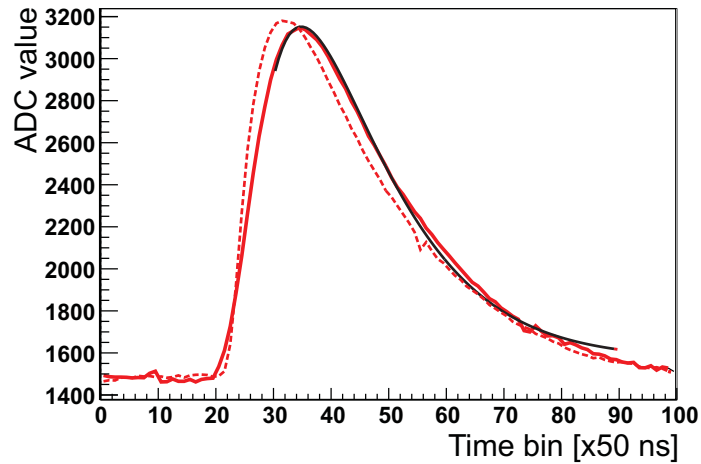
Figure 6.14: Fit status 7 event (3782). The solid black line represents the adapted fit. A normal event, number 2831 from the same file, is drawn for comparison (dashed red line).

6.9 Appendix 9: Additional background studies

This section presents some additional background studies (see tab. 4.5). They were omitted in the main section concerning background because they do not show any APV-dependency of background:

6.9.1 Environmental background: Neutron beam, magnetic field and detector HV switched off

Environmental background can be measured without magnetic field, without detector HV and neutron beam "off". The background level is expected to be negligibly low. Environmental background is mainly produced by cosmic rays and neighboring beam lines. Fig. 6.15a shows a spectrum (data set "150408_night") measured in the beginning of the beam time. The spectrum was averaged over all measurements at 780 V APV. In fig. 6.15b, the corresponding count rates are plotted vs. the APV-setting. Two integration windows were used: 100^2 to 1200 ADC channels and 1200 to 4000 ADC channels. The count rates vary only statistically and are independent from the APV. Tab. 6.2 gives the average count rates for all APV-settings.

---

[2]Due to insufficient cooling of the detector electronics, the noise peak was minimally wider in the beginning of the beam time. Therefore, the lower integration limit was set to 100 instead of 80 ADC ch.

Index	Integration window [ADC channels]	Count rate [s^{-1}]	Neutron beam on/ off
1	100...1200	0.013(3)	off
2	1200...4000	0.107(12)	off

Table 6.2: Count rates of environmental background: Measured with magnetic field, detector HV and neutron beam switched off. Mainly cosmic rays and radiation by neighboring experiments contribute.
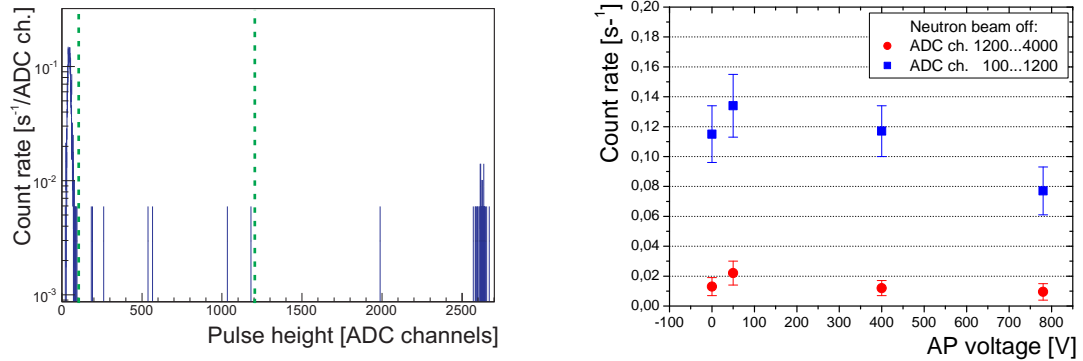
(a) Exemplary spectrum for 780 V APV.

(b) Average count rates in defined windows.

Figure 6.15: Environmental background: (a) Spectrum measured with magnetic field, detector HV and neutron beam switched off. The peak on the left border represents the electronic noise, the one on the right border high energetic background. (b) Shows count rates extracted between ADC ch. 100 to 1200 (red dots) and ADC ch. 1200 to 4000 (blue rectangles). Different APV-settings were used.

6.9.2 Beam related background (B): Magnetic field and detector HV switched off

In this measurements, the neutron beam was switched on. Without detector HV, decay protons can not be detected. Without magnetic field, charged particles from neutron decay are not guided along the field lines to the detector. Therefore, mainly beam related gamma radiation (e.g., by (n,γ)-processes) is expected as an additional source of background to environmental background. Neutrons are mainly absorbed in the entrance and exit window and in the internal ^{6}LiF-diaphragms. The measured spectrum in fig. 6.16a looks similar to fig. 6.15a. The integral spectrum in fig. 6.16b shows no APV-dependence. The integrated count rates in tab. 6.3 (index 3 and 4) give the average of all APV-settings. The background does not significantly differ from the environmental background in tab. 6.2 (index 1 and 2). This means, that the detection of beam related γ-radiation is suppressed by the small solid angle projected onto the detector in our experiment.
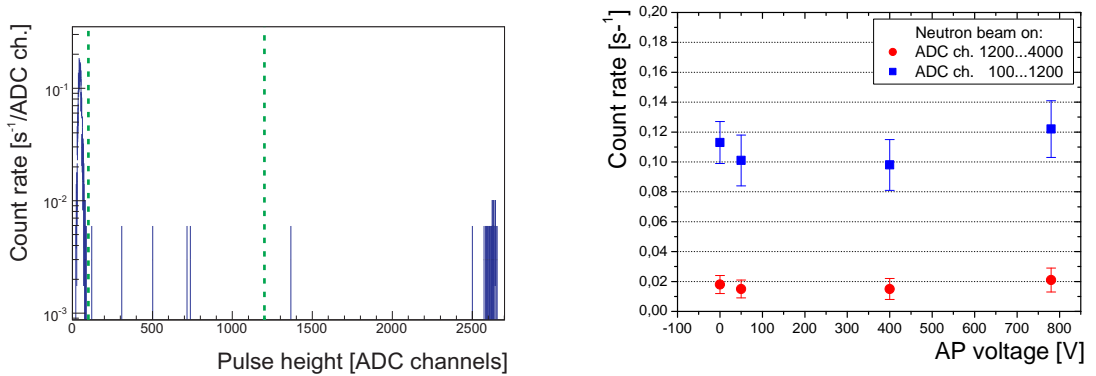
(a) Exemplary spectrum for 780 V APV.

(b) Average count rates in defined windows.

Figure 6.16: Beam related background (B): (a) Spectrum measured with magnetic field and detector HV switched off. The neutron beam was switched on. The peak on the left border represents the electronic noise, the one on the right border high energetic background. (b) Shows count rates extracted between ADC ch. 100 to 1200 (red dots) and ADC ch. 1200 to 4000 (blue rectangles). Different APV-settings were used. No APV-dependence of the background was determined in this measurement.

6.9.3 Beam related background (C): Detector HV switched off, magnetic field switched on

In this measurement, the main magnetic field of *a*SPECT was switched on. Therefore, charged particles emitted inside the flux-tube are now guided along the magnetic field lines

Index	Integration window [ADC channels]	Count rate [s^{-1}]	Neutron beam on/ off
3	100...1200	0.017(3)	on
4	1200...4000	0.108(8)	on

Table 6.3: Integrated, average count rates of beam related background measured with both magnetic field and detector HV switched off.

towards the detector. Mainly electrons are detected, since protons and ionized residual gas atoms have insufficient energy to pass the dead layer of the detector.

When the detector HV is set on -15 kV, the low energetic tail of the electron spectrum (e.g., all electrons with kinetic energies T < 15 keV) is reflected by the negative detector potential. Now, low energetic electrons contribute to the spectrum and therefore the background count rate is slightly increased. Fig. 6.17 shows the measured spectra: In (a), the neutron beam was switched on. The spectrum shows the continuous electron spectrum between the electronic noise peak (left border) and the peak due to high energetic particles (right border). (b) shows a spectrum when the neutron beam was switched "off". The measured background with neutron beam on (c) and off (d) is independent from the APV-setting. This is an indication, that any observed APV-dependence of background must be due to ionization of rest gas.

Tab. 6.4 lists the integrated count rates extracted at 780 V APV. The background with neutron beam "off" (index 1, 2) is minimally increased compared to measurements without magnetic field in tab. 6.3. The additional, charged background must be produced inside the flux-tube of aSPECT to reach the detector (e.g., by field emission at HV electrodes, Penning discharges or trapped particles). The background level is negligibly low.

Index	Integration window [ADC channels]	Count rate [s^{-1}]	Neutron beam on/ off
1	100...1200	0.0506(88)	off
2	1200...4000	0.318(17)	off
3	100...1200	13.32(11)	on
4	1200...4000	101.74(22)	on

Table 6.4: Background count rates measured with detector HV switched off and magnetic field switched on. The neutron beam was "off" (index 1, 2) or "on" (index 3, 4).
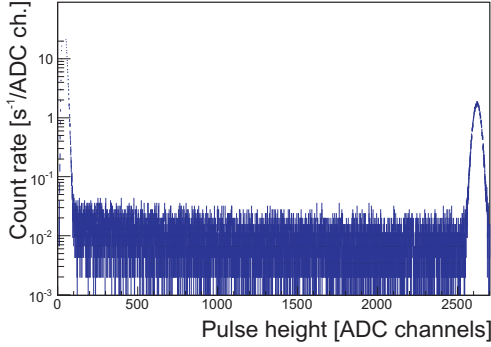
(a) Spectrum for 50 V APV with neutron beam "on".
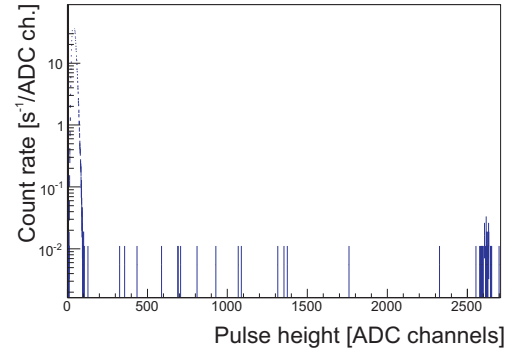
(b) Spectrum for 50 V APV with neutron beam "off".
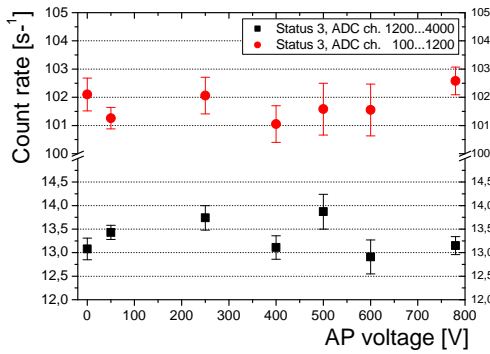
(c) Count rates with neutron beam "on".
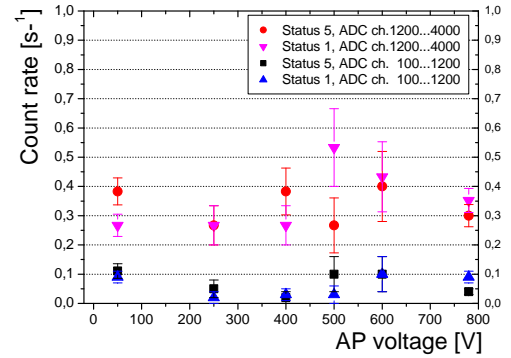
(d) Count rates with neutron beam "off".

Figure 6.17: Data set: "060508_noHV". Background measurements with detector HV switched off, but with main magnetic field on (B_0=2.177 T). (a) and (b) show the pulse height spectra measured at 50 V APV with neutron beam "on" and "off". The dominant contributions come from electronic noise (ADC ch 0...80) and electrons at pulse heights around 2500 ADC channels. Protons and ionized residual gas atoms have insufficient energy to pass the dead layer of the detector. (c) shows the measured integrated count rates with neutron beam on (Status 3: ADC ch. 100...1200, ADC ch. 1200...4000). (d) shows the measured integrated count rates with neutron beam "off" (Status 1 and 5: ADC ch. 100...1200, ADC ch. 1200...4000). The integrated background count rates show no APV-dependence. This is an indication, that rest gas ions must be the constituents of APV-dependent background.

Conclusion: The background studies in appendix 6.9.1 to 6.9.2 showed, that environmental as well as beam related electron- and γ-background is independent from the APV-settings.

6.9.4 Analysis of APV-dependent background at standard parameter settings

It had to be investigated, in which way the APV-dependent background measured with neutron beam "off" is related to the data taken with neutron beam "on". In particular, the applicability of the background subtraction method has to be proven. Several open question arise in this context:

- Do the background peaks appear regularly or occasionally?

- Is there a correlation between measurements at shutter status 3 and shutter status 5?

- Can one extrapolate from background count rates with neutron beam "off" to the background with neutron beam "on"?

- What is the nature of the two background peaks?

- How are the background peaks depending on various spectrometer settings (e.g., detector HV, ExB drift potentials, neutron flux, ME switched off)?

- Is a correction on the APV-dependence of the background necessary and how can it be implemented?

A short outline on the characteristics of the background peaks will answer some of these questions. A proposal how to treat the APV-dependent background in data analysis will follow afterwards. The focus of the outline will be on the discussion of a typical data set "160508_night".

Fig. 6.18a shows the integral count rates extracted in the PIW for shutter status 1 (red dots) and 5 (blue squares) at different APV-settings for a single data set "160508_night". Each data point in fig. 6.18(a) was calculated by averaging over all measurements of this data set. Both shutter states differ in their count rate characteristics: The count rates at shutter status 1 are generally lower. In fig. 6.18b and c, the count rates are drawn individually for the pulse height regions of peak1 (ADC ch. 300 to 450) and peak2 (ADC ch. 500 to 600): At shutter status 1 (fig. 6.18b), peak1 increases minimally with the APV, peak2 shows no dependence. At shutter status5 (fig. 6.18c), peak 1 increases as well with the APV, peak2 shows up clearly for 0 V and 50 V APV. For APV-settings >50 V, peak2 is not detected as a clear peak in the pulse height spectra on our level of statistical accuracy. A closer look on the count rate distributions of about 540 sub-runs (about t=17 h measurement time) in fig. 6.19 for different APV-settings shows as well strong systematic differences of the two background peaks: In the pulse height region of peak1
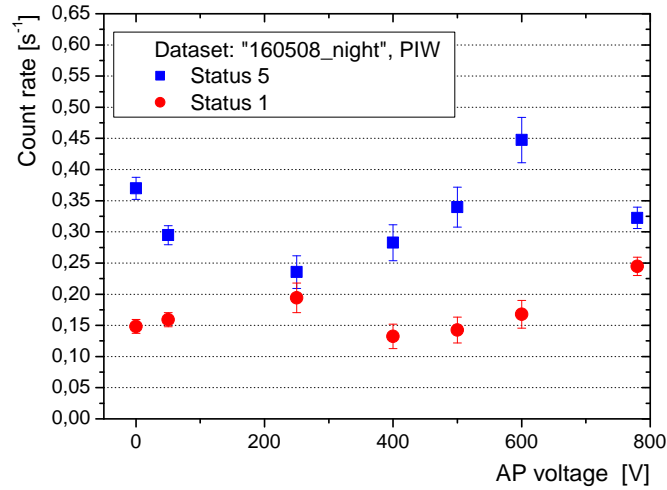
(a) Shutter status 1+5, PIW. Data set: "160508_night"
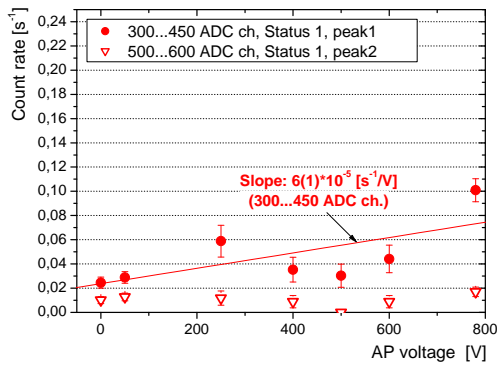
(b) Shutter status 1.
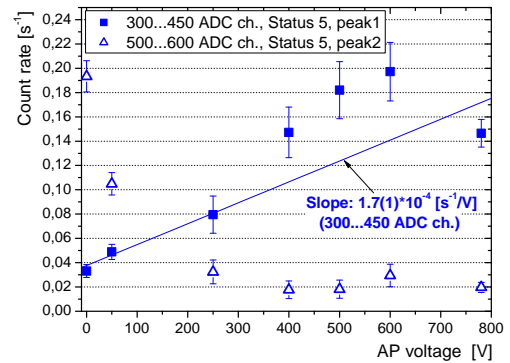
(c) Shutter status 5.

Figure 6.18: Integral spectra with neutron beam closed (data set: "160508_night", shutter status 1 and 5). All count rates were extracted by averaging all measurements at the given shutter state for a certain APV. (a) shows the spectra for the PIW. (b) and (c) focus on the pulse height regions of the two background peaks: 300...450 ADC ch. for peak1, 500...600 ADC ch. for peak2. Peak2 shows up only at shutter status 5 (red and blue triangles) and at APV-settings of 0 V and 50 V. Peak1 is increasing for both shutter states with the APV.

(see plots on the left side, (a)/(c)/(e)), the amount of measurements with non-vanishing count rates ($>0 \, [\text{s}^{-1}]$) increases with the APV for both shutter status 1 and 5. At status 1, the amount of measurements with 0 counts is overbalanced. In the pulse height region of peak2 (see plots on the right side, (b)/(d)/(f)), most of the measurements at shutter status 5 at 0 V have count rates $>0 \, [\text{s}^{-1}]$, but nearly no measurements at status 1: Peak2 is obviously beam related. Its source might be situated below the center of the AP electrode since APV-settings $\geq$250 V seem to block the particles that generate peak2. Low energetic residual gas ions ($< 250 \, \text{eV}$) would be a possible explanation.

The following conclusions can be drawn: The production mechanisms, which induce the background peaks, are not effective in all sub-runs of background measurements with neutron beam "off". Measurements with (at least) 1 or more counts in 10 s (i.e., $\geq 0.1 \, \text{s}^{-1}$) should show more clearly the characteristic APV-dependence of those mechanisms. The exclusion of measurements with low background count rates should increase the sensitivity on the characteristics of the effects. The average environmental background determined in sect. 6.9.2 for all APV-settings was already $\approx 0.05(1) \, \text{s}^{-1}$ (see fig. 6.17d). Therefore, the exclusion of measurements with lower background count rates represents also a kind of second order background subtraction. The procedure of excluding sub-runs can only provide a qualitative approach to the strength of the mechanisms.

The vertical-bar charts in fig. 6.20 present the relative occurrence (in [%]) of background measurements with count rates $>0 \, \text{s}^{-1}$ and $>0.1 \, \text{s}^{-1}$. 100% indicates all sub-runs at a given APV-setting of the data set "160508_night" (e.g., about 125 sub-runs at 50 V APV). The upper plots represent shutter status 1, the lower plots represent shutter status 5. The left side shows always peak1, the right side shows peak2. These charts emphasise the dependence of the production mechanisms of both background peaks on the APV-settings.

The exclusion of sub-runs was also applied to the integral spectra in fig. 6.21: In a first step, all measurements of $0 \, \text{s}^{-1}$ count rate (red points) were excluded. In a second step, count rates $>0.1 \, \text{s}^{-1}$ (blue rectangles) were required. Due to the exclusion, the APV-dependence of peak1 is increased by about a factor of 2 compared to the spectra in fig. 6.18b and c. The maximum background count rate at 780 V APV in the pulse height region of peak1 is about 0.4^{-1}.
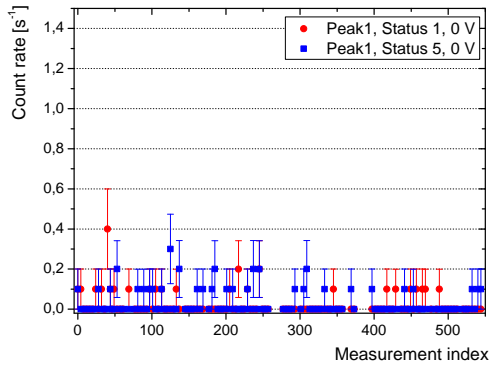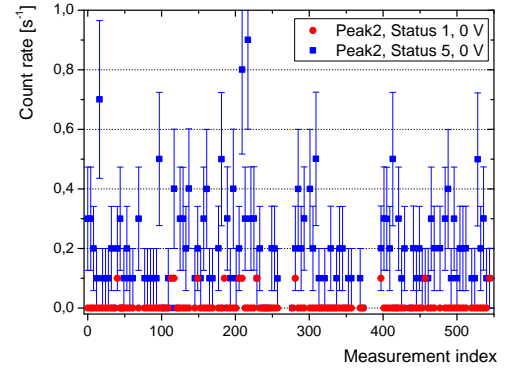
(a) 0 V APV, peak1.

(b) 0 V APV, peak2.
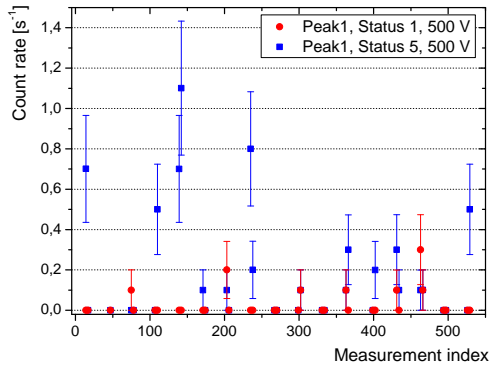
(c) 500 V APV, peak1.
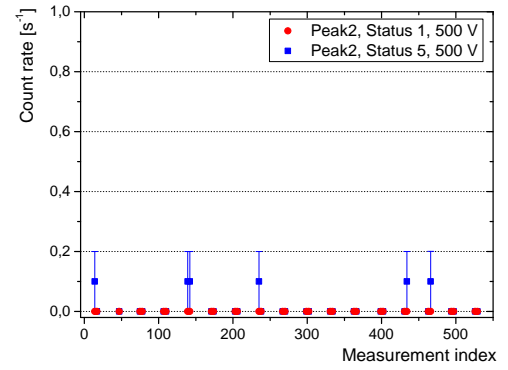
(d) 500 V APV, peak2.
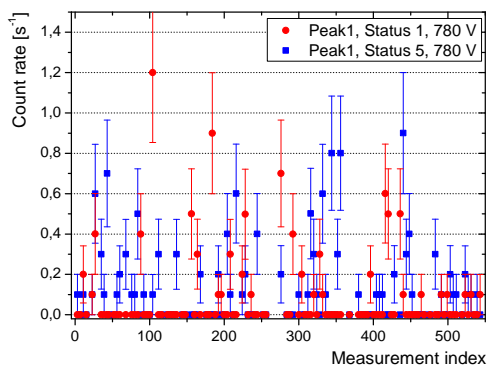
(e) 780 V APV, peak1.
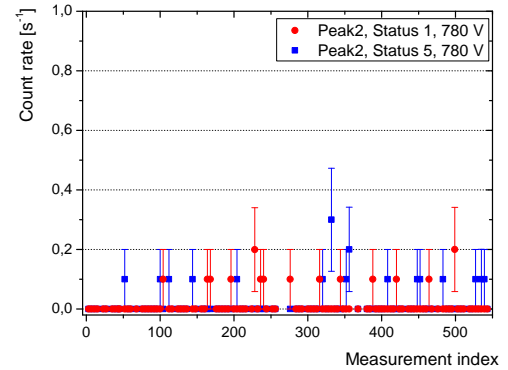
(f) 780 V APV, peak2.

Figure 6.19: Count rate distributions extracted from all measurements with neutron shutter closed (shutter status 1 and status 5) of a typical data set "160508_night". The count rates are shown for the pulse height regions of the two background peaks. (a), (c) and (e) represent peak1: ADC ch. 300...450. Measurements with high count rates appear more often at high APV-settings (e.g., 780 V) than at low settings (e.g., 50 V). (b), (d) and (f) represent peak2: ADC ch. 500...600. For APV-settings <250 V at shutter status 5, the amount of measurements with high count rates is strongly increased.
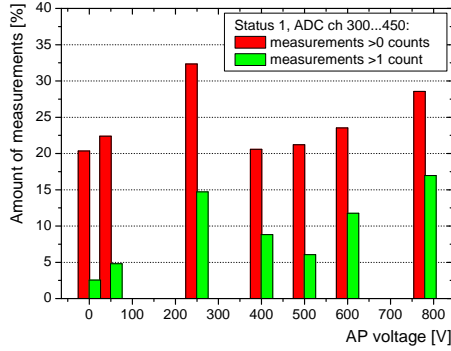
(a) Status 1, peak1.
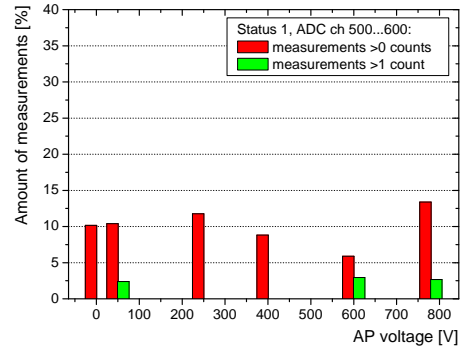
(b) Status 1, peak2.
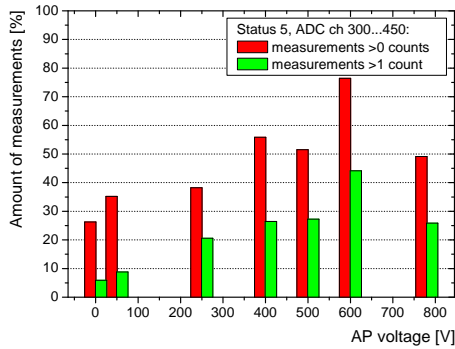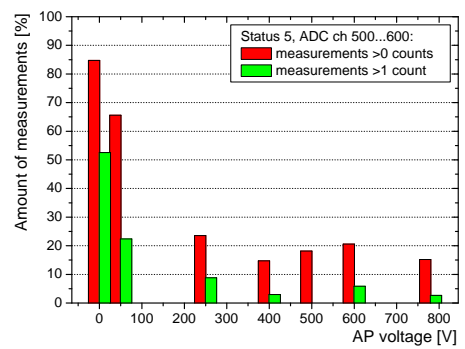
(c) Status 5, peak1.

(d) Status 5, peak2.

Figure 6.20: Relative occurrence of measurements >0 and >1 count (i.e., count rates $>0\,[\mathrm{s}^{-1}]$ and $>0.1\,[\mathrm{s}^{-1}]$, respectively) with neutron shutter closed. 100% indicates all measurements at a given APV-setting of the data set "160508_night" (e.g., about 125 sub-runs at 50 V APV). The plots are subdivided by the shutter states (1 and 5) and by the pulse height regions of the two background peaks. Peak1 (ADC ch. 300 to 450) appears by a factor of 2-3 less often at shutter status 1 (a) than at status 5 (c). Count rate contributions to peak2 (ADC ch. 500 to 600) at status 1 (b) show no APV-dependence. At status 5 (d), increased count rates appear in 85% of the 0 V and 65% of the 50 V APV measurements. The graphs show, that the occurrence of both peaks varies systematically with the APV.
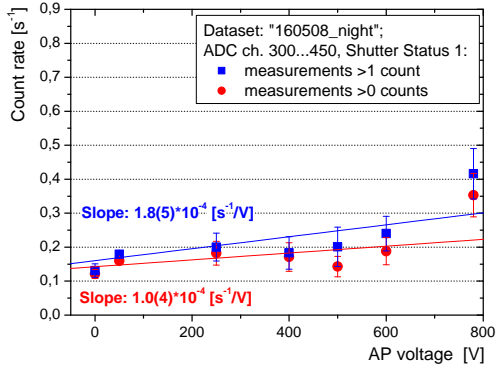
(a) Status 1, peak1.
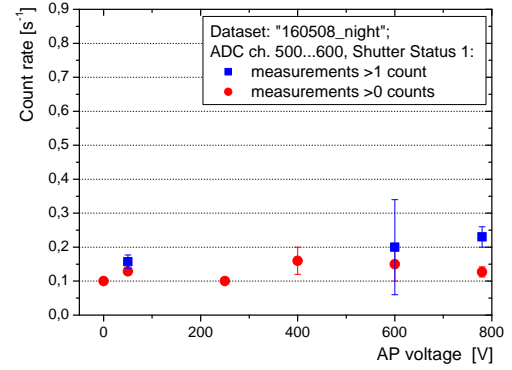
(b) Status 1, peak2.
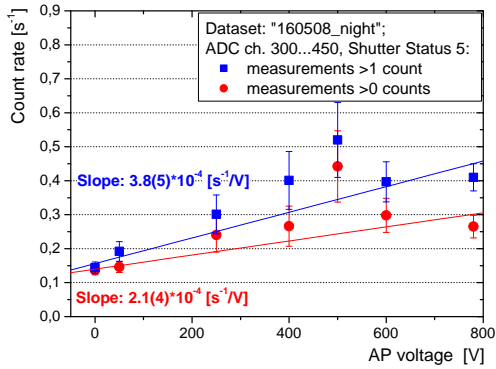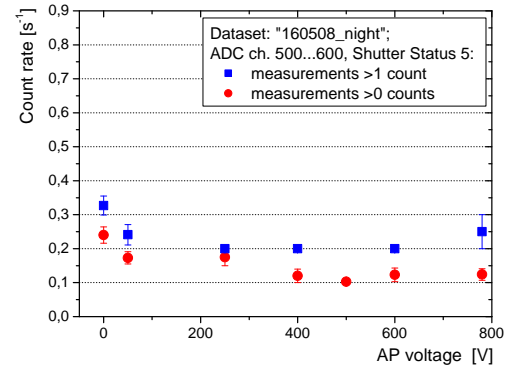
(c) Status 5, peak1.

(d) Status 5, peak2.

Figure 6.21: Integral spectra at shutter status 1 and 5. All count rates were extracted by averaging only measurements with more than 0 or 1 count in 10 sec measurement time. (a) and (c) show the spectra for peak1, (b) and (d) for peak2. It is obvious, that the effect that produces peak1 has a small linear dependence on the APV. This might be the background source which we observed in the FRM-II beam time. It is strongly reduced, since the detector HV settings were reduced from -35 kV to -15 kV for the ILL beam time. This resulted in drastically decreased field emission current which was pointed out in sect. 3.6.2 as a primary source for the APV-dependent background.

6.9.5 Background in the pulse height regions (IIIa) and (IIId)

Apart from peak1 and peak2, the background measured with neutron beam "off" in the pulse height regions (IIIa) ADC ch. 80 to 300 and (IIId) ADC ch. 600 to 1200 should be discussed: (IIIa) shows average count rates which are comparable to the two background peaks in the regions (IIIb) and (IIIc). But there is no peak structure visible. Fig. 6.22 shows the count rate dependence on the APV which is statistically insignificant. For that reason it is not important to treat this region separately. In the pulse height region ADC ch. 600 to 1200 nearly no events are measured. The average count rate is about a factor of 10 lower than in the other 3 regions and as well constant for all APV-settings.

(a) ADC ch. 80 to 300, status 1.

(b) ADC ch. 80 to 300, status 5.
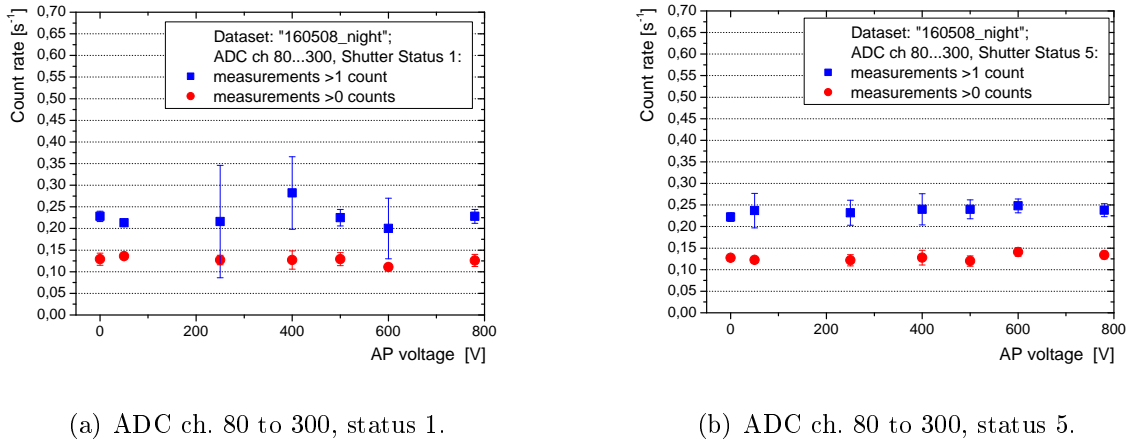
Figure 6.22: Integral spectra in the pulse height region ADC ch. 80 to 300 for shutter status 1 (a) and 5 (b). The plots show no significant dependence on the APV.

6.10 Appendix 10: Studies on the nature of APV-dependent background

In this section, some characteristics of the APV-dependent background will be investigated from measurements at non-standard parameter settings. As introduced in sect. 3.6.2, the electromagnetic field configuration of aSPECT automatically shows penning trap characteristics (see fig. 3.28 and fig. 6.23). Two regions are of main interest: (1) The trap for positive charged particles (e.g., protons) between the AP and the ME. (2) The trap for negative charged particles (e.g., electrons) between the lower and the upper ExB-drift electrode. During the ILL beam time, we performed various systematic measurements in order to study the properties of these particle traps under variation of essential parameter

settings (i.e., electric potentials, neutron beam width, magnetic field strength). For non-standard settings, non-statistical contributions to the count rates might be higher and additional effects may appear (e.g., changes in the spectral shape). These observations can be used for deducing a qualitative description of the trapping effects. This section will focus on the influence of trapping effects on the APV-dependent background. Mainly the nature of background peak1 will be investigated. Tab. 6.5 lists five data sets and their specific parameter settings. These data sets will be discussed on-going.

Data set	Specific settings
(1) 190508_lExB	lower ExB held on (a) -2.47/ 0 V and (b) -10.6/ 0V
(2) 150508_night	neutron beam width reduced to 20 mm
(3) 060508_night	detector at -10 kV HV
(4) 090508_MirrorOff	ME grounded
(5) 210508_night	main magnetic field reduced to 30 A

Table 6.5: Data sets used for description of APV-dependent background.
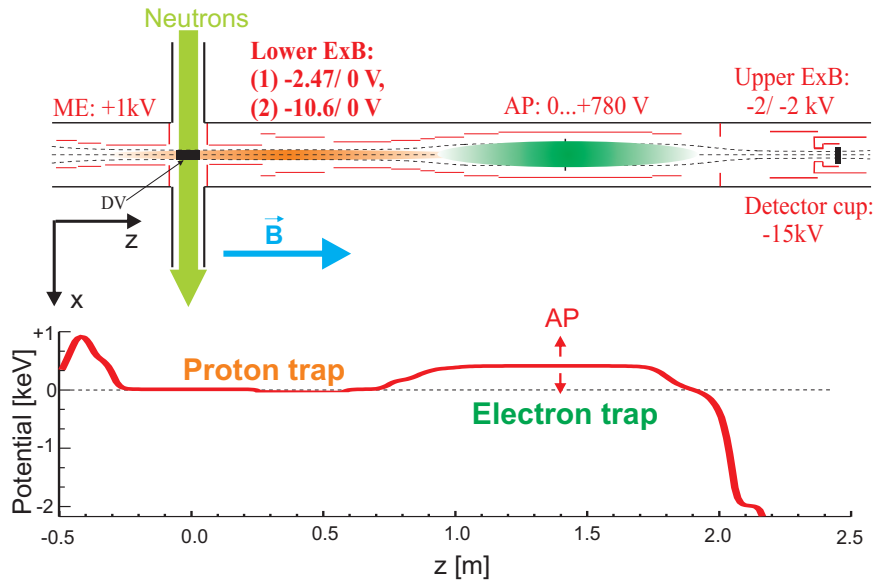
Figure 6.23: Scheme for the discussion of data set "190508_lExB". Top: The electrode system of aSPECT showing the traps for positive (orange region) and negative (green region) charged particles. Only the most relevant electrodes are shown. Bottom: Schematic shape of the electric potential in the regions of interest.

6.10.1 Studies on lower ExB drift potential

The variation of the lower ExB drift potential is helpful to study the mechanisms of filling and emptying of the particle trap between AP and ME. For an effective emptying, a drift potential of several hundred eV was proposed by F. Glück (e.g., voltages of -200/0 V or -1000/-50 V were applied during standard operation). For the data set "190508_lExB", the lower ExB-drift electrode was set on voltages which were well below these recommended settings: About 100 single measurements (at 0, 50 and 780 V APV) were performed for "ExB"-voltages of (a) -2.47/0 V and about 170 for (b) -10.6/0 V (a scheme is drawn in fig. 6.23). An insufficient emptying of the trap leads to unstable conditions: The trapped protons can gain (or lose) energy in particle collisions with the residual gas atoms and thus may pass the AP potential. At 780 V APV all protons get trapped, so the effect should be maximal there.

The plots in fig. 6.24 show the impact of the lowered drift potential at the lower ExB-electrode measured at 780 V APV: For the setting (a) (i.e., -2.47 eV drift potential), the count rates with neutron beam "on" are fluctuating non-statistically. The average count rate is about a factor of 1.5 higher compared to measurements under standard parameter settings. The fluctuations are non-statistical and persist in the measurements with neutron beam "off" (c). The background count rates with neutron beam "off" are highly increased, in particular at shutter status 5. For setting (b) (i.e., -10.6 eV drift potential), the fluctuations are reduced. But the average background level with shutter closed (d) is still slightly increased. Tab. 6.6 compares the average count rates for both ExB-settings (see the discussion in the caption).

Trapped protons (or positive charged residual gas ions) can leave the trap via the AP electrode in random flushes as illustrated by fig. 6.25. The count rate fluctuations depend strongly on the settings of the lower ExB-electrode: For the lowest setting of -2.47/0 V (red points), the count rates start to fluctuate as soon as the shutter is opened. Even when the shutter gets closed, particles are detected for up to 10 s. For the standard setting of -200/0 V (black points), the count rates are statistically distributed and stable in time. When the neutron beam gets closed, the count rates drop back immediately to a typical background level.

The pulse height spectrum at 780 V APV with neutron beam "off" (status 5) in fig. 6.26 shows a previously unobserved peak structure. Beside peak1 (ADC ch. 300 to 450), which was so far dominant at 780 V (at standard settings), also peak 2 (ADC ch. 500 to 600) is clearly visible in the rebinned spectrum (b). Furthermore, a third peak "peak0" shows up around ADC ch. 100 to 300. At standard settings, only peak1 could be discovered at 780 V APV (see fig. 4.25b). Apparently, the standard drift potential suppresses the appearance of peak0 and peak2 (at 780 V APV).

Fig. 6.27 illustrates the dependence of the average count rates with neutron beam "off" (status 5) on the APV (in the respective pulse height regions of the 3 peaks). For (a)
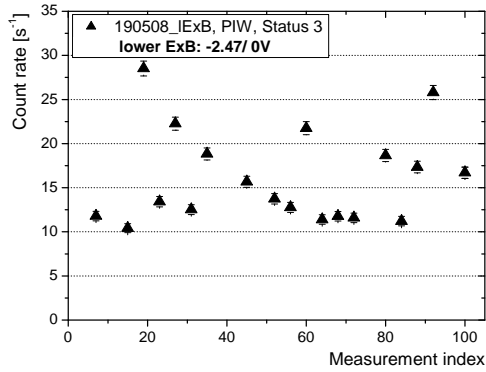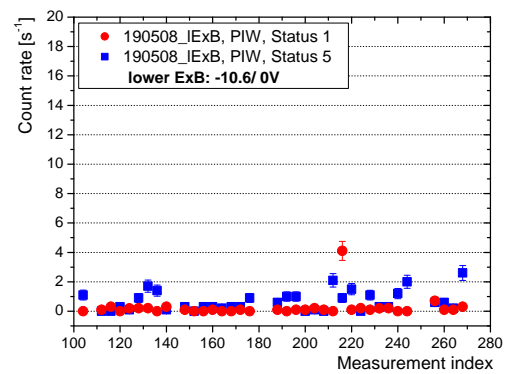
(a) Lower ExB: -2.47/0 V; status 3
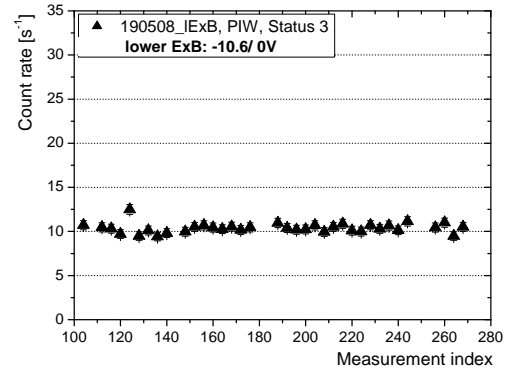
(b) Lower ExB: -10.6/0 V; status 3
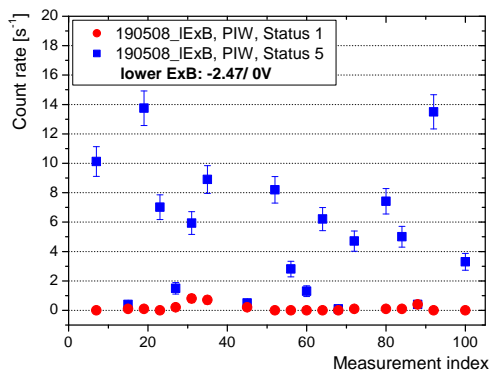
(c) Lower ExB: -2.47/0 V; status 1 and 5

(d) Lower ExB: -10.6/0 V; status 1 and 5

Figure 6.24: Count rate distributions in the PIW for all 780 V APV measurements of data set "190508_lExB". (a) and (b) show the count rates with open shutter, (c) and (d) with shutter closed. Obviously, the increased drift potential (-10.6/0 V) stabilizes the count rate fluctuations and reduces the total count rate, too

Lower ExB settings	Count rate status 3 [1/s]	Count rate status 1 [1/s]	Count rate status 5 [1/s]
(a) **-2.47/ 0 V**	14.6±1.0 (χ^2=54)	0.153±0.046	5.3±1.0
(b) **-10.6/ 0 V**	10.20±0.09 (χ^2=1.07)	0.147±0.037	0.68±0.17

Table 6.6: Average count rates (data set: "190508_lExB") in the PIW at 780 V APV. The data set is split into two parts of different settings of the lower drift voltages: (a) -2.47/ 0 V, (b) -10.6/ 0 V. The count rates of (a) are fluctuating stronger with open and closed shutter. $\chi^2 = 54$ indicates that the count rate distribution is non-statistical. Whereas the count rates of (b) are statistically distributed ($\chi^2 \approx 1$). The measurements with neutron beam "off" show, that the fluctuations are beam related and correlated to trapped particles: Before the neutron beam is opened (status 1), the count rates for both lower ExB settings are the same and comparable to measurements at standard settings. After the beam was opened and closed again (status 5), the count rate in (a) is by a factor of about 15 higher compared to standard settings. For the settings used in (b), the count rate is strongly reduced but still by a factor of about 1.8 higher than at standard settings. Obviously, the lower ExB-drift potential had to be increased further to provide stable conditions.
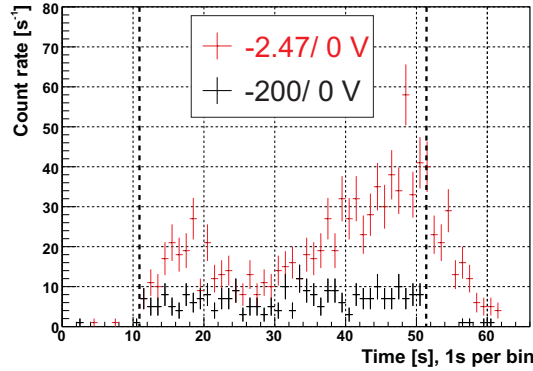
Figure 6.25: Time sequence (1s/bin) of measurements at 780 V APV for different settings of the lower ExB-electrode: (a) -2.47/ 0 V (red), (b) -200/ 0 V (black). The thick vertical lines (dashed) denote, when the neutron beam was opened and closed. The count rates for (a) fluctuate strongly in time and show unsteady, random phases of increased count rates. When the neutron beam is closed, the count rates need about 10 s to fall back on the initial background level. In case of (b), the count rates are statistically distributed. When the beam is closed, the count rates drop immediately.

(a) 780 V APV, status 5.　　　　　(b) 780 V APV, status 5, rebinned.
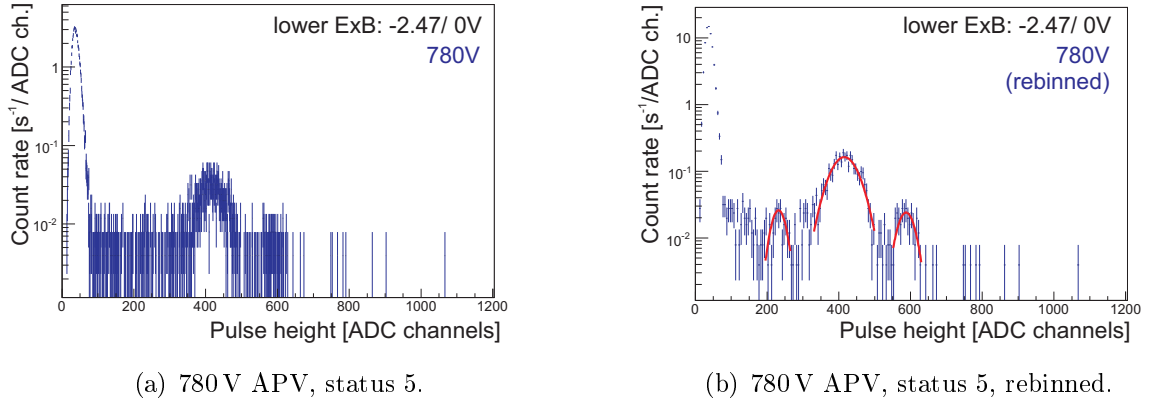
Figure 6.26: Lower ExB: -2.47/ 0 V. A so far unobserved peak structure for 780 V APV appears in the rebinned spectrum (b): Beside peak1, which is dominant for standard settings, also peak2 appears. An additional peak (peak0) shows up between ADC ch. 100 and 300. Obviously, the ExB-drift at standard settings is more effective and suppresses peak0 and peak2 (see fig. refSpectraShutterS5b).

-2.47/ 0 V, the count rate of peak1 increases strongly with the APV. Peak0 and peak2 are somewhat higher at 780 V APV than at lower APV-settings. The reason is the depth of the particle trap between AP and ME (see also fig. 3.28 in sect. 3.5.2) which exalts with the AP potential. The more particles stored, the higher gets the collision rate. Collisions enable particles to pass the AP. For (b) -10.6/ 0 V the count rates behave already like for standard settings but on a slightly increased absolute level. At 780 V APV there is no clear peak observed anymore in the pulse height region of peak2. Peak0 is constant for all APV-settings.

　　　Another alteration is apparent in the spectra with open shutter in fig. 6.28: At 780 V APV, peak1 and peak2 are clearly visible in (a) for a lower ExB-setting of -2.47/ 0 V. Compared to a spectrum measured with an ExB-setting of -10.6/ 0 V in (b), the peaks are reduced but they remain still observable. This suggests that even this setting is still to low to provide stable trap cleaning conditions. Trap cleaning and filling have to be in a stable equilibrium, therefore the minimal drift potential that we applied was -200/0 V. In most measurements, the voltage setting of the lower ExB-drift electrode was -1000/-50 V. We observed no significant difference in the measured background between these settings at shutter status 1 and 5.

Correlations between shutter status 3 and status 5:
Correlations between measurements with open and closed neutron shutter could deliver informations on the characteristics of the APV-dependent background. For example, two questions arise from the previously discussed background measurements: (1) Does an increased count rate with open neutron beam indicate also a high count rate with neutron

(a) Lower ExB: -2.47/ 0 V.

(b) Lower ExB: -10.6/ 0 V.
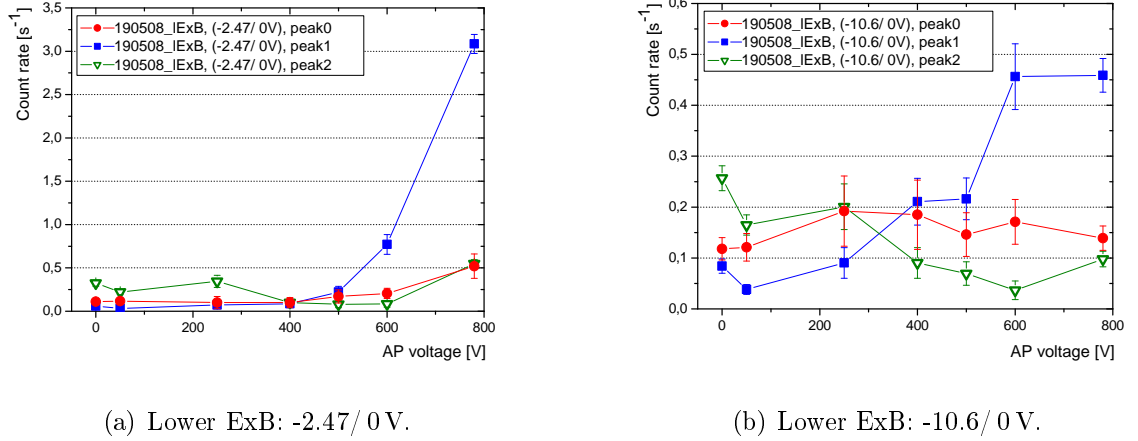
Figure 6.27: Average count rates at shutter status 5 for the data set "190508_lExB"'
(peak0: ADC ch. 80 to 300, peak1: ADC ch. 300 to 450, peak2: ADC ch. 500 to
600). In (a), the count rate for peak1 increases strongly with the APV-setting.
Peak0 and peak2 are higher at 780 V APV than at lower APV-settings. In (b),
peak0 is suppressed and shows no dependence on the APV. The increase of
peak1 is still stronger than for measurements with standard settings.
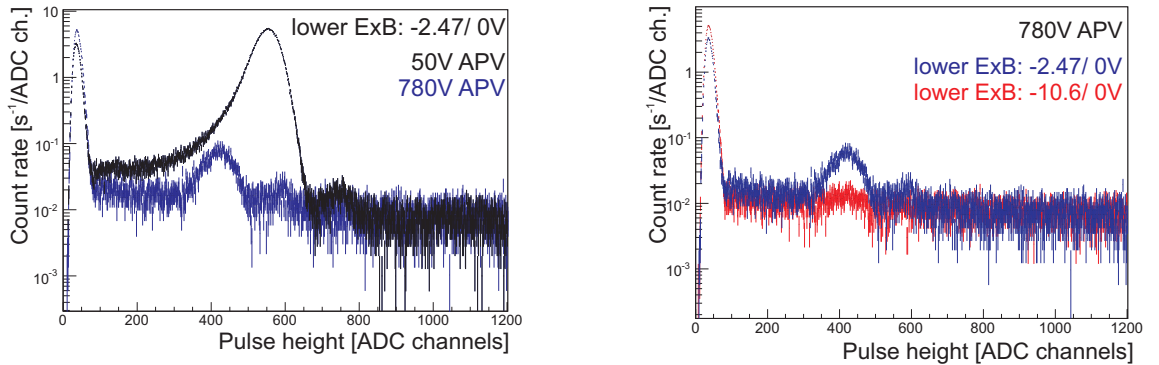
(a) Spectra for 50 V (black) and 780 V APV
(blue). Lower ExB-settings: -2.4/ 0 V.

(b) Spectrum for 780 V APV for two ExB-
settings: -2.4/ 0 V (blue), -10.6/ 0 V (red).

Figure 6.28: Spectra with open neutron shutter. (a) Lower ExB: -2.47/ 0 V. The two peaks,
which where previously only detected for closed shutter, appear clearly in the
spectrum for 780 V APV. (b) By increasing the drift potential (-10.6/ 0 V, red
spectrum), the peaks are reduced but peak1 can be still observed.

beam closed? (2) Is the average amount of APV-dependent background with open neutron beam comparable to the average APV-dependent background with neutron beam closed?
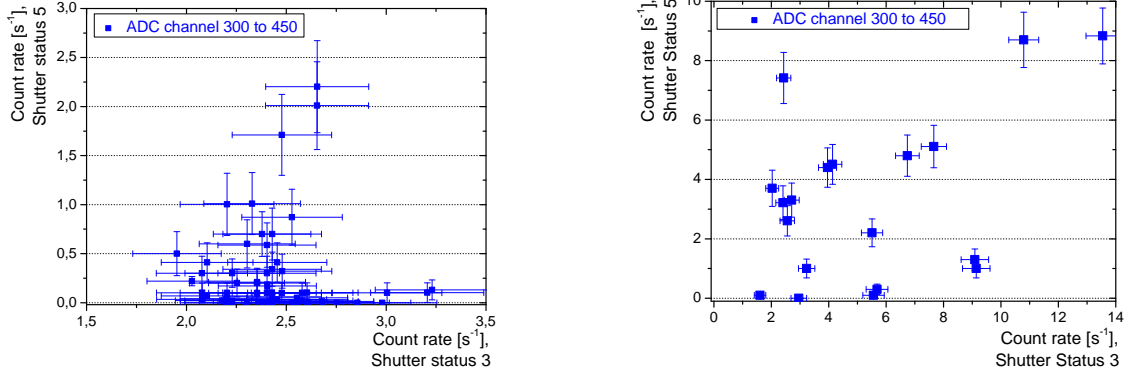
(a) Data set: "190508_night". Lower ExB-settings: -1000/-50 V.

(b) Data set: "190508_lExB". Lower ExB-settings: -2.47/ 0 V.

Figure 6.29: Correlation plots for 780 V APV between measurements at shutter status 3 (x-axis) and status 5 (y-axis). Each point corresponds to a single measurement file. The integration window was chosen to be ADC ch. 300 to 450 (peak1) since peak1 is dominant for 780 V APV. In both cases, there is no significant correlation observable, although the background with closed shutter is highly increased in (b). This supports the assumption that the effect is fluctuating non-statistically.

Only measurements at 780 V APV are sensitive to possible correlations in the pulse height region of peak1 (ADC ch. 300 to 450): With open neutron shutter (status 3), the statistical error of a single measurement is about $\pm 0.2\,\mathrm{s}^{-1}$. With neutron shutter closed (Status 5), the average count rate for peak1 is also about $0.2\,\mathrm{s}^{-1}$ but single measurements show count rates up to $2\,\mathrm{s}^{-1}$. If these high count rates at status 5 would be correlated to high count rates at status 3, the 780 V APV measurements should be sensitive to this correlation. Measurements at lower APV-settings are insensitive since their statistical error with open neutron beam is too high.

Fig. 6.29 shows two correlation plots (status 3 vs. status 5) for all 780 V measurements of the data sets (a) "190508_night" (standard settings: -1000/-50 V) and (b) "190508_lExB" (ExB-settings: -2.47/ 0 V). In fig. 6.29a, no significant correlation is visible. In fig. 6.29b, the detected amount of APV-dependent background was strongly increased due to the reduced ExB-settings at the lower ExB-drift electrode. Therefore, a possible correlation is supposed to be stronger. But even under that extreme conditions, the measurements with open and closed neutron beam show no significant correlation. The

correlation plots support the thesis, that APV-dependent background is not permanently produced but occurs randomly.

6.10.2 Background study with reduced neutron beam
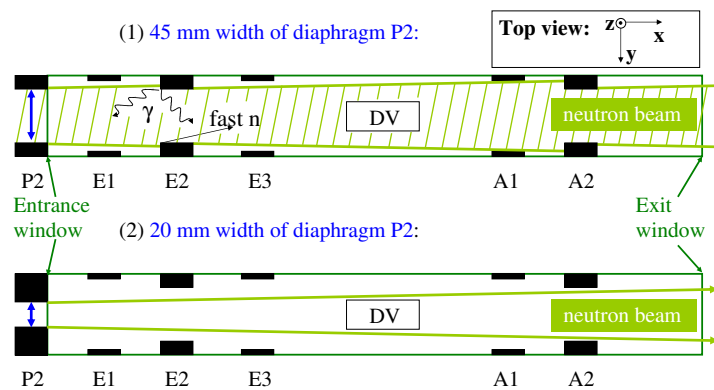
Figure 6.30: Scheme concerning the internal beam line for different widths of the diaphragm P2: (1) 45 mm and (2) 20 mm. Obviously, the direct irradiation of diaphragms downstream of P2 is stronger for the standard beam width (1). Scattering and backscattering effects are not included in this scheme. Please note, that the dimensions in the two plots are not at scale.

For edge effect studies (see sect. 3.6.3), an additional diaphragm was inserted in front of the entrance window of aSPECT for some data sets. It reduced the neutron beam width from 45 to 20 mm whereas the height stayed constant. The additional diaphragm decreases the total neutron flux through aSPECT by a factor of about 1.85 (calculated flux). But the neutron flux through the effective flux-tube is only reduced by a factor of about 1.1: The additional diaphragm absorbs mainly neutrons from the edges of the neutron beam (see beam profiles fig. 3.18e/f and fig. 3.19c). But these edges are not completely imaged via the decay protons onto the detector. The reduced beam width reduces the amount of neutrons that decay outside the flux-tube by a factor >10. Fig. 6.30 shows schematically the impact of the additional diaphragm on the neutron beam. One of the data sets measured with 20 mm beam width is "150508_night". Apart from the beam width, "150508_night" has the same parameter settings as "160508_night" (see tab. 4.2 and tab. 4.4). The average proton count rate in the PIW is reduced by a factor of 1.12 with the additional diaphragm, whereas the count rate at 780 V APV (mostly from decay electrons) is not affected as listed in tab. 6.7. For the discussion of the background behavior with reduced beam width, the amount of electrons that is imaged onto the detector will

Data set	Proton count rate [1/s] ADC ch.80...1200 at 50 V APV	Electron count rate [1/s] ADC ch. 80...4000 at 780 V APV	Beam width at the Entrance Window
150508_night	419.5(3)	97.52(8)	20 mm
160508_night	471.5(3)	97.45(8)	45 mm

Table 6.7: Comparison of count rates of data sets with 20 mm and 45 mm neutron beam width.

be of minor impact. But a short remark on the expected electron count rates should be foreclosed. The electrons imaged onto the detector split up into 2 categories (see also sect 4.8): First, there are electrons which are emitted inside the decay volume into the upper hemisphere of the spectrometer and follow the flux tube towards the detector. The second category are backscattered electrons. For example, electrons emitted into the lower hemisphere and reflected (backscattered) on the surface of an electrode, the wires of the grid electrode (e1) or the bottom flange of aSPECT. The analysis of measurements with

(a) Peak1.

(b) Peak2.
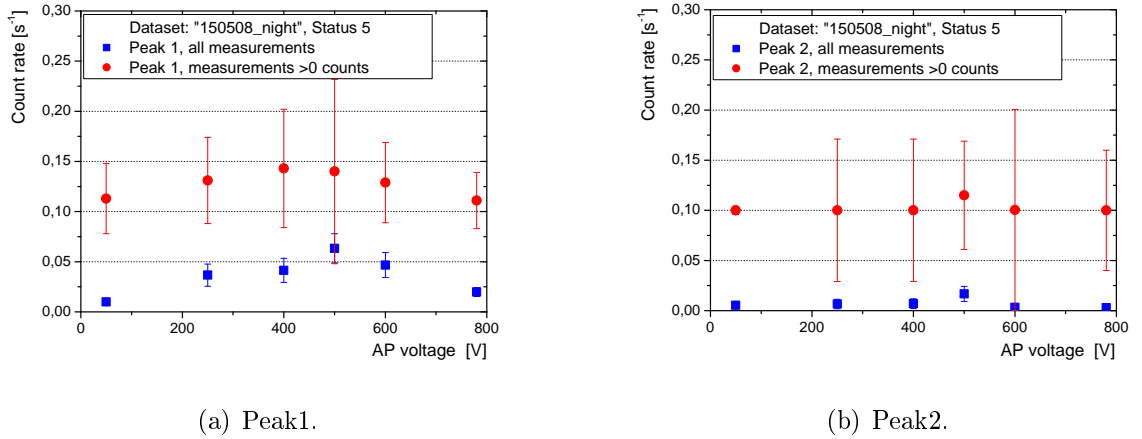
Figure 6.31: Data set "150508_night": Measurements with neutron beam closed (status 5) with a reduced beam width of 20 mm. In the measured pulse height spectra, no background peaks are visible. Therefore the count rates in plot (a) and (b) show no dependence on the APV.

neutron beam "off" of data set "150508_night" (with reduced beam width) unfolds new information on the origin of the background peaks: Neither peak1 (ADC ch. 300 to 450) nor peak2 (ADC ch. 500 to 600) is visible in the pulse height spectra at any APV-setting. Even by exclusion of measurements without any event in the pulse height region of peak1 and peak2 in 10 s measurement time, no dependence on the APV can be observed as shown in fig. 6.31. The average count rates are on the level of the environmental background (i.e., $\approx 0.05\,[\mathrm{s}^{-1}]$). Measurements without events in the pulse height region of peak1 and peak2

are dominant. The vertical-bar charts in fig. 6.32a illustrate, that less than 30% of the measurements show a contribution to peak1 at all APV-settings. And less than 15% of the measurements show a contribution to peak2. Fig. 6.32b shows the same plot for data set "160508_night" with standard beam width for comparison. The production mechanisms

(a) Data set: "150508_night".

(b) Data set: "160508_night".
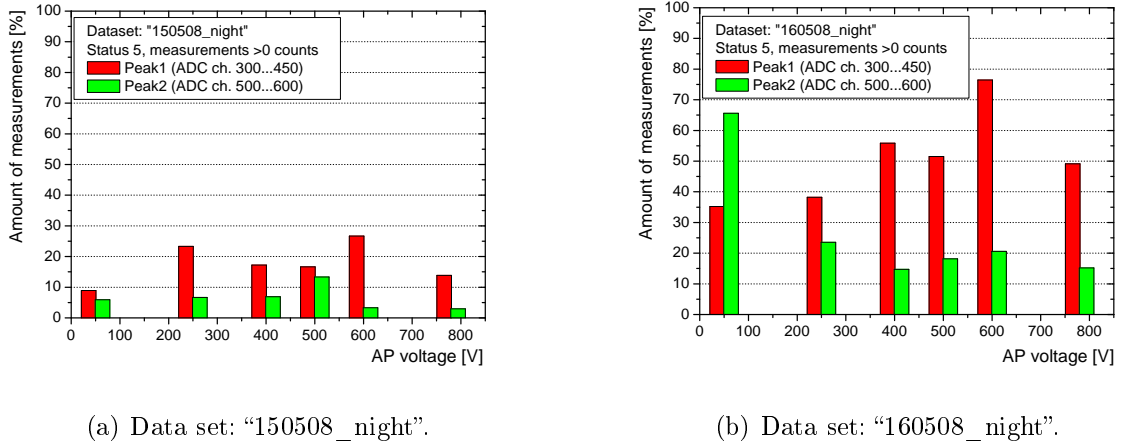
Figure 6.32: Amount of single measurements with >0 counts in 10 s for neutron beam closed (status 5). In (a), the beam was reduced to 20 mm in front of the entrance window. (b) has a width of 45 mm at that position. All other parameter settings were identical. Obviously, in data set "150508_night" nearly no measurements with background counts occur, neither in the pulse height region of peak1 nor of peak2.

which are responsible for the APV-dependent background, are obviously suppressed or at least reduced below the statistically detectable level for a narrow beam of 20 mm width. There are two feasible explanations for that observation:

(1) The reduced neutron flux also reduces the total amount of decay electrons in the region of the DV. Therefore, less electrons are available for ionization of residual gas and for the production of secondary electrons.

(2) Moreover, the narrow beam reduces the irradiation of all parts of the internal beam line downstream of the diaphragm P2: In particular, the MgAl3Zn1 entrance window and the LiF-pieces of the diaphragms. Both produce γ-radiation of several MeV energy by (n,γ)-reactions [73], [74]. For ^{6}Li, this process is suppressed by a factor of 10^{-4} but still about $10^5 \, \text{s}^{-1}*\text{cm}^{-2}$ γ´s might be emitted. Additionally, one has to take into account neutrons which are scattered and backscattered on the LiF diaphragms. The high energetic γ´s may interact with the surfaces of, for example, the DV electrode (cold coated copper), the grid of the mirror electrode or the bottom flange (stainless steel) and can produce secondary electrons by Compton scattering and Pair Production. The secondary electrons can ionize residual gas.

From the measurements taken at ILL, it is not possible to distinguish which of the two

processes is dominant. But for future beam times I recommend further tests with different beam widths (e.g., 25 mm, 30 mm, 35 mm). For example, a retractable diaphragm could be implemented in front of the external diaphragm P2 using a linear vacuum feed-through. Via an additional vacuum chamber, separated by a valve, the diaphragm could be easily replaced. The aim would be to find a good compromise between the detected amount of APV-dependent background (with its corresponding systematic corrections in data analysis) and the beam profile. A reduced beam width results in a stronger edge effect at the detector (see sect. 3.6.3). The combined errors from the edge effect correction and from the correction on APV-dependent background must be minimized.

6.10.3 Background study with lower detector HV and 2 detector pads (peak1)
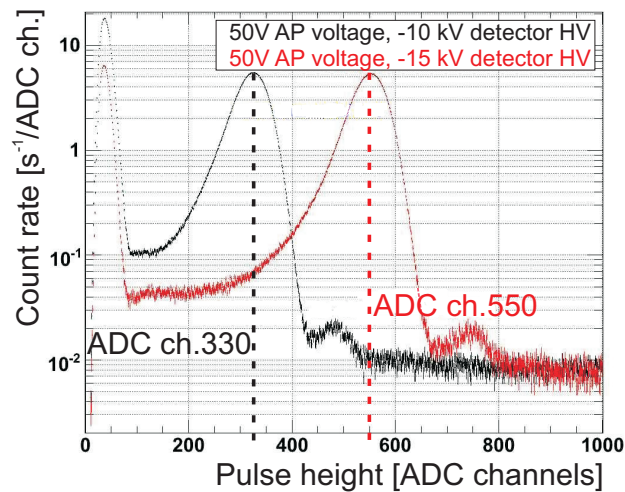
Figure 6.33: Comparison of pulse height spectra measured at 50 V APV for -10 and -15 kV detector HV. The proton peak shifts about 220 ADC channels whereas the small peak on the right tail shifts by about 265 ADC channels. The number of channels is not directly proportional to the energy difference of 5 keV: The energy loss in the dead layer of the detector is energy dependent at low proton energies of several keV ([32]).

When we ramped up the detector HV in the beginning of the beam time, persistent leakage currents and resulting discharges forced us to stop at -10 kV. Therefore, we measured for several days with this lower HV setting and waited for better HV-conditioning. Unfortunately, one of the discharges damaged the outer detector pads (channel 5 and 7) and we could only measure with the central pad. Surprisingly, one of the outer channels (ch.5) "resurrected" for one day during data set "060508_night". Although the reason for that stayed undetermined, this was the only recorded data set with 2 detector pads. It

could contain additional informations on the off-center characteristics of the proton beam and the APV-dependent background. The outer detector channels could show effects induced by particles or radiation hitting the electrode system. Therefore, they could be an indicator for the discussed irradiation of electrodes in the DV.

Nevertheless, malfunctions of detector ch.5 during the data set "060508_night" could not be excluded in the off-line data analysis (e.g., if the trigger settings and amplification were comparable to the central detector pad ch. 6). Therefore, the main observations will be of qualitative nature: (1) The proton peak at -10 kV detector HV is by about 220 ADC ch. shifted to lower pulse heights (compared to -15 kV) as shown in fig. 6.33. The number of ADC ch. is not directly proportional to the difference of the proton impact energy (-5 keV): The energy loss in the dead layer of the detector depends as well on the impact energy for low energetic protons of several keV (see sect. 3.5, eq. 3.39) [32].

(2) The spectral shape measured at -10 kV detector HV differs from detector ch.5 to ch.6 as illustrated by the plots in fig. 6.34. The electronic noise peak is shifted to higher ADC channels for detector ch.5. The proton peak is wider and shifted to lower ADC channels. Therefore, the separation from the electronic noise peak is much worse. For the comparison of count rates, the lower integration limit had to be increased from ADC ch. 80 to 120. The electron count rate measured at 780 V APV (fig. 6.34b) in the limits ADC ch. 120 to 4000 is $121.28(17)\,\mathrm{s}^{-1}$ for detector pad ch.5 and $100.83(15)\,\mathrm{s}^{-1}$ for ch.6 (i.e., a deviation of $20.45(23)\,\mathrm{s}^{-1}$ or about 20%). The higher electron count rate on the outer detector ch.5 might be an indication for the discussed primary irradiation of electrodes by γ´s, neutrons and decay electrons. The proton count rates differ also but are higher for the central ch.6 as shown in fig. 6.35.

(3) In the spectra with neutron beam "off" (status 5) (see fig. 6.36a at 780 V APV), there is only one background peak (peak1) clearly visible for all APV-settings. Its intensity increases linearly with the APV as shown in fig. 6.36b. The APV-dependence is comparable to measurements at -15 kV detector HV. The observed background peak is centered at ADC ch. 230 ± 5 (for 780 V APV) which is about 188 ADC channels lower than for -15 kV detector HV. The shift indicates that protons or positive charged ions generate peak1. A possible explanation for the absence of background peak2 would be the negligible production of initial electrons by field emission at the detector cup (e17) at -10 kV.

6.10.4 Background study without electrostatic mirror (peak1)

For several systematic tests we grounded the electrostatic mirror electrodes $e1$ and $e2$. We performed one long-time measurement (data set "090508_MirrorOff") in this configuration at -10 kV detector HV. There is no comparable data set available at -15 kV detector HV which has sufficient statistical accuracy. Hence, only the impact on background peak1 could be studied and compared to the previously discussed measurement "060508_night" (all other parameter settings are equal).
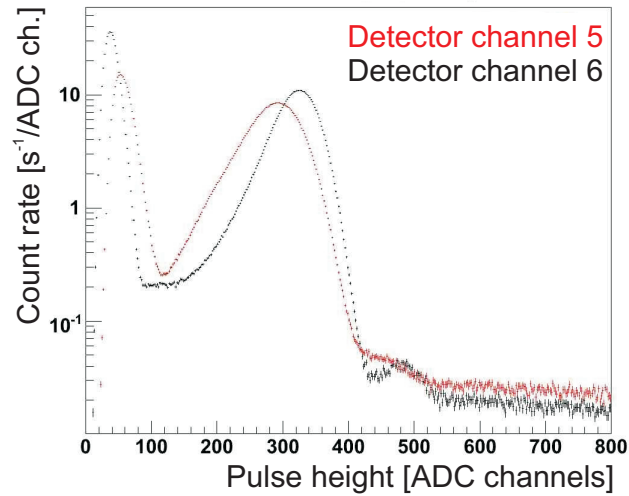
(a) Status 3, 50 V APV
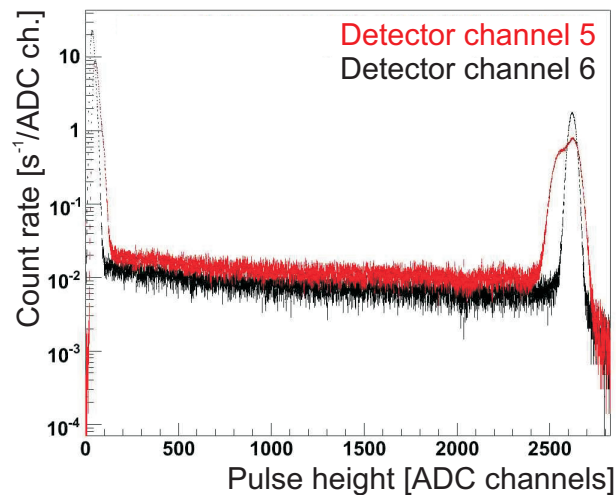
(b) Status 3, 780 V APV

Figure 6.34: Spectra measured at -10 kV detector HV with neutron beam "on" (status 3) for data set "060508_night". Two detector pads were working: Ch.6 is the central pad which was working all the time. Ch.5 was only working during that data set, but it is not clear, if it was working properly! (a) 50 V APV spectra: Ch.5 has a higher electronic noise level and the proton peak is wider and shifted. The spectra are rebinned to show more clearly the peak on the right tail of the proton peak which looks more flat for ch.5. (b) 780 V APV: Ch.5 shows a higher level of electron background in the entire spectrum and about $+20 \, \mathrm{s}^{-1}$ between ADC ch. 120 to 4000.- The electron peak on the right border of the spectrum has a broader shape compared to channel 6.
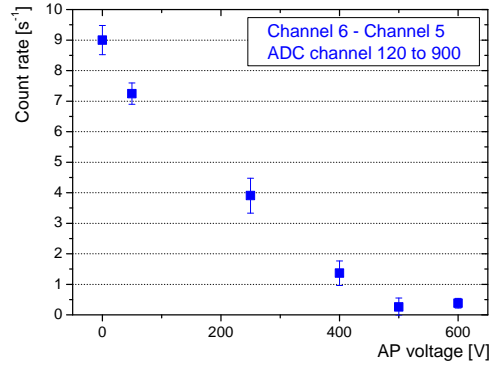
Figure 6.35: Count rate difference between detector ch.6 (central pad) and ch.5 after sub-
traction of 780 V background. The count rates were extracted in the limits
ADC ch. 120 to 900.
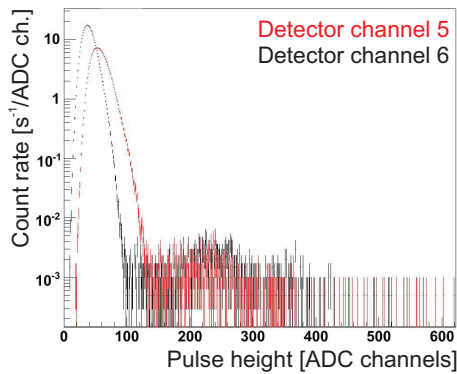
(a) Status 5, 780 V APV.
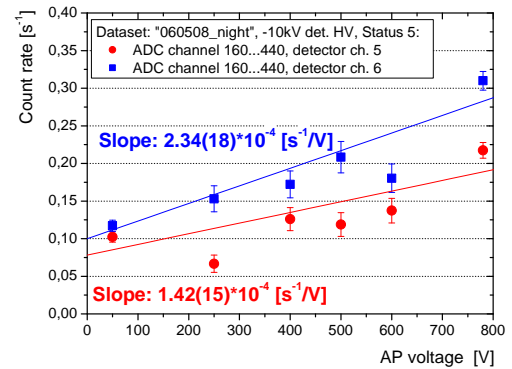
(b) Status 5, peak1.

Figure 6.36: (a) Spectrum for 780 V APV with neutron beam "off" (status 5). Only one
peak is clearly visible around ADC ch. 230. The dependence on the APV
in (b) is comparable to the behavior determined for background peak1 at -
15 kV detector HV. Both detector channels detect this peak, ch.5 with a lower
intensity. Peak2 can not be detected for any APV.
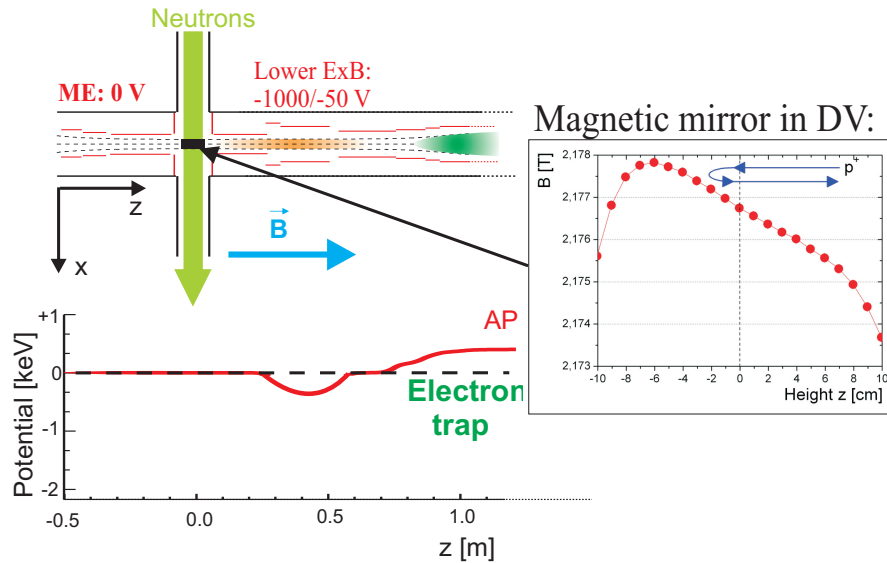
Figure 6.37: Scheme for the discussion of data set "090508_Mirror_Off". Top: The electrode system of *a*SPECT. Bottom: Schematic shape of the electric potential in the regions of interest. The main trap for protons between AP and ME is not effective when the ME is grounded. Only a small trap remains between AP and the magnetic mirror below the center of the DV.

Without electric mirror potential, the particle trap for positive charged particles between the ME and the AP is not effective anymore. Only a small trap of minor depth between AP and the magnetic mirror below the center of the DV remains (see: magnetic field shape in fig. 3.20a). A scheme of the electromagnetic setup without ME is drawn in fig. 6.37 as a reminder. Fig. 6.38 shows the count rates with neutron beam "off" in the integration window ADC channel 160 to 440 (peak1). They were extracted in the same integration limits as for "060508_night" before. The slope of the linear fit is equivalent to the one in fig. 6.36b for detector ch.6. Obviously, not the proton trap is dominant for the production of background peak1 but the electron trap between lower and upper ExB drift electrode. This explains also the linear dependence of the background count rates on the APV: The depth of the trap increases with the AP potential. Thus, more electrons can be trapped which can ionize residual gas.

The measurements for shutter status 5 were recorded over a longer time, 30 s instead of 10 s. The count rate distributions in fig. 6.39a and (b) confirm the assumption that the production mechanism of background peak1 is effective all the time and fluctuates randomly (e.g., even 22 s after the neutron beam was closed in (b)).
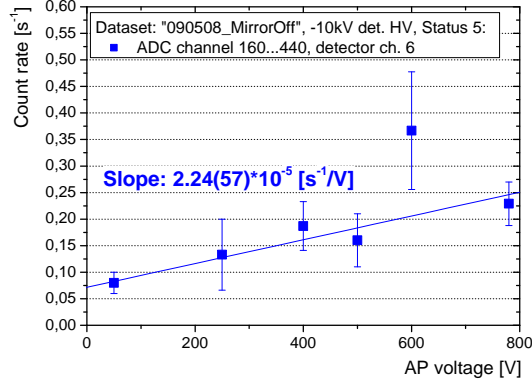
Figure 6.38: Measurements at -10 kV detector HV with neutron shutter closed (data set "090508_MirrorOff"). The electrostatic mirror electrodes $e1/e2$ were grounded. Thus, the trap for positive charged particles between AP potential and ME was switched off. Only a small amount of particles could be trapped between DV and AP due to the magnetic mirror effect. Nevertheless, a background peak around ADC ch. 220 could still be observed. Its dependence on the APV is comparable to the data set "060508_night" in fig. 6.36b (blue line for channel 6).

(a) Status 5, 600 V APV.

(b) Status 5, 780 V APV.
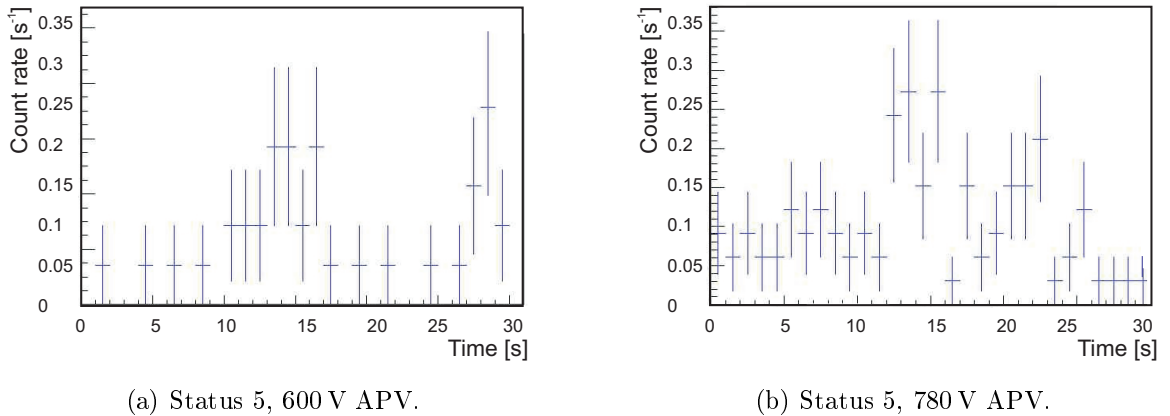
Figure 6.39: Count rate distribution in the pulse height region of background peak1 (ADC ch. 160 to 440) for shutter status 5 of the data set "090508_MirrorOff". The measurements were 30 s instead of 10 s long. Obviously, the count rate fluctuates and the source for that background peak is effective all the time.

6.10.5 Background study with reduced main magnetic field (peak1)

In the last days of the beam time, we reduced the main field current from 70 A to 30 A in order to test the influence of non-adiabatic proton motion on the coefficient a. This corresponds to a magnetic field strength of $B_0 \approx 0.933\,[\mathrm{T}]$ in the DV and $B_A \approx 0.189\,[\mathrm{T}]$ in the AP. Apart from the fact, that the adiabatic approximation does not hold, the reduced field strength increases the gyration radii of protons. Therefore, the imaging of the DV area on the detector is less focused and might include some new information on the background. Fig. 6.40 shows the dependence of background peak1 for shutter status 1 and 5. It looks different to previous results: For both shutter states, the count rates increase clearly linearly and are maximal for 780 V APV. The slope is by a factor of 2 higher than for measurements at 70 A main current. Calculations of proton trajectories in [30] might help to draw a more quantitative conclusion from this observations.
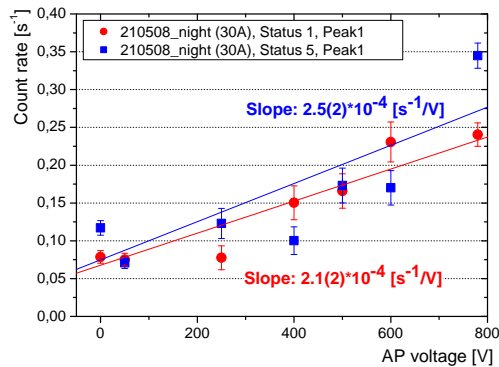
Figure 6.40: Data set: "200508_night". The main field current was reduced from 70 A to 30 A. Count rates for background peak1 with neutron shutter closed (status 1 and 5) are drawn. Obviously, the count rates depend linearly on the APV, the slope is increased by a factor of about 2 compared to measurements at 70 A. It can not be answered by this measurement, why the effect that produces peak1 is strengthened. Generally, the proton trajectories are influenced by the lower magnetic field and the impact of non-adiabatic motion. Also the focusing onto the detector is different to standard parameter settings, a wider neutron beam is "seen" by the detector.

6.11 Appendix 11: Additional TOF-studies

6.11.1 TOF-spectra I: Impact of ExB drift electrodes

The upper ExB-drift electrode (see fig. 3.9) was kept on 3 different voltage settings: (1) -2/-2 kV, (2) -4.2/-0.2 kV and (3) -3.7/-4.3 kV. Setting (1) introduces no drift and (2) a strong drift whereas the average acceleration potential on the flux-tube axis is close to -2 keV as well. The influence of these two settings can be seen in fig. 6.41. All measurements with setting (1) show higher count rates for short time differences. The average count rates

APV [V]	(1) upper ExB: -2/-2 kV Count rate [1/s]	(2) upper ExB: -4.2/-0.2 kV Count rate [1/s]	Ratio (1)/(2)	Difference (1)-(2)
50	45.9(9)	35.3(7)	1.30(4)	10.6(11)
400	18.8(7)	14.4(6)	1.31(7)	4.4(9)
600	3.26(29)	2.50(23)	1.30(17)	0.76(37)

Table 6.8: Average count rates measured at the upper ExB settings (a) and (b) by integrating from 0 to 100 μs coincidence time difference. The ratio stays constant.

extracted from the coincidence time interval 0-100 μs are listed in tab. 6.8. The rates are a factor of 1.3 higher for measurements with settings (1) -2/-2 kV in the upper ExB electrode. The ratio stays constant for all APV-settings. The total proton count rates extracted from pulse height spectra in the PIW (i.e., correlated and uncorrelated proton events) do not show such high deviations as shown by fig. 6.42 (e.g., 2.06(43) [1/s] instead of 10.6(11) [1/s] at 50 V APV). This count rate difference might be due to the changed alignment of the flux-tube onto the detector for both upper ExB-settings. Thus, one can conclude that some coincidences get lost (at the edges of the detector) due to the spatial separation of electrons and protons by the ExB-drift. The amount of detected electrons in the EIW is comparable for all measurements and therefore not responsible for the reduction of coincidences. The lower ExB electrode influences as well the TOF-spectra. Two standard settings were used: (a) -1000/-50 V and (b) -200/0 V. Fig. 6.43 shows the comparison of spectra for both ExB settings at -10 and -15 kV detector HV. In both cases, the weaker drift corresponds to higher count rates. But the higher average potential with setting (a) shows a minimal shift of the shortest flight times (5-7.5 μs). Although the shortest time difference was calculated to be about 6 μs, all spectra start earlier at about 5 μs. This fact can be explained by the occurrence of uncorrelated events. G. Konrad discusses simulations on the influence of the ExB-drifts on the TOF-Spectra in [30].
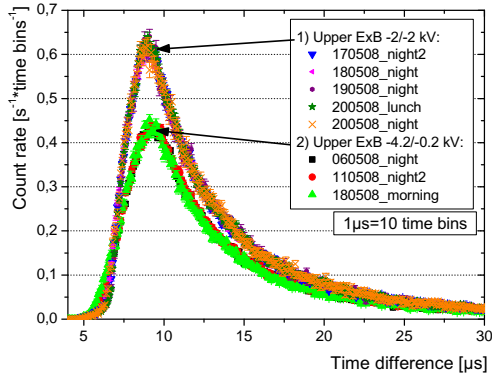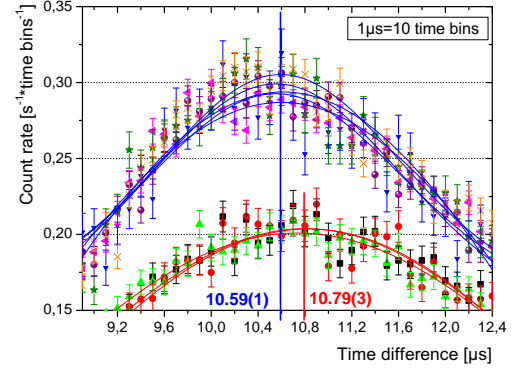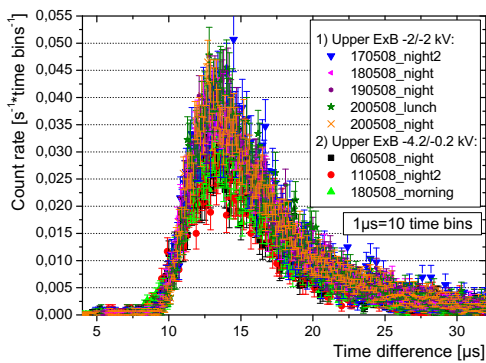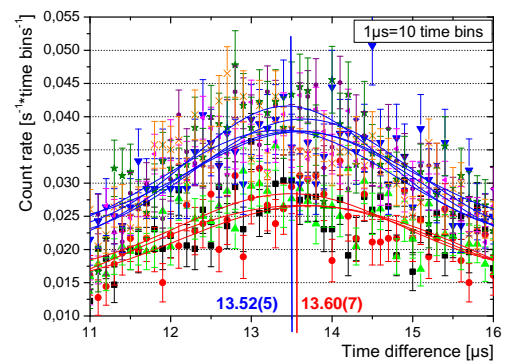
(a) 50 V APV.
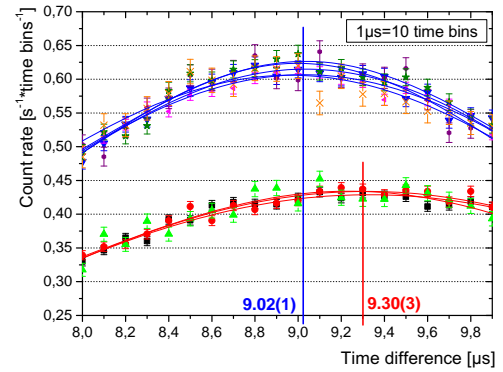
(b) 50 V APV, zoom.
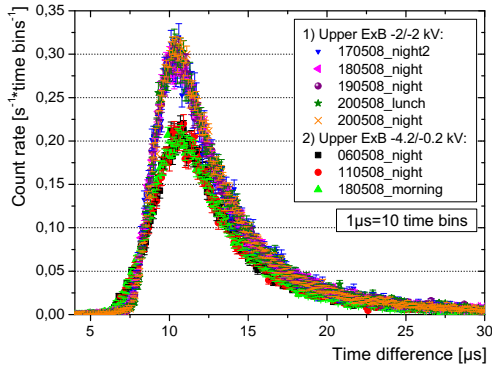
(c) 400 V APV.

(d) 400 V APV, zoom.

(e) 600 V APV.

(f) 600 V APV, zoom.

Figure 6.41: TOF-spectra for different upper ExB voltage settings: (1) -2/-2 kV and (2) -4.2/-0.2 kV. The count rates for the setting (2) are lower than for (1). At the edges of the detector, some of the coincidences might get lost due to the drift in (2) that spatially separates coincident events. In addition, the TOF-spectra are distorted minimally for short time differences (5-8μs). This can be explained by the different acceleration potentials: For setting (1), all protons see a mean potential of -2 keV. For setting (2), protons at the borders of the flux-tube might see potentials of >-3 keV and <-1 keV. The position of the maximum shifts as shown in the zoomed plots (b, d, f). The blue and red lines are Gaussian fits at the peak positions.
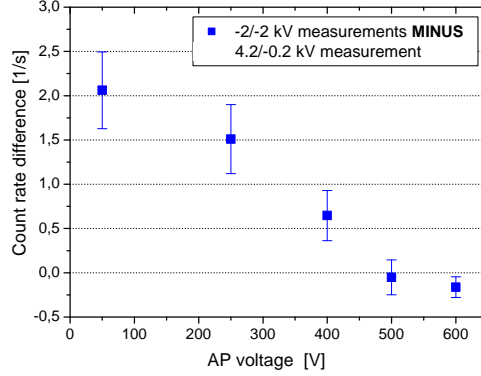
Figure 6.42: Count rate differences (1-2) between measurements at different settings of the upper ExB voltages: (1) -2/-2 kV and (2) -4.2/-0.2 kV. The count rates were extracted from proton pulse height spectra (correlated and uncorrelated proton events) measured at -15 kV detector HV in the PIW. They are much lower compared to the count rate differences in tab. 6.8, which were extracted from TOF-spectra (only correlated proton events) in a coincidence time interval from 0 to 100 μs.
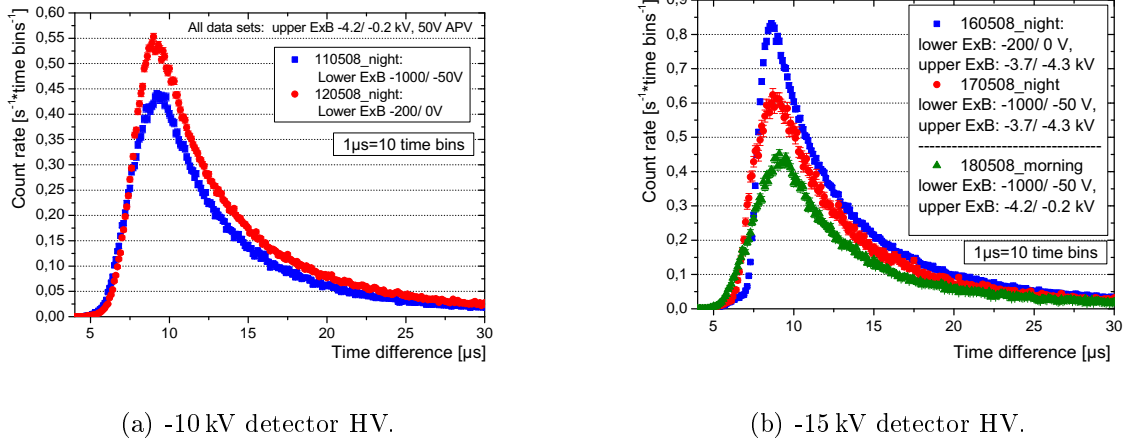

(a) -10 kV detector HV.   (b) -15 kV detector HV.

Figure 6.43: Influence of lower ExB drift on the TOF-spectra. The red curves always correspond to -200/0 V and the blue curves to -1000/-50 V. In (b) a second spectrum (green) for -1000/-50V lower ExB potential but -4.2/0.2 kV in the upper ExB is included. It points out the dominant influence of the upper ExB on the shape of the TOF-spectrum at very short time differences (about 5-7.5 μs)

6.11.2 TOF-spectra II: Backscattered electrons

For the major fraction of detected coincidences the electrons were emitted in the upper and the protons in the lower hemisphere (type (1) in fig. 4.45). By grounding the mirror electrode, mainly events of type (2) can occur in which backscattered electrons play a crucial role. Fig. 6.44 illustrates the results of these measurements.
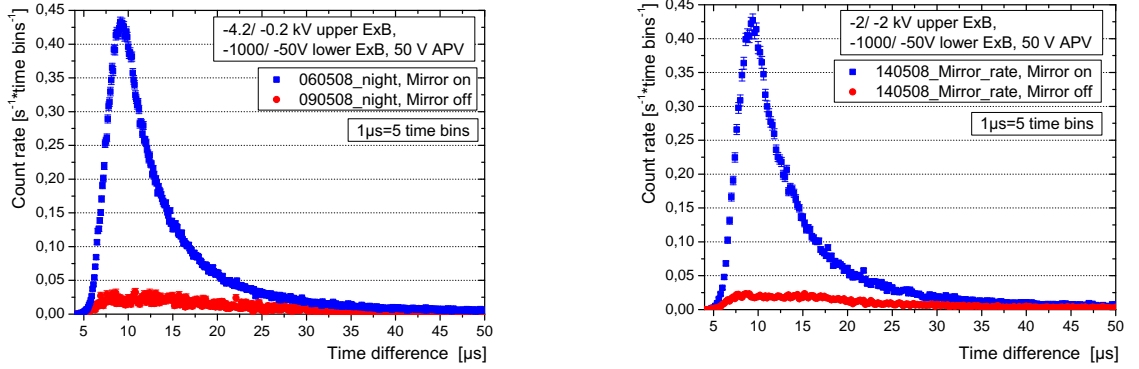
(a) Mirror on/off, 50 V APV, -10 kV det. HV.

(b) Mirror on/off, 50 V APV, -15 kV det. HV.
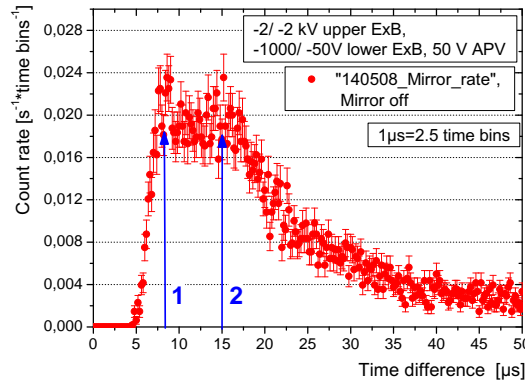
(c) Mirror off, 50 V APV, -15 kV det. HV. Zoom.

Figure 6.44: Measurements with and without ME. (a) Taken from the data sets "060508_night" and "090508_MirrorOff" at -10 kV. (b) Data set "140508_Mirror_rate" at -15 kV measured with reduced beam width of 20 mm (see profile in fig. 3.19, but the detected proton count rate with reduced neutron beam width is only by a factor of 1.1 lower. Therefore, the results are comparable to (a). In the zoom (c), two peaks are observed: The first one corresponds to coincidences by backscattered electrons (type 2 in fig. 4.45) and the second one to direct electrons with protons emitted in steep angles in the upper hemisphere (type 1c in fig. 4.45) as calculations by G. Konrad showed. From these spectra and further calculations a count rate of 20-30 s^{-1} would be possible for backscattered electrons.

6.12 Appendix 12: A first implementation of a calibration source

As discussed in sect. 3.6.1 an accurate knowledge of the transmission function is recommended. One possibility is to scan the transmission function by a mono-energetic calibration source. The best way would be to place it inside the DV moveable in x-y-direction (z=0). Since the time between the FRM-II and ILL beam time was too short, we decided to implement first of all an ion source to be able to perform detector tests inside of aSPECT in Mainz. It is an electron impact gaseous source usable with helium or hydrogen. It was mounted below the bottom flange of aSPECT using the magnetic field for guidance of the ions. The vacuum system can be separated from the main vacuum with a CF35 gate valve and is pumped separately with a roughing and turbo mulecular pump.

The principle is the following: Gas flows through an U-shaped tube to the center of the spectrometer which can be aligned by a belows (fig. 6.45a, left side). The tube has a small opening with a funnel-like electrode in z-direction. Below the hole an electron source is placed. This can be a simple tungsten wire filament or a BaO-cathode (ES-015 from KIMBALL PHYSICS INC.) for better energy resolution. The gas-tube as well as the electron source can be set on different potentials and the potential difference is used to accelerate the electrons onto the gas ions in the hole of the tube. Above the hole a set of extraction electrodes attracts the positive ions and retracts the electrons. Also these electrodes are hold on potentials which can be ramped relatively to each other. A disc with a hole of 0.5 mm diameter in the middle of the extraction electrodes separates the source vacuum from the main vacuum (when the gate valve is open). This was necessary since the gas inlet control system had to be tested first and I could not risk to vent or inflate the spectrometer. I calculated that the gas flow from the source vacuum through this hole would not critically affect the main vacuum, requiring a given pumping power. Gas which is not ionized is pumped away from the outlet tube (fig. 6.45b). The electron source can be aligned via a viewing port (fig. 6.45c), when using a tungsten filament the glowing can be checked. First tests with the source were done in July 2007 in Mainz. At that time the electrode system of aSPECT was partly in preparation for the ILL beam time, therefore only the additional electrodes of the source, the upper ExB drift electrodes and the detector electrode were powered. The silicon drift detector was not implemented yet and thus, all test were done with the PIN-diodes used at FRM-II at -30 kV detector HV. Helium gas was used for ionization. I had only a view days for the tests since several other components had to be tested for the ILL beam time, therefore a real characterization was not possible. The fig. 6.46 only gives first impressions of spectra for different electron energies (a) and various extraction voltages (b). In 2008 (between the mounting of aSPECT and the beam time) I built up the source at the ILL. Again only a small time gap was open since magnetic field measurements and the repair of a part of the electrode system forced us to turn the spectrometer several times which meant dismounting of the source. But the vacuum performance of the source was improved by insertion of another leak
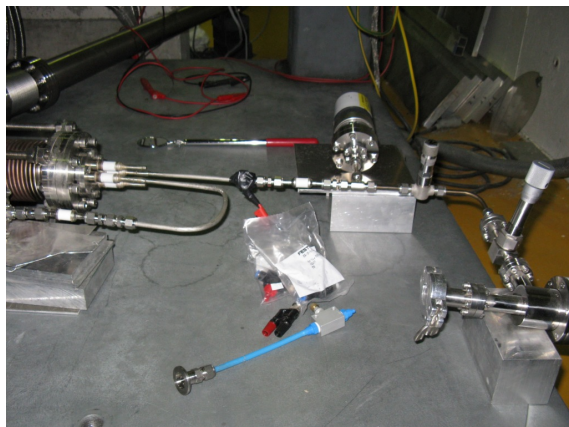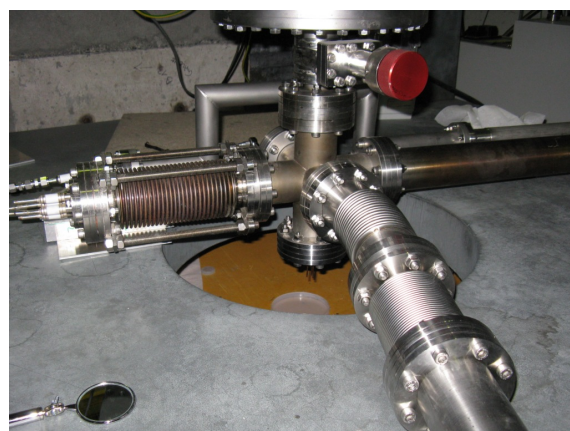
(a) Gas inlet (right).
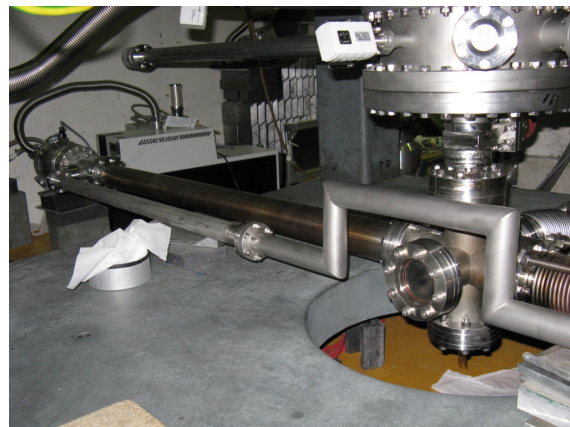
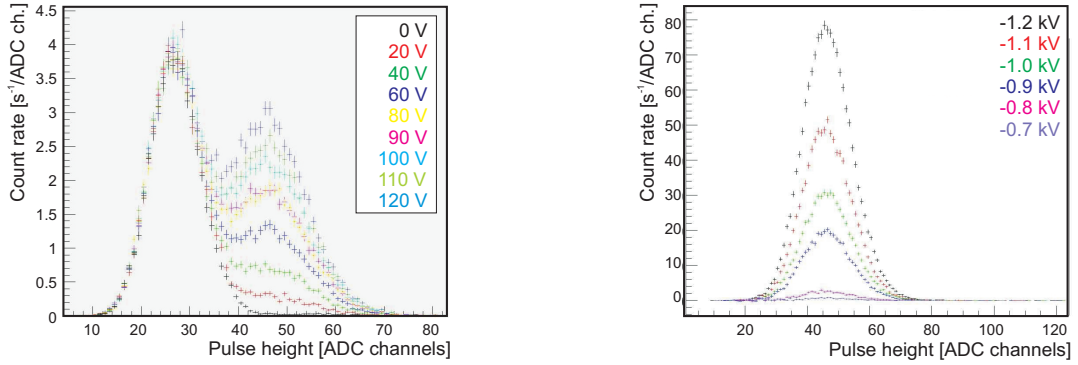(b) Gas is pumped from the outlet via CF35-tubes to the pump (left).
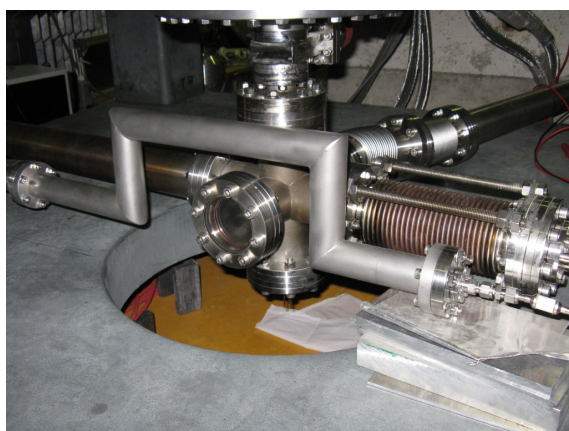
(c) Vacuum chamber with viewing port on electron source.

(d) Vacuum chamber, backside.

Figure 6.45: Impressions from the source built up in 2008 at the ILL.

(a) Variation of the acceleration voltage of electrons (heating current 1.5 V).

(b) Variation of the extraction voltage for ions.

Figure 6.46: Impressions from the first source tests in 07/2007. Due to the high count rates in (b) the thermal noise peak on the right tail is suppressed.

valve at the gas inlet. The pressures in the gas inlet tube was $p_{inlet}^{source}=1.3\times10^{-5}$ mbar with closed gas inlet and $p_{inlet}^{source}=5.8\times10^{-3}$ mbar when it was open. The pressure in the source chamber was $p_{chamber}^{source}=3.3\times10^{-8}$ mbar with closed gas inlet and $p_{inlet}^{source}=8.8\times10^{-7}$ mbar else. The increased but stable pressure in the source chamber also influenced the main vacuum. It dropped from $p^{main}=7.4\times10^{-9}$ mbar to $p^{main}=4\times10^{-8}$ mbar but stabilized at $p^{main}=1.4\times10^{-8}$ mbar after 5 min.

Source tests with the electrode system inserted and the SDD resulted in the induction of voltage breakdowns and strong discharges which destroyed one of the detectors: The source was driven as in the tests before in Mainz. When applying an additional extraction voltage to the grid electrode e1 suddenly an avalanche of particles was registered by the detector and the HV crashed down. This effect was tested to be reproducible (without detector) and therefore we stopped the source tests to protect the detectors. It is not clear, what went wrong. One assumption is, that the grid electrode might have as well ionized helium gas which was flowing from the source into the spectrometer and the ions induced a sudden potential drop in the detector region.

(a) Required material for cleaning: 2 beakers (1 for crushed LiF, 1 for powder), mortar, 1-2 sieves (raw/ fine), scalpel, gloves, paper.

(b) A mill (type "Retsch S1000") is needed to make powder out of the pieces. Duration: 45 min at "Speed=70".

Figure 6.47

6.13 Appendix 13: Production of LiF-plates

(a) Separation of old, used LiF parts with and w/o glue and removal of glue with scalpel.

(b) Crushing in small pieces in a mortar.

Figure 6.48

(a) Container with 5 ceramic balls.

(b) Filled container.

(c) After the mill the powder is sieved to filter out unseen pieces of glue.

(d) Required material: steel plate (5 mm thick, $18 \times 18 \, cm^2$), funnel, container for LiF powder left over, thin plate, brush, Al-plate, AL-frame (11 mm thick, $11 \times 11 \, cm^2$) + AL-plate that fits in, breathing protection, AlO-foil (3 pieces, each $12 \times 12 \, cm^2$).
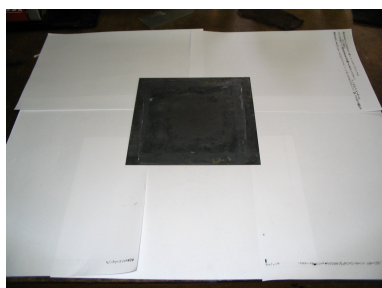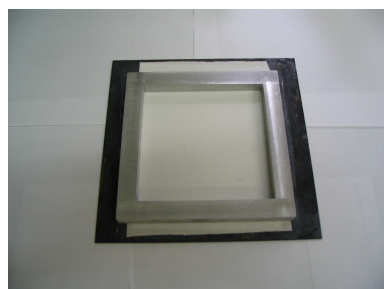

(e) Clean the table and place steel plate on paper.

(f) Cover it with two pieces of AlO-foil which prevents the LiF to react with the steel surface while baking.
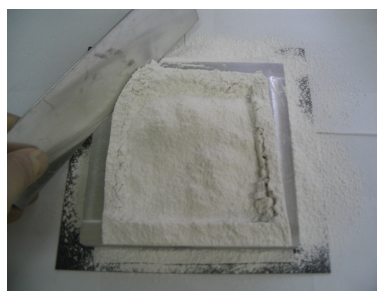
Figure 6.49

(a) Place Al-frame in the middle.

(b) Place sieve in the center and fill it with LiF-powder .

(c) Distribute the powder in the complete frame with powder.

(d) Use a long thin Al-plate to wipe off the excessive powder.

(e) After wiping off: Sometimes powder is missing in the edges of the frame. Then redo the last 2 steps.

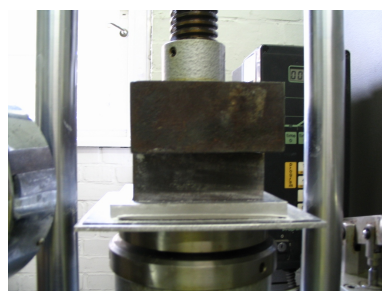(f) Use brush to remove the LiF from top the frame and around the frame and recollect the powder.
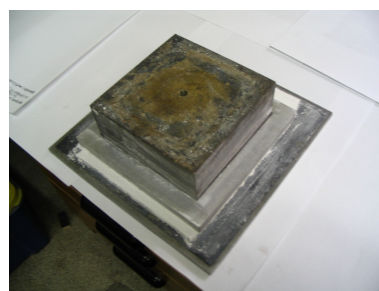
Figure 6.50

(a) The hydraulic press is used to solidify the powder into a ≈5 cm thick plate.
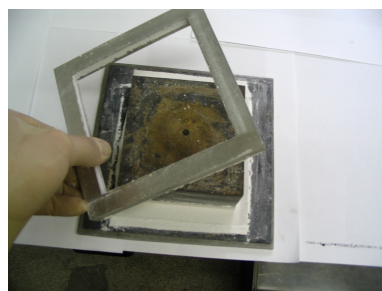

(b) The fitting AL-plate has to be placed on the powder inside the frame (w/o picture). A steel brick with the same dimensions comes on top and can be hold be a screw.
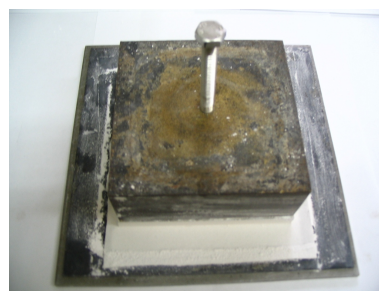

(c) Pressing of the plate by applying a second brick to bridge the distance to the piston. A pressure of 20 tons is applied for 30 s.
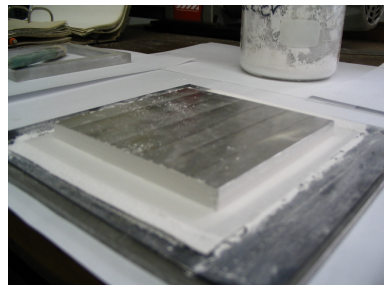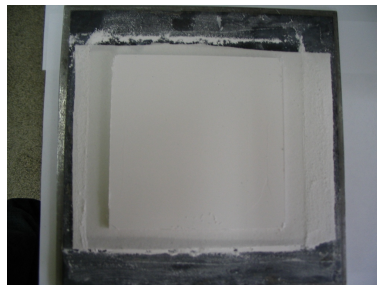

(d) After pressing.

(e) Remove the Al-frame.

(f) Remove the steel brick carefully with the screw.

Figure 6.51

(a) The Al-plate has to be removed by hand touching two edges.

(b) LiF-plate after pressing. If there are visible fissures in the plate, continue with next step, else with step (b) in fig. 6.50.
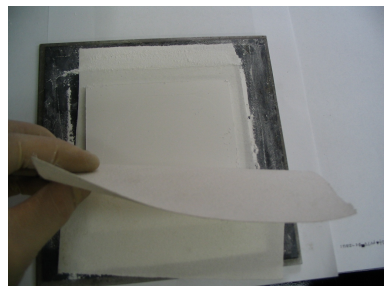
(c) Cover plate with one AlO-foil.
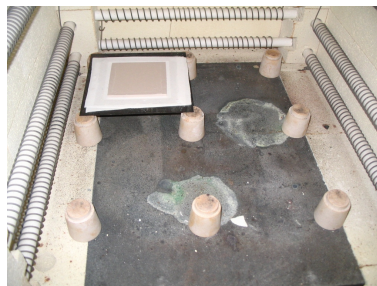
(d) Place it in the oven. 4 plates can be baked at the same time. The oven is heated linearly in $360\,\mathrm{min}$ to $740^\circ\mathrm{C}$. It stays on this temperature for $360\,\mathrm{min}$ and it takes nearly 1 day to cool down to $50^\circ\mathrm{C}$.

(e) After backing. Sometimes the edges may brake.

(f) Sometimes more brakes.

Figure 6.52

Bibliography

[1]   Baeβler, S. *et al.*, 2008, Europhys. Journ. A, **38**, p.17-26

[2]   C. Stratowa, R. Dobrozemsky, and P. Weinzierl, 1978, Phys. Rev. D **18**, 3970

[3]   Byrne, J., P.G. Dawber, M. G. D. van der Grinten, C.G. Habeck, F. Shaikh, J.A. Spain, R. D. Scott, C. A. Baker, K. Green and O. Zimmer, 2002, J. Phys. G **28**, 1325

[4]   Severijns, N., Beck, M., Naviliat-Cuncic, O., 2006, Rev. Mod. Phys. **78**, 991

[5]   Abele, H., 2008, Prog. Part. Nucl. Phys. **60**, 1

[6]   Lamoreaux, S.K., Golub, R., 2009, *Experimental searches for the neutron electric dipole moment*, J.Phys. G, 36(10):104002 (37pp)

[7]   Amsler, C., *et al.*, 2008, *Particle Data Group*, Physics Letters B **667**, 1

[8]   Arzumanov, S., L. Bondarenko, S. Chernyavsky, W. Drexel, A. Fomin, P. Geltenbort, V. Morozov, Y. Panin, J. Pendlebury, and K. Schreckenbach, 2000, Phys. Lett. B **483**, 15

[9]   Serebrov, A. *et al.*, 2005a, Phys. Lett. B **605(1-2)**, 72-78

[10]   Jackson, J. D., Treiman, S. B. and Wyld Jr., H. W., 1957, Phys. Rev. **106(3)**, 517-521

[11]   de Simon, Patricia, for the KLOE collaboration, 2009, *$|V_{us}|$ and CP violation from kaon decays with the KLOE detector*, Journal of Physics: Conference Series 171 (2009) 012051

[12]   Goudzovski, E., 2009, *Recent results from the NA48 experiment at CERN: CP violation and CKM parameter $|V_{us}|$*, Journal of Physics: Conference Series 110 (2008) 052019

[13]   Varvell,K.E., 2006, *Experimental Review of Exclusive Semileptonic B Meson Decays and Measurements of $|V_{ub}|$*, Flavor Physics and CP Violation Conference, Vancouver

[14]   Blucher, E. *et al.*, 2005, *Status of the Cabibbo Angle*, Proceedings of the CKM 2005 conference, arXiv:hep-ph/0512039

[15]   Towner, I. S., Hardy, J. C., 2007 -> arXiv:0710.3181v1

[16]   Wu, C. S., Ambler, E., Hayward, R. W., Hoppes, D. D. and Hudson, R. 1957, Phys. Rev. **105**, 1413

[17]   Bopp, P., D. Dubbers, L. Hornig, E. Klemt, J. Last, H. Schütze, S. J. Freedman and O. Schärpf, 1989, Phy. Rev. Lett. **56**, 919

[18]   Abele, H., M. A. Hoffmann, S. Baeβler, D. Dubbers, F. Glück, U. Müller, V. Nesvizhevsky, J. Reich, and O. Zimmer, 2002, Phys, Rev. Lett. **88**, 211801

[19]   Yerozolimsky, B., I. Kuznetsov, Y. Mostovoy, and I. Stepanenko, 1997, Phys. Lett. B **412**, 240

[20]   Liaud, P., K. Schreckenbach, R. Kossakowski, H. Nastoll, A. Baussière, J. P. Guillaud and L. Beck, 1997, Nucl. Phys. A **612**, 53

[21]   Märkisch, B. *et al.*, 2009, *The new neutron decay spectrometer Perkeo III*, Nucl. Instr. and Meth. A, **611**, 216-218

[22]   Glück, F. *et al.*, 2005, Europhys. Journ. A **23**, 135

[23]   Nachtmann, O., 1968, *Zeitschrift für Physik* **215(5)**, 505-514

[24]   Glück, F., 1993, Phys. Rev. D, **47**, 2840

[25]   Muñoz Horta, R., 2010, PhD thesis (not submitted yet in September 2010), Mainz, Germany

[26]   Zimmer, O., J. Byrne, M. G. D. v.d. Grinten, W. Heil, F. Glück, 2000, Nucl. Inst. Meth. A **440**, 548

[27]   Ayala Guardia, F., 2005, Master's Thesis, Johannes Gutenberg Universität Mainz

[28]   Simson, M., 2006, Master's thesis, Technische Universität München

[29]   Petzoldt, G., 2007, Doctoral Thesis, Technische Universität München

[30]   Konrad, G., 2011, PhD thesis (not submitted yet in November 2010), Mainz, Germany

[31]   Ayala Guardia, F., 2011, PhD Thesis (not submitted yet in November 2010), Johannes Gutenberg Universität Mainz

[32]   Simson, M., 2010, PhD thesis (submitted in August 2010), Technische Universität München

[33]   Povh, B. *et al.*, 2002, *Particles and Nuclei*, Springer, Berlin, Heidelberg, New York, 3rd edition

[34]   Fermi, E., 1934, *Zeitschrift für Physik* **88**, 161

[35]   Bjorken, J.D. and Drell, S.D., 1963, *Relativistic Quantum Mechanics*, McGraw-Hill, New York

[36]   Gamow, G. and Teller, E., 1936 Phys. Rev. **49(12)**, 895-899

[37]   Glück, F., 1995, *Measurable parameters of neutron decay*, Nuc. Phys. A, **593(2)**, 125-150

[38]   Lee, T. D. and Yang, C. N., 1956, Phys. Rev. **104**, 254

[39]   Cabibbo, N., 1963 Phys. Rev. Lett. **10(12)**, 531-533

[40]   Kobayashi, M. and Maskawa, T., 1973, Prog. Theo. Phys. **49**, 652

[41]   Wietfeldt, F.E. *et al.*, 2009, *acorn: An experiment to measure the electron-antineutrino correlation in neutron decay*, Nucl. Instr. and Meth. A,**611(2-3)**, 207-211

[42]   Grigorev, V.K. *et al.*, 1968, *Experimental test of parity conservation in beta decay*, Sov. J. Nuc. Phys., 6-239

[43]   Habeck, C. G., 1997, Doctoral Thesis, University of Sussex

[44]   Hsu, T., Hirshfield, J. L., Rev. Sci. Instrum. **47**, 236

[45]   Beamson, G., Porter, H. Q., Turner, D. W., 1980, J. Phys. E **13**, 64

[46]   Wilkinson, D.H., 1982, Nucl. Phys. A **377**, 474

[47]   Otten, E.W., Weinheimer, C., 2008, Rep. Prog. Phys. **71**, 086201

[48]   Soldner, T., 2010, PhD thesis, Technical University Munich

[49]   Kruit, P., Read, F. H., 1983, J. Phys. E **16**, 313

[50]   Lobashev, V. M., Spivak, P. E., 1985, Nucl. Instrum. Methods A **240**, 305; Picard, A., Backe, H., Barth, H., Bonn, J. *et al*, 1992, Nucl. Instrum. Methods B **63**, 345; Weinheimer, Ch., Degen, B., Bleile, A., Bonn, J., Bornschein, L., Kazachenko, O., Kovalik, A., Otten, E. W., 1999, Phys. Lett. B **460**, 219

[51]   Osipowicz, A. *et al.*, 2001, arXiv:hep-ex/0109033; Weinheimer, Ch., 2008, arXiv:hep-ex/0210050v2

[52]   Abele, H. *et al.*, 2006, Nucl. Instr. Meth. A **562**, 407

[53]   Schumann, M., 2007, PhD thesis, University of Heidelberg, Germany

[54]   Knöpfler, A. *et al.*, 2001, Nucl. Instr. and Meth. in Phys. Res. A **485**, 453-457

[55]   National Nuclear Data Center (NNDC), Brookhaven National Lab., www.nndc.bnl.gov/sigma

[56]   Krempel, J., 2004, Diploma thesis, University of Heidelberg, Germany

[57]   Scott, G. B., M. Springford and J. R. Stockton, 1968, Journ. of Phys. E **1**, 925

[58]   Kittel, C., *Einführung in die Festkörperphysik.*, 2006, Oldenbourg, München, 14th edition

[59]   Lutz, G., 1999, *Semiconductor Radiation Detectors.*, Springer, Berlin, Heidelberg, New York, 1st edition

[60]   Kleinknecht, K., 1992, *Detektoren für Teilchenstrahlung.*, Teubner, Stuttgart, 3rd edition

[61]   Bethe, H., *Zur Theorie des Durchgangs schneller Korpusstrahlen durch Materie.*, 1930, *Ann. Physik*, 397(3): 325-400

[62]   Bloch, F., *Zur Bremsung rasch bewegter Teilchen beim Durchgang durch Materie.*, 1933, *Ann. Physik*, 408(3): 285-320

[63]   Simson, M. *et al.* 2007, Nucl. Instr. and Meth. A **581**, 772-775

[64]   Lechner, P. *et al.* ,2004, XRS, **33**, 256-261

[65]   Gatti, E. and Rehak, P., 1984, Nucl. Instr. and Meth. A **225**, 608

[66]   Semiconductor   Laboratory   of   the   Max-Planck-Institut   für   Physik and   the   Max-Planck-Institut   für   extraterrestrische   Physik (http://www.hll.mpg.de)

[67]   PNSensor GmbH (http://www.pnsensor.de)

[68]   Brun, R. and Rademakers, F., 1997, *ROOT - An Object Oriented Data Analysis Framework*, Proceedings AIHENP'96 Workshop, Nucl. Instr. and Meth. A 389, 81-86, http://root.cern.ch

[69]   Northrop, T.G., *The Adiabatic Motion of Charged Particles*, 1963, Interscience Publ.

[70]   The Controlled Fusion Atomic Data Center, www-cfadc.phy.ornl.gov (go to: ELASTIC, Isotopomers of hydrogen ions)

[71]   Mueller, A.R. *et al.*, *PAFF, a low-energy, low-flux proton accelerator for detector tests.* 582(2):395 - 400, 2007

[72]   Leo, W. R., 1994, *Techniques for Nuclear and Particle Physics Experiments*, Springer-Verlag, 2nd edition

[73]   Vogt, H.-G. and Schultz, H., *Grundzüge des praktischen Strahlenschutzes*, Hanser, München, 2010, 5th edition

[74]   Lone, M. A., D. C. Santry and W. M. Inglis, 1980, Nucl. Instr. Meth. **174**, 521

         Further publications on aSPECT:

[75]   Baeβler, S. *et al.*, 2006 Proceedings of the CIPAN06 Conference. Puerto Rico, AIP Conf. Proc. **870**, 287

[76]   Simson, M. *et al.* 2008, Proceedings of the IWPPSN Workshop. Institut Laue-Langevin, Grenoble, France. Nucl. Instr. and Meth. A **661**, 203-206

[77]   Konrad, G. *et al.* 2009, Proceedings of the PANIC08 conference. Eilat, Israel. Accepted for publication at Nucl. Phys. A

[78]   Muñoz Horta, R. *et al.*, 2006, Proceedings of the XIV International Seminar on Interaction of Neutrons with Nuclei. Joint Institute for Nuclear Research, Dubna, Russia.